ADVANCED STEEL CONSTRUCTION

An International Journal

Volume 21 Number 4

August 2025

CONTENTS

Technical Papers

Website: *http://www.hkisc.org*
ISSN 1816-112X
Science Citation Index Expanded, Materials Science Citation Index and ISI Alerting
Cover: Greater Bay Area Cultural and Sports Center, China. Photo@ Li Hua-Bo
e-copy of IJASC is free to download at "www.ascjournal.com" in internet and mobile apps.

ADVANCED STEEL CONSTRUCTION

VOL.21, NO.4 (2025)

ADVANCED STEEL CONSTRUCTION

an International Journal

ISSN 1816-112X

Volume 21 Number 4 *August 2025*

ISSN 1816-112X

Science Citation Index Expanded, Materials Science Citation Index and ISI Alerting

Advanced Steel Construction
an international journal

Cover: Greater Bay Area Cultural and Sports Center, China. Photo@ Li Hua-Bo
e-copy of IJASC is free to download at "www.ascjournal.com" in internet and mobile apps.

General Information
Advanced Steel Construction, an international journal

Aims and scope

The International Journal of Advanced Steel Construction provides a platform for the publication and rapid dissemination of original and up-to-date research and technological developments in steel construction, design and analysis. Scope of research papers published in this journal includes but is not limited to theoretical and experimental research on elements, assemblages, systems, material, design philosophy and codification, standards, fabrication, projects of innovative nature and computer techniques. The journal is specifically tailored to channel the exchange of technological know-how between researchers and practitioners. Contributions from all aspects related to the recent developments of advanced steel construction are welcome.

Subscription inquiries and change of address. Address all subscription inquiries and correspondence to Member Records, IJASC. Notify an address change as soon as possible. All communications should include both old and new addresses with zip codes and be accompanied by a mailing label from a recent issue. Allow six weeks for all changes to become effective.

The Hong Kong Institute of Steel Construction
HKISC
c/o Prof. SL Chan,
Unit 209B, Photonics Centre, No. 2 Science Park East Avenue,
Hong Kong Science Park, Shatin, N.T., Hong Kong, China.
Tel: 852- 3595 6150 Fax: 852- 3619 7238
Email: ceslchan@connect.polyu.hk Website: *http://www.hkisc.org/*
ISSN 1816-112X
Science Citation Index Expanded, Materials Science Citation Index and ISI Alerting

ISSN 1816-112X

Science Citation Index Expanded, Materials Science Citation Index and ISI Alerting

Advanced Steel Construction
an international journal

VOLUME 21 NUMBER 4 August 2025

Technical Papers

Advanced Steel Construction – Vol. 21 No. 4 (2025) 277–293
DOI:10.18057/IJASC.2025.21.4.1

LATERAL DYNAMIC RESPONSES OF GFRP TUBE CONCRETE-ENCASED STEEL COMPOSITE COLUMN WITH FIXED ENDS

Hai-Xia Zhang * and Shi-Long Ju

School of Civil Engineering, Shenyang Jianzhu University, Shenyang 110168, China
** (Corresponding author: E-mail: zhanghaixia@sjzu.edu.cn)*

ABSTRACT

In this study, a finite element (FE) model of a GFRP tube concrete-encased steel composite column (GTCES) with fixed ends was established to investigate its dynamic behavior under vehicle collisions, with the accuracy of the FE results was verified and calibrated by comparisons with the experimental results. The impact force, lateral displacement, local indentation, reaction and inertia force, bending moment and shear force, energy absorption, damage evolution and failure model, and GFRP tube confinement effect were analyzed, with the results illustrating that the impact process can be divide into three stage. Concrete is an important factor in carrying the impact loads. Subsequently, the influences of the axial force ratio, concrete strength, encased steel yield strength, steel ratio, and impact velocity on the dynamic behavior of the GTCES columns were investigated using parametric experiments. The findings revealed that the peak local indentation decreased by 22.78% and the peak impact force increases by 19.49%, respectively, with increasing the axial force ratio from 0 to 0.6. When the strength of concrete increased from 30 MPa to 40 MPa, the decreases of peak and residual lateral displacements were 23.91% and 25.89%, respectively. Additionally, the more severe damage on the GTCES column was observed at the higher impact velocities.

ARTICLE HISTORY

Received: 31 October 2024
Revised: 4 January 2025
Accepted: 8 January 2025

KEYWORDS

Impact response;
Finite element model;
GFRP tube;
Concrete-encased steel column

1. Introduction

Fiber-reinforced polymer (FRP) composites have been applied in civil engineering due to their exceptional material qualities, which include high strength, superior corrosion resistance, and low self-weight [1-3]. One wide application is that the FRP composites as tubes combined with steel and concrete to develop new composite constructions, such as FRP-concrete steel double-skin tubular columns (DSTCs) [4-8], concrete-filled in FRP tubes with longitudinal steel bars and FRP-confined concrete-filled steel tubes(CCFTs) [9-12]. The FRP tube serves as a formwork during concrete pouring, and provide a corrosion-resistant skin to protect core concrete from corrosion when the composite construction serves in corrosive engineering environments. Furthermore, the FRP tubes serve as a confinement system that enhances the mechanical properties of the concrete [13,14].

Simultaneously, GFRP tube concrete-encased steel composite columns (GTCES), a novel form of hybrid columns [15], are prepared by surrounding the encased steel with an outer GFRP tube, which is then filled with concrete. The concept of the GTCES column was proposed by Liu, as a rehabilitation technique for strengthening the corroded steel members [16]. The corroded steel members were enclosed by two semi-circular GFRP tubes, which were then filled with lightweight expanded concrete. An axial compressive test was conducted on the composite columns. The composite columns exhibited suitable mechanical properties. Since then, a few investigations have been conducted on the composite column [17-22]. The investigations revealed that the GTCES column had a superior mechanical performance under static and seismic loading conditions. And axial, flexural and eccentric carrying ability calculation methods and hysteretic restoring force models were proposed for GTCES columns [17,20,22,23]. Thus, GTCES columns have promising applications in vital members such as buildings and bridges.

With the increase in transport accidents, the composite columns may be exposed to impact loads from vehicles while in the service. When accidents happen, the composite columns is destroyed, causing the structural collapse and posing a threat to life safety. Recently, the dynamic behaviors of hybrid composite columns with FRP tubes have been studied. Pham et al. [24] used the drop weight tests on a CFTs column to research its axial impact performance. These findings presented that the mechanical resistance of columns could be enhanced by the outer FRP tube confinement effect. Meanwhile, the axial impact performance of the CFTs column with inner steel spiral reinforcement was studied by Huang [25]. The results showed that the inner steel spiral reinforcement improved damage resistance of the CFTs. The lateral dynamic performance of the CFTs was also investigated. Wang et al. [26] studied the lateral dynamic behaviors of CFTs. They found that the peak displacement of the column decreased with increasing fiber volume fraction of FRP tubes, due to the confinement effect of FRP tube was enhanced. Chen et al. [27] also found that improving the confinement effect of FRP tube would lead to a reduction in maximum displacement of CFTs. Furthermore, the impact resistance of CFTs would be improved with embedding the steel spiral reinforcement [28]. Simultaneously, the lateral dynamic performance of DSTCs was investigated and the main parameters analysis were conducted. Chen et al. [27] tested and numerically simulated DSTCs under the lateral impact loads. These findings indicated that the DSTCs exhibited a higher impact resistance with increasing the thickness of FRP tube. Abdelkarim et al. [29,30] established the numerical simulation models for DSTCs under vehicle collisions to study its dynamic responses. The results demonstrated that the main resistance of DSTCs came from inner steel tube and dynamic resistance were affected by the mass and velocity of impactor. Wang et al. [31] carried out the test investigations on the DSTCs members to explore their dynamic responses. The findings demonstrated that the impact resistance of DSTCs was significantly influenced by the impact velocity. Furthermore, the numerical simulation models were established according to test results [31], and the numerous parameter studies were analyzed [32]. Zhang et al. [33] studied the response of DSTCs members under impact load. The results revealed that the specimens presented flexural failure and that a large void ratio decreased the maximum displacement of members. In summary, the previous investigations mainly concentrated on the static and seismic responses of the GTCES column and the dynamic behaviors of the CFFs and DSTc members. However, the investigations on the impact performance of GTCES columns were limited under vehicle collision conditions, thus making it essential to reveal its dynamic behaviors.

In this study, the finite element models of the GTCES columns with fixed-ends were developed to explore their dynamic behavior under vehicle collisions. The simulation results were verified. Subsequently, to reveal the mechanical characteristics, failure modes, the role of each component of GTCES column, the valid model was employed to perform an analysis on the impact process, inertial force, the distribution of bending moment and shear force, the change rule of energy dissipation, damage evolution and failure modes and the GFRP tube confinement effect were discussed in detailed. Finally, the influences of several parameters such as axial force ratio, concrete strength, encased steel strength, steel ratio and impact velocity were analyzed to clarify the main parameters affecting on the lateral impact performance. This study provides a reference to develop the numerical model of GTCES under the dynamic load and reveals its dynamic behaviors. The results offer a reference for anti-impact designs and reinforcement maintenance.

2. Validation of numerical simulation techniques

2.1. Exiting experiments

The experiments in Ref. [31] were selected to calibrate the accuracy of the finite element models of the GTCES under lateral impact. The material components of the specimens were FRP tube, concrete and steel, that were identical to the GTCES columns. Furthermore, the dynamic performance of the GTCES un-

der an axial load was studied. The experimental results in Ref. [34] were employed to verify the modeling technique for coupling the lateral impact and axial loads.

2.2. Establishment of finite element model

The finite-element software ANSYS/LS-DYNA was used to simulate the specimens subjected to the impact load. The details of the finite element model development were presented as follows.

2.2.1. Materials model

The steel responses in numerical models were evaluated by *MAT_PIECEWISE_LINEAR_PLASTICITY model [34], which can be used to define an elasto-plastic material, and consider an arbitrary strain rate dependency. The strain rate effect on the steel was considered and the dynamic increase factor for the steel was employed by the Cowper and Symonds Model [35], as expressed in Eq. (1).

$$\mathrm{DIF} = 1 + \left(\frac{\dot{\varepsilon}}{C}\right)^{\frac{1}{p}} \tag{1}$$

where DIF is the dynamic increase factor, which means the ratio between dynamic stress and static stress; $\dot{\varepsilon}$ is strain rate; C and p were the strain rate parameters, and the values of C and p were 40.4 s^{-1} and 5, respectively [36].

The *MAT_CSCM _CONCRETE model (CSCM) was used to characterize the dynamic behavior of concrete. And it is a smooth continuous surface cap model that effectively considers the strain rate effect on the concrete, and predicts its hardening, softening and shear damage of the concrete [37]. Besides, to prevent computational difficulties with a very low stiffness, the erosion algorithm was used in this material model which was determined by the value of maximum principle strain. Referring to Ref. [38], the ERODE was set to 1.08 to accomplish element erosion. Moreover, many studies have indicated that this model can model the nonlinear response of concrete accurately under impact load [36,38,39].

The FRP material was modeled using *MAT_LAMINATED_COMPOSITE_FABRIC which is a damage mechanics-based model that can be utilized to simulate composite materials with woven fabrics complete laminates and unidirectional layers. Many studies have demonstrated that the FRP material shows a minor strain rate effect under the impact loading compared with steel and concrete [28,32,40]. The strain rate effect on FRP material was neglected in the finite element.

The *MAT_RIGID model is designed to simulate the impactor in this study, which can save the computational time and have achieved accurate results in previous studies [28,32].

2.2.2. Contact definition, boundary conditions and applying axial load

The Contact_Automatic_Surface_Surface algorithm was utilized to model the interactions between the different components. The contact algorithm can be implemented to treat contact between bodies with dissimilar material properties. In the contact algorithm, the dynamic and static friction coefficients for interface between the steel and concrete were set as 0.5 and 0.6, respectively [41]. And for the interface between impactor and FRP tube the dynamic and static friction coefficient were taken as 0.25, 0.25 for the interface between the FRP tube and concrete [28].

The keyword *Boundary_SPC_SET was used to establish the boundary conditions which were identical to the tests. The coupling of axial force and lateral impact can be divided into two phases. Phase I: The end of column was exposed to an axial force using a distributed pressure through a dynamic relaxation analysis. Phase II: The FE analysis was restarted and a lateral impact was applied to the column.

2.2.3. Hourglass type and element type

The hourglass control type 4 was introduced into the numerical model to reduce the hourglass energy effect on the simulation precision [32]. The FRP tube was simulated by the Belyschko-Tsay element. The steel, concrete and impactor were simulated using the 8-node solid hexahedron element with single point integration algorithm.

2.3. Verification of the FE model

The FEM results were shown in Fig. 1, Fig. 2 and Table 1. From Fig.1, the bending failure mode of the experimental specimens [31,34] was reasonably predicted by FE model. From Fig. 2 (a) and Fig. 2 (b), the deviations of peak impact force and plateau vale of the impact force between the predictions and test results were 5.14% and 10.07% for specimen F3L01, and were 3.15% and 3.98% for specimen F3M01. The FEM model accurately captured the trend of the impact-time history observed in experimental results. Furthermore, the maximum displacements of the FEM were lower than the experimental results, with the deviations of 13.79% and 12.93%, respectively. This can be attributed to that the slippage occurred between the clamping system and specimen [31]. Whereas, the specimens were tightly constrained in the numerical model.

From Fig.2 (c) and Fig.2 (d), the impact force-time histories of the FEM fitted the experimental results well. For specimens DBF19 and DBF20, the deviations in peak impact force between the simulations and tests were 13.91% and 4.21%, respectively. The differences in the impact plateau force between the predicted and test results were 11.22% and 3.65%, respectively. Furthermore, the deviations in the maximum displacement between the predicted and experimental results were 14.04% and 13.04% for specimens DBF19 and DBF20, respectively.

In general, the comparative analysis demonstrates that the simulation method as above can be utilized to simulate the impact responses of a GTCES column when the lateral impact and axial load are coupled.

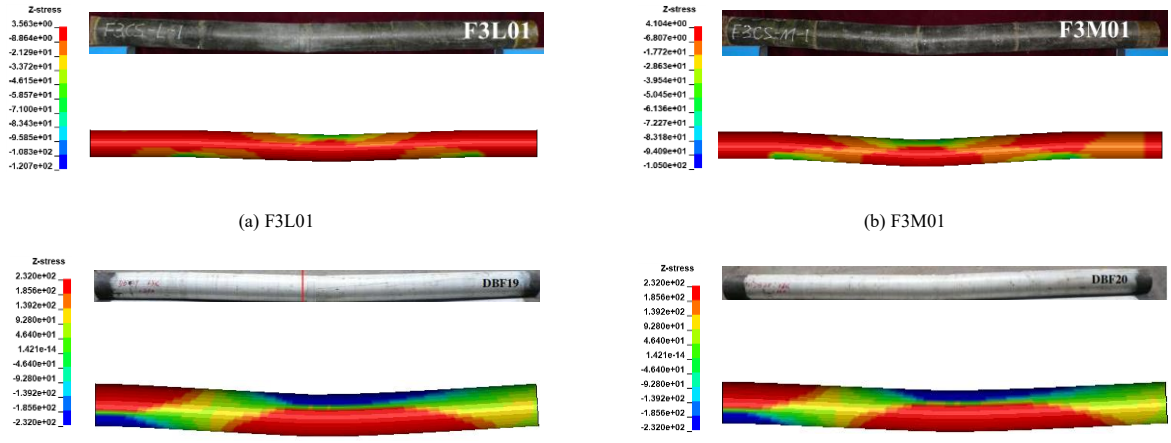

(a) F3L01 (b) F3M01

(c) DBF19 (d) DBF20

Fig. 1 Failure modes obtained from simulations and experiments

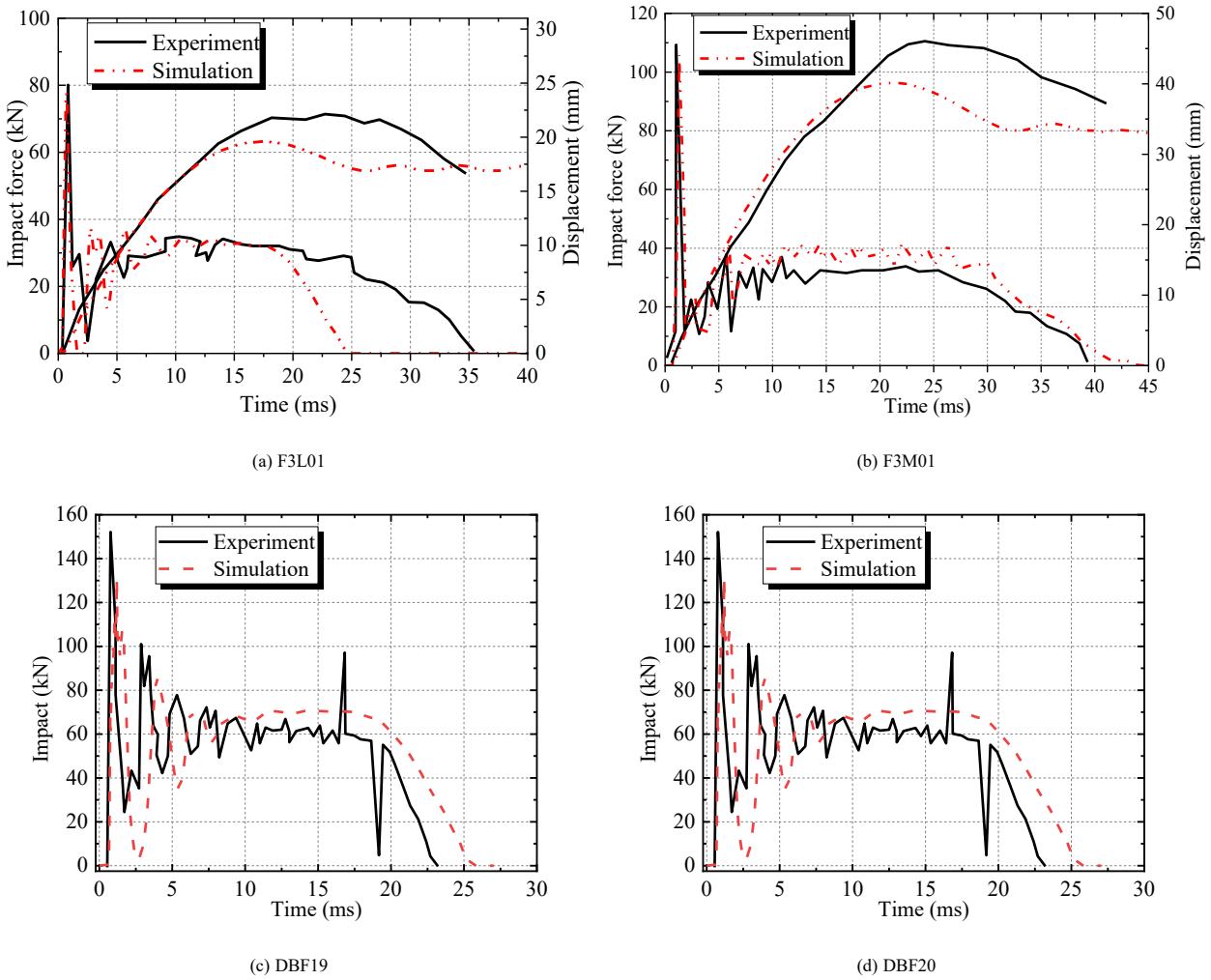

Fig. 2 Comparison of time-history curves between simulations and experiments

Table 1
Comparisons of key results [31,36]

Specimen	F_p (kN)	$F_{p,FEM}$ (kN)	Δ_{Fp}	F_{plat} (kN)	$F_{plat,FEM}$ (kN)	Δ_{plat}	δ_{max} (mm)	$\delta_{max,FEM}$ (mm)	Δ_δ
F3L01	78.8	74.7	5.14%	34.0	30.4	10.07%	23.4	19.6	13.79%
F3M01	107.8	104.4	3.15%	36.4	34.9	3.98%	47.1	40.1	12.93%
DBF19	152.1	131.5	13.91%	60.9	68.3	11.22%	17.8	20.3	14.04%
DBF20	118.1	116.3	4.21%	62.7	65.0	3.65%	25.3	28.6	13.04%

Note: F_p and $F_{p,FEM}$ are the peak impact force of test results and prediction, respectively; F_{plat} and $F_{plat,FEM}$ are the impact plateau force of test results and prediction, respectively; δ_{max} and $\delta_{max,FEM}$ are the maximum displacement of test results and prediction; Δ_{Fp}, Δ_{plat} and Δ_δ are the error of peak impact force, the impact plateau force and maximum displacement between test results and predictions, respectively.

3. FEM simulations of GTCES column

3.1. FEM modeling of GTCES column

Based on the modeling techniques described in the Section 2, a numerical simulation model of the GTCES column subjected to lateral impact was establish, as presented in Fig. 3. In this study, a 1/3 scale model of the GTCES column with a diameter of 270 mm and a height of 1300 mm and was investigated. The dimensions of the column referred to those using in office buildings [42]. The dimensions of the encased steel were plotted in Fig. 3. And the GFRP tube thickness was 5 mm, with its material properties described in Ref. [43]. The yield strength of encased steel was 235 MPa and the compressive strength of concrete was 30 MPa. The steel ratio was 3.41%, and axial force ratio was 0.3. And the calculated equations of steel ratio and axial force ratio were presented in Section 4. The axial force was applied on the column with a dynamic relaxation analysis in phase I (Fig. 3); In phase II, the freedoms of the column head were all fixed, with the stress on each component of the column were initiated using a FE analysis restarted. Finally, the impact load was applied on column.

A 10 t truck was chosen to as a vehicle model to impact the column. The vehicle mode was simplified as a flat-head impactor, which considers a rigid bumper of a truck and reduces the computational cost in simulations [38]. Referring to the [44], the heights of bumper upper and lower flanges of 10 t truck from the floor are 770 mm and 650 mm, respectively, when the truck is stationary. And the height of impact region was from 216.7 mm to 256.7 mm as considering the 1/3 scale model. Therefore, the length and width of the impactor were designed to be 280mm and 40mm as considering the diameter of the column and the width of the bumper. Referring to the scaling laws in Ref. [38], the initial kinetic energy of impactor in a small-scale model would be K^3 of those in a full-scale model and the K is the scale factor. While the velocity of the impactor is independent of scale factor K. Therefore, the impactor mass was decreased from 10 t to 0.3704 t by applying a reduction factor of 27 with a scale factor K=1/3. The impactor velocity was taken to be 10 m/s (36 km/h) in the numerical model, referring to the velocity grade of the vehicle [45].

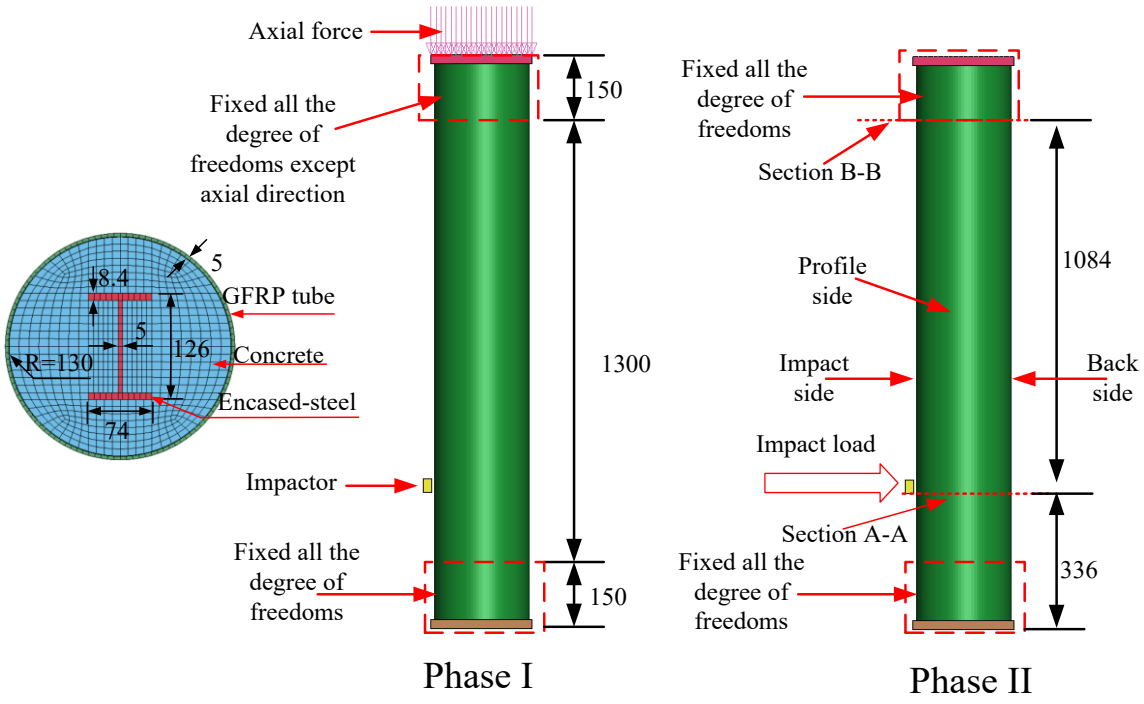

Fig. 3 Finite element model of GTCES column under lateral impact (unit/mm)

3.2. Response characteristics

3.2.1. Impact force, lateral displacement, local indication and velocity-time histories

Fig.4 showed the time-history curves of the impact force, lateral displacement (Position B), local indentation (Position A), velocity of the impactor, and velocity of the specimen. The time-histories were observed to consisted of three stages. Stage I (impact peak stage): The impactor and specimen were in contact at point O, and then the impact force rapidly increased to a peak value (1370 kN) at point A (1.409 ms); At point A, the lateral displacement was 3.98 mm, which was 30.90% of its maximum value. Additionally, the local indentation reached the maximum value 7.31 mm. Furthermore, the velocity of the specimen increased, due to the total energy transferred from impactor to the specimen as the velocity of the impactor decreased. After point A, the velocity of the specimen exceeded that of the impactor within a short period, thus indicating the specimen and impactor were separated. Which resulted in a sharp decrease in impact force until time B. Stage II (plateau stage): After point B, the velocity of specimen and impactor remained nearly constant and decreased, and underwent a small-amplitude oscillation. Additionally, the trend of impact force presents a relatively constant state. The lateral displacement gradually increased and reached its maximum value (12.88 mm) at point B (3.899 ms), indicating the ending of plateau stage. Furthermore, the impact force plateau value (F_{plateau}) was typically adopted to evaluate the impact performance of a member and was given as Eq. (1) [30,33]. The impact force plateau value of member was 844 kN.

$$F_{\text{plateau}} = \frac{\int_{t_1}^{t_2} F(t)dt}{t_2 - t_1} \tag{1}$$

where $F(t)$ was the impact force versus time curves; The t_1 and t_2 were the time points at time B and time C, respectively.

Stage III (descending stage): The velocities of the impactor and specimen were inconsistent in this stage, indicating the impactor and specimen were separated. And the specimen gradually bounced back. The impact force of the specimen decreased to zero at point D (6.719 ms). Furthermore, the residual lateral displacement and residual indentation were 10.62 mm and 4.21 mm, respectively.

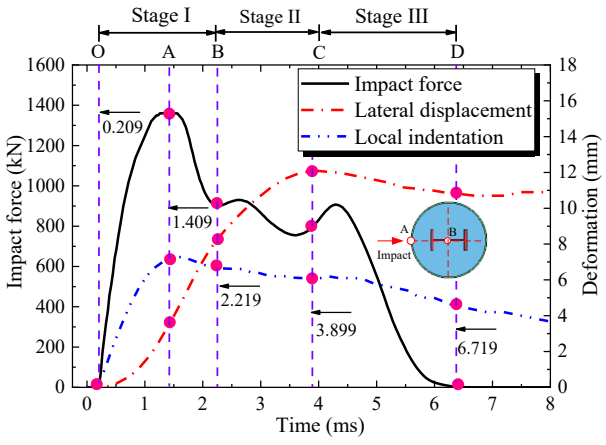

(a) Impact force, lateral displacement and local indication

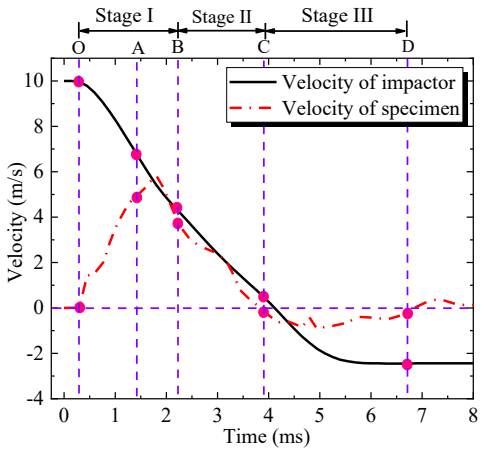

(b) Velocity of impactor and specimen

Fig. 4 Impact force, lateral displacement, local indication and velocity-time history curves

3.2.2. Shear force and bending moment along column height

The distributions of shear force and bending moment along column height were shown in Fig. 5. At 1.409 ms, the maximum shear force (-944.3 kN) and bending moment (95.8 kN·m) were observed at column height of 216 mm and 0 mm, respectively, corresponding to the lower edge of the impact area and bottom of the columns. From 1.409 ms to 3.899 ms, the maximum shear force remained at the lower edge of the impact area. With the development of impact time, the maximum shear force showed a decreasing trend. And the maximum bending moment shifted to the top of column. It demonstrated the column underwent a redistribution of the internal force. Furthermore, the highest value for bending moment showed 9.92% increment as compared to that at 1.409 ms, which was different to that of the shear force. This is because that the decrease in shear force resulted from the decrease in the impact force and the effect of inertia force. However, the lateral displacement of column gradually increased, leading to an increment in bending moment. At the end of impact, the largest shear force and bending moment appeared at the bottom of column and decreased significantly. Furthermore, a larger shear force was mainly concentrated in the area extending from the bottom column to impact area. The lager shear force area can be as a reinforcing specific region to prevent shear failure when GTCES columns subject to lateral impact.

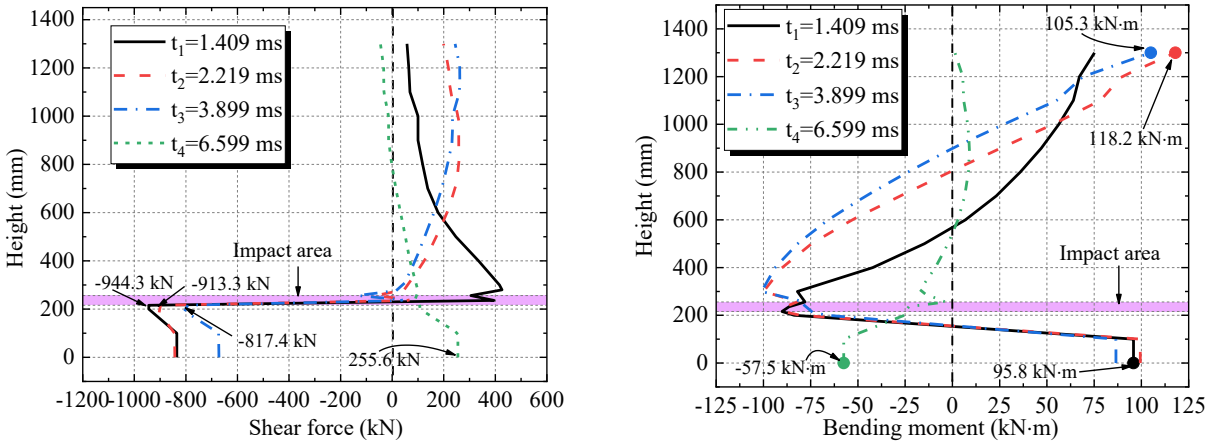

(a) Shear force (b) Bending moment

Fig. 5 Distribution of shear force and bending moment along column height

From the above discussion, the maximum shear force and bending moment occurred at the lower edge of impact area (Section A-A as shown in Fig. 3) and the top of column (Section B-B as shown in Fig. 3) during the impact, respectively. Therefore, the two sections were selected to investigate the internal force. The shear force and bending moment versus the impact time, as shown in Fig. 6. The contributions of different components to withstand shear force and bending moment were presented. From Fig. 6(a), the sign of shear force remained unchanged in the initial stage owing to that the section A-A was near the impact area. Besides, the shear force reached its maximum value (-990.3 kN) at AB stage. From Fig. 6(b), the bending moment presented negative in the initial stage, owing to the stress wave propagation. Then the bending moment gradually reached its maximum value (122.2 kN·m) at the initial of plateau stage. After the peak point, the shear force and bending moment showed downward trends. And the sign of shear force and bending moment changed at the end of descending stage due to the deformation of column recovered elastically. It can be concluded that the maximum shear force and bending moment were -990.3 kN and 122.2 kN·m and occurred at the Section A-A and Section B-B, respectively, which can provide a practical design value for dynamic shear force and bending moment.

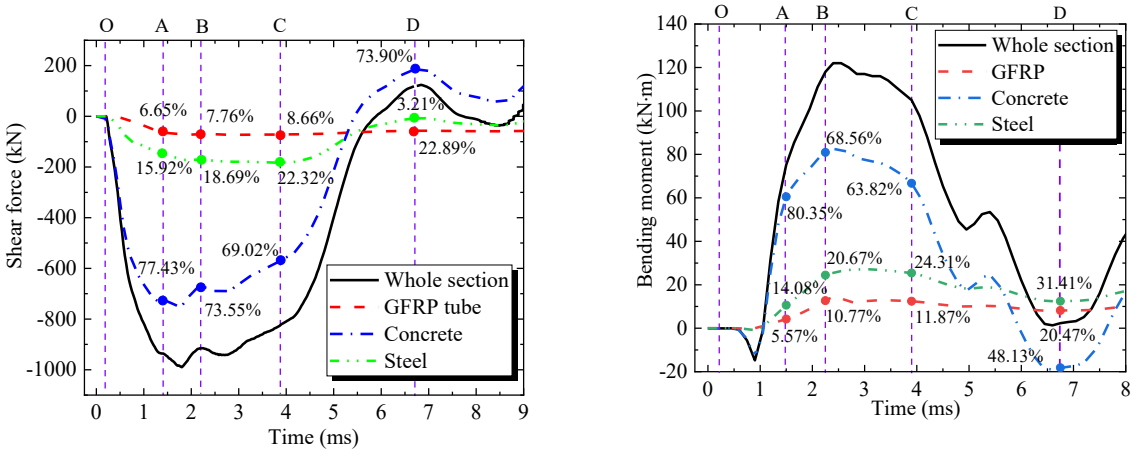

(a) Shear force at section A-A (b) Bending moment at section B-B

Fig. 6 Shear force and bending moment-time history curves

Furthermore, it can be found the shear force and bending moment were mainly withstood by the concrete, followed by the encased steel and GFRP tube. For instance, the shares of concrete in carrying the shear force and bending moment were up to 77.43% and 80.35% at A moment, respectively. During the AD stage, the share of GFRP tube and encased steel showed an increment as compared to that in OA stage. This indicated that the section underwent stress redistribution due to the concrete damage and the stress initially borne by the concrete transferred to the GFRP tube and encased steel.

3.2.3. Inertia force

When the impactor impacted the specimen, the inertia force was induced by the acceleration of specimen. The reaction and inertia force were calculated with Eq. (2), based on the force equilibrium.

$$F_{\text{impa}} + F_R + F_{\text{I}} = 0 \tag{2}$$

where F_{impa}, F_R and F_I were impact force, reaction force and inertia force, respectively.

Fig. 7 showed that the inertia and reaction force-time histories. The direction of impact force was considered to be positive. Fig. 7(a) showed that a time lag of 0.12 ms existed between the occurrence of the impact force and reaction force, indicating the response of the supports was delayed. This delay was attributed to the time required for the stress wave transfer from the impact point to supports. From Fig. 7(b), the trends of reaction and inertia forces were similar and the inertia force reached to a peak value at 0.99 ms. Furthermore, the inertia force resisted approximately 50% of the impact force in this stage. In the AC stage, the reaction force reached to a peak value in positive direction at 2.97 ms. The effect of inertia force on specimen was weaker than that during the OA stage. In the CD stage, the reaction force gradually decreased. Whereas, in the opposite direction, the inertia force increased compared to the BC stage to balance the force generated by the rebound of specimen. After the impact process, the specimen vibrated freely and the reaction force is balanced with reaction force. In summary, the influence of inertia force on GTCES column was significant in the initial and descending stages.

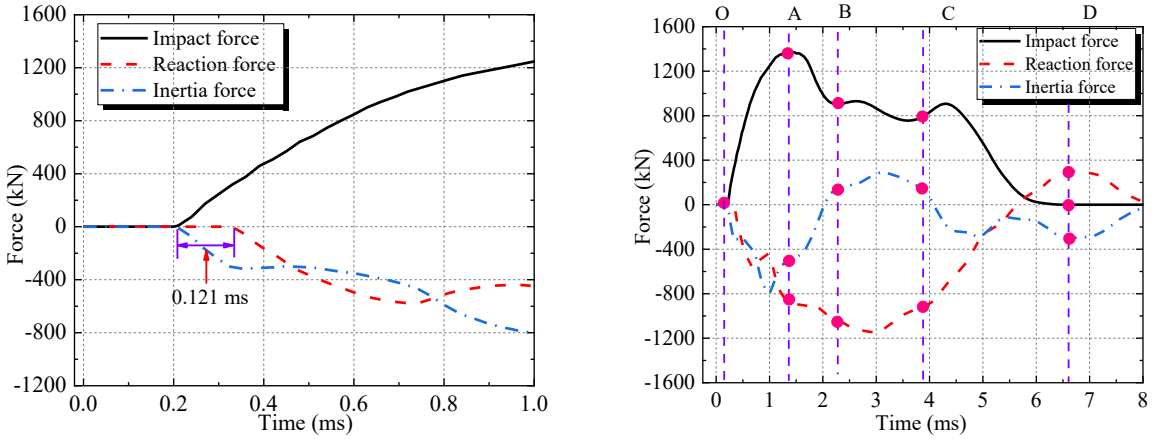

(a) Initial stage (b) Full stage

Fig. 7 Impact force, reaction force and inertia force-time histories

To investigate the influence of inertia force on the shear force and bending moment, Section A-A and Section B-B were selected. The internal shear force (F_C in Section A-A) and bending moment (M_C in Section B-B) were obtained from FEM results, and the shear force (F_F in Section A-A) and bending moment (M_F in Section B-B) induced by the impact load were calculated using Eq. (3) and Eq. (4).

$$F_F = \frac{F_{imp} \times b^2}{l^2} \tag{3}$$

$$M_F = \frac{F_{imp} \times a^2 \times b}{l^2} \tag{4}$$

where the a and b were the distance from the center of impactor to bottom and top of the column, respectively. And the l was the height of the column.

Fig. 8 plotted the F_C, F_F, F_C/F_F, M_C, M_F, and M_C/M_F time history curves. In the OA stage, the values of F_C and F_F were almost identical, and the average value of F_C/F_F was 0.99, as shown in Fig. 8(a). It suggested the inertia force had almost no influence on sectional shear force during this stage. In the AB stage, F_C/F_F increased from 1.03 to 1.52. The inertia force contributed to an increase in the sectional shear force. In the BC stage, the average F_C/F_F was 1.55 and tended to stabilize. In the CD stage, the value of F_C/F_F gradually decreased and reduced to 1.00 at 5.071 ms, demonstrating that the effect of inertia force on sectional shear force gradually decreased. From 5.071 ms to 5.882 ms, the value of F_C/F_F gradually decreased to 0, suggesting that the direction of sectional force induced by inertia force was opposite of impact load. After 5.882 ms, the value of the impact load tended to be 0 and the sectional shear force changed to opposite direction. In this stage, the sectional shear force was balanced with inertia force.

As seen in Fig. 8(b), it was possible to find that in the initial stage, the value of M_C/M_F was negative and the maximum value was -0.029, indicating bending moment due to impact load and inertia force were in opposite directions. The inertia force had a positive effect on sectional moment. After the initial stage, the sign of M_C/M_F changed and increased to 1.37 at time A. Subsequently, the value of M_C/M_F continued to increase until time B, indicating the inertia force increased the M_C. In the BC stage, the M_C/M_F tended to be consistent with an average value of 3.91. This phenomenon was similar to the inertia force effect on sectional shear force. During this stage, internal bending moment was more affected by the inertia force. In the CD stage, the value of M_C/M_F exhibited a downward trend until 4.829 ms, indicating that the effect of inertia force on sectional moment decreased. Subsequently, as the impact load decreased, the development of sectional moment was mainly driven by inertia force. Additionally, the inertia force had a greater effect on the sectional moment than the sectional shear force.

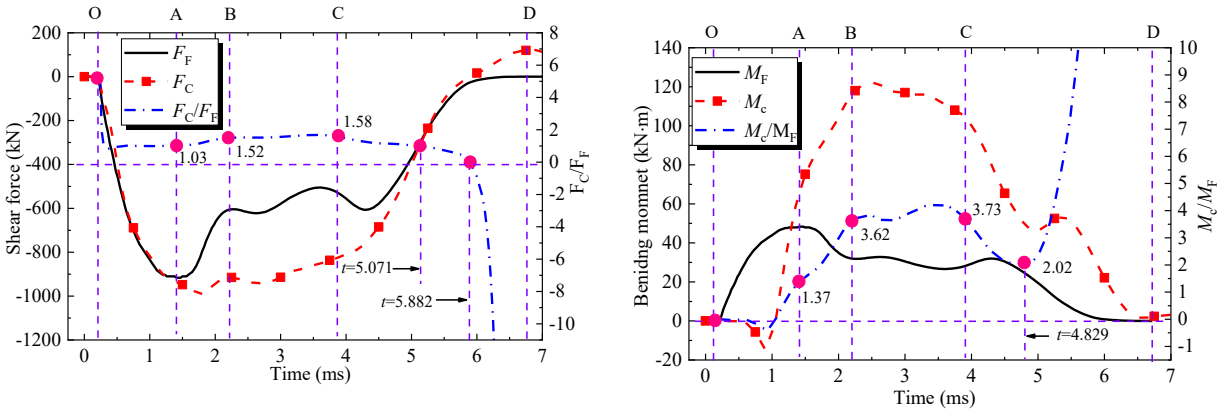

(a) F_F, F_c and F_F/F_c at section A-A (b) M_F, M_c and M_F/M_c at section B-B

Fig. 8 Effect of inertia force on shear force and bending moment

3.2.4. Energy absorption

Fig. 9 showed the energy absorption diagram of the column, which were obtained from the FEM analysis. During the OC stage, the total absorbed energy increased continuously with a decrease in the kinetic energy of impactor, reaching a maximum value at time C. Meanwhile, the kinetic energy of impactor descended to zero. This suggested the kinetic energy of impactor transferred to column continuously during this stage. After time C, the kinetic energy of impactor and total absorbed energy showed upward and downward trends, respectively. This is because the column underwent elastic recovery and the movement of the impactor reversed to the opposite direction.

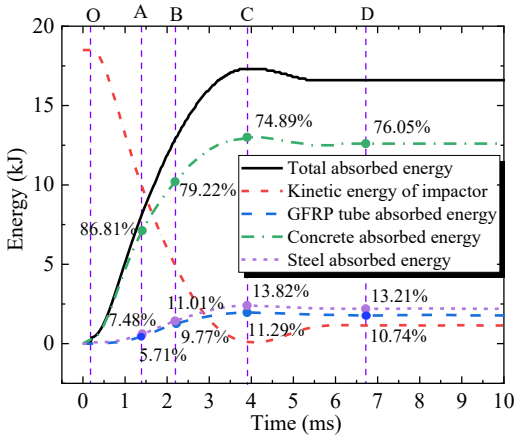

Fig. 9 Energy absorption-time history curve

Furthermore, the concrete absorbed a greater proportion of energy than other parts during the impact process. At time A, the concrete absorbed 86.81% of the energy, whereas the GFRP tube and encased steel absorbed 5.71% and 7.48%, respectively. And the concrete absorbed the higher energy owing to the local damage in impact area, which can be found in the local indentation of the column and concrete damage patterns. In addition, the total absorbed energy was 8.41kJ which was up to 48.61% of its peak value at this time, indicating that almost half of the internal energy was absorbed in this stage and the concrete in the impact area played an important role in this. In the AD stage, the concrete continued to made a significant contribution to energy absorption. Furthermore, the contribution of the encased steel and GFRP tube to absorbed energy presented an upward trend in comparison to that during the OA stage. This is because that each component of the column underwent stress redistribution as the impact developed during the AD stage.

3.2.5. Damage evolution and failure mode

The damage evolution in the column was plotted in Fig. 10. The damage to the concrete and encased steel was described by effective plastic strain. Matrix damage was used to describe damage to the GFRP tube.

At time A, the matrix damage of the GFRP tube occurred from the bottom of column to the impact area. A 45° damage path was formed between the impact side and back side. Additionally, slight damage occurred at the top of the column region on the impact side. In Section A-A, the damaged area was above 75% of the cross section. For the concrete, the cracking was initiated at the bottom of column and the impact area. The damaged area penetrated to the inner side of the flange of encased steel in Section A-A. The encased steel between the bottom of column and impact area was yielded. And the stress level on the web was higher than that on the flange. In addition, the entire cross section of the web developed into a plastic state in Section A-A. Furthermore, no damage was observed in Section B-B at time A. Subsequently, the matrix damage at the top of column and impact area propagated towards the middle of column. The more severe matrix damage to the GFRP tube was found between the bottom of the column and impact area. And the matrix damage occurred across the entire cross section in Section A-A. For the concrete, the damage level at the same location more was more severe than that at the time A. In addition, the concrete in the top zone of the column was damage on the impact side. The length of the damage zone was 19.2% of the height of the column. In Section A-A, the damaged area of the concrete increased compared to that at time A at impact side.

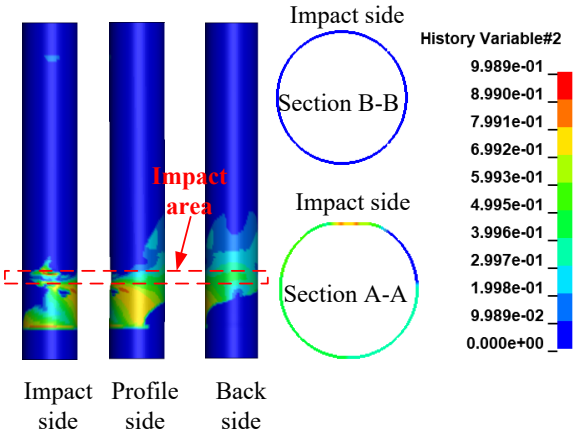

(i) GFRP tube

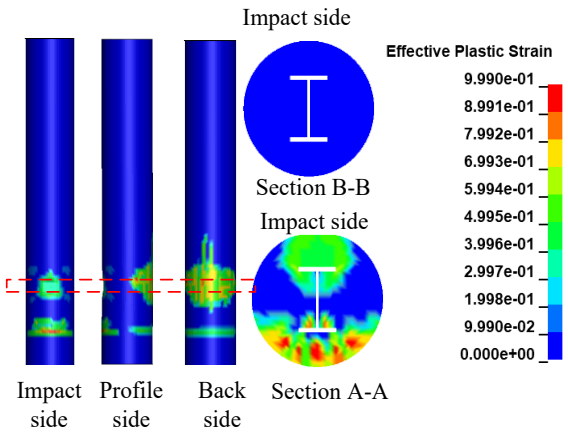

(ii) Concrete

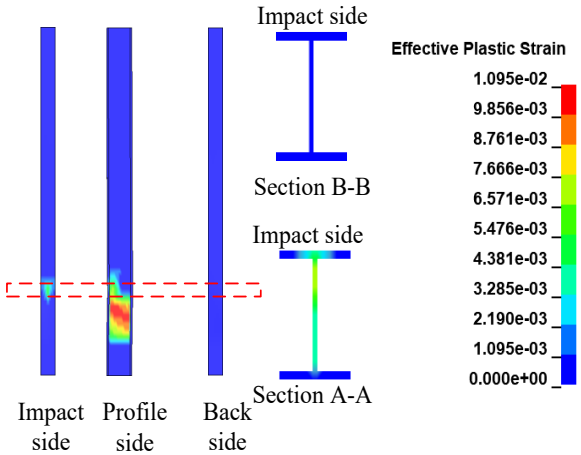

(iii) Encased steel

(a) At time A

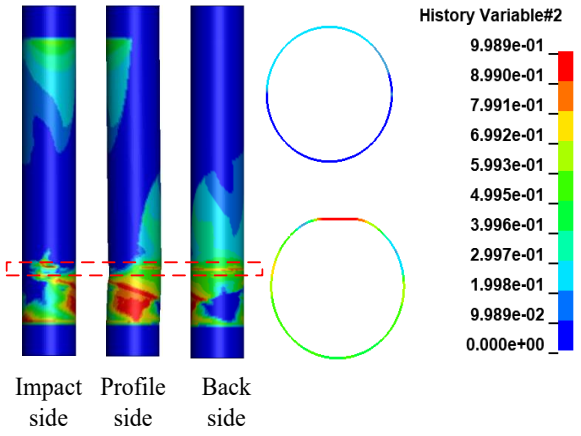

(i) GFRP tube

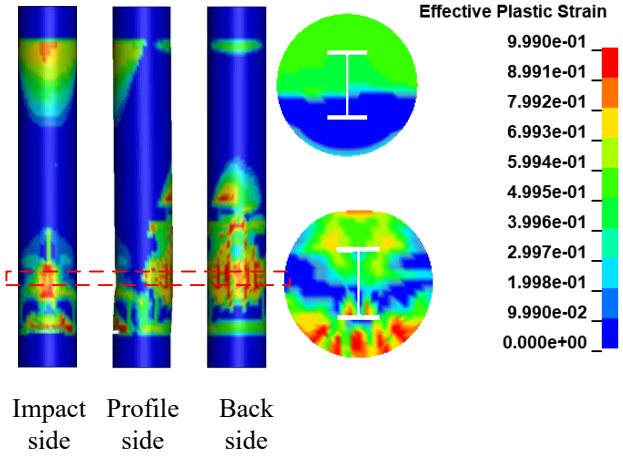

(ii) Concrete

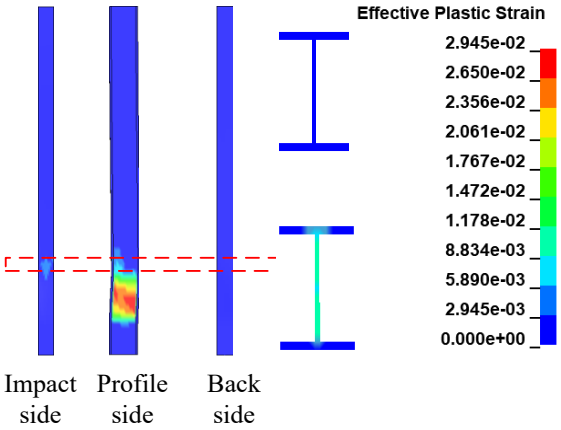

(iii) Encased steel

(b) At time B

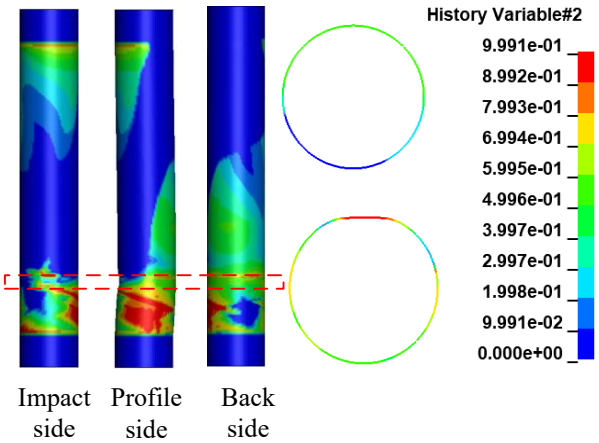

(i) GFRP tube

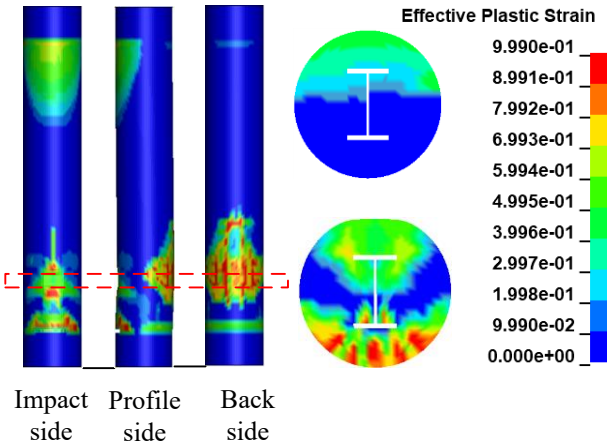

(ii) Concrete

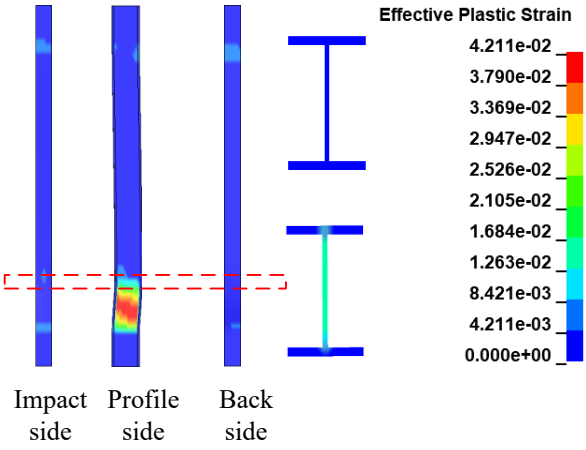

(iii) Encased steel

(c) At time C

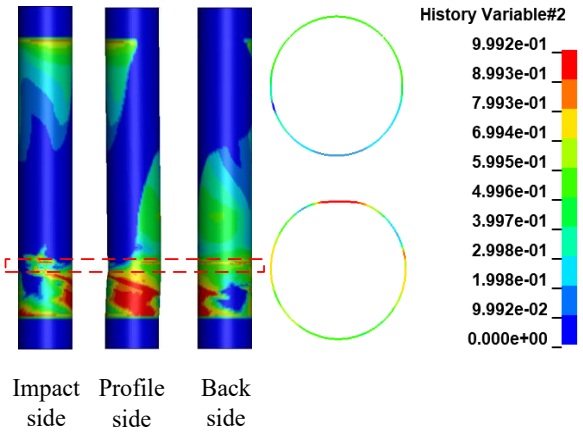

(i) GFRP tube

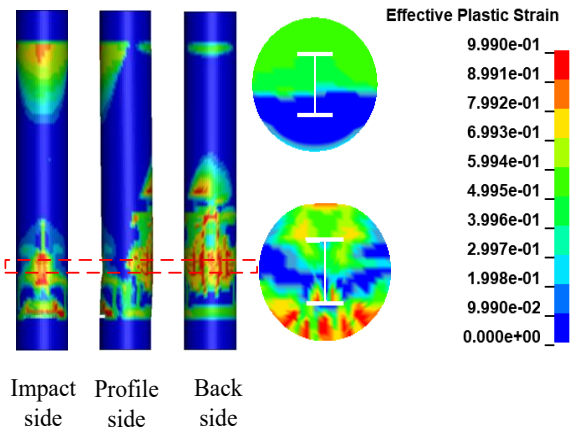

(ii) Concrete

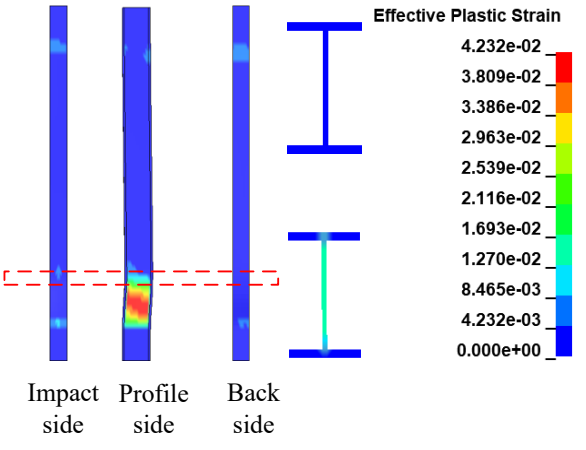

(iii) Encased steel

(d) At time D

Fig. 10 Damage evolution of the column

Furthermore, effective plastic strain area of the encased steel remained constant. Whereas, the maximum effective plastic strain value was 0.02945 which increased approximately 1.68 times compare with that at time A. Moreover, the GFRP tube and concrete at impact side presented a damage level at Section B-B. Half of the cross section was almost damage.

At time C, the matrix damage to the GFRP tube at the top of the column was severe. And the damage evolved from the impact side to back side in Section B-B. For the concrete, the damage level in the top zone increased. The damaged area had expanded to the middle of the column height. And in Section A-A and Section B-B, the damaged area increased further. Moreover, the encased steel flanges in the top and bottom zones yielded. A higher effective plastic strain area also concentrated between the bottom surface of column and impact area, and the maximum effective plastic strain was 0.04211. At time D, the concrete damage level at the contact surface between the impactor and column increased, owing to column rebound. This behavior had a minor influence on the encased steel and GFRP tube in terms of damage. Furthermore, the encased steel in Section B-B was in an elastic state during the entire impact process.

Moreover, the more severely damaged area was mainly concentrated at the

bottom of the column which was a region of higher shear force, as discussed in Section 3.2.3. And the bending moment was observed in this region. Thus, the failure model of the GTCES column under lateral impact was flexural-shear dominant.

3.2.6. GFRP tube confinement effect

The above analysis suggested that the GFRP tube made a relatively minor contribution to carrying the shear force, resisting the bending moment, and absorbing energy. However, the GFRP tube may have made a significant indirect contribution to strengthen the impact performance of column. Based on this hypothesis, a column without the GFRP tube was simulated under the identical conditions. Fig. 11 showed a comparisons of impact force and lateral displacement-time histories. The maximum impact force and plateau force of the column without a GFRP tube were 1140 kN and 655 kN, respectively. The maximum lateral displacement was 17.4 mm. The presence of GFRP tube increased the maximum impact force and plateau force by 16.78% and 22.39%, respectively. The maximum lateral displacement reduced up to 30.46%. Additionally, the column damage was shown in Fig. 12. The concrete damaged area was larger than that of column with GFRP tube. This damage was significantly more severe. And the area of the encased steel yielded remained was almost unchanged. Whereas, the maximum value of the effective plastic strain increased approximately 1.07 times compared to the column with GFRP tube. Therefore, the GFRP tube can sustain a higher impact force on the column, because the GFRP tube confined the concrete, which indirectly improved the column's dynamic resistance. The circular stress of GFRP tube under impact was presented in Fig. 13, and was used to investigate the confinement effect that benefited from GFRP tube. The GFRP tube was almost in a tensile state along the hoop direction, except for a few areas at the bottom and top of column. It indicated that the GFRP tube can effectively provide concrete confinement. Compared with the column without a GFRP tube, the confinement effect reduced the concrete damage level. The location of the more severe concrete damage in the column without a GFRP tube coincided with areas where the GFRP tube in the GTCES column provided higher confinement effect. Furthermore, the circular stress of the GFRP tube was higher in the impact region during the plateau stage (Fig. 13 (b) and Fig. 13(c)). It would provide the excellent confinement effect for concrete, thus preventing the concrete damage and reducing the deformation of encased steel, resulting in higher plateau force and lower lateral displacement.

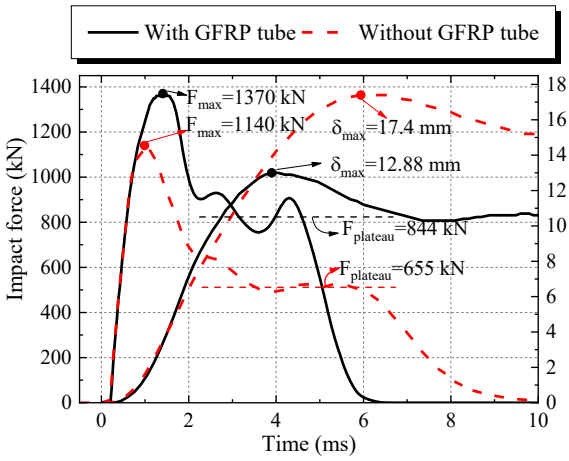

Fig. 11 Impact force and lateral displacement-time histories of the column without GFRP tube

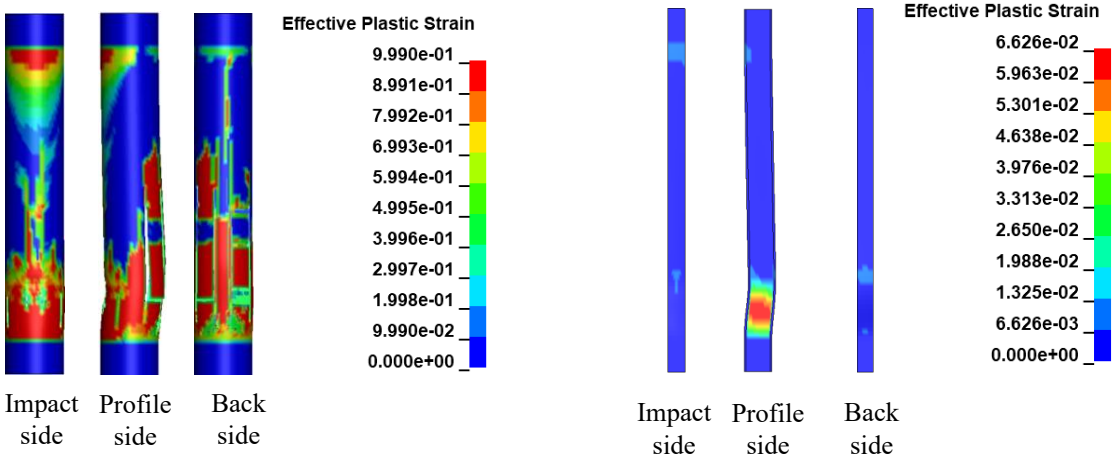

(a) Concrete (b) Encased steel

Fig. 12 Failure modes of the column without GFRP tube

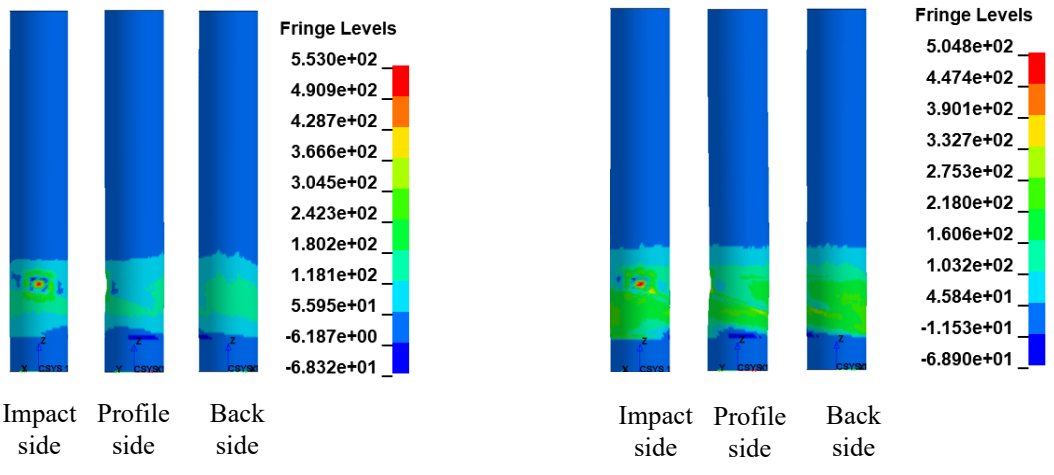

(a) At time A (b) At time B

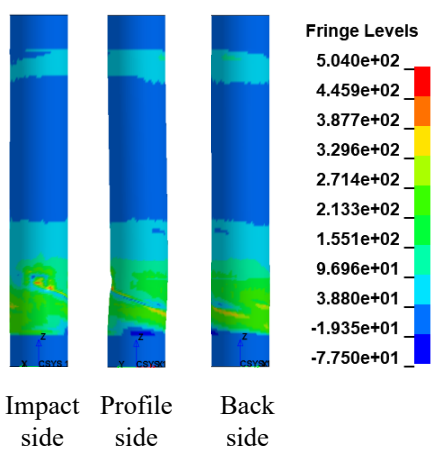

(c) At time C

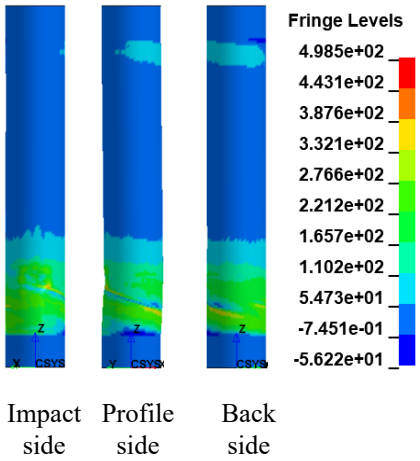

(d) At time D

Fig. 13 Stress of the GFRP tube along the circular direction

Table 2
The results of parametric analysis

Group	n	f_c(MPa)	f_y(MPa)	α	v (m/s)	F_p (kN)	F_{plat} (kN)	Δ_{1max} (mm)	Δ_{1resi} (mm)	Δ_{2max} (mm)	Δ_{2resi} (mm)
Axial force ratio	0	30	235	3.41%	10	1180	801	13.81	10.62	8.69	5.12
	0.15	30	235	3.41%	10	1310	802	13.32	10.62	7.61	4.23
	0.3	30	235	3.41%	10	1370	844	12.88	10.31	7.31	4.21
	0.45	30	235	3.41%	10	1400	854	12.63	10.25	7.18	4.22
	0.6	30	235	3.41%	10	1410	868	12.51	10.21	6.71	4.20
Concrete strength	0.3	30	235	3.41%	10	1370	844	12.88	10.62	7.31	4.21
	0.3	40	235	3.41%	10	1520	927	11.52	9.07	6.59	2.83
	0.3	50	235	3.41%	10	1590	998	10.71	8.08	6.81	3.12
Encased Steel yield strength	0.3	30	235	3.41%	10	1370	844	12.88	10.31	7.31	4.21
	0.3	30	355	3.41%	10	1410	874	12.31	9.82	7.33	4.18
	0.3	30	390	3.41%	10	1430	887	12.02	9.41	7.39	4.19
	0.3	30	420	3.41%	10	1440	899	11.83	9.23	7.23	3.57
Steel ratio	0.3	30	235	3.41%	10	1370	844	12.88	10.31	7.31	4.21
	0.3	30	235	4.92%	10	1450	932	11.51	9.67	7.22	4.19
	0.3	30	235	6.69%	10	1630	1129	8.58	6.45	6.68	4.15
Impact velocity	0.3	30	235	3.41%	10	1370	844	12.88	10.31	7.31	4.21
	0.3	30	235	3.41%	15	1700	836	27.81	24.83	11.31	6.71
	0.3	30	235	3.41%	20	2030	797	55.72	51.03	11.32	7.32
	0.3	30	235	3.41%	25	2280	787	85.83	79.91	15.61	7.31

Note: n was the axial force ratio; f_c was the compressive strength of concrete; f_y was the encased steel yield strength; α was the steel ratio; v was the impact velocity; F_p and F_{plat} were the impact force and impact force plateau value, respectively; Δ_{1max} and Δ_{1resi} were peak and residual lateral displacement; Δ_{2max} and Δ_{2resi} were peak and residual local indentation.

4. Parametric analysis

The impact response of GTCES column for different influence parameters were analyzed in this section. The parameters included the axial force ratio, concrete strength, encased steel yield strength, steel ratio and impact velocity. The results were listed in Table 2.

4.1. Axial force ratio

Five axial force ratios (0, 0.15, 0.3, 0.45, 0.6) were selected to explore the effects of axial force ratio on GTCES column under impact. The axial force ratio was calculated by:

$$n = \frac{N_0}{N_u} \tag{5}$$

where N_0 is the applied axial force and N_u is the ultimate axial force of the column, which was determined as described previously [46].

Fig. 14(a) showed the impact force-time histories and impact force values under different axial force ratios. The impact force-time histories exhibited the same trend. With increasing of axial force ratio, the peak and plateau impact force increased. When the axial force ratio ranged from 0 to 0.6, the peak impact force increased by 11.01%, 16.10%, 18.64% and 19.49%, indicating that applying the axial force enhanced the local stiffness of the impact area. The increase in plateau force was slight, and corresponding increases of 0.21%, 5.34%, 6.67% and 8.33% were observed. Meanwhile, the increase in impact force values was small when the axial force ratio exceeded 0.3.

Fig. 14(b) showed that the lateral displacement-time history curves under different axial force ratios. The changing trends of displacement-time histories under different axial force ratios were almost identical. Both the peak and residual lateral displacements exhibited downward trends by increasing the axial force ratio. The peak lateral displacements were reduced by 3.62%, 5.79%, 8.69% and 9.42%, the residual lateral displacement decreased by 2.75%, 5.51%, 5.96% and 6.42%, when the axial force ratio increased from 0 to 0.15, 0.3, 0.45 and

0.6, respectively. Furthermore, Fig. 14(c) showed the local indentation-time histories under different axial load ratios. The peak local indentation decreased by 12.54%, 15.60%, 17.38% and 22.78%, respectively, with increasing axial force ratio. The residual local indentation remained relatively unchanged as the axial force ratio exceeded 0.

The damage of column (n=0) at times A and C was presented in Fig. 15. At time A, the damage level of each component in the impact area was severe than that of the column (n=0.3), as presented in Fig. 15(a). This suggested that increasing the axial force ratio enhanced the local stiffness of the impact area, thereby contributing to an increase in the peak impact force. At the time C, the column (n=0) damage level was much more severe in comparison to that of the column (n=0.3), as presented in Fig. 10(d), indicating a higher axial force ratio can reduce the damage level of the column during plateau stage, thereby leading to higher impact performance. This was owing to that the stiffness of the column can be improved by increasing the axial force ratio.

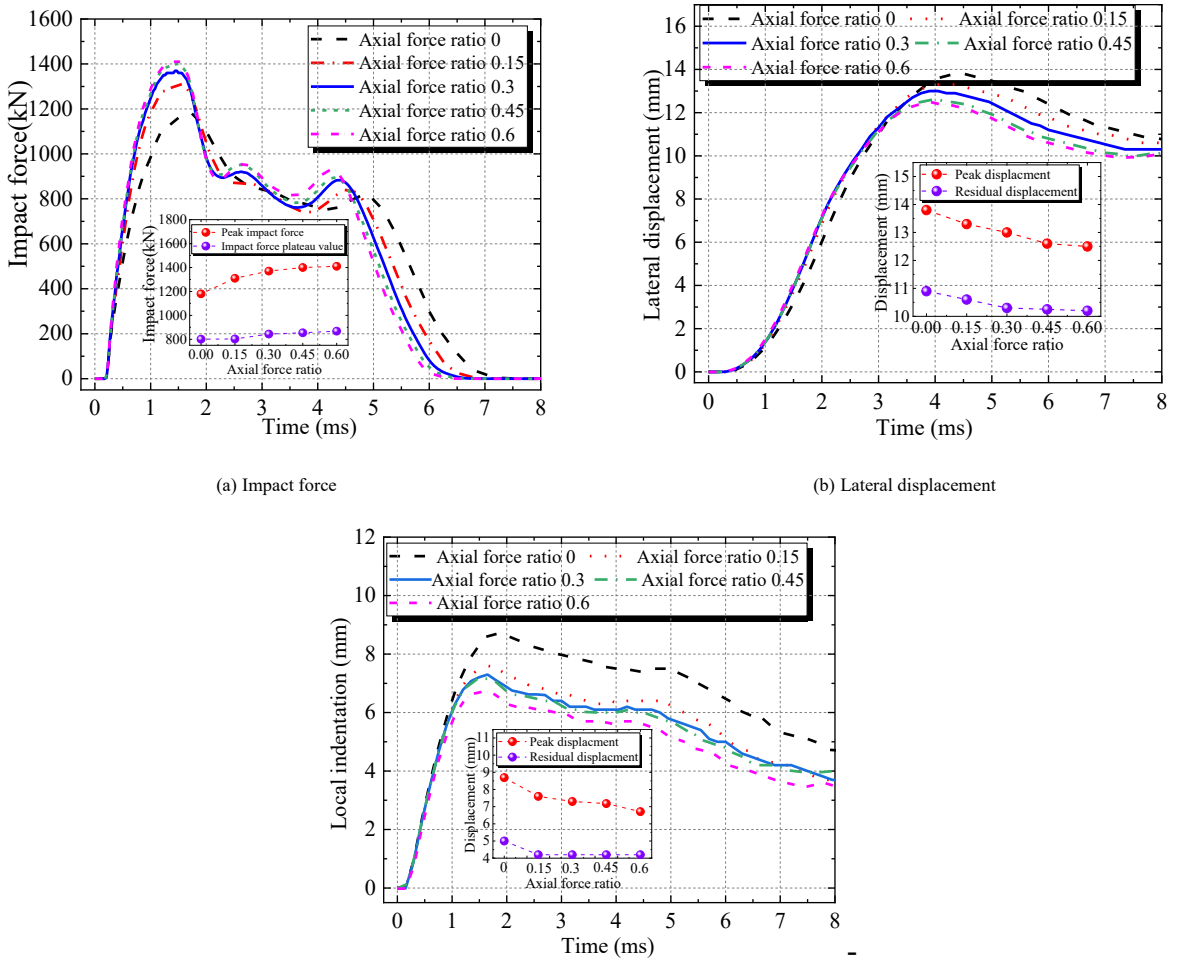

(a) Impact force

(b) Lateral displacement

(c) Local indentation

Fig. 14 Impact force, lateral displacement and local indentation-time history curves under different axial forces

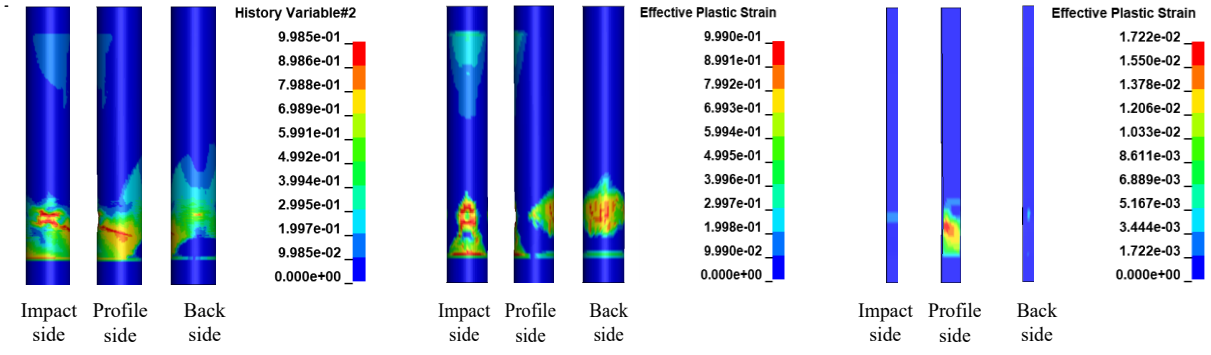

(a) GFRP tube

(b) Concrete

(c) Encased steel

(a) At time A

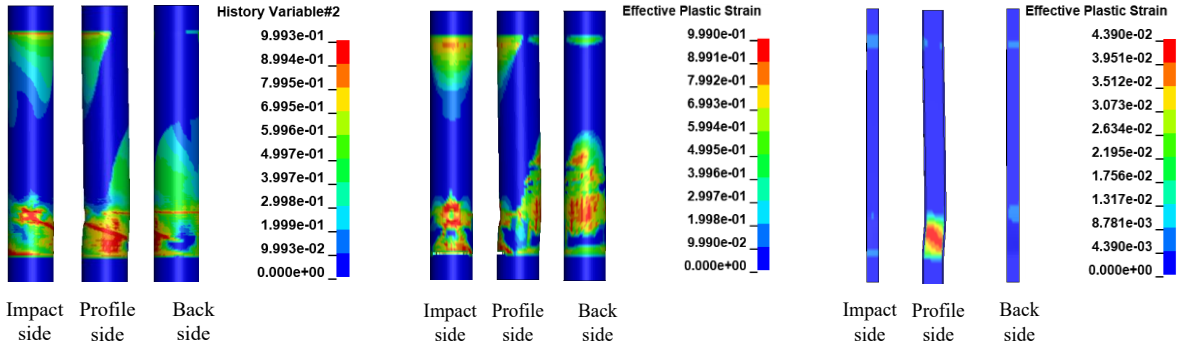

(d) GFRP tube (e) Concrete (f) Encased steel

(b) At time B

Fig. 15 Damage evolution of the column (n=0)

4.2. Concrete strength

The effects of three different concrete strengths (30MPa, 40MPa, and 50MPa) on the impact characteristics of the GTCES columns were explored. Table 2 and Fig. 16 showed the numerical simulation results. Fig. 16(a) illustrated that the concrete strength significantly affected on impact force. As the concrete strength increasing from 30MPa to 40MPa and 50MPa, the peak impact force increased by 10.95% and 16.06%, and led to an enhancement of 9.83% and 18.25% for impact force plateau value, respectively. This phenomenon differed from that observed in previous study [32]. Fig. 16(b) showed that the peak and residual lateral displacements could be reduced by increasing the concrete strength. The peak lateral displacements decreased to 10.56% and 16.84%, and the decreases of residual lateral displacements were 14.59% and 23.91%, respectively. Meanwhile, Fig. 16(c) showed that increasing the concrete strength can reduce local indentation. The peak local indentation was reduced by 9.84% and 6.84%, and the residual local indentation was reduced by 32.77% and 25.89%, respectively. Increasing the concrete strength is a useful approach to improve the dynamic performance of the GTCES.

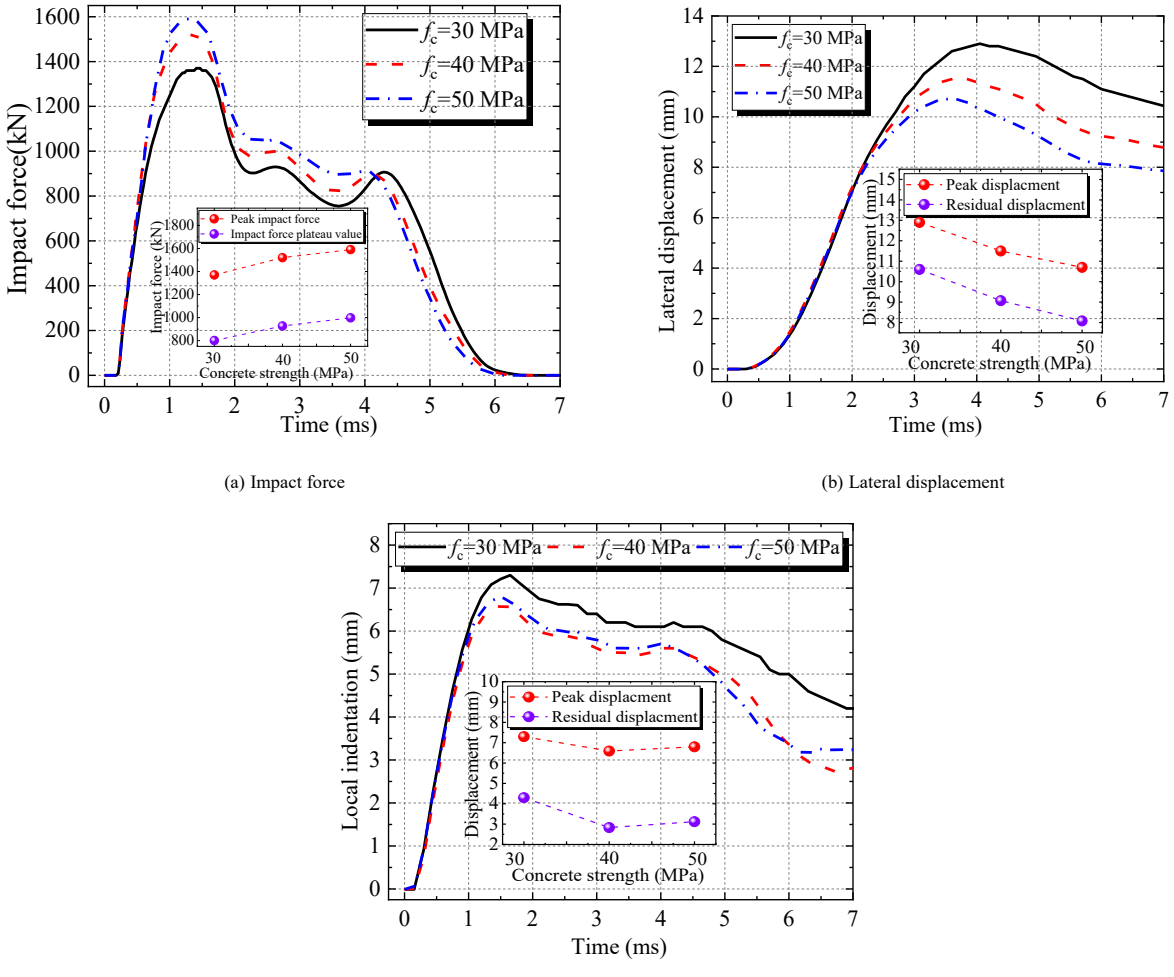

(a) Impact force (b) Lateral displacement

(c) Local indentation

Fig. 16 Impact force, lateral displacement and local indentation time history curves under different concrete strengths

4.3. Encased steel yield strength

Fig. 17 and Table 2 presented the dynamic responses of the GTCES with various encased yield strengths (235MPa, 355MPa, 390MPa and 420MPa). The findings indicated the peak impact force increased by 2.92%, 4.38% and 5.11%, and the plateau force increased by 3.55%, 5.09% and 6.52%, by increasing the encased steel yield strength from 235 MPa to 355 MPa, 390 MPa and 420 MPa, respectively. Which indicated that increasing the yield strength of the encased steel had a slight influence on the impact force value. The reason for this was that the contribution of encased steel to impact resistance was lower.

Fig. 17(b) showed that the lateral displacement-time histories and its characteristic displacement values under different steel strengths. The peak and residual lateral displacements were slightly decreased by increasing the yield strength of encased steel. When the encased steel yield strength increased from 235 MPa to 355 MPa, 390 MPa and 420 MPa, the peak lateral displacement decreased by 3.91%, 6.25% and 7.81%, and the residual lateral displacement decreased by 7.53%, 11.39% and 13.09%, respectively. From Fig. 10(c) and Fig. 18, as the encased steel yield strength increased, the effective plastic strain of the encased steel correspondingly decreased. This demonstrated that increasing the encased steel yield strength would produce less plastic deformation and more elastic deformation, thereby reducing the residual lateral displacement. From Fig. 17(c), the encased steel yield strength had a minor influence on the local indentation. This was because that the local indentation was induced by concrete deformation.

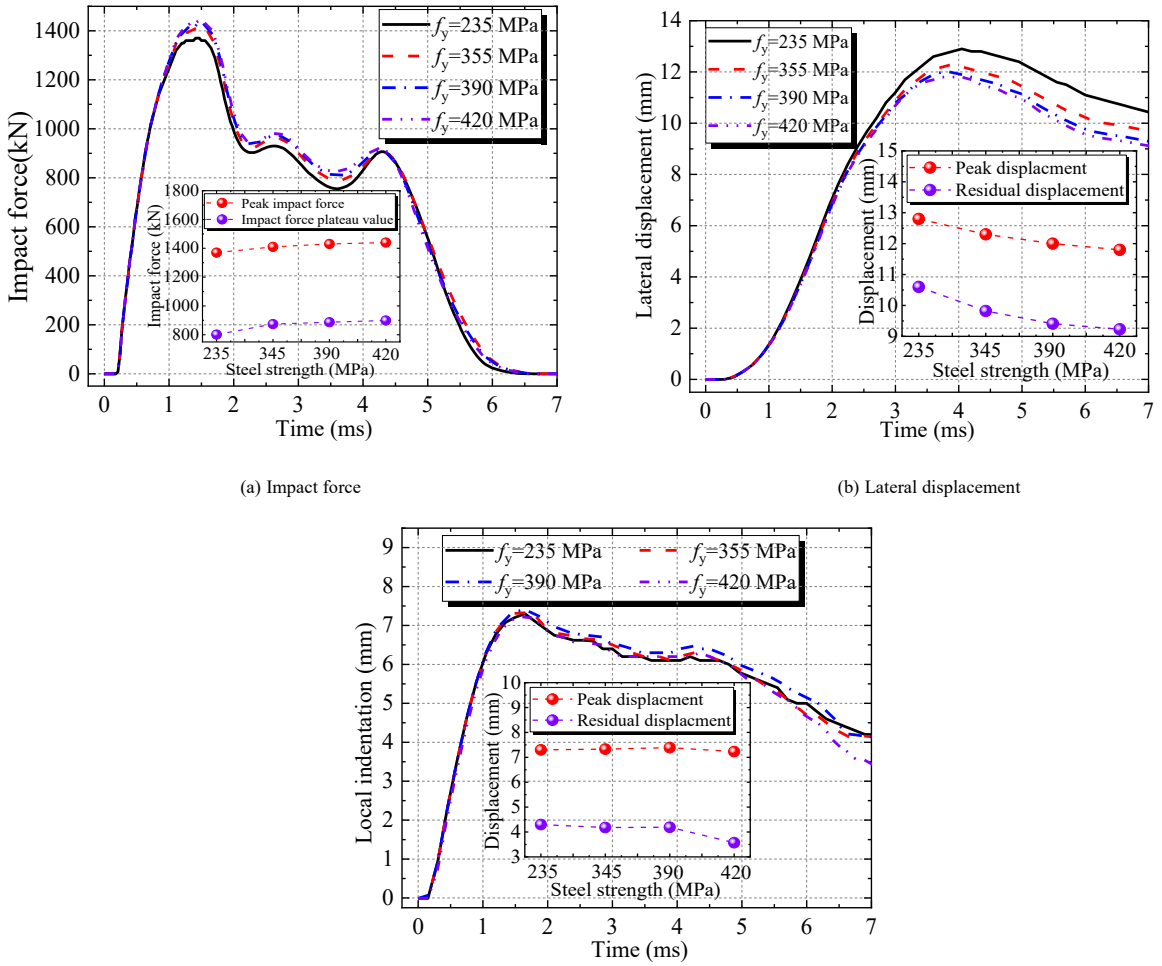

(a) Impact force

(b) Lateral displacement

(c) Local indentation

Fig. 17 Impact force, lateral displacement and local indentation time history curves under different encased steel yield strengths

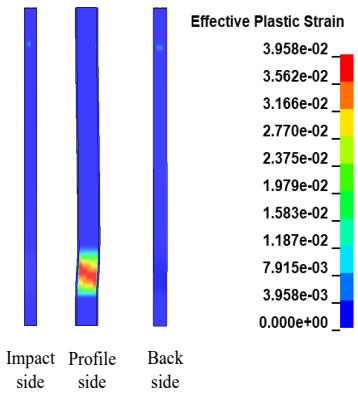

Fig. 18 Effective plastic strain of the encased steel at time C (420 MPa)

4.4. Steel ratio

The simulation results for the GTCES with varying the steel ratios (3.41%, 4.92% and 6.69%) were shown in Fig. 19. The steel ratio was determined according to the method described in Ref. [22], with the actual dimensions of the encased steel considered [47].

Fig. 19(a) illustrated that when the steel ratio increased from 3.41% to 4.92% and 6.69%, the peak impact force increased by 5.84% and 18.98%, respectively. This suggested that the local stiffness of the impact area was enhanced by an increase in steel ratio. Meanwhile, the enhancements in the impact force plateau values were 10.42% and 33.77%, respectively. The steel ratio had a greater effect on the impact force plateau value than on the peak impact force. This was because that encased steel played a greater role in absorbing energy and bearing the load in the plateau stage than in the initial stage, as discussed in Section 3.

Furthermore, Fig. 19(b) illustrated that the lateral displacement decreased as the steel ratio increased. The reductions in the peak lateral displacement were 10.63% and 33.39%, while the reductions in the residual lateral displacement were 8.95% and 39.27%, via increasing the steel ratio from 3.41% to 4.92% and 6.69%. This was because that the sectional bending stiffness of the column was enhanced by increasing the steel ratio. Whereas, the steel ratio contributed slightly to reduction in local indentation, as shown in Fig. 19(c).

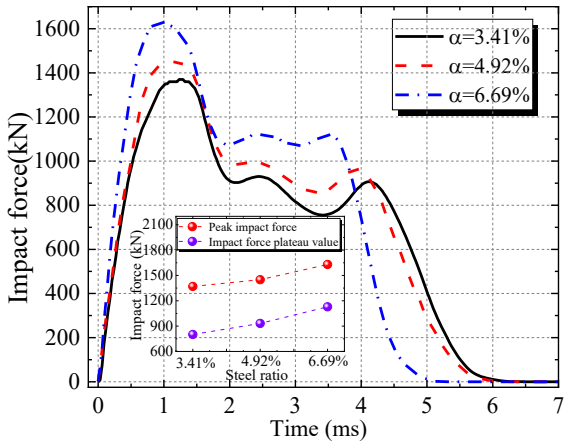

(a) Impact force

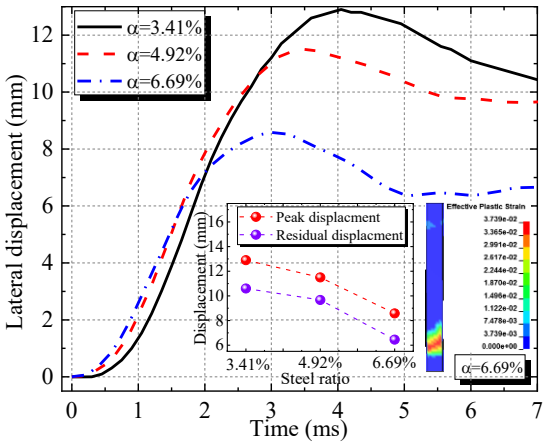

(b) Lateral displacement

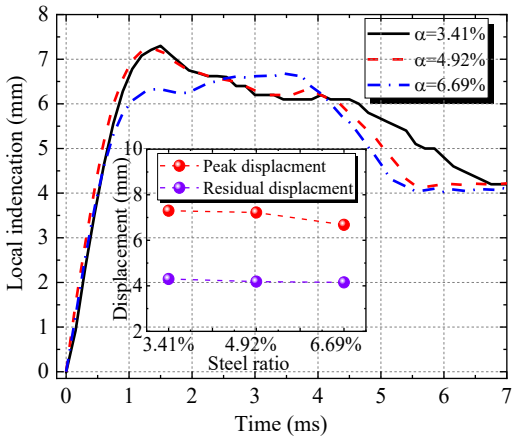

(c) Local indentation

Fig. 19 Impact force, lateral displacement and local indentation time history curves under different steel ratios

4.5. Impact velocity

Four different impact velocities were considered to explore the impact performance of GTCES column. Fig. 20 exhibited a comparison of the GTCES with varying impact velocities. From Fig. 20 (a), when the impact velocity increased from 10 m/s to 15 m/s, 20 m/s and 25 m/s, the enhancements of the peak impact force were 24.09%, 48.18% and 66.42%, respectively. It suggested that the local dynamic response increased under a higher impact velocity. Nevertheless, Fig. 21 showed that the more severe damage occurred on the column in the initial stage. This was because a higher proportion of impact energy was absorbed in this stage.

Increasing the impact velocity reduced the impact resistance. The impact force plateau value showed a minor reduction (6.75%), as the impact velocity increased from 10 m/s to 25 m/s. However, this reduction level was not significant. A possible reason was that the strength of encased steel and concrete was improved owing to the strain rate effect under a higher impact velocity, thereby improving their ability to resist the impact load.

From Fig. 20(b), the increases in the lateral peak displacement were 1.16 times, 3.33 times and 5.66 times, and the increases in the lateral residual displacement were 1.34 times, 3.81 times and 6.54 times, via increasing impact velocity from 10m/s to 15 m/s, 20 m/s and 25 m/s, respectively. And the increases in the peak and residual lateral displacements were significant. This was because of the severe damage that occurred in the column during the initial stage under a higher impact velocity, which significantly reduced the stiffness of the column. In addition, a greater proportion of the impact energy was absorbed during the plateau stage, resulting in a more significant deformation of the column to absorbed impact energy.

Fig. 20(c) showed that the increases in the local peak indentation were 54.79%, 55.86% and 1.13 times, respectively, and the increases in the local residual indentation were 55.81%, 69.76% and 70.02%, respectively. It was evident that the local damage in the impact area was more severe under higher impact velocity. Furthermore, the increase in the local indentation was lower than that in the lateral displacement. This illustrated that the lateral deformation of column contributed significantly to absorb impact energy.

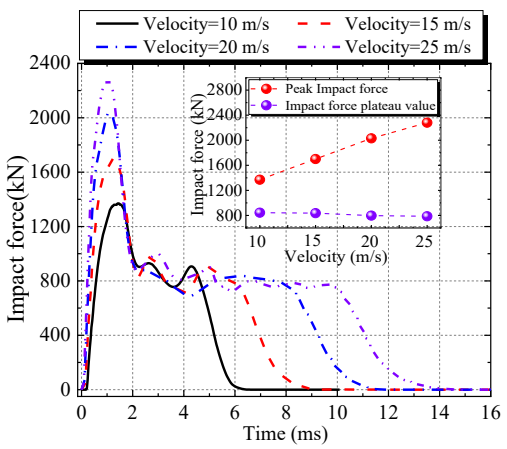

(a) Impact force-time history

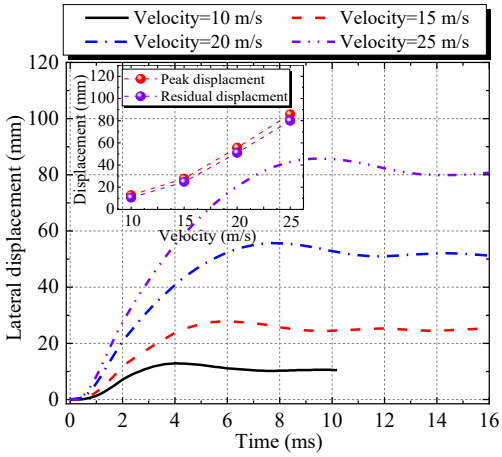

(b) Lateral displacement-time history

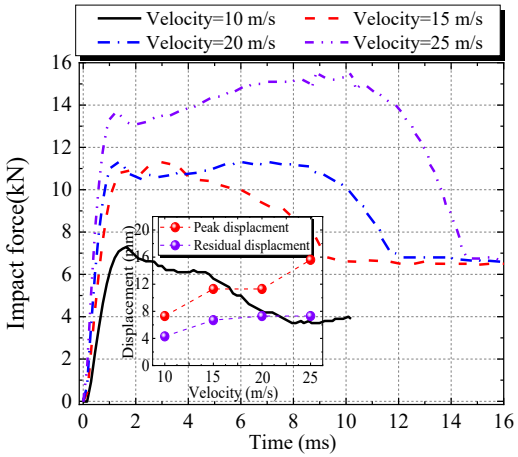

(c) Local indentation-time history curve

Fig. 20 Impact force, lateral displacement and local indentation time-history curves under different impact velocities

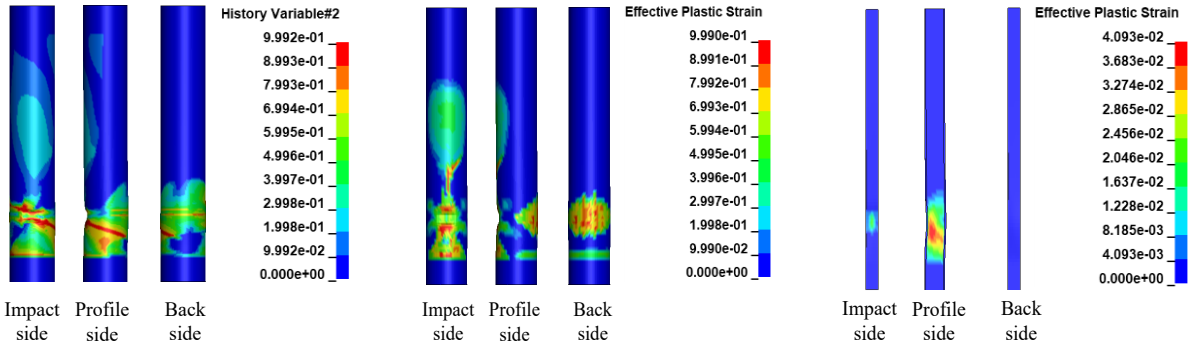

(a) GFRP tube (b) Concrete (c) Encased steel

(a) At time A

Fig. 21 Damage evolution of the column under the impact velocity of 25m/s (at time A)

5. Conclusions

The dynamic behaviors of the GTCES column with fixed ends under lateral impact load were investigated using a finite element technique in this study. According to these findings, it can be concluded as:

(1) The inertial and reaction force combine to resist the impact, with the inertial force resisting approximately 50% of the impact force during the impact peak stage. The inertia force increases the sectional bending moment and shear force.

(2) Before the unloading stage, the proportions of the bending moment, shear force and energy absorption borne by the concrete are significant and can reach over 63%, 75% and 74%, respectively. The GFRP tube as a confinement system for the concrete can significantly reduce the damage to the column, which indirectly enhances the impact performances of the GTCES column.

(3) More severe damage concentrates in the area from the bottom of the column to the impact region, which is a region of higher shear. The lager shear force area can be as a reinforcing specific region to prevent shear failure. The failure model of GTCES column was flexural-shear dominant.

(4) Increasing the axial force ratio can enhance the local stiffness of the column, the peak local indentation decreases by 22.78% and the peak impact force increases by 19.49%, respectively, with increasing the axial force ratio from 0 to 0.6. A higher impact velocity will induce more severe damage in the impact peak stage, thus the impact resistance of the column is reduced significantly.

(5) The steel ratio significantly affects the impact resistance of the column, followed by the concrete strength and encased steel yield strength. Additionally,

increasing the concrete strength can effectively reduce the peak and residual local indentations.

Data availability

All data, models, and code generated or used in this study appear in the submitted article.

Funding

This work was supported by the National Natural Science Foundation of China (grant number 52278196); Key Projects of National Natural Science Foundation of China (grant number 51938009).

Declaration of conflicting interests

The authors declared that there are no conflicts of interest.

References

[1] L. Huang, S.S. Zhang, T. Yu, Z.Y. Wang, Compressive behaviour of large rupture strain FRP-confined concrete-encased steel columns, Constr. Build. Mater. 183 (2018) 513-522, http://dx.doi.org/10.1016/j.conbuildmat.2018.06.074.
[2] L. Huang, P. Yin, L. Yan, B. Kasal, Behavior of hybrid GFRP-perforated-steel tube-encased concrete column under uniaxial compression, Compos. Struct. 142 (2016) 313-324, http://dx.doi.org/10.1016/j.compstruct.2016.02.016.
[3] K. Karimi, W.W. El-Dakhakhni, M.J. Tait, Performance enhancement of steel columns using concrete-filled composite jackets, J. Perform. Constr. Facli. 25 (2011) 189-201, http://dx.doi.org/10.1061/(ASCE)CF.1943-5509.0000162.
[4] T. Yu, J.G. Teng, Y.L. Wong, Stress-strain behavior of concrete in hybrid FRP-concrete-steel double-skin tubular columns, J. Struct. Eng. 136 (2010) 379-89, http://dx.doi.org/10.1061/ASCEST.1943-541X.0000121.
[5] T. Yu, Y.L. Wong, J.G. Teng, Behavior of hybrid FRP-concrete-steel double-skin tubular columns subjected to eccentric compression, Adv. Struct. Eng. 13 (2010) 961-74, http://dx.doi.org/10.1260/1369-4332.13.5.961.
[6] T. Yu, J.G Teng, Behavior of hybrid FRP-concrete-steel double-skin tubular columns with a square outer tube and a circular inner tube subjected to axial compression, J. Compos. Constr. 17 (2013) 271-9, http://dx.doi.org/10.1061/(ASCE)CC.1943-5614.0000331
[7] T. Ozbakkaloglu, Y. Idris, Seismic behavior of FRP-high-strength concrete-steel double-skin tubular columns, J. Struct. Eng. 140 (2014) 04014019, http://dx.doi.org/10.1061/(ASCE)ST.1943-541X.0000981.
[8] B. Zhang, T.G. Teng, T. Yu, Experimental behavior of hybrid FRP-concrete-steel double-skin tubular columns under combined axial compression and cyclic lateral loading, Eng. Struct. 99 (2015) 214-31, http://dx.doi.org/10.1016/j.engstruct. 2015.05.002.
[9] Xiao, Applications of FRP composites in concrete columns, Adv. Struct. Eng. 7 (2004) 335-43, http://dx.doi.org/10.1260/1369433041653552.
[10] Y.M. Hu ,T. Yu, J.G. Teng, FRP-confined circular concrete-filled thin steel tubes under axial compression, J. Compos. Constr. 15 (2011) 850-60, http://dx.doi.org/10.1061/(ASCE)CC.1943-5614.0000217.
[11] J.G. Teng, Y.M. Hu, T. Yu, Stress-strain model for concrete in FRP-confined steel tubular columns, Eng. Struct. 49 (2013) 156-67, http://dx.doi.org/10.1061/ASCEST.1943-541X.0000121.
[12] T. Yu, Y. Hu, J.G Teng, FRP-confined circular concrete-filled steel tubular columns under cyclic axial compression, J. Constr. Steel. Res. 94 (2014) 33-48, http://dx.doi.org/10.1061/10.1016/j.jcsr.2013.11.003.
[13] A. Mirmiran, M. Shahawy, Behavior of concrete columns confined by fiber composites, J. Struct. Eng. 123 (5) (1997) 583-590, http://dx.doi.org/10.1061/(asce)0733-9445(1997)123:5(583).
[14] T. Jiang, J.G. Teng, Analysis-oriented stress-strain models for FRP-confined concrete, Eng. Struct. 29 (11) (2007) 2968-2986, http://dx.doi.org/10.1016/j.engstruct.2007.01.010.
[15] T. Yu, G. Lin, S.S. Zhang, Compressive behavior of FRP-confined concrete-encased steel columns, Compos. Struct. 154 (2016) 493-506, http://dx.doi.org/10.1016/j.compstruct.2016.07.027.
[16] X. Liu, A. Nanni, P.F. Silva, Rehabilitation of compression steel members using FRP pipes filled with non-expansive and expansive light-weight concrete, Adv. Struct. Eng. 8 (2) (2005) 129–42, http://dx.doi.org/10.1260/1369433054038029.
[17] K. Karimi, M.J. Tait, W.W. El-Dakhakhni, Testing and modeling of a novel FRP-encased steel-concrete composite column, Compos. Struct. 93 (5) (2011) 1463-73, http://dx.doi.org/10.1016/j.compstruct.2010.11.017.
[18] K. Karimi, W.W. El-Dakhakhni, M.J. Tait, Performance enhancement of steel columns using concrete-filled composite jackets, J. Perform. Constr. Facil. 25(3) (2011) 189-201, http://dx.doi.org/10.1061/(asce)cf.1943-5509.0000162.
[19] K. Karimi, M.J. Tait, W.W. El-Dakhakhni, Influence of slenderness on the behavior of a FRP-encased steel-concrete composite column, J. Compos. Constr. 16 (2012) 100-9, http://dx.doi.org/10.1061/(asce)cc.1943-5614.0000235.
[20] K. Karimi, M.J. Tait, W.W. El-Dakhakhni, Analytical modeling and axial load design of a novel FRP-encased steel-concrete composite column for various slenderness ratios, Eng. Struct. 46 (2013) 526-34, http://dx.doi.org/10.1016/j.engstruct.2012.08.016.
[21] F.M. Ren, Y.W. Liang, J.C.M. Ho, M.H. Lai, Behaviour of FRP tube-concrete-encased steel composite columns, Compos. Struct. 241 (2020) 112139, http://dx.doi.org/10.1016/j.compstruct.2020.112139.
[22] H.X. Zhang, S.L. Ju, H. Chen, Seismic performance of GFRP tube concrete-encased steel composite columns under axial compression, J. Constr. Steel. Res. 200 (2023) 107641, http://dx.doi.org/10.1016/j.jcsr.2022.107641.
[23] L. Wang, B. Chen, Steel reinforced concrete-filed glass fiber reinforced polymer or steel tubular structures, Liaoning Science and Technology Press, Shenyang, China, 2013, pp. 125–131 (in Chinese).
[24] T.M. Pham, H. Hao, Axial impact resistance of FRP-confined concrete, J. Compos. Construct. 21 (2) (2017) 04016088, http://dx.doi.org/10.1061/(ASCE)CC.1943-5614.0000744
[25] L. Huang, X. Sun, L. Yan, B. Kasal, Impact behavior of concrete columns confined by both GFRP tube and steel spiral reinforcement, Construct. Build. Mater. 131 (2017) 438-448, http://dx.doi.org/10.1016/J.CONBUILDMAT.2016.11.095
[26] J. Wang, H.T. GangaRao, R.F. Liang, W.Q. Liu, Experimental and analytical responses of Hollow and concrete-filled GFRP tube columns under Impact, J. Compos. Constr. (2017) 04017013, http://dx.doi.org/10.1061/(ASCE)CC.1943-5614.0000793
[27] Z. Chen, J. Wang, J.Y. Chen, H.T. GangaRao, R.F. Liang, W.Q. Liu, Responses of concrete-filled FRP tubular and concrete-filled FRP-steel double skin tubular columns under horizontal impact, Thin-Walled Struct. 155 (3) (2020) 106941, http://dx.doi.org/10.1016/j.tws.2020.106941.
[28] Y. Qasrawi, P.J. Heffernan, A. Fam, Dynamic behaviour of concrete filled FRP tubes subjected to impact loading, Eng. Struct. 100 (2015) 212-225, http://dx.doi.org/10.1016/j.engstruct.2015.06.012.
[29] O.I. Abdelkarim, M.A. ElGawady, Performance of hollow-core FRP-concrete-steel bridge columns subjected to vehicle collision, Eng. Struct. 123 (2016) 517-531, http://dx.doi.org/10.1016/j.engstruct.2016.05.048.
[30] O.I. Abdelkarim, M.A. ElGawady, Dynamic and static behavior of hollow-core FRP-concrete-Steel and reinforced concrete bridge columns under vehicle collision, Polymers. 8 (12) (2016) 432, http://dx.doi.org/10.3390/polym8120432.
[31] R. Wang, L.H. Han, Z. Tao, Behavior of FRP–concrete–steel double skin tubular members under lateral impact: experimental study, Thin-Walled Struct. 95 (2015) 363-73, http://dx.doi.org/10.1016./j.tws.2015.06.022.
[32] W.Q. Wang, C.Q. Wu, Y. Yu, J.J. Zeng, Dynamic responses of hybrid FRP-concrete-steel double-skin tubular column (DSTC) under lateral impact, Structures. 32 (2021) 1115-1144, http://dx.doi.org/10.1016/j.istruc.2021.02.062.
[33] B. Zhang, S.H. Lin, S.M. Zhang, Y.E. Jiang, C.C. Lai, X.Z. Fu, FRP-concrete-steel tubular columns with a large inner void under lateral impact loading: Experimental study and finite-element modelling, J. Buil. Eng. 80 (2023) 108006, https://doi.org/10.1016/j.jobe.2023.108006.
[34] R. Wang, L.H. Han, C.C. Hou, Behavior of concrete filled steel tubular (CFST) members under lateral impact: experiment and FEA model, J. Constr. Steel Res. 80 (2013) 188-201, http://dx.doi.org/10.1016/j.jcsr.2012.09.003.
[35] S. Gao, Y. Xu, S.M. Zhang, A. Derlatka, Performance of square concrete-filled steel tubular columns under repeated lateral impact, Eng. Struct. 280 (2023) 115719, http://dx.doi.org/10.1016/j.engstruct.2023.115719.
[36] W.Q. Wang, C.Q. Wu, J. Li, Z.X. Liu, Y.P Lv, Behavior of ultra-high performance fiber reinforced concrete (UHPFRC) filled steel tubular members under lateral impact loading, Int. J. Impact Eng. 132 (2019) 103314, https://doi.org/10.1016/j. ijimpeng.2019.103314.
[37] Murray YD. Users manual for LS-DYNA concrete material model 159. McLean, VA: Department of Transportation; 2007.
[38] G. Gholipour, A.M. Billah, Dynamic behavior of bridge columns reinforced with shape memory alloy rebar and UHPFRC under lateral impact loads, Int. J. Impact Eng. 168 (2022) 104297, https://doi.org/10.1016/j.ijimpeng.2022.104297.
[39] C.C. Hou, L.H. Han, F.C. Wang, C.M. Hu, Study on the impact behaviour of concrete encased CFST box members, Eng. Struct. 198 (2019), 109536, https://doi.org/ 10.1016/j.engstruct.2019.109536.
[40] A.A. Mutalib, H. Hao H, Development of PI diagrams for FRP strengthened RC columns, Int. J. Impact. Eng. 38 (2011) 290-304, http://dx.doi.org/10.1016/j.ijimpeng.2010.10.029.
[41] W.C. Zhao, J.H. Ye, Dynamic behavior and damage assessment of RC columns subjected to lateral soft impact, Eng. Struct. 251 (2022) 113476, https://doi.org/10.1016/j.engstruct.2021.113476.
[42] G.C. Li, J.L. Wang, C. Fang, X. Li, Y. Zhou, Performance of CFST members internally strengthened with I-shaped CFRP under impact load, J. Constr. Steel Res. 211 (2023) 108132, https://doi.org/10.1016/j.jcsr.2023.108132.
[43] Q.J. Wu, X.D. Zhi, Q.X. Li, M.H. Guo, Experimental and numerical studies of GFRP-reinforced steel tube under low-velocity transverse impact, Int. J. Impact. Eng. 127 (2019) 135-153, http://dx.doi.org/10.1016/j.ijimpeng.2019.01.010
[44] QC/T 487-2009, China Planning Press, Beijing, 2009. (in Chinese)
[45] H. Sharma; S. Hurlebaus; P. Gardoni, Performance-based response evaluation of reinforced concrete columns subject to vehicle impact, Int. J. Impact Eng. 43 (2012), 52-62, http://dx.doi.org/10.1016/j.ijimpeng.2011.11.007
[46] W.T. Xie, Y. Chen, S.H. Han, W.B. Zhou, Research on I steel reinforced concrete-filled GFRP tubular short columns, Thin-Walled Struct. 120 (2017) 282-296, http://dx.doi.org/10.1016/j.tws.2017.08.031.
[47] GB/T 706-2016, Hot rolled section steel China standard Press, Beingjing, 2016. (in Chinese)

Advanced Steel Construction – Vol. 21 No. 4 (2025) 294–303
DOI:10.18057/IJASC.2025.21.4.2

INVESTIGATION ON THE SEISMIC BEHAVIOR OF END-PLATE CONNECTION BETWEEN STEEL BEAM AND CIRCULAR CONCRETE-FILLED STEEL TUBULAR COLUMN

Shao-Feng Nie [1, *], Zi-Teng Zhao [1], Si-Yuan Chen [1], Yong-Zhen Lin [1], Geng Qin [1] and Xiao-Hui Dong [2]

[1] *School of Civil Engineering, Chang'an University, Shaanxi, China*
[2] *China Railway 16th Bureau Group Corporation Limited, Beijing, China*
** (Corresponding author: E-mail: niesf@chd.edu.cn)*

ABSTRACT

The application and promotion of concrete-filled steel tube (CFST) columns and H-shaped steel beam joints have been extensive in structural engineering. To mitigate stress concentration on columns and protect the panel zone from damage, a fabricated assembly joint was proposed and investigated. This joint comprises a precast concrete-filled steel tube (CFST) column connected to an H-shaped steel beam via an end-plate connection. The joint is assembled conveniently using high-strength bolts, outer diaphragm, and end-plate. Numerical simulation was employed to investigate the seismic behavior of this novel CFST column and H-shaped steel beam joints. Detailed analysis was conducted on failure modes, moment-rotation hysteretic curves, and skeleton curves of specimens subjected to cyclic loading. The results demonstrated that the joint exhibited a full hysteretic curve with excellent seismic performance. Subsequently, a parametric study was conducted to explore a wide range of designs. The results revealed negligible pinch effects in the hysteretic curves and demonstrated excellent joint energy dissipation capacity. All specimens exhibited ductility greater than 3.5. Increasing the thickness of beam end-plate from 12mm to 22mm resulted in a 23.59% increase in initial stiffness but led to a decrease of 13.78% in ductility. Connector end-plates with less than 16mm thickness experienced high stress levels. The position of outer diaphragm significantly influenced the joint's failure mode. Increasing the axial compression ratio from 0.3 to 0.8 reduced the joint's ductility coefficient by 5.2%, suggesting that the axial compression ratio of column limit of 0.7 is recommended for design purposes. Furthermore, increasing the linear stiffness ratio of beam-to-column from 0.18 to 0.59 resulted in a substantial increase in the maximum moment (108.78%) and initial stiffness (90.3%) within specimens. Finally, the reasonable ranges for the thickness of end-plate, the position of outer diaphragm, the axial compression ratio of column, and the linear stiffness ratio of beam-to-column are proposed in this study.

ARTICLE HISTORY

Received: 12 November 2024
Revised: 7 January 2025
Accepted: 8 January 2025

KEYWORDS

End-plate connection;
Concrete-filled steel tubular;
Seismic behavior;
Numerical analysis;
Failure mode;
Design method

1. Introduction

Concrete-filled steel tube (CFST) columns have gained increasing popularity in structural engineering due to their advantageous properties of high ductility and compressive strength. However, the conventional joint connection method for CFST columns to steel beams poses several challenges, including reduced production efficiency and difficulties ensuring construction quality. Therefore, it is crucial to investigate a rational prefabricated joint configuration for the application and advancement of CFST structures.

Based on the recommended code and specification for CFST column-beam joints, various connection forms of CFST column-steel beam composite joints have been proposed. Deng [1] introduced a novel joint design connecting the CFST column and H-shaped beam by welding a vertical diaphragm to the column, thereby enhancing the seismic performance of the panel zone. The study investigated various aspects of the joint's seismic behavior, including failure modes, hysteretic curves, skeleton curves, and ductility. Behrooz [2] proposed a joint connection between a square steel tube column and a steel beam using a connector and an end-plate. Both experimental and numerical analyses have shown that this joint exhibits a full hysteretic curve. Ansari [3] conducted a numerical investigation on stiffener steel beams connected to circular concrete-filled steel tube columns under cyclic loading to explore the effects of different parameters on connection failure modes. Mou [4] proposed a self-centering CFST column-to-H-shaped beam joint that exhibited increased bending capacity with higher axial compression ratios and width-thickness ratios of the steel tube. Tjahjanto [5] investigated the behavior of square CFST columns with direct-welded connections, revealing shear fracture in the column tube plates caused by high-stress concentration at the beam flange and limited joint capacity. Tao et al. [6] conducted an experimental and numerical analysis study on the seismic behavior of composite joints comprising CFST columns, steel beams, and through-bolt connections. The results demonstrated a significant improvement in initial stiffness and ductility. Nie [7-9] performed experimental and numerical investigations on the seismic behavior of steel and composite beam-to-column joints. The findings from both experiments and simulations indicated favorable seismic performance and bearing capacity for these joints.

In the end-plate connection of the composite column, the current research trend is to directly weld the end-plate onto the concrete-filled steel tube and connect the steel beam with high-strength bolts. Experimental research conducted by Wang et al. [10-11] investigated end-plate connections between concrete-filled steel tubular columns and steel beams. The results demonstrated that these single-sided bolted joints were semi-rigid, exhibiting satisfactory ductility according to both American code [12] and Chinese code [13]. Liu et al. [14] presented a numerical study on moment-rotational characteristics of joints between steel beams and circular tubular columns using reverse channels, revealing that all such joints possessed sufficient strength and stiffness to be classified as semi-rigid. Málaga [15] performed an experimental study on beam-to-tubular column connections utilizing combined channel components, examining their stiffness, strength, and energy dissipation properties. Lopes [16] conducted an experimental investigation into the fire resistance of a frame with a U-shaped connection, finding that this type of connection exhibited superior ductility. Nie [17-18] proposed an end-plate connection between an H-shaped steel beam and weak axis of an H-shaped column using a U-shaped connector; results indicated that placing the U-shaped connector in the weak axis formed a box-shaped panel zone with increased volume within which shear deformation resistance was enhanced.

There is limited research available on fabricated circular steel tube concrete-steel beam joints in current literature. Existing connection methods for circular steel tube concrete columns and beams primarily focus on outer diaphragm connections, welded connections, and end-plate connections. The single connection method exhibits several significant drawbacks. Specifically, the welding connection incurs considerable construction costs, and the seismic and energy dissipation performance of end-plate connected joints requires further improvement. Additionally, the connection between H-shaped steel beams and circular steel tubular columns presents challenges due to the non-uniform outer surface. This paper innovatively integrates outer diaphragm and end-plate connections to address these issues.

The novel joint, which integrates the outer diaphragm, end plate, and stiffener, demonstrates significantly improved seismic behavior. These components effectively mitigate stress concentration on columns, thereby protecting the panel zone from damage. A finite element model (FEM) was developed using Abaqus to analyze the novel joint. The comprehensive analysis included discussions on failure modes, hysteresis curves, skeleton curves, bearing capacity and ductility. Furthermore, parametric investigations were conducted to assess the impact of parameters such as beam end-plate, connector end-plate, position of the outer diaphragm, axial compression ratio and linear stiffness ratio of the beam-to-column on bearing capacity. Based on these analytical results, design recommendations were proposed for CFST structures. The joint is illustrated in Fig. 1.

2. Design of specimen

The basic specimen was designed following the 'Technical Code for Steel Structure of Light-weight Building with Gabled Frames' (GB 51022-2015) [19]. M22 high-strength bolts of grade 10.9 were used to connect the column and beam, while concrete with a strength grade of C40 was utilized in all specimens. The steel used was documented in Q235. The preloading force of the bolt was 190 kN. The configuration and dimension of the basic specimen are illustrated in Fig. 2.

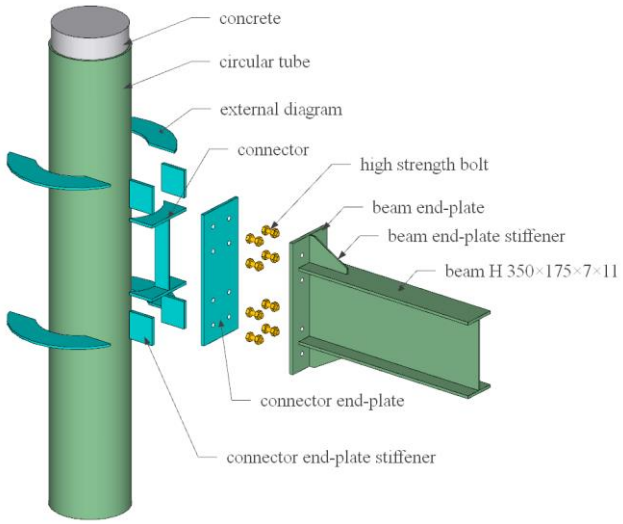

Fig. 1 Connection of the basic specimen configurations

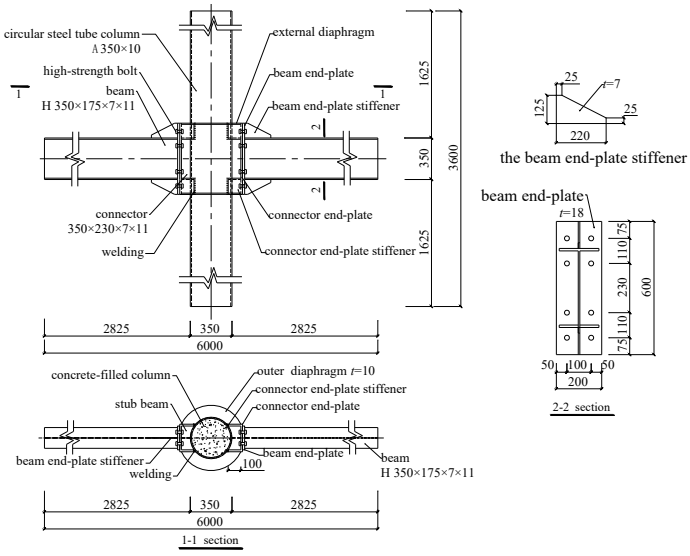

Fig. 2 Detail of the BASIC specimen (unit: mm)

3. Establishment and verification of finite element model

3.1. Constitutive relationship setting and element selection

A double-broken line model was employed to simulate the stress-strain relationships of steel and high-strength bolts. The elastic modulus of steel was 206,000 MPa, with a Poisson's ratio of 0.3. The yielding strength, ultimate strength, and ultimate strain of the steel were determined as 235 MPa, 420 MPa, and 0.15 respectively. For the high-strength bolts, the yielding strength, ultimate strength and ultimate strain were found to be 940 MPa, 1130 MPa, and 0.10 respectively.

Solid elements (C3D8R) were utilized throughout the finite element model FEM analysis for all components involved in this study.

3.2. Boundary conditions and interactions

The loading scheme is shown in Fig. 3. The boundary conditions were designed to accurately replicate real-world scenarios. Incorrect boundary conditions could result in erroneous outcomes. For the BASIC specimen, reference points RP1 and RP5 were established at the top and bottom of the column, respectively. All degrees of freedom at the top and bottom surfaces of the column were coupled with RP1 and RP5, respectively. Additionally, the degrees of freedom on the side flange surface of the top column with a length of 50 mm were coupled with RP2. Displacement constraints were applied to prevent lateral displacement instability during loading by restricting movement within 50 mm from the loading point on the side surface of the beam flange.

'Tie' contact was implemented for welding positions. According to the "Steel Structure Design Standard" (GB 50017-2017) [20], the tangential friction coefficient between the contact surfaces of the beam, end-plate, and high-strength bolts was specified as 0.4. For the interface between the steel tube and infilled concrete, a frictional contact model with a tangential friction coefficient of 0.2 [21] was employed, while hard contact behavior was used in the normal direction to accurately simulate realistic contact conditions.

To ensure that no instability occurred when the axial compression and the displacement were applied to the column. X, Y direction displacement constraints and X, Z direction rotational constraints were applied to RP1. Y, Z direction displacement constraints and X, Z direction rotational constraints were applied to RP3 and RP4. X, Y, Z direction displacement constraints and X, Z rotational constraints were applied to RP5. The boundary conditions and mesh division are depicted in Fig. 4.

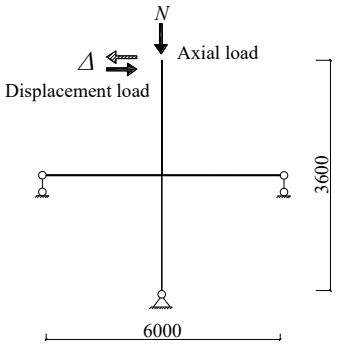

Fig. 3 Loading scheme (unit: mm)

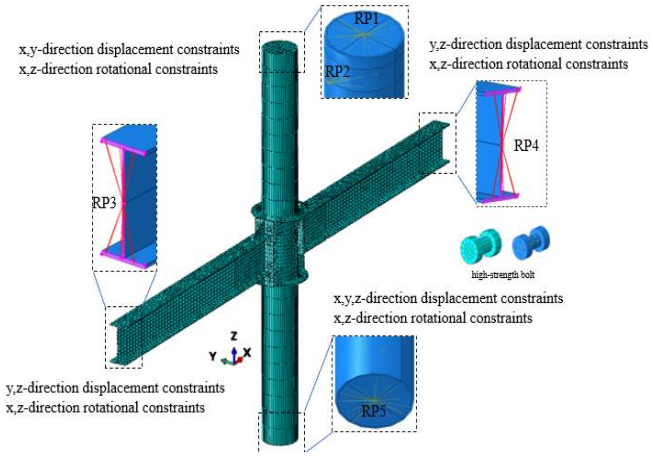

Fig. 4 Boundary Conditions and grid division of the BASIC specimen

3.3. Loading process

The loading process is illustrated in Fig. 5. Initially, a constant axial compression load was applied at the top of the column which remained throughout the entire loading process followed by low cyclic loading applied to RP2 as per American seismic provision ANSI/AISC341-10 [22]. The loading control was based on inter-story drift angle criteria until reaching an ultimate value corresponding to an inter-story drift angle equaling 0.06 rad.

3.4. Verification of FEM

To validate the feasibility and accuracy of the FEM analysis method adopted herein, the first SB-4E model based on reference [23] was established using the aforementioned approach. Secondly, FEM results obtained through

analysis were compared against experimental findings to verify correctness. The experimental setup, loading scheme and detailed information of the SB-4E specimen are illustrated in Figs. 6, 7 and 8. The material properties are presented in Table 1. The cyclic loading point for specimen SB-4E is located at the beam end, and the loading process, as detailed in reference [23], is identical to that applied to the specimens shown in Fig. 5.

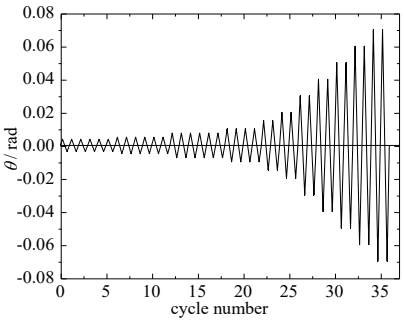

Fig. 5 Loading process

Fig. 6 Experimental setup and specimen

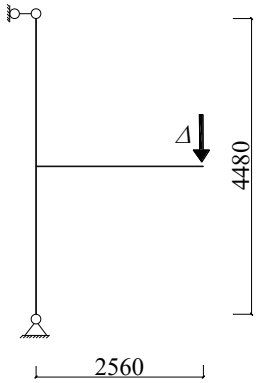

Fig. 7 Loading scheme of the SB-4E specimen

The failure modes, moment-rotation hysteretic curves, and skeleton curves obtained from both FEM analysis and experiments are presented in Figs. 9 and 10. A comparison between the FEM analysis and test results is provided in Table 2. The inter-story drift angle θ and beam moment M are calculated using Eqs (1) and (2), respectively [24-25].

$$\theta = \arctan\frac{\Delta}{H} \tag{1}$$

$$M = R_1 l \tag{2}$$

Where Δ represents the horizontal displacement; H represents the height from the loading point to the bottom of the column; R_1 represents the reaction force of the end of the left beam; l represents the distance from the beam end to the surface of the connector; M_p represents the plastic moment of the whole section of the beam.

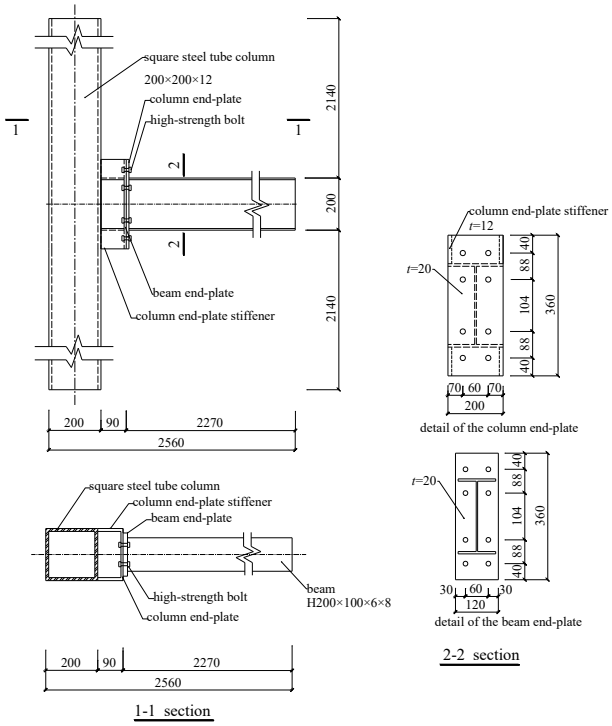

Fig. 8 Details of the SB-4E specimen (unit: mm)

Table 1
Material properties of SB-4E

Element	Thickness or Diameter / mm	Yield stress / MPa	Ultimate strength / MPa
Beam flange & stiffener	8	327.0	480.2
Beam web & stiffener	6	307.0	410.0
Beam end-plate	20	262.8	428.0
Column end-plate	12	270.5	459.7
High-strength bolt	16	925.0	1147.8

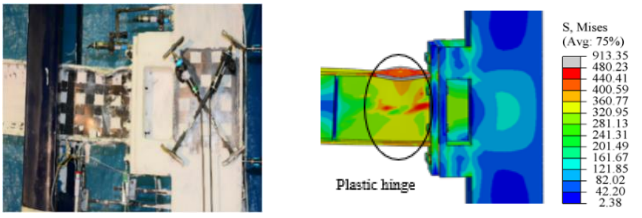

(a) Failure mode of the test result (b) Failure mode of the FEM result

Fig. 9 Comparison of failure mode

Figs. 9 and 10 demonstrated that the skeleton curves obtained from FEM analysis align well with those obtained from experiments. During the experiment, significant deformation occurred on the beam flange. In the FEM analysis, high-stress regions were concentrated near the beam flange and web where stress values reached their ultimate limits.

Table 2 revealed that there was less than a 5% difference between M_y and M_{max} as determined by FEM analysis compared to experimental results. The

FEM analysis demonstrated that the failure mode and hysteresis curve obtained from the simulation align well with the experimental results, indicating the validity and reliability of the FEM model for subsequent analyses.

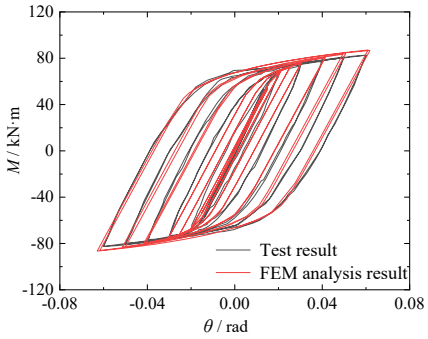

(a) Hysteretic curves

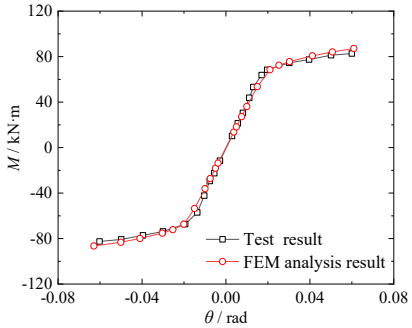

(b) Skeleton curve

Fig. 10 Comparison of hysteretic curves, and skeleton curves

Table 2
Comparison of FEM analysis and test results

Loading direction	M_y / kN·m			M_{max} / kN·m		
	Test	FEM	comparison	Test	FEM	comparison
+	69.4	71.1	2.39%	82.7	86.8	4.72%
−	67.9	70.7	3.96%	82.6	86.5	4.51%

Note: M_y and M_{max} represent the yielding moment and the maximum moment of the joint, respectively.

4. Seismic behavior of BASIC specimen

To investigate the seismic behavior of specimen BASIC, we analyzed its failure mode, hysteretic curve, skeleton curve, and ductility using FEM analysis. In this study's approach to damage assessment during the testing phase within elastic range was defined as load dropping to below 85% of maximum load value.

4.1. Moment-rotation hysteretic curve and skeleton curve

A mesh-sensitivity analysis was performed in the numerical simulations for joints to examine the influence of varying mesh sizes on the mechanical behavior of the specimens. The mesh-sensitivity analysis is illustrated in Fig. 11. Considering both the accuracy of the results and the computational cost, a 40 mm × 40 mm grid was selected for the panel zone, while a 100 mm × 100 mm grid was chosen for the beam, column, and concrete elements. Fig. 11 illustrates both the moment-rotation hysteretic curve and skeleton curve for specimen BASIC while Table 3 provides corresponding results.

As shown in Fig. 11 and Table 3, the hysteretic curve of the BASIC specimen was full and exhibited no pinching behavior, indicating that strong energy dissipation capacity was possessed by the BASIC specimen. The hysteretic loop area of the specimen BASIC increased continuously with the loading process, indicating that the energy dissipation behavior of the specimen was improved. The ductility coefficient of the BASIC specimen was 3.89, indicating excellent resistance to deformation under cyclic loading conditions.

The FEM analysis results were compared with those of the joint proposed by Brehooz [2]. Both types of joints exhibited an optimal failure mode by positioning the end-plate at the connection, ensuring that the plastic hinge formed well outside the panel zone. The presence of the outer diaphragm in this study effectively protected the end-plate and column, preventing stress concentrations from reaching the yield stress in this critical area.

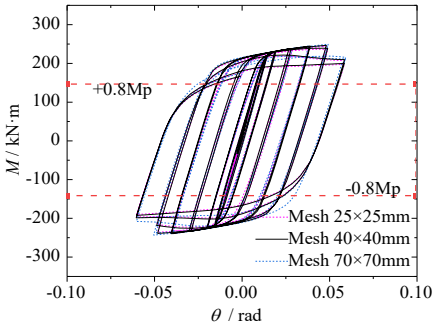

(a) Hysteretic curve

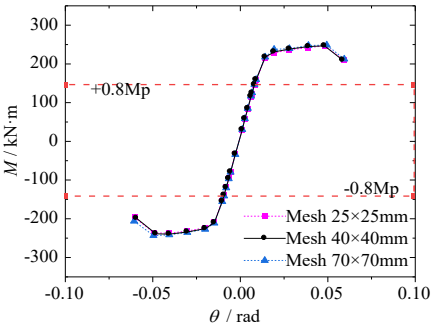

(b) Skeleton curve

Fig. 11 Hysteresis and skeleton curves of the BASIC specimen under varying mesh sizes

Table 3
FEM analysis results of the BASIC specimen

Mesh size	M_y /kN·m	θ_y /rad	M_{max} /kN·m	θ_{max} /rad	M_u /kN·m	θ_u /rad	μ
40×40mm	215.8	0.02	244.1	0.05	207.5	0.06	3.89
25×25mm	215.6	0.02	243.9	0.05	207.3	0.06	3.87
70×70mm	216.4	0.02	246.9	0.05	209.8	0.06	3.86

Note: M_u represents the failure moment of the joint. θ_y, θ_{max} and θ_u represent the inter-story drift angles at the yielding moment, maximum moment, and failure moment, respectively. μ represents the rotational ductility coefficient, calculated as $\mu=\theta_u/\theta_y$

4.2. Failure mode and failure process

Fig. 12 illustrates the failure mode and Von Mises stress distribution of the BASIC specimen.

It can be observed from Fig. 12 that plastic hinges formed at the beam when the joint was damaged. The outer diaphragm effectively protected the connection region between the connector and circular steel tube column, while minimal damage occurred in the panel zone, end-plate and high-strength bolts.

5. Parametric study

The study further investigated various parameters including the thicknesses of beam end-plate and the connector end-plate, the position of outer diaphragm, the axial compression ratio of the column, and the linear stiffness ratio of beam-to-column. The detailed parameters and results of specimens is shown in Table 4

5.1. The thickness of beam end-plate

Three specimens were established for the A series with different thicknesses: A-1 (0.55 d_0), A-2 (0.73 d_0), and A-3 (1.00 d_0) where d_0 represents the M22 bolt diameter. Contours depicting Von Mises stress distribution under failure modes for A series specimens are presented in Fig 13 while hysteretic curves and skeleton curves are shown in Figs. 14 and 15 respectively.

As shown in Fig. 13, The failure modes of specimens BASIC and A-3 exhibited similarities to the BASIC specimen, with plastic deformation

occurring at both the beam flange and web, far away from the joint. The stress experienced by the beam end-plate was relatively low. In contrast, for specimen A-1, under the applied failure load, significant deformation was observed in the beam end-plate, accompanied by a concentration of stress at the weld between the beam flange and end-plate.

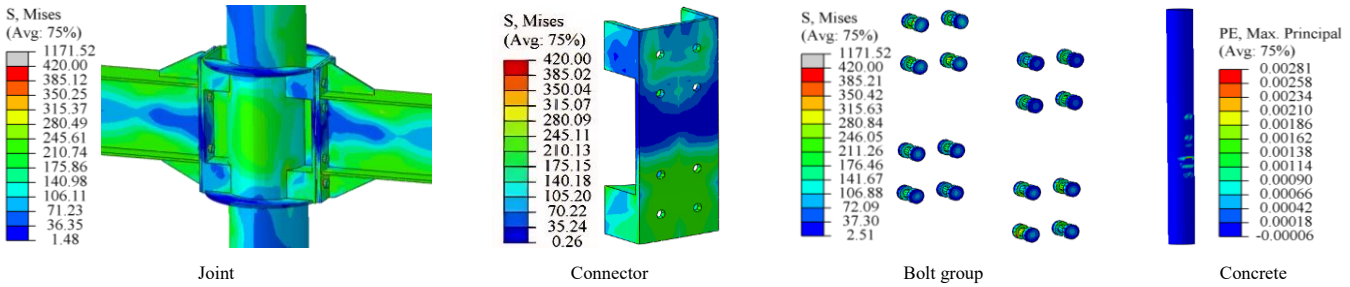

(a) Von Mises stress and strain at yielding load

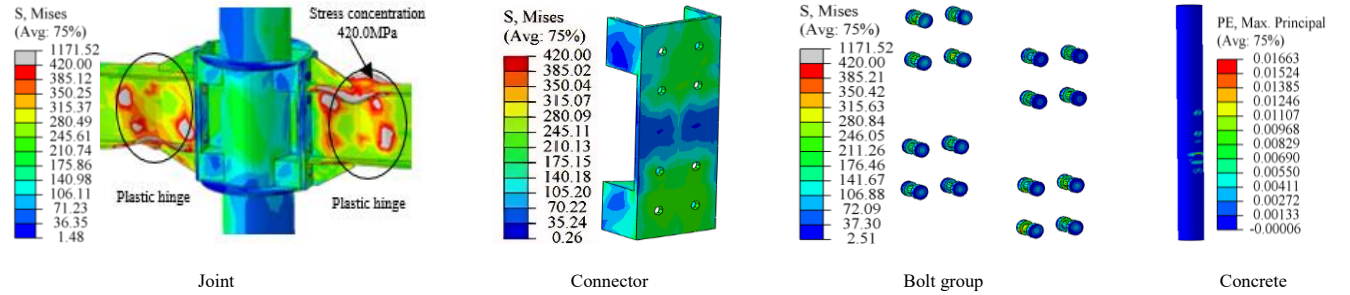

(b) Von Mises stress and strain at failure load

Fig. 12 Contour of the Von Mises stress and strain of BASIC specimen

Table 4
The parameters and results of specimens

Specimen	t_1 / mm	t_2 / mm	d	n	k	M_y / kN·m	θ_y / rad	M_{max} / kN·m	θ_{max} / rad	M_u / kN·m	θ_u / rad	μ
A-1	12	14	1.00	0.3	0.33	176.0	0.017	235.1	0.060	235.1	0.080	4.71
A-2	16	14	1.00	0.3	0.33	211.1	0.015	243.9	0.050	207.3	0.059	3.90
BASIC	18	14	1.00	0.3	0.33	215.8	0.015	244.1	0.050	207.5	0.059	3.89
A-3	22	14	1.00	0.3	0.33	213.7	0.015	244.7	0.050	208.0	0.057	3.88
B-1	18	10	1.00	0.3	0.33	183.2	0.016	243.6	0.060	207.1	0.069	4.29
B-2	18	16	1.00	0.3	0.33	216.2	0.015	244.3	0.050	207.6	0.059	4.02
B-3	18	20	1.00	0.3	0.33	217.5	0.014	244.7	0.050	208.0	0.058	4.10
C-1	18	14	0	0.3	0.33	214.3	0.015	243.2	0.050	206.7	0.059	3.84
C-2	18	14	0.50	0.3	0.33	214.9	0.015	243.4	0.050	206.9	0.059	3.86
C-3	18	14	1.00	0.3	0.33	215.8	0.015	244.11	0.05	207.49	0.059	3.88
D-1	18	14	1.00	0.4	0.33	214.4	0.015	244.1	0.050	207.4	0.059	3.88
D-2	18	14	1.00	0.5	0.33	213.0	0.015	244.0	0.050	207.4	0.059	3.82
D-3	18	14	1.00	0.6	0.33	211.9	0.015	243.9	0.040	207.3	0.059	3.78
D-4	18	14	1.00	0.7	0.33	210.8	0.015	243.7	0.040	207.2	0.059	3.76
D-5	18	14	1.00	0.8	0.33	208.5	0.015	243.2	0.040	206.8	0.059	3.68
E-1	18	14	1.00	0.3	0.18	143.1	0.015	168.0	0.050	142.8	0.068	4.59
E-2	18	14	1.00	0.3	0.46	267.8	0.015	320.4	0.050	272.4	0.059	3.87
E-3	18	14	1.00	0.3	0.59	301.9	0.018	350.8	0.050	304.6	0.059	3.39

Note: t_1 represents the thickness of beam end-plate; t_2 represents the thickness of connector end-plate; d represents the ratio of the vertical distance of the outer diaphragm to the height of the connector end-plate; n represents the axial compression ratio; k represents the linear stiffness ratio of the beam-to-column.

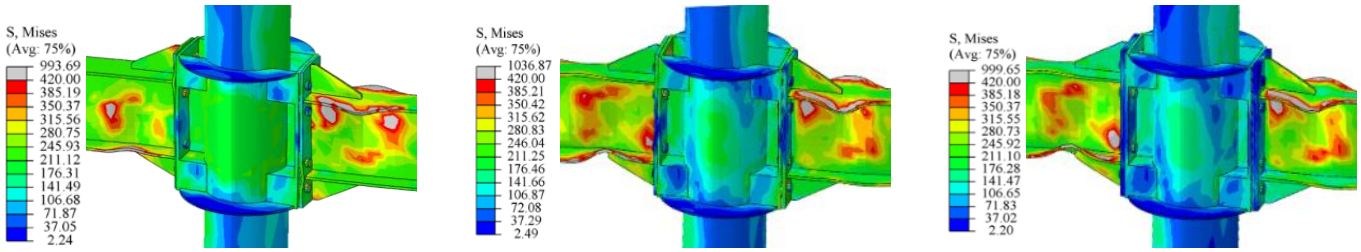

(a) A-1 (b) A-2 (c) A-3

Fig. 13 The contour of the Von Mises stress of A series specimens under failure modes

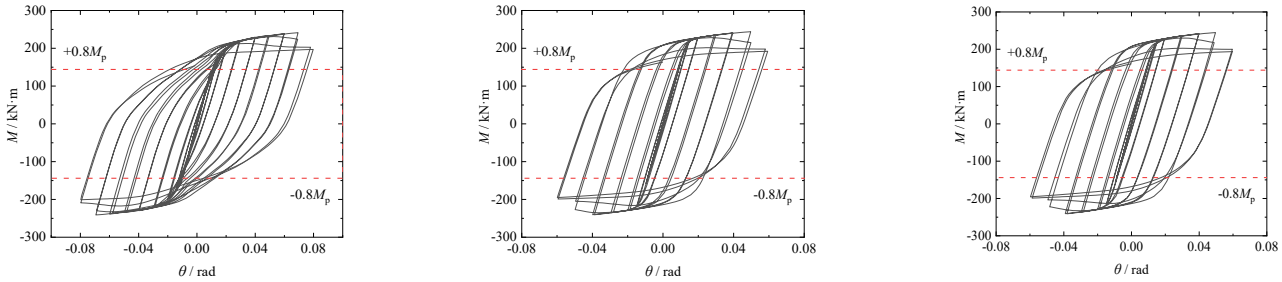

(a) A-1 (b) A-2 (c) A-3

Fig. 14 Hysteretic curves of A series specimen

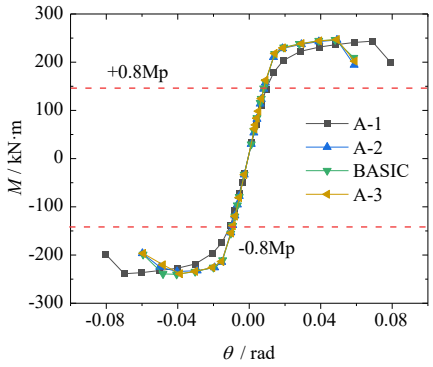

Fig. 15 Skeleton curves of A series specimen

As shown in Figs. 14 and 15, all specimens within the A series exhibited full hysteretic curves during loading cycles with similar initial-stage skeleton curves. However, the maximum moment slightly increased as a function of increasing beam end-plate thickness. Specifically, varying beam end-plate thickness from 12 to 22mm resulted in a maximum moment increase of approximately 4.1% accompanied by a reduction in ductility coefficient by 23.5%. Despite this decrease in ductility coefficient values among all joints remained above 3.6, indicating satisfactory ductile behavior. The influence of the beam end-plate thickness on both the ductility and failure mode of the joint was found to be significant, while its effect on bearing capacity was comparatively minor.

To ensure a reasonable formation of the plastic hinge within an acceptable range of deformation for the beam end-plate, it is recommended that the thickness t_1 should exceed 16mm (0.73 d_0).

5.2. The thickness of connector end-plate

The thickness of connector end-plate was varied with values of 10mm (0.45d_0), 16mm (0.73d_0), and 20mm (0.91d_0). B-1, B-2 and B-3 specimens were established correspondingly. Von Mises stress of B series specimens under failure mode was shown in Fig. 16, hysteresis curves and skeleton curves were shown in Figs. 17 and 18, respectively.

As shown in Fig. 16, the B-1 specimen failed to form an obvious plastic hinge on the beam. The deformation of the joint was primarily concentrated at the connector end-plate due to its thinner thickness. Once the thickness of the connector end-plate exceeded 14mm, a consistent failure mode was observed across all specimens. Plastic hinges formed away from the panel zone in the beam while maintaining an elastic state without significant deformation in the panel zone itself. Moreover, when surpassing a thickness of 16mm, the end-plate effectively protected both the column and panel zone, facilitating plastic hinge formation in the beam. Varying connector end-plate thickness from 10 to 20mm resulted in a mere increase of 0.45% maximum moment and a reduction of ductility coefficient by 4.6% for specimens."

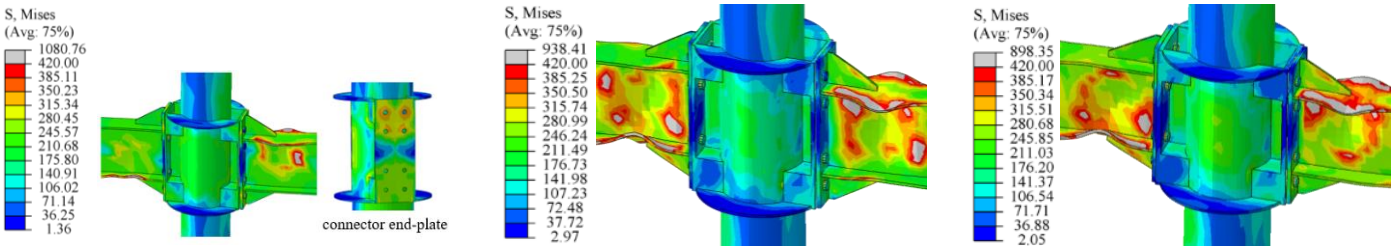

(a) B-1 (b) B-2 (c) B-3

Fig. 16 The contour of the Von Mises stress of B series specimens under failure modes

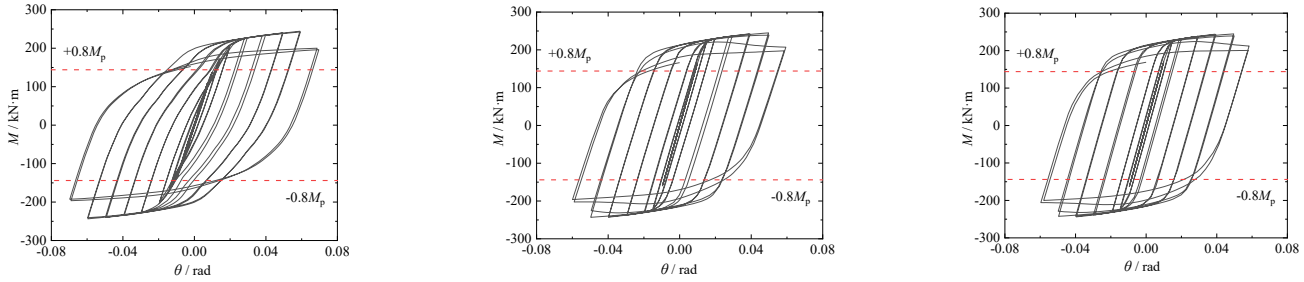

(a) B-1 (b) B-2 (c) B-3

Fig. 17 Hysteretic curves of B series specimens

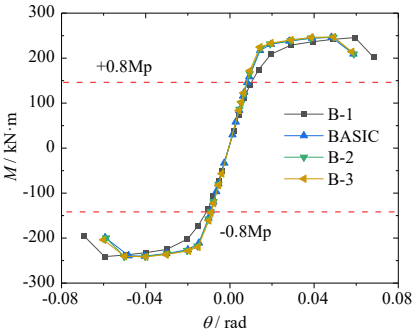

Fig. 18 Skeleton curves of B series specimens

As depicted in Figs. 17 and 18, specimen B-1 exhibited incomplete hysteretic loops due to the reduced thickness of the connector end-plate. This deficiency led to significant deformation of the end-plate during loading, insufficient development of plastic hinges at the beam, and suboptimal energy dissipation behavior of the specimens. However, when the thickness of the connector end-plate exceeded 12mm ($0.55d_0$), all specimens demonstrated complete hysteretic loops. Moreover, across all specimens, skeleton curves indicated that a connector end-plate thickness exceeding 14mm weakened its influence on seismic behavior, thereby satisfying seismic requirements [19].

5.3. The position of outer diaphragm

The position of outer diaphragm represents the ratio of the vertical distance of the outer diaphragm to the height of the connector end-plate. Three different positions of outer diaphragm were considered, namely 0, 0.50, and 1.00. Consequently, C-1, C-2, and C-3 specimens were established correspondingly. Fig. 19 illustrates the contours of Von Mises stress for E series specimens under various failure modes, while Figs. 20 and 21 present hysteretic and skeleton curves respectively.

As shown in Fig. 19, If the outer diaphragm position of the specimen is less than 0.50, the connector end-plate would also yield when the joint was damaged. If the outer diaphragm position of the specimen was 0.50, the failure mode of the joint was similar to that of the basic specimen. When the plastic deformation was formed at the beam, there was no obvious deformation in the panel zone.

Figs. 20 and 21 indicated that C-2 and C-3 exhibit superior energy dissipation capacity compared to other specimens, suggesting that the elevated position of the outer diaphragm effectively safeguards the column and panel zone. This configuration ensured predominantly elastic behavior with minimal deformation in both the panel zone and column. Furthermore, as the position of the outer diaphragm ascended from the beam flange towards the upper end-plate connector, there was a slight increase in maximum load and ductility for this specimen. It was recommended that a minimum outer diaphragm position greater than 0.5 be adopted to ensure an optimal failure mode for specimens.

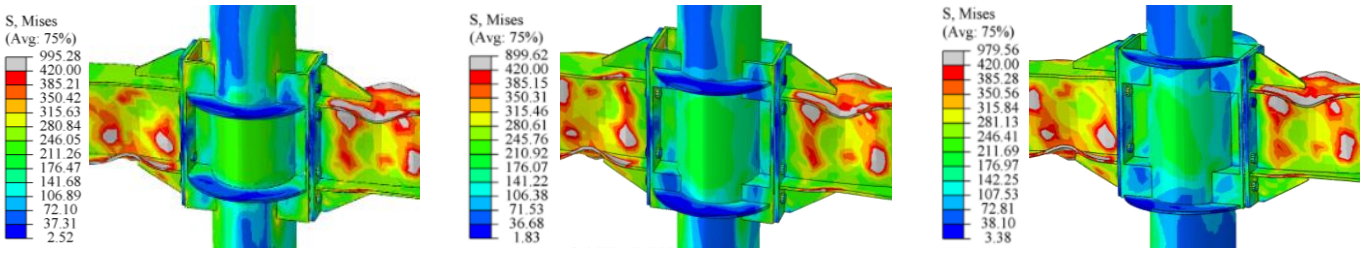

(a) C-1 (b) C-2 (c) C-3

Fig. 19 The contour of the Von Mises stress of C series specimens under failure modes

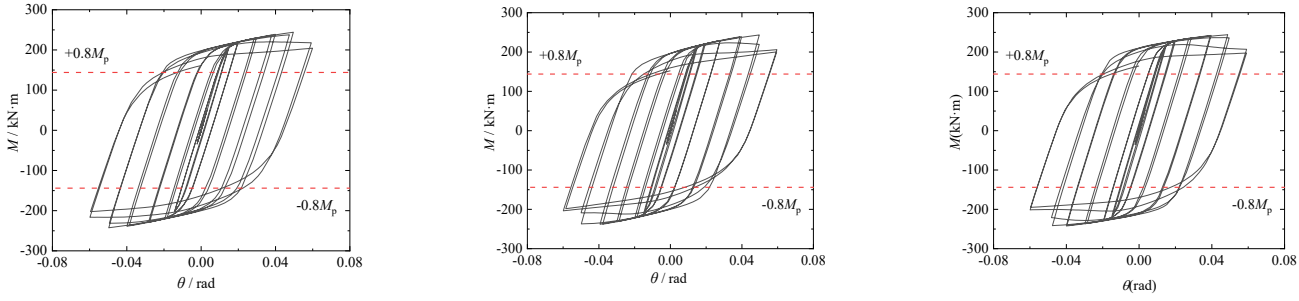

(a) C-1 (b) C-2 (c) C-3 (BASIC)

Fig. 20 Hysteretic curves of E series specimens

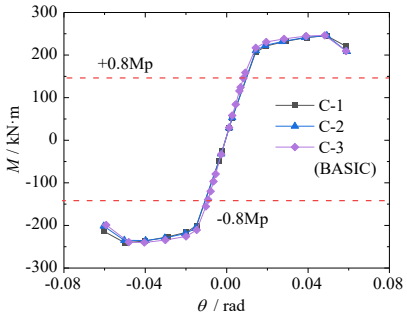

Fig. 21 Skeleton curves of E series specimens

*5.4. The axi*al compression ratio of column

The axial compression ratio of the column was determined following the Chinese code [26]. The axial compression ratio '*n*' for the concrete-filled steel tubular column is calculated using Eq (3).

$$n = \frac{N}{f_c A_c + f_s A_s} \tag{3}$$

Where N represents the design value of the concentrated load; f_c and f_s represent the design compressive strength of concrete within the column and the design compressive strength of steel, respectively; A_c and A_s represent the concrete cross-sectional area and steel pipe cross-sectional area, respectively.

The axial compression ratio of the column was varied, with values ranging from 0.4 to 0.8. Specimens D-1, D-2, D-3, D-4, and D-5 were established correspondingly.

Fig. 22 illustrates the contours of Von Mises stress for the failure modes observed in the series of specimens labeled as "D". Additionally, Figs. 23, 24 and 25 present the hysteretic and skeleton curves respectively.

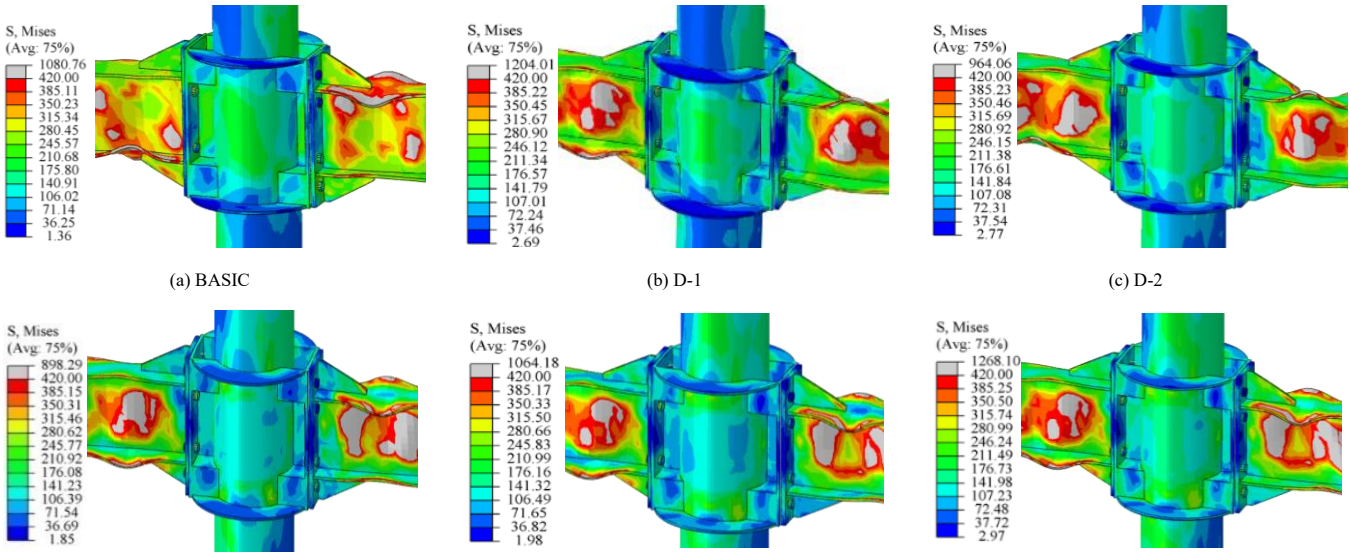

(a) BASIC (b) D-1 (c) D-2

(d) D-3 (e) D-4 (f) D-5

Fig. 22 The contour of the Von Mises stress of D series specimens under failure modes

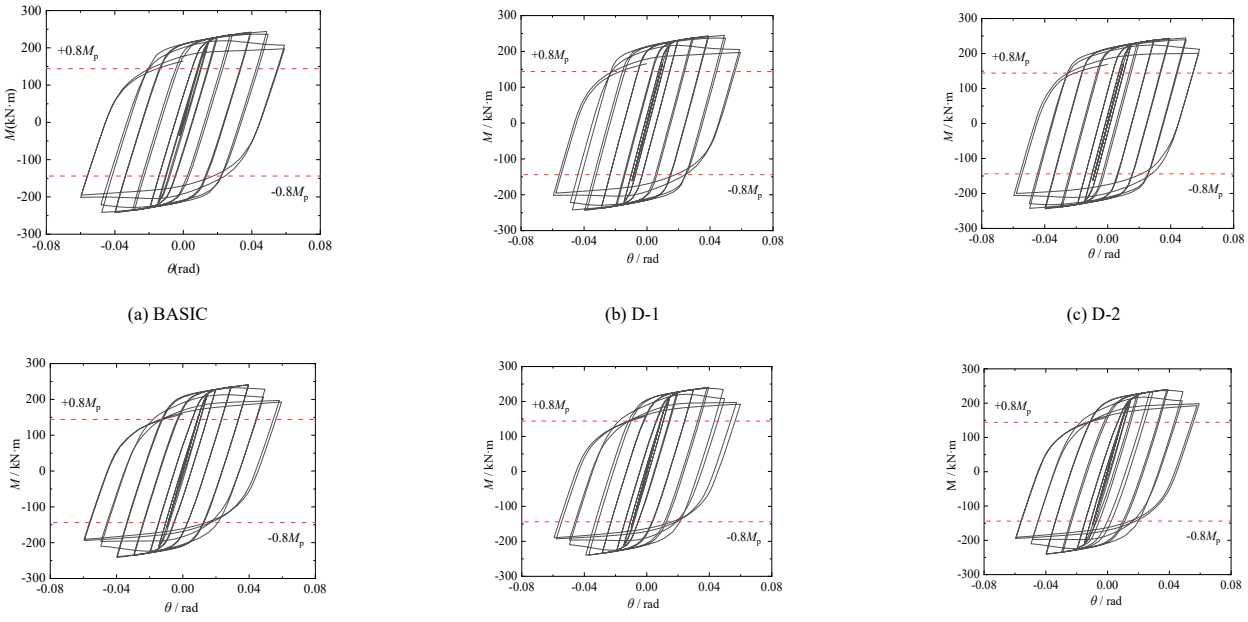

(a) BASIC (b) D-1 (c) D-2

(d) D-3 (e) D-4 (f) D-5

Fig. 23 Hysteretic curves of D series specimens

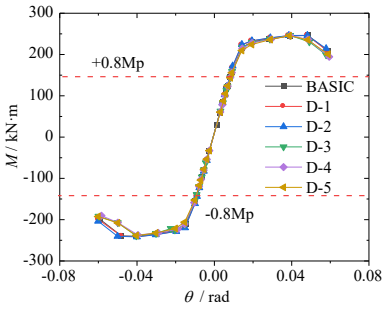

(a) *M-θ* skeleton curves

Fig. 24 *M-θ* Skeleton curves of D series specimens

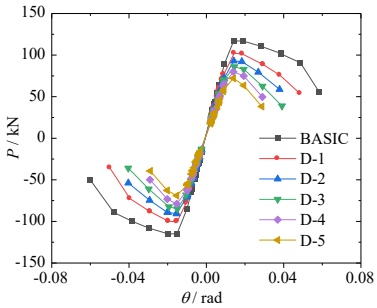

(b) *P-Δ* skeleton curves

Fig. 25 *P-Δ* Skeleton curves of D series specimens

As depicted in Fig. 22, an increase in the axial compression ratio from 0.3 to 0.8 resulted in the formation of plastic hinges at the beam of each D specimen, and similar failure modes were observed for all D specimen joints, indicating that the axial compression of the column had minimal influence on the failure mode.

The *M-θ* hysteretic curves of each specimen in the D series exhibited the same shape, as depicted in Figs. 23 and 24. During the initial loading phase, there was minimal variation in the initial stiffness of the skeleton curve among specimens. Furthermore, an increase in the axial compression ratio resulted in reductions in both the initial and peak loads of specimens, accompanied by an accelerated load reduction rate. As shown in Fig. 25, the *P-Δ* skeleton curves revealed that with increasing axial compression ratio, there were significant decreases observed in the initial stiffness, maximum load, and decline rate of bearing capacity for each specimen. This phenomenon indicated an enhanced second-order effect due to an increased axial compression ratio.

As the axial compression ratio continued to rise, a gradual decrease was observed in ductility for all specimens examined. Specifically, when increasing from 0.3 to 0.8, there was only a marginal reduction from 3.88 to 3.81 observed for rotational deformation's ductility coefficient—a relatively minor decrease overall. It is recommended that designers maintain the axial compression ratio below 0.7 to ensure satisfactory ductility behavior within specimens.

5.5. The linear stiffness ratio of beam-to-column

The linear stiffness ratio of beam-to-column '*k*' is calculated by Eq (4).

$$k = \frac{E_b I_b / l_c}{E_c I_c / l_b} \tag{4}$$

Where E_bI_b and E_cI_c represented the elastic flexural rigidity of beams and columns respectively. l_c represented the vertical distance between the upper and lower support centers of the column, and l_b represented the horizontal distance of the beam.

The section sizes of the beams were modified to H300 × 150 × 6.5 × 9, H350 × 175 × 7 × 11, H450 × 150 × 8 ×13, and H400×200×8×13 for E-1, E-2, and E-3 specimens with linear stiffness ratios varying between 0.18 to 0.59 relative to the column. Fig.26 illustrates the Von Mises stress of the H series specimens under failure modes while Figs.27 and 28 depict their hysteretic and skeleton curves.

As depicted in Figs. 26 and 27, for linear stiffness ratios of 0.18, 0.33, and 0.46 between the beam and column, these specimens exhibited significant plastic deformation of the beam flange upon reaching failure load, while maintaining low stress levels in the panel zone and column. However, when the beam-column stiffness ratio was increased to 0.59, local plastic deformation occurred at the connector end-plate during specimen damage. The plastic hinge of the beam was located near the beam end-plate but not fully developed. Consequently, with a linear stiffness ratio of 0.59, the joint design failed to meet seismic design requirements.

The maximum moment increased by 108.8% as depicted in Fig. 28, while the ductility coefficient of specimens decreased by 33.1% when varying the linear stiffness ratio of the beam-to-column from 0.18 to 0.59. The maximum moment of the beam is significantly influenced by the linear stiffness ratio of the beam-to-column, which exhibits a negative correlation with its ductility behavior.

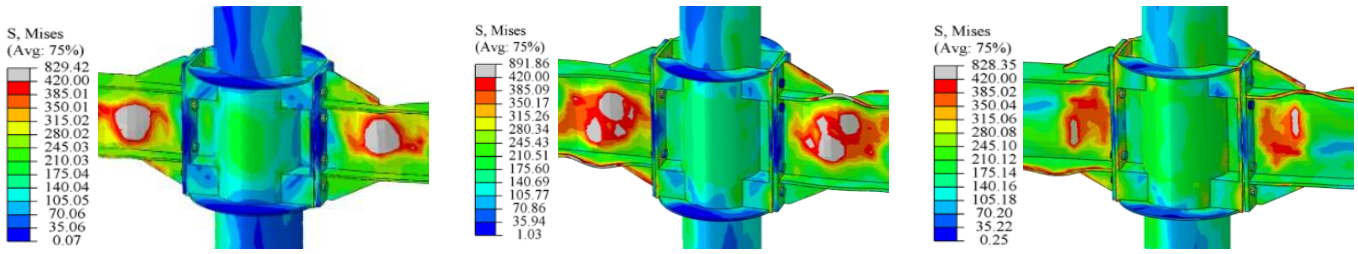

(a) E-1 (b) E-2 (c) E-3

Fig. 26 The contour of the Von Mises stress of E series specimens under failure modes

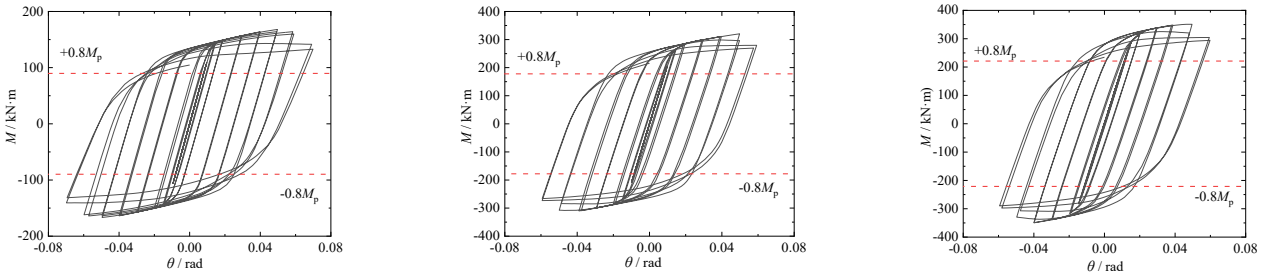

(a) E-1 (b) E-2 (c) E-3

Fig. 27 Hysteretic curves of E series specimens

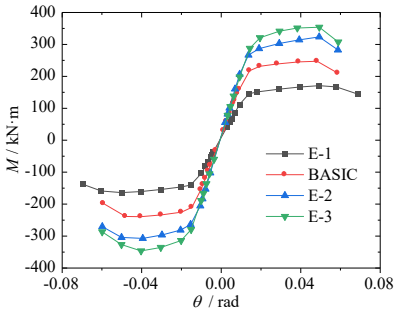

Fig. 28 Skeleton curves of E series specimen

The ideal failure mode of the specimen occurred when the linear stiffness ratio of the beam-to-column was below 0.59. To ensure a joint with strong bearing capacity and an optimal failure mode, it is recommended to limit the linear stiffness ratio of beam-to-column between 0.35 and 0.55.

6. Conclusions

Based on the finite element analysis of the seismic behavior exhibited by the BASIC specimen, a comprehensive investigation is conducted to further scrutinize the intricate effects of various parameters. Consequently, meticulous examination of these outcomes leads to the formulation of the subsequent conclusions.

(1) The end-plate connection between a steel beam and a circular CFST column exhibits excellent rotation and deformation capacity, making it a semi-rigid joint. By incorporating stiffeners and an outer diaphragm in the panel zone, the plastic hinge can be effectively relocated away from the panel zone, thereby preventing stress concentration on the end-plate. The failure mode of the BASIC specimen satisfies the principle of 'strong joints and weak members'.

(2) The seismic behavior of the joint is influenced by the thickness of the beam end-plate. Optimal end-plate thickness not only maximizes the load-bearing capacity of bolts and end-plates but also ensures superior joint ductility. The position of outer diaphragm significantly impacts the failure mode of the joint. The ductility of the joint decreases as axial compression ratio increases. When the linear stiffness ratio of beam-to-column is less than 0.59, specimens exhibit high bearing capacity and good ductility.

(3) The proposed parameter values are as follows: the thickness of beam end-plate should exceed 16mm, and the thickness of connector end-plate should be greater than 12mm. The position of outer diaphragm should be above 0.5. The axial compression ratio of the specimen is limited to 0.7. It is recommended that the linear stiffness ratio of beam-to-column falls within a range of 0.35 to 0.55.

(4) The joint proposed in this paper integrates the outer diaphragm with bolts, significantly enhancing construction efficiency and reducing costs. These advantages will be further investigated in subsequent research. The findings presented in this paper provide a theoretical foundation for engineering applications.

Notations

N - The design value of the axial load
Δ - The horizontal displacement
H - The height from the loading point to the bottom of the column
R_1 - The reaction force of the end of the left beam
l - The distance from the beam end to the surface of the connector
M_p - The plastic moment of the whole section of the beam
M_y - The yielding moment of the joint
M_{max} - The maximum moment of the joint
θ_y - The inter-story drift angle under the yielding moment of the joint
θ_{max} - The inter-story drift angle under the maximum moment of the joint
M - The beam moment
θ - The inter-story drift angle
R_{ki} - The initial stiffness
M_u - The failure moment of the joint
θ_u - The inter-story drift angle under the failure moment of the joint
μ - The rotational ductility coefficient
t_1 - The thickness of beam end-plate
t_2 - The thickness of connector end-plate
d - The position of outer diaphragm
n - The axial compression ratio of column
k - The linear stiffness ratio of beam-to-column
A_c - The concrete cross-sectional area.
A_s - The steel pipe cross-sectional area
E_bI_b - The elastic flexural rigidity of the beam
E_cI_c - The elastic flexural rigidity of column
l_c - The vertical distance between the upper and lower support centers of the column.
l_b - the horizontal distance of the beam.

Acknowledgments

The authors sincerely acknowledge the financial support provided by the Key Research and Development Program of Shaanxi (No.2021SF-519, No.2024GX-YBXM-374).

References

[1] Deng F.E., Wu T.S. and Qian H., "Seismic Performance and Design of an Innovative Dual Vertical Diaphragms Joint Between Flat CFST Column and H-Beam", Journal of Building Engineering, 2024, 87: 108945.
[2] Behrooz M.S. and Erfani S., "Parametric Study of Stub-Beam Bolted Extended End-Plate Connection to Box-Columns", Journal of Constructional Steel Research, 2020, 171: 106155.
[3] Ansari M., Jeddi M.Z., Badaruzzaman W.H.W., Tahir M.M., Osman S.A. and Hosseinpour E. "A Numerical Investigation on the Through Rib Stiffener Beam to Concrete-Filled Steel Tube Column Connections Subjected to Cyclic Loading", Engineering Science and Technology, An International Journal, 2020, 24(3): 728-735.
[4] Mou B., Yan X.C., Yu Y.J. and Wang Z.A. "Composite CFST Column to H-shaped Steel Beam Joint: Experimental and Numerical Investigation[J]. Engineering Structures", 2024, 299: 117083
[5] Tjahjanto H., MacRae G. and Abu A., "Behaviour of Improved Direct-Welded Connections in Square CFST Column Moment Frames Under Bidirectional Loading", Advanced steel construction, 2020, 16(02): 156-169.
[6] Tao Z., Li W., Shi B.L. and Han L.H, "Behaviour of Bolted End-Plate Connections to Concrete-Filled Steel Columns", Journal of Constructional Steel Research, 2017, 134: 194-208.
[7] Nie S.F., Zhang B. and Ye M.N., "An Investigation on the Seismic Behavior of Circular Steel Tube Confined SRC Column-RBS Joints with RC Ring Beam", Progress in Steel Building Structures, 2022, 24(09): 1-11. (in Chinese)
[8] Nie S.F., Ye M.N., Wu Y.F., Ding, W.X. and Zhu, J.Z., "Seismic Behavior of Square Tube Confined Steel-Reinforced Concrete Column-RC Ring Beam Joint", Journal of Architecture and Civil Engineering, 2019, 36(02): 84-91. (in Chinese)
[9] Nie S.F., Zhu J.Z. and Ma Y., "Study on Mechanical Behavior of Castellated Beam-Solid Column Cruciform Joints", Journal of Architecture and Civil Engineering, 2018, 35(04): 63-71. (in Chinese)
[10] Wang J.F., Zhang L. and Dai Y, "Seismic Experimental Study of End-Plate Connections for Semi-Rigid Concrete-Filled Steel Tubular Frames". China Civil Engineering Journal, 2012, 45(11): 13-21. (in Chinese)
[11] Wang J.F., Jiang S. and Guo L., "Experimental Study on Seismic Performance of Concrete-Filled Double Steel Tubular Column Composite Connections with High Strength Blind Bolts", Journal of Building Structures. 2021, 42(01): 93-102. (in Chinese)
[12] FEMA-350, Recommended Seismic Design Criteria for New Steel Moment-Frame Buildings, Federal Emergency Management Agency, Washington, American, 2009.
[13] GB 50011-2016, Code for Seismic Design of Buildings, Ministry of Housing and Urban-Rural Development of the People's Republic of China, Beijing, China, 2016. (in Chinese)
[14] Liu H. and Wang Y.C., "A Numerical Study of the Behaviour of Steel Beam to Tubular Column Joints Using Reverse Channel", Progress in Steel Building Structures, 2010, 12(04): 5-10. (in Chinese)
[15] Málaga-Chuquitaype C. and Elghazouli A., "Behaviour of Combined Channel/Angle Connections to Tubular Columns under Monotonic and Cyclic Loading", Engineering Structures, 2010, 32(6): 1600-1616.
[16] Lopes, F. and Santiago, A., "Sub-Frames with Reverse Channel Connections to CFT Composite Columns - Experimental Evaluation", Advanced Steel Construction, 2015, 11(1): 111-125.
[17] Nie S.F., Wang S., Liu B., Liu Z. and Han, Y., "Study on The Seismic Behavior of Weak-Axis End-Plate Joint of the Reinforced Beam to the Column with U-Shaped Connector", Progress in Steel Building Structures, 2023, 25(01): 38-48. (in Chinese)
[18] Nie S.F., Chen S.Y., Wu W.J., Jiang X., Wang S., Lin Y Z. and Liu M X. "An Investigation on the Seismic Behavior of the End-Plate Connection between a Steel Beam and the Weak-Axis of an H-Shaped Column Using a U-Shaped Connector", Buildings, 2024,14(4): 1087.
[19] GB 51022-2015, Technical Code for Steel Structure of Light-Weight Building with Gabled Frames, Ministry of Housing and Urban-Rural Development of the People's Republic of China, Beijing, China, 2015. (in Chinese)
[20] GB 50011-2017, Standard for design of steel structures, Ministry of Housing and Urban-Rural Development of the People's Republic of China, Beijing, China, 2017. (in Chinese)
[21] Baltay, P and Gjelsvik, A. Coefficient of Friction for Steel on Concrete at High Normal Stress[J]. Journal of Material in Civil Engineering,1990,2(1):46-49.
[22] ANSI/AISC 341-10; Seismic Provisons for Structural Steel Buidings. American Institute of Steel Construction: Chicago, IL, USA, 2010.
[23] Goudarzi, A. and Erfani, S. Seismic Performance of Beam to Box-Column Connection by a Short Stub Beam. Journal of Constructional Steel Research, 2022, 190: 107145.
[24] Lou, G.B., Li, G.Q. and Lei, Q., "Recent Developments in the Behavior and Design of High-Strength Bolted End Plate Connections (I)", Progress in Steel Building Structures, 2006, 8, 8–21. (in Chinese)
[25] Lou, G.B., Li, G.Q., Lei, Q., "Recent Developments in the Behavior and Design of High-Strength Bolted End Plate Connections (II)", Progress in Steel Building Structures, 2006, 8, 16–23. (in Chinese)
[26] JGJ 138-2016 Code for Design of Composite Structures, Ministry of Housing and Urban-Rural Development of the People's Republic of China, Beijing, China, 2016. (in Chinese)

Advanced Steel Construction – Vol. 21 No. 4 (2025) 304–315
DOI:10.18057/IJASC.2025.21.4.3

CYCLIC BEHAVIOR AND SHEAR CAPACITY OF A SINGLE-FRAME MODULAR STEEL STRUCTURE–COLD-FORMED STEEL WALL WITH SEMI-RIGID CONNECTIONS

Qing-Lin Wang [1, 2], Ji-Hong Ye [1, 2] and Ming-Zhou Su [3, 4, *]

[1] *Jiangsu Key Laboratory of Disaster Impact and Intelligent Prevention in Civil Engineering, China University of Mining and Technology, Xuzhou 221116, China*

[2] *Xuzhou Key Laboratory for Fire Safety of Engineering Structures, China University of Mining and Technology, Xuzhou 221116, China*

[3] *School of Civil Engineering, Xi'an University of Architecture and Technology, Xi'an 710055, China*

[4] *Key Lab of Structural Engineering and Earthquake Resistance, Ministry of Education (XAUAT), Xi'an 710055, China*

** (Corresponding author: E-mail: sumingzhou@xauat.edu.cn)*

ABSTRACT

Refined finite element models of a single frame comprising a modular steel structure–cold-formed steel wall (MSS-CFSW) with semi-rigid connections were established using connector parameters calibrated based on shear tests of self-drilling screw connections, then verified against existing test results. The influence of the vertical inter-module semi-rigid connection and steel frame stiffness on the cyclic behavior of the single MSS-CFSW frame was subsequently analyzed. The shear test results indicated that the direction of load relative to the plate edge significantly affected the shear performance of self-drilling screw connections near the edges. The model analysis results indicated that increasing the rotational stiffness and moment capacity provided by the semi-rigid connections increased the initial stiffness of the frame by 31.5% and its shear capacity by 20.2–79.4%; these connections restrained the single frame prior to yielding, but their effects could be disregarded afterwards. Increases in ceiling beam stiffness, floor beam stiffness, and column stiffness increased the shear capacity of the frame by 14.0–41.0%, 15.8–61.1%, and 2.2–6.5%, respectively, and its initial stiffness by 8.1–25.8%, 9.7–21.1%, and 9.9–25.4%, respectively. Finally, the semi-rigid connections were considered equivalent to rotational springs to derive an equation for the shear capacity of a single MSS-CFSW frame with semi-rigid connections and verify it against the numerical simulation results.

ARTICLE HISTORY

Received: 24 November 2024
Revised: 3 January 2025
Accepted: 8 January 2025

KEYWORDS

Semi-rigid connections;
Modular steel structure;
Numerical simulation;
Cyclic behavior;
Cold-formed steel wall

1. Introduction

Given the increasing prominence of uneven construction quality, low efficiency of on-site construction, and serious environmental pollution at construction sites, the traditional construction industry has begun to shift towards industrialization by developing prefabricated buildings. The modular steel structure, which comprises the highest proportion of prefabricated components, is among the most critical approaches for realizing construction industrialization [1].

The walls of a modular steel structure unit are not only a prerequisite for prefabricating its interior but also serve as major lateral resistance members. Given that container construction was a predecessor of modular building systems, a great deal of research on module unit walls has focused on corrugated steel plates. Ding et al. [2,3], Dai et al. [4], and Liu et al. [5] conducted quasi-static tests on one-story and two-story single-span modular steel structures infilled with corrugated steel plate shear walls (CSPSWs), which significantly improved the lateral resistance of modular steel structures. However, the shear stiffnesses of the vertical inter-module connections can be relatively small [6], resulting in a potential mismatch between the stiffness of the module unit and its connections that causes damage to the overall structure. Furthermore, as an independent room, the module unit must provide certain functions such as heat preservation, heat insulation, and sound insulation. However, CSPSWs cannot provide these functions and are difficult to combine with other materials. In addition, the welding of CSPSWs to beams and columns is time-consuming and labor-intensive, making their installation inconvenient during assembly.

The cold-formed steel wall (CFSW) is composed of framing members connected to wallboards by self-drilling screws. Notably, the interior of a CFSW can be filled with relevant functional materials such as thermal insulation materials, and both the CFSWs and steel frame of a module unit can be standardized, produced simultaneously, and assembled in the factory. Furthermore, piping can be pre-embedded inside the CFSW as required, allowing for the full preparation of module units for decoration, plumbing, and electrical requirements. Factory-prefabricated CFSWs can not only be rapidly assembled and erected with high construction quality but are also easy to dismantle and reassemble—a critical characteristic of modular steel structures. Therefore, Wang et al. [7,8] proposed the modular steel structure infilled with cold-formed steel walls (MSS-CFSWs). Fig. 1 shows the novel connection applied between the CFSW and steel frame using high-strength bolts to join connector angles to frame-welded connector plates and self-drilling screws to fix tracks to the connector plates. Test results have confirmed the effectiveness of this connection.

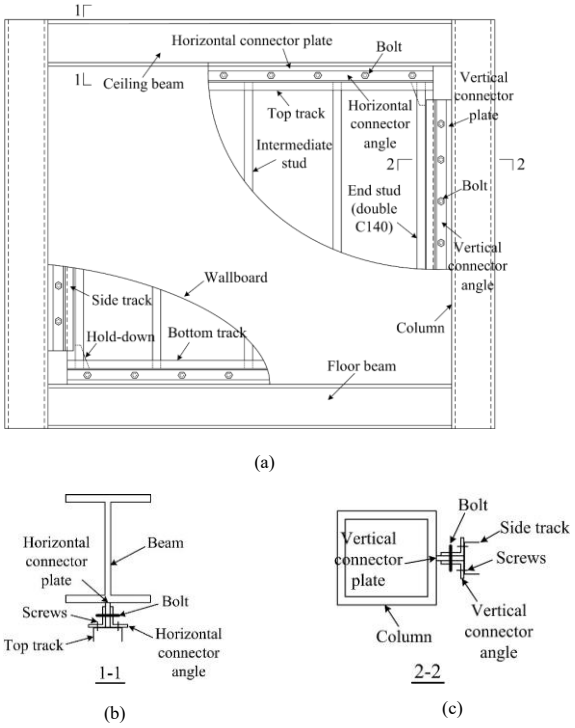

Fig. 1 Configuration of the novel connection: (a) configuration diagram; (b) beam connection; (c) column connection

The unique construction method associated with modular steel structures makes the vertical inter-module connections a critical focus of research. These connections must not only ensure convenience but also provide reliable force transmission. Researchers have accordingly proposed the use of non-welded, interlocking, post-tensioned, and plug-in self-locking inter-module connections [9-14]. As these semi-rigid connections are different from the semi-rigid beam–column joints of traditional steel structures, research into their influence on overall structural performance has been necessary. Chua et al. [15] proposed a horizontal spring model for inter-module connections and reported that the connection modeling method had a significant impact on the performance of the

overall structure. Investigations using finite element (FE) models have determined that the horizontal stiffness of the vertical inter-module connections had the greatest impact on structural performance [16], deformation was frequently concentrated in the vertical inter-module connections, the modules remained in the elastic stage, and their displacements were extremely small [6]. Wang and Su [17] derived theoretical equations for the critical buckling load of columns in sway modular steel structures with semi-rigid connections and conducted numerical simulations indicating that the critical buckling load increased with increasing connection rotational stiffness. Indeed, previous studies have indicated that the effects of vertical inter-module semi-rigid connections should be considered when studying the cyclic behavior of a single MSS-CFSW frame. However, owing to test limitations, the boundary conditions of the specimens evaluated in references [7,8] were all hinged; thus, the results did not fully reflect the cyclic behavior of a single MSS-CFSW frame.

Numerical simulations based on refined FE models can improve and expand upon experimental research. A critical aspect of any refined FE model for a single MSS-CFSW frame with semi-rigid connections is the method employed to simulate the self-drilling screw connections. Huang [18], Xu [19], and Yu [20] used nonlinear spring elements to effectively simulate self-drilling screw connections and the corresponding shear performance of the CFSW. The parameters of these elements were generally determined through shear tests of actual self-drilling screw connections. Buonopane et al. [21] conducted numerical simulations indicating that the shear force acting on self-drilling screws can be decomposed into components parallel and perpendicular to the plate edge; the test observations presented in reference [7] confirm this conclusion. However, previous evaluations of self-drilling screw connection shear performance have typically only applied shear force perpendicular to the plate edge. For example, Hao et al. [22], Li et al. [23], and Ye et al. [24] found that, in addition to the wallboard material, a larger distance from the screws to the plate edge increased the shear capacity of the connection. Furthermore, Han [25] evaluated two self-drilling screw connection specimens loaded in shear perpendicular or parallel to the plate edge and reported different shear performances.

Therefore, this study conducted shear tests on self-drilling screw connections and employed the results to develop a refined FE model of a single MSS-CFSW frame in ABAQUS. This model was validated against previous test results, then applied to evaluate the effects of the vertical inter-module connection rotational stiffness and moment capacity as well as beam and column stiffnesses on the cyclic behavior of the frame. Finally, a method for calculating shear capacity of a single MSS-CFSW frame considering the semi-rigid connections was derived and validated against the model results.

2. Shear tests on self-drilling screw connections

2.1. Specimens

Shear tests were conducted on self-drilling screw connections to inform the simulation of their behaviors and determine the parameters of the connector unit. Three types of self-drilling screw connection specimens were designed using different connected plate configurations with the dimensions shown in Fig. 2. These connection specimens joined gypsum or oriented strand board (OSB) to a cold-formed steel plate (CFSP) loaded perpendicular or parallel to its edge (Figs. 2(a) and (c)) with distances from the screws to the plate edge e of 15 mm, 125 mm, and 155 mm. The CFSP was 1.0 mm thick with lengths of L_1 and L_2 at the loaded and fixed ends, respectively; the length of the gypsum or OSB was L_b, its width was W_b, and its thickness was 12 mm. When the shear force was parallel to the plate edge, the constraint effect of the wallboard far from the plate edge on the self-drilling screw connection was considered by taking the W_b of the wallboard as (e+200) mm. A single self-drilling screw was used to connect the wallboard to the CFSP at the loaded end, whereas three self-drilling screws were used for the connection at the fixed end to avoid damage there. Furthermore, a single-screw CFSP to CFSP connection was evaluated as shown in Fig. 2(e).

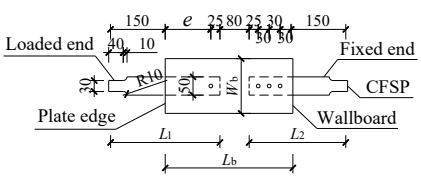

(a)

(b)

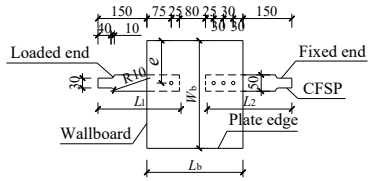

(c)

(d)

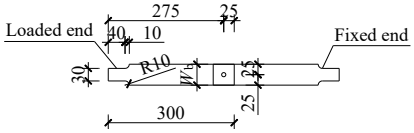

(e)

(f)

Fig. 2 Connection details: (a) connection diagram and (b) test setup for shear perpendicular to the plate edge; (c) connection diagram and (d) test setup for shear parallel to the plate edge; (e) connection diagram and (f) test setup for CFSP self-drilling screw connection (units: mm)

Table 1
Shear test specimen parameters

Specimen	Number	e (mm)	L_1 (mm)	L_2 (mm)	L_b (mm)	W_b (mm)
G-V-15	3	15	190	265	235	150
G-V-115	3	115	290	265	335	150
G-V-160	3	160	335	265	380	150
G-H-15	3	15	250	265	295	215
G-H-115	3	115	250	265	295	315
G-H-160	3	160	250	265	295	360
OSB-V-15	3	15	190	265	235	150
OSB-V-115	3	115	290	265	335	150
OSB-V-160	3	160	335	265	380	150
OSB-H-15	3	15	250	265	295	215
OSB-H-115	3	115	250	265	295	315
OSB-H-160	3	160	250	265	295	360
S-SPC-25	3	25	-	-	300	50

All connections were made using 4.8 mm diameter self-drilling screws. The specimen parameters are shown in Table 1. Each connection type was evaluated using different connection materials and e values, and a group of three specimens was tested for each configuration. In the specimen group nomenclature, the first value denotes the connected materials as OSB–CFSP (OSB), gypsum board–CFSP (G), or CFSP–CFSP (S); the second value indicates the connection type with shear acting on the screws perpendicular to the plate edge (V), parallel to the plate edge (H), or on a single self-drilling screw steel plate connection (SPC); and the third value denotes the distance from the screws to the plate edge.

The self-drilling screw connection shear tests were conducted using a 20 kN microcomputer-controlled electronic universal testing machine for loading and data collection as shown in Fig. 2. Each specimen was subjected to a displacement-controlled loading rate of 1 mm/min until it was damaged.

2.2. Failure modes

The failure process of each shear specimen was directly related to its wallboard type, e value, and applied shear direction. Five failure modes were observed, as shown in Fig. 3: plate edge bearing failure (mode B), screw pull-out failure (mode P), plate side pull-out failure (mode SP), OSB delamination tearing failure (mode T), and hole bearing failure (mode HB).

The failure modes of each specimen are reported in Table 2. When e was small (15 mm), the plate edge was prone to cracking under the compression applied by the screw, and the specimens failed owing to damage to the plate edge and side. The specific type of damage depended on the shear direction: when the shear was perpendicular to the plate edge, the specimens exhibited plate edge bearing failure; when the shear was parallel to the plate edge, the specimens failed through the thickness of the plate along its side. In contrast,

when e was large (125 mm and 155 mm), the plate edge exerted a strong restraining effect on the screw hole, and the specimens were damaged when the self-drilling screws pulled out of the plate regardless of shear direction.

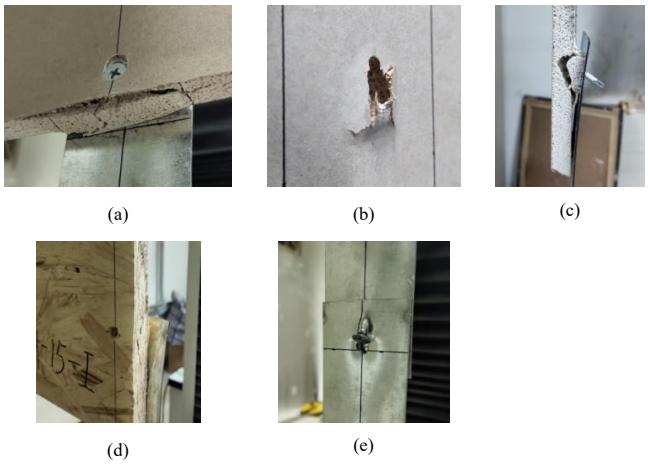

Fig. 3 Typical failure modes: (a) plate edge bearing; (b) screw pull-out; (c) plate side pull-out; (d) OSB delamination tearing; (e) hole bearing

Table 2
Characteristic values of shear test specimen skeleton curves

Specimen	Elastic point		Peak point		Failure point		Failure mode
	δ'_e (mm)	P'_e (kN)	δ'_m (mm)	P'_m (kN)	δ'_u (mm)	P'_u (kN)	
G-V-15	0.135	0.128	1.141	0.323	1.384	0.162	B
G-V-125	0.491	0.195	6.128	0.487	14.871	0.243	P
G-V-155	0.528	0.206	5.332	0.516	12.786	0.257	P
G-H-15	0.643	0.198	4.266	0.494	9.320	0.248	SP
G-H-125	0.857	0.209	6.545	0.523	12.580	0.267	P
G-H-155	0.320	0.281	4.760	0.491	11.935	0.246	P
OSB-V-15	1.330	0.756	6.269	1.892	10.628	0.946	B
OSB-V-125	2.339	0.968	12.074	2.422	18.889	1.211	P
OSB-V-155	1.740	0.903	11.351	2.259	13.856	1.195	P
OSB-H-15	2.007	0.887	8.750	2.217	13.181	1.108	T
OSB-H-125	1.509	0.888	9.606	2.221	13.883	1.111	P
OSB-H-155	1.542	0.984	13.024	2.461	17.898	1.230	P
S-SPC-25	2.876	2.929	11.703	7.319	14.478	3.708	HB

2.3. Load–displacement responses

Fig. 4 shows that the load–displacement curves for each group of specimens exhibited obvious ascending and descending segments, but the initial stage of each ascending segment followed an oblique straight line. The curves exhibited strong nonlinearity and the test data possessed a certain degree of discreteness owing to differences among the densities of the boards and specimen fabrication characteristics. The decrease in relative strength from steel to OSB and gypsum board caused the specimen shear capacities to decrease from the S series to the OSB series, then the G series. Notably, each curve for the S series specimens rapidly decreased after reaching its peak, indicating poor ductility resulting from the compression failure of the hole wall; the elastic modulus and stiffness of the connection rapidly decreased once the steel plate entered the plastic stage.

The point with the highest load in the curve was the peak point, and the load and displacement at this point were the peak load P'_m and peak displacement δ'_m, respectively. The elastic point was identified at $0.4P'_m$ in the ascending segment of the curve, and the corresponding load and displacement were the elastic load P'_e and elastic displacement δ'_e, respectively; thus, $P'_e = 0.4P'_m$. To comprehensively reflect the shear performance of each specimen, the point corresponding to $0.5P'_m$ in the descending segment of the curve was taken as the failure point; that is, the failure load $P'_u = 0.5P'_m$, and the displacement at this point was defined as the failure displacement δ'_u. The average test results for the three specimens of each group are listed in Table 2 as the characteristic values of the load–displacement curve for that specimen.

When the shear was perpendicular to the plate edge, the specimen failure mode changed from plate edge bearing failure to screw pull-out failure as e increased and the shear capacity increased accordingly. Once e exceeded a certain value, the failure mode and shear capacity remained unchanged. Clearly, e had a significant influence on the shear capacity of the G series specimen but a relatively small influence on that of the OSB series specimen. When the shear was parallel to the plate edge, e had little influence on the shear capacity and peak displacement of any specimen.

When e was small, the change in the direction of shear relative to the plate edge was typically accompanied by a change in the failure mode. Furthermore, the shear capacity of the specimen under shear parallel to the plate edge was superior to that under shear perpendicular to the plate edge. When e was large, the specimen exhibited screw pull-out failure when subjected to shear in either direction and there was no significant change in the corresponding shear capacity.

A refined FE model of a single MSS-CFSW frame specimen was established by simplifying the experimentally obtained load–displacement curves for the self-drilling screw connections using a multilinear model with reference to [18], as shown in Fig. 5. The peak points in Fig. 4 divide each curve into ascending and descending segments. The initial stage of the ascending segment of each curve was approximated by a diagonal line, but as the damage to the connection specimens intensified, the later stage of the ascending segment exhibited obvious nonlinearity and required a different slope; the elastic point was used to demarcate between these two stages. The overall slope of the descending segment was fairly consistent and was approximated as a single diagonal line with the failure point as its endpoint. Thus, the elastic point, peak point, and failure point were used as the characteristic points of the simplified model.

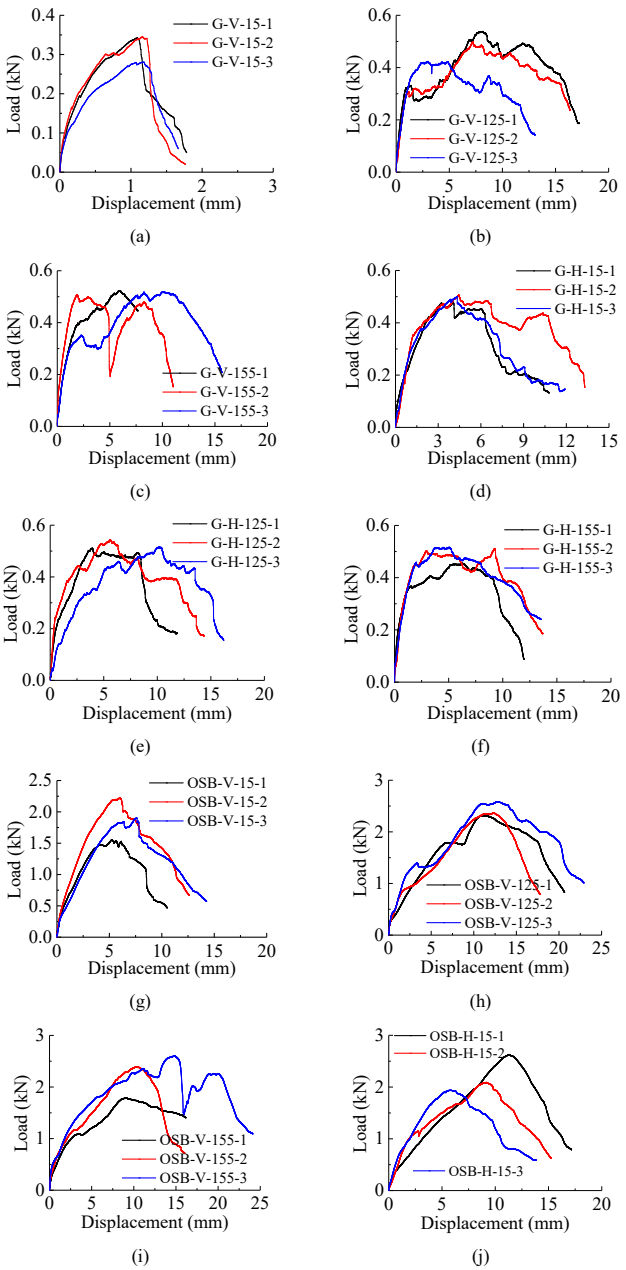

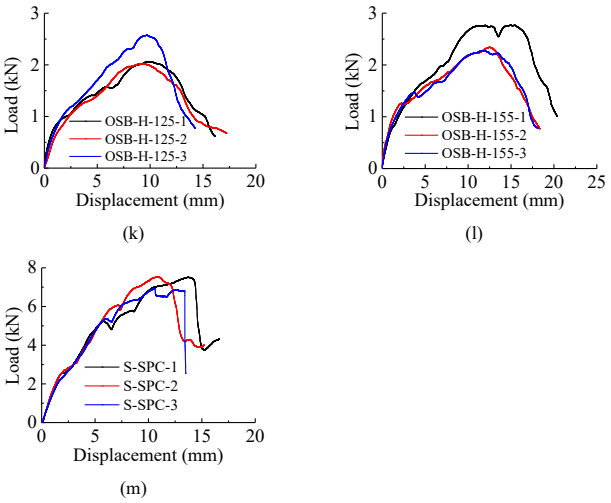

Fig. 4 Curves of the shear test specimens: (a) G-V-15; (b) G-V-125; (c) G-V-155; (d) G-H-15; (e) G-H-125; (f) G-H-155; (g) OSB-V-15; (h) OSB-V-125; (i) OSB-V-155; (j) OSB-H-15; (k) OSB-H-125; (l) OSB-H-155; (m) S-25

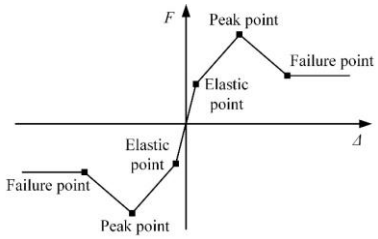

Fig. 5 Simplified load–displacement curve model for self-drilling screw connections

3. FE modeling

3.1. Single-frame substructure of the MSS-CFSW

A short-span single frame from a prototype MSS-CFSW structure was taken as the target substructure. Three full-scale specimens of this substructure were previously designed for cyclic loading tests: two single MSS-CFSW frames and one single steel frame [7]. A refined FE model of specimen MSS-CFSW-1, shown in Fig. 6, was established and validated in this study to investigate the cyclic behavior of a single MSS-CFSW frame with a four-sided connection between the CFSW and steel frame. The specimen details, material properties, test setup, and loading protocol are detailed in reference [7]. The boundary condition of the MSS-CFSW substructure should be semi-rigid, but the existing test setup could not impose the appropriate rotational constraints. Instead, hinge constraints were applied to the top and bottom of each substructure specimen during physical testing with reference to related research [2-5]. The cyclic behavior of a single MSS-CFSW frame under semi-rigid constraints was subsequently analyzed in this study using the refined FE model.

3.2. Model construction

3.2.1. Constitutive model

The steel constitutive model comprised a kinematic hardening model following the von-Mises yield criterion. This model considers the Bauschinger effect, which to some extent influences the performance of steel under cyclic loading. The material properties of the steel in specimen MSS-CFSW-1 were determined by tensile coupon tests as listed in reference [7].

Although gypsum board and OSB are anisotropic materials, studies in reference [18] indicated that both can be assumed to be isotropic in FE models. The stress–strain relationship of the wallboard was described using an ideal elastic–plastic model following the von-Mises yield criterion. The elastic modulus and static bending strength of each wallboard type were determined in previous three-point bending tests [26]. The elastic modulus and bending strength of the OSB were 2347 MPa and 19.8 MPa, respectively, and those of the gypsum board were 2391 MPa and 2.1 MPa, respectively. The Poisson's ratios of the OSB and gypsum board were both 0.2 [27].

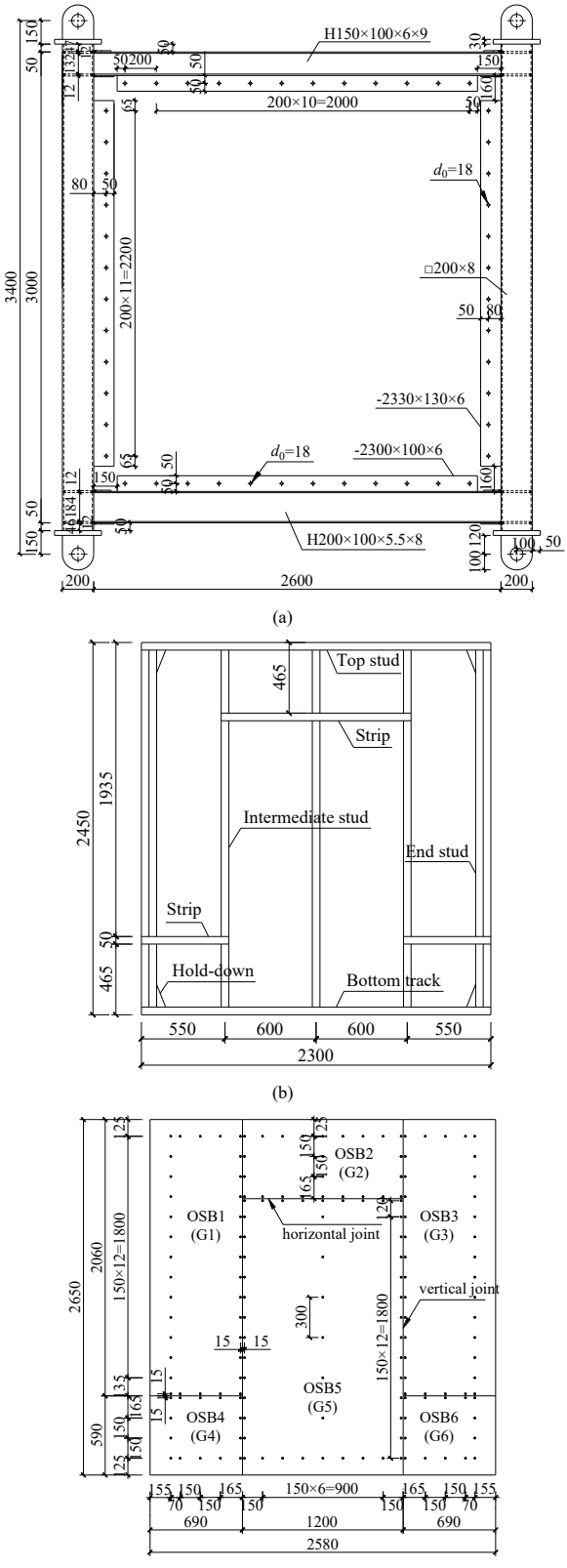

Fig. 6 Details of specimen MSS-CFSW-1: (a) steel frame; (b) framing; (c) wallboards (units: mm)

3.2.2. Element types and meshing

The components of the refined FE model included two columns, one ceiling beam, and one floor beam as well as the necessary cover plates, connector plates, connector angles, angle stiffeners, tracks, studs, strips, and wallboards. As the dimensions of the tracks, studs, strips, and wallboards were much smaller in the thickness direction than in the other directions, they were modeled using S4R shell elements. The remaining components were modeled using C3D8R solid elements with the mesh divided into two layers along the component thickness.

A mesh refinement investigation was conducted to ensure accuracy and computational efficiency. The results indicated optimal element sizes for the column, ceiling beam, floor beam, cover plates, and angle stiffeners of 70 mm,

80 mm, 80 mm, 25 mm, and 20 mm, respectively; the element sizes for the remaining components were all 50 mm. Local refined element meshes of 30 mm and 20 mm were used within 300 mm of the connection regions at the column ends and beam ends, respectively. The final FE mesh results are shown in Fig. 7.

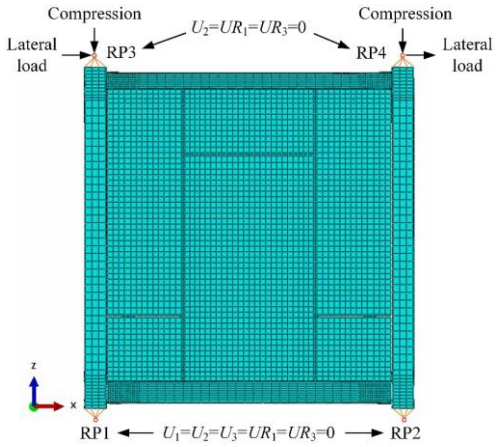

Fig. 7 Mesh and boundary conditions of refined FE model

3.2.3. Interactions

As there was no significant slip between connected components [7,8], computational efficiency was improved by removing the high-strength bolts from the refined FE model and not considering the self-drilling screw connections between the connector angles and tracks or between end stud webs. Instead, a tie constraint was applied to the contact surface between each connector angle and connector plate and each connector angle and track. Furthermore, as all four corners of the CFSW remained undamaged during the test, the FE model was simplified by tying the end faces of each end stud to the webs of the top and bottom tracks to simulate hold-downs. Welds were also simulated using tie constraints, including those between beams and columns, cover plates and flanges, and stiffeners and connector angles. General contact was assigned between wallboard units, wallboard units and framings, and studs and tracks; "hard contact," which transmits pressure while preventing contacting elements from penetrating each other, was applied in the normal direction, and a penalty function, which transmits shear between contacting surfaces, was adopted in the tangent direction using a friction coefficient of 0.4 [28].

3.2.4. Self-drilling screw connection simulation

As the lateral resistance of the CFSW depends on the shear performance of its self-drilling screw connections, accurate simulation of these connections is critical to the refined FE model. ABAQUS connector units were used to simulate the self-drilling screw connections based on the direction of shear relative to the plate edge. The parameters of these units were calibrated according to the relationship between load and displacement along the x and z directions, in the wallboard plane, and the relative rotation of the two points connected by a self-drilling screw was not limited. The self-drilling screw connection was assumed to be rigid in the out-of-plane direction. The in-plane relationship between load and displacement was defined using the simplified model with the characteristic points reported in Table 2.

3.2.5. Boundary conditions and loading

The refined FE model did not include auxiliary test devices such as the loading beam, ground beam, or lateral supports. Instead, reference points were established at the positions corresponding to the pins and were coupled with the top and bottom surfaces of the column. The refined FE model was located in the *xoz* plane. Three translational degrees of freedom and two rotational degrees of freedom were constrained at the coupling points at the bottoms of the columns such that they could only rotate around the y axis, simulating a hinge, i.e. $U_x = U_y = U_z = UR_x = UR_z = 0$. The out-of-plane translational and rotational degrees of freedom were constrained at the coupling points at the tops of the columns to simulate the presence of the lateral supports, i.e. $U_y = UR_x = UR_z = 0$. The load was applied to the coupling points at the column tops using the same loading protocol applied during the tests: first, a constant vertical load was applied, then the displacement-controlled cyclic lateral load was applied.

Not only were material, boundary, and geometric nonlinearities considered in the refined FE model, but nonlinear connector units were also used to simulate the considerable quantity of self-drilling screw connections. The ABAQUS/Explicit module was accordingly applied to perform quasi-static analysis on the refined FE model considering complex contact and high nonlinearity. Although there was no convergence issue, the computed time increment must be smaller than the stable time increment to obtain stable and reliable results. The stable time increment is often quite small, indicating that the computational efficiency is low. Therefore, the method of defining a fixed time increment, taken as 3×10^{-6} s, was employed to improve computational efficiency. There are two main reasons for choosing a fixed time increment. Firstly, finding suitable time increments for each loading level required significant computational costs. Secondly, using different time increments for different loading levels did not result in a significant decrease in computational cost. The ratio of kinetic energy to internal energy of the model was less than 5%, meeting the requirements for a quasi-static analysis.

3.3. Verification

3.3.1. Hysteretic and skeleton curves

The load–inter-story drift hysteresis and skeleton curves obtained from the refined FE model are compared with the previously obtained test results in Fig. 8. The shape of the numerically simulated hysteresis curve is basically consistent with that of the test curve, though the former appears plumper owing to the use of the simplified multilinear load–displacement curve for the connector units, which cannot accurately reflect self-drilling screw connection slip during unloading, eliminating the pinching phenomenon observed in the test results. The skeleton curves obtained from the numerical simulation and test agreed well, though the refined FE model did not accurately reflect the load degradation process. This occurred because the unloading and reloading paths for the self-drilling screw connections could not be defined using connector units. Indeed, the descending segment of the simplified load–displacement curve only decreased to 50% of the peak load, after which the load carrying capacity remained unchanged. However, note that the load-bearing and energy dissipation capacities of the MSS-CFSWs are respectively provided by the module units and energy dissipation devices. As a result, this study of single MSS-CFSW frames have focused on lateral performance, and the failure of the numerical simulation to accurately capture the energy dissipation capacity of the frame has little impact on this behavior. Therefore, subsequent analyses based on the refined FE model only evaluated the influence of the considered parameters on the skeleton curve, characteristic points, and stiffness degradation of the frame.

A comparison of the peak points obtained from the test and refined numerical simulation is provided in Table 3. The maximum error of peak story drift (θ'_m/θ_m) was relatively large at 13.7%, primarily owing to the occurrence of negative peak loads at different loading levels during the experiments and numerical simulations. The maximum error of peak load (P'_m/P_m), which is of greater concern, was only 2.8%, indicating that the refined FE model accurately reflected the lateral bearing capacity of the MSS-CFSW.

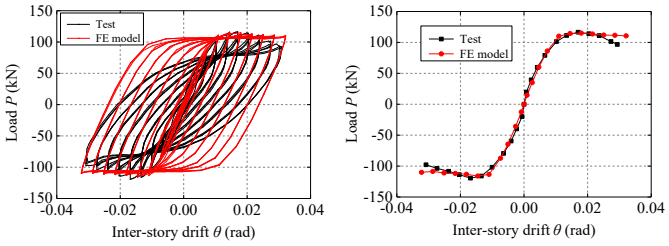

Fig. 8 Comparisons of (a) hysteretic curves and (b) skeleton curves

Table 3
Peak points obtained by the test and simulation of MSS-CFSW-1

Direction	Test		Refined FE model		Comparison result	
	θ_m	P_m (kN)	θ'_m	P'_m (kN)	θ'_m/θ_m	P'_m/P_m
Positive	0.0170	116.5	0.0180	115.1	1.058	0.988
Negative	-0.0169	-119.5	-0.0145	-116.1	0.863	0.972

3.3.2. Failure characteristics and modes

Fig. 9 compares the failure characteristics of the test specimen with those simulated by the refined FE model. The stress distribution of the refined FE model indicates that the stress in the wallboard unit was concentrated at its corners during the initial loading stage, which is consistent with the observation that the corner self-drilling screw connection was the first to exhibit damage and the wallboard units squeezed against each other during the test. As the load

increased, the numerical simulation and test both indicated that the horizontal joints opened owing to the failure of the self-drilling screw connections. Two completely different behaviors occurred at the horizontal strips during both the test and numerical simulation, as shown in Fig. 9 (c): the horizontal strip connected to the gypsum board exhibited almost no deformation, whereas that connected to the OSB exhibited serious out-of-plane deformation.

Fig. 10 compares the specimen failure modes obtained from the test and refined FE model. At the beginning of loading, both the test and model exhibited damage to the self-drilling screw connections at corners of the wallboard units. As the load increased, the wallboard units underwent relative rotation owing to the large number of failed self-drilling screw connections. At the end of loading, the equivalent plastic strain in the refined FE model was primarily concentrated in the flanges at the end of the floor beam, which was consistent with the test-observed local buckling in the floor beam flange. These comparisons confirm that the refined FE model can accurately reflect the specimen failure mode and deformation.

In summary, the refined numerical simulation results agreed well with the test results in terms of the skeleton curve, lateral bearing capacity, failure mode, deformation, and stress distribution. Thus, the refined FE modeling method was confirmed to be effective and it was employed to conduct a parametric analysis on the cyclic behavior of a single MSS-CFSW frame accordingly.

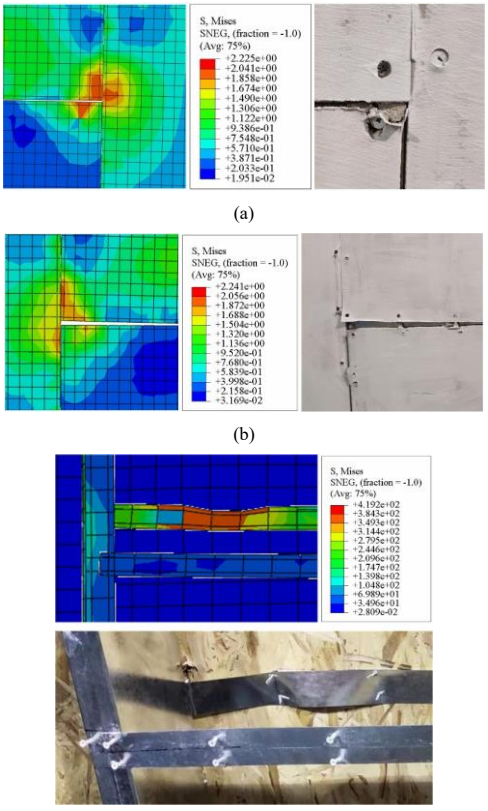

Fig. 9 Comparison of local damage characteristics: (a) corner crushing; (b) horizontal joint opening; (c) strip deformation

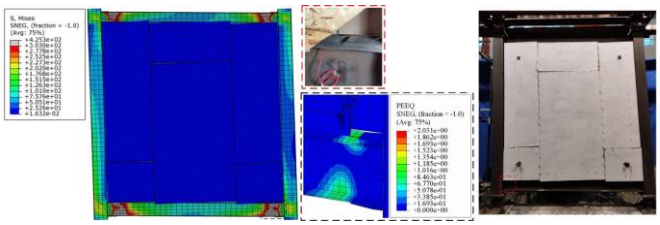

Fig. 10 Comparison of failure mode

4. Parametric analysis

4.1. Model establishment

The refined FE modeling method presented in Section 3.2 was used to establish FE models for parametric analysis. As the verification model was designed to consider a specific test situation, the “Base” parametric analysis model differed from the verification model in the following aspects: (1) The yield strength and tensile strength of the steel were based on the nominal values in GB 50017-2017 [29] and the hardening modulus was $0.01E$, where E is the elastic modulus. (2) Given that the vertical inter-module connections in the prototype structure were 150 mm high, the reference points of the parametric analysis model were no longer located at the center point of the pin, but 150 mm away from the top and bottom surfaces of the column. (3) When applying lateral load, the yield displacement Δ_y was first determined by monotonic loading and a displacement-controlled cyclic load was applied accordingly. Before the parametric analysis model yielded, the displacement increment was $0.25\Delta_y$ with one cycle at each loading step; after the parametric analysis model yielded, the displacement increment was $0.5\Delta_y$ with three cycles at each loading step. The parametric analysis model was considered to have failed when the lateral load decreased to 85% of the peak load or the inter-story drift reached 1/30. (4) When investigating the influence of the vertical inter-module semi-rigid connections, the top and bottom surfaces of the each column were coupled to its center point, and the reference point was set 150 mm away from that center point outside the column surface and fixed. A connector unit was subsequently established between the center and reference points, as shown in Fig. 11. During structural design, the moment–rotation curve of each vertical inter-module connection was simplified to an ideal elastic–plastic model with a bias towards safety, as shown in Fig. 12, in which the elastic point of the curve was taken as the critical point between the elastic and plastic stages. The tangent stiffness of the critical point was considered the connection rotational stiffness, and the load corresponding to the critical point was considered the connection moment capacity. Thus, the connection rotational stiffness and moment capacity were defined for the connector unit used to establish the simplified FE model of the inter-module connection in this study; reference [17] verified the effectiveness of this modeling method using experimental data.

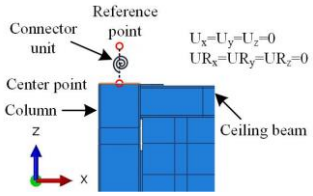

Fig. 11 Diagram of connector unit

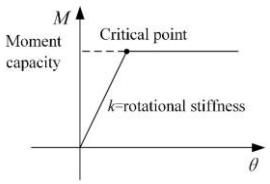

Fig. 12 Simplified model of moment–rotation curve for semi-rigid connections

4.2. Parameter design

4.2.1. Base model

The verified specimen MSS-CFSW-1 model was used as the reference model for parametric analysis, denoted as the “Base” model. The relevant dimensions of each component in the Base model were consistent with those of MSS-CFSW-1, detailed in reference [7], and adjusted according to the requirements in Section 4.1.

4.2.2. Vertical inter-module connection rotational stiffness

The rotational stiffnesses of the vertical inter-module connections at the tops and bottoms of the columns will constrain the rotation of the beam–column joints inside the module unit, thereby affecting its deformation and lateral stiffness. The CRS model series was designed to investigate the influence of the vertical inter-module connection rotational stiffness on the cyclic behavior of a single MSS-CFSW frame with semi-rigid connections. Models CRS-1, CRS-2, and CRS-3 were defined with connection rotational stiffnesses of $0.01R_m$, $0.025R_m$, and $0.05R_m$, respectively, where R_m is the rotational stiffness of the module unit as determined according to reference [29]; the connection moment capacity for each model was $M_{p,cb}$, defined as the full-section plastic bending moment at the end of the ceiling beam, and the other parameters were the same as those of the Base model. The Base model connection rotation stiffness and moment capacity were set to 0.

4.2.3. Vertical inter-module connection moment capacity

The moment capacity also affects the mechanical performance of the vertical inter-module semi-rigid connection and to some extent reflects the constraint of the connections on the module unit. The CMC model series was designed to quantify the influence of the vertical inter-module connection moment capacity on the cyclic behavior of a single MSS-CFSW fame with semi-rigid connections. Models CMC-1, CMC-2, and CMC-3 were defined with connection moment capacities of $0.5M_{p,cb}$, $M_{p,cb}$, and $2M_{p,cb}$, respectively; the Base model connection rotational stiffness and moment capacity were set to 0. The connection rotational stiffness for each model was $0.025R_m$ and the other

parameters were the same as those of the Base model.

4.2.4. Ceiling beam stiffness

In addition to transmitting lateral loads to the CFSW, module beams also constrain the deformation of the CFSW. Therefore, the stiffnesses of the module beams will affect their interaction with the CFSW. The CBS model series was designed to investigate the influence of ceiling beam stiffness on the cyclic behavior of a single MSS-CFSW frame with semi-rigid connections. Models CBS-1, CBS-2, and CBS-3 used ceiling beam sections of H140×70×5×7 mm, H220×110×5×7 mm, H240×120×5×8 mm, respectively, corresponding to moments of inertia of 5.171×10^6 mm^4 ($0.51I_1$), 2.112×10^7 mm^4 ($2.09I_1$), and 3.053×10^7 mm^4 ($3.02I_1$), respectively, where I_1 is the moment of inertia of the H150×100×6×9 ceiling beam in the Base model, 1.011×10^7 mm^4. The remaining parameters were the same as those of the Base model.

4.2.5. Floor beam stiffness

The loads acting on the floor beam are often greater than those acting on the ceiling beam; therefore, the cross-section of the former is typically larger. The FBS model series was designed to quantify the influence of floor beam stiffness on the cyclic behavior of a single MSS-CFSW frame with semi-rigid connections. Models FBS-1, FBS-2, and FBS-3 used floor beam sections of H160×80×5×8 mm, H250×125×6×8 mm, and H280×140×6×8 mm, respectively, corresponding to moments of inertia of 8.644×10^6 mm^4 ($0.49I_2$), 3.570×10^7 mm^4 ($2.02I_2$), and 5.064×10^7 mm^4 ($2.88I_2$), respectively, where I_2 is the moment of inertia of the H200×100×5.5×8 floor beam in the Base model, 1.761×10^7 mm^4. The remaining parameters were the same as those of the Base model.

4.2.6. Column stiffness

As the module columns constrain the deformation of the CFSW, their stiffness will affect their interaction with the CFSW. The CS model series was designed to analyze the influence of column stiffness on the cyclic behavior of a single MSS-CFSW frame with semi-rigid connections. Models CS-1, CS-2, and CS-3 used column sections of 160×8 mm, 250×8 mm, and 280×8 mm, respectively, with moments of inertia of 1.878×10^7 mm^4 ($0.50I_c$), 7.567×10^7 mm^4 ($2.00I_c$), and 1.074×10^8 mm^4 ($2.83I_c$), respectively, where I_c is the moment of inertia of the column in the Base model, 3.781×10^7 mm^4. The remaining parameters were the same as those of the Base model.

4.3. Results and discussion

4.3.1. Effects of connection rotational stiffness

Fig. 13(a) shows the skeleton curves of the CRS model series and the characteristic points are listed in Table 4. Since the semi-rigid connections all had the same moment capacity, the peak loads of the three models were basically consistent with each other and significantly higher than that of the Base model. Compared with CRS-1, CRS-2 and CRS-3 both exhibited a 2.4% increase in positive lateral bearing capacity and a 3.9% increase in negative lateral bearing capacity, indicating that the connection rotational stiffness had a limited effect on the lateral bearing capacity. Furthermore, the yield and peak inter-story drifts of CRS-1–CRS-3 generally decreased with the connection rotational stiffness.

Fig. 13(b) shows that the stiffness degradation curves for CRS-1–CRS-3 were consistently above that of the Base model, indicating that semi-rigid connections can strengthen the lateral stiffness of the frame. The initial stiffnesses of the Base, CRS-1, CRS-2, and CRS-3 models were 5.20 kN/mm, 5.59 kN/mm, 6.15 kN/mm, and 6.84 kN/mm, respectively, representing increases of 7.5%, 18.1%, and 31.5% as the connection rotational stiffness increased from 0 to $0.01R_m$, $0.025R_m$, and $0.05R_m$, respectively. This implied that the connection rotational stiffness significantly affected the initial stiffness of the model. Since the connection moment capacities of the three CRS models were the same, the semi-rigid connections of these models successively reached their moment capacities according to connection stiffness. The connections of CRS-3 reached their moment capacities first, where they achieved the maximum constraint of the steel frame before their rotational stiffnesses decreased. Indeed, the stiffness degradation curve of CRS-3 decreased significantly faster than that of CRS-2 or CRS-3. When the connections of CRS-2 reached their moment capacities, the connection rotational stiffnesses of CRS-2 and CRS-3 were both 0, both exhibited the same lateral stiffness (labelled as point A in Fig. 13(b)), and the stiffness degradation laws of the two models were similar, with their curves basically overlapping. When the inter-story drift reached point B in Fig. 13(b), the connection rotational stiffnesses of all three CRS models decreased to 0 and their boundary conditions were the same. At this time, the curves of the three models basically overlapped, as shown in Fig. 13(a).

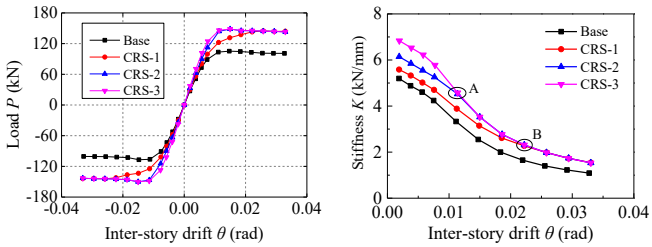

Fig. 13 CRS model series results: (a) skeleton curves; (b) stiffness degradation curves

Table 4
Characteristic values of CRS model series skeleton curves

Model	Direction	Yield point		Peak point		Failure point	
		θ_y	P_y (kN)	θ_m	P_m (kN)	θ_u	P_u (kN)
Base	Positive	0.0075	88.9	0.0147	105.3	0.0327	100.9
	Negative	-0.0075	-90.9	-0.0148	-107.0	-0.0328	-100.5
CRS-1	Positive	0.0112	122.3	0.0258	145.0	0.0330	144.2
	Negative	-0.0113	-124.7	-0.0259	-144.5	-0.0331	-143.9
CRS-2	Positive	0.0076	112.4	0.0150	148.5	0.0330	142.9
	Negative	-0.0077	-114.6	-0.015	-150.1	-0.0331	-143.1
CRS-3	Positive	0.0077	124.5	0.0150	148.5	0.0330	142.9
	Negative	-0.0077	-127.4	-0.015	-150.2	-0.0331	-143.1

4.3.2. Effects of connection moment capacity

The skeleton curves of the CMC model series are given in Fig. 14(a) and the corresponding characteristic points are listed in Table 5. The lateral bearing capacity significantly increased with increasing connection moment capacity, which can be attributed to the fact that the semi-rigid connections carried part of the lateral load. When the connection moment capacity increased from 0 to $0.5M_{p,c}$, $M_{p,c}$, and $2M_{p,c}$, the positive lateral bearing capacities of CMC-1, CMC-2, and CMC-3 increased by 20.2%, 42.0%, and 77.8%, respectively, and their negative lateral bearing capacities increased by 20.2%, 38.3%, and 75.5%, respectively. In addition, the presence of semi-rigid connections improved the ability of the model to resist lateral loads, with the yield load, yield drift, and peak drift generally increasing to varying degrees with the connection moment capacity.

The stiffness degradation curves of the CMC model series are shown in Fig. 14(b), indicating that the initial stiffnesses of the CMC-1–CMC-3 models were obviously larger than that of the Base model. This occurred because the tops and bottoms of the columns in the Base model were hinged with a connection rotational stiffness of 0, whereas the connection rotational stiffnesses of CMC-1–CMC-3 were $0.025R_m$. Thus, the higher constraint of the connections on the steel frame generally increased the initial stiffness. However, the initial stiffnesses of CMC-1, CMC-2, and CMC-3 were 6.14 kN/mm, 5.97 kN/mm, and 5.97 kN/mm, respectively, with the latter two stiffnesses both 2.8% smaller than that for CMC-1, indicating that the specific connection moment capacity had little effect on the initial stiffness. Given that the semi-rigid connections of

CMC-1–CMC-3 were all elastic during the initial loading stage, the constraint effect of the connections on the steel frame was the same. Furthermore, the stiffness degradation trends of the three models were consistent, with the corresponding curves basically overlapping. As the load increased, the semi-rigid connections of CMC-1 reached their moment capacities first, their constraint on the steel frame achieved its limit, and the corresponding stiffness degradation curve decreased significantly faster than those for CMC-2 and CMC-3. The stiffness degradation curve of CMC-2 also rapidly decreased once its semi-rigid connections reached their moment capacities. Finally, the stiffness degradation laws of all three models were basically the same in the late stage of loading when the semi-rigid connections reached their moment capacities.

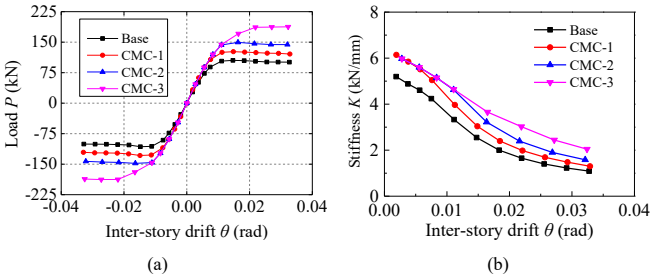

Fig. 14 CMC model series results: (a) skeleton curves; (b) stiffness degradation curves

4.3.3. Effects of ceiling beam stiffness

Fig. 15(a) shows the skeleton curves of the CBS model series and Table 6 lists their characteristic points. The lateral bearing capacity of the model and initial slope of the skeleton curve increased with increasing ceiling beam stiffness; the former was caused by the corresponding increase in plastic bending moment. Compared to model CBS-1, the positive lateral bearing capacities of the Base, CBS-2, and CBS-3 models increased by 14.3%, 31.9%, and 41.0%, respectively, while their negative lateral bearing capacities increased by 14.0%, 31.0%, and 39.8%, respectively. Furthermore, the yield load, yield drift, and peak drift of the models generally increased with increasing ceiling beam stiffness. However, once the ceiling beam stiffness increased to a certain limit, the yield drift and peak drift no longer increased and the rate of increase in the yield load slowed significantly.

Fig. 15(b) shows that the stiffness degradation curves of the CBS model series were similar, following the same stiffness degradation law. The stiffness degradation rates all changed slowly, then rapidly before remaining flat. The stiffness degradation curves increased from the CBS-1 to Base, CBS-2, and CBS-3 models, indicating that the lateral stiffness of the model increased with increasing ceiling beam stiffness. The initial stiffnesses of the CBS-1, Base, CBS-2, and CBS-3 models were 4.81 kN/mm, 5.20 kN/mm, 5.82 kN/mm, and 6.05 kN/mm, respectively, representing increases of 8.1%, 21.0%, and 25.8% as the stiffness increased from $0.51I_1$ to I_1, $2.09I_1$, and $3.02I_1$, respectively. The initial stiffness increase in CBS-3 was significantly smaller than that in CBS-2, indicating that the ceiling beam stiffness provided limited improvement to the initial stiffness of the model.

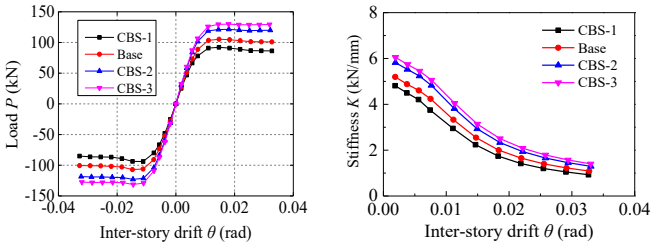

Fig. 15 CBS model series results: (a) skeleton curves; (b) stiffness degradation curves

Table 5
Characteristic values of CMC model series skeleton curves

Model	Direction	Yield point		Peak point		Failure point	
		θ_y	P_y (kN)	θ_m	P_m (kN)	θ_u	P_u (kN)
Base	Positive	0.0075	88.9	0.0147	105.3	0.0327	100.9
	Negative	-0.0075	-90.9	-0.0148	-107.0	-0.0328	-100.5
CMC-1	Positive	0.0076	107.3	0.0148	126.6	0.0328	120.9
	Negative	-0.0076	-109.7	-0.0149	-128.6	-0.0329	-120.8
CMC-2	Positive	0.0083	119.8	0.0163	149.5	0.0321	144.0
	Negative	-0.0084	-123.0	-0.0164	-148.0	-0.0322	-143.1
CMC-3	Positive	0.0110	144.2	0.0271	187.2	0.0323	186.8
	Negative	-0.0111	-146.4	-0.0272	-187.8	-0.0325	-186.6

Table 6
Characteristic values of CBS model series skeleton curves

Model	Direction	Yield point		Peak point		Failure point	
		θ_y	P_y (kN)	θ_m	P_m (kN)	θ_u	P_u (kN)
CBS-1	Positive	0.0066	72.6	0.0147	92.1	0.0327	86.3
	Negative	-0.0056	-66.6	-0.0111	-93.9	-0.0328	-85.1
Base	Positive	0.0075	88.9	0.0147	105.3	0.0327	100.9
	Negative	-0.0075	-90.9	-0.0148	-107.0	-0.0328	-100.5
CBS-2	Positive	0.0074	101.6	0.0180	121.5	0.0322	119.9
	Negative	-0.0075	-103.9	-0.0146	-123.0	-0.0323	-118.5
CBS-3	Positive	0.0075	106.8	0.0179	129.9	0.0319	129.3
	Negative	-0.0074	-108.1	-0.0145	-131.3	-0.0320	-127.5

4.3.4. Effects of floor beam stiffness

Fig. 16(a) shows the skeleton curves of the FBS model series and the corresponding characteristic points are listed in Table 7. The lateral bearing capacity of the model and initial slope of its skeleton curve increased as the floor beam stiffness increased. Indeed, compared with model FBS-1, the positive lateral bearing capacities of the Base, FBS-2, and FBS-3 models increased by 16.4%, 42.4%, and 61.1% respectively, and their negative lateral bearing capacities increased by 15.8%, 38.0%, and 56.2% respectively, indicating that the increasing the floor beam stiffness significantly improved the lateral bearing capacity of the model. Indeed, the floor beam stiffness had a greater impact on lateral bearing capacity than the ceiling beam stiffness. In addition, the yield drift, yield load, and peak drift generally increased with the floor beam stiffness.

The stiffness degradation curves of the FBS model series are shown in Fig. 16(b). Similar to the influence of ceiling beam stiffness on lateral stiffness, each model exhibited the same stiffness degradation law. The stiffness degradation curves increased from the FBS-1 to Base, FBS-2, and FBS-3 models. The initial stiffnesses of the FBS-1, Base, FBS-2, and FBS-3 models were 4.74 kN/mm, 5.20 kN/mm, 5.49 kN/mm, and 5.74 kN/mm, respectively, representing increases of 9.7%, 15.8%, and 21.1% when the floor beam stiffness increased from $0.49I_2$ to I_2, $2.02I_2$, and $2.88I_2$, respectively. Clearly, the initial stiffness gradually increased with the floor beam stiffness.

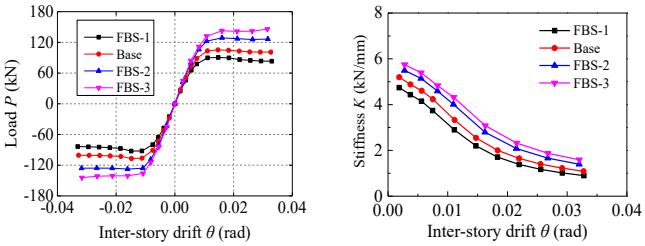

Fig. 16 FBS model series results: (a) skeleton curves; (b) stiffness degradation curves

Table 7
Characteristic values of CBS model series skeleton curves

Model	Direction	Yield point		Peak point		Failure point	
		θ_y	P_y (kN)	θ_m	P_m (kN)	θ_u	P_u (kN)
FBS-1	Positive	0.0074	77.5	0.0148	90.5	0.0330	83.2
	Negative	-0.0074	-78.8	-0.0149	-92.4	-0.0331	-83.6
Base	Positive	0.0075	88.9	0.0147	105.3	0.0327	100.9
	Negative	-0.0075	-90.9	-0.0148	-107.0	-0.0328	-100.5
FBS-2	Positive	0.0082	106.2	0.0161	128.9	0.0317	126.5
	Negative	-0.0082	-108.7	-0.0161	-127.5	-0.0318	-125.9
FBS-3	Positive	0.0108	132.1	0.0315	145.8	0.0315	145.8
	Negative	-0.0109	-136.1	-0.0317	-144.3	-0.0317	-144.3

4.3.5. Effects of column stiffness

Fig. 17(a) shows the skeleton curves of the CS model series and the corresponding characteristic points are listed in Table 8. All skeleton curves were relatively close to each other, and the lateral bearing capacities of the models remained basically unchanged as the column stiffness increased. Equations (28)–(31) in reference [7] indicate that the lateral bearing capacity of a steel frame primarily depends on the cross-sectional dimensions of its ceiling and floor beams, whereas increasing the cross-sectional areas of its columns cannot improve its lateral bearing capacity. Indeed, compared with model CS-1, the positive lateral bearing capacities of the Base, CS-2, and CS-3 models increased by 2.3%, 5.1%, and 6.5%, respectively, and their negative lateral bearing capacities increased by 2.2%, 5.0%, and 6.5%, respectively. The yield drift and peak drift for each model were basically the same, but the yield load increased significantly with the column stiffness.

Fig. 17(b) shows the stiffness degradation curves of the CS model series, indicating that the influence of the column stiffness on the lateral stiffness of the model can be divided into two stages. Before plastic hinges formed at the beam ends, the lateral stiffness of the model was positively correlated with the column stiffness: the initial stiffnesses of the CS-1, Base, CS-2, and CS-3 models were 4.74 kN/mm, 5.20 kN/mm, 5.49 kN/mm, and 5.74 kN/mm, respectively, representing increases of 9.9%, 20.3%, and 25.4% as the column stiffness increased from $0.5I_c$ to I_c, $2.0I_c$, and $2.83I_c$, respectively. Thus, the rate of increase in the initial stiffness of the model gradually slowed with increasing column stiffness. The stiffness degradation curves for all models basically overlapped after plastic hinges were formed at the beam ends, indicating that the influence of the column stiffness on the lateral stiffness of the model was negligible because the beam end sections no longer had the ability to resist bending moments. At this point, the steel frame can be simplified as a hinged frame with a lateral stiffness of 0, and as the lateral stiffness of the model was entirely provided by the CFSW, the stiffness of the columns had little effect.

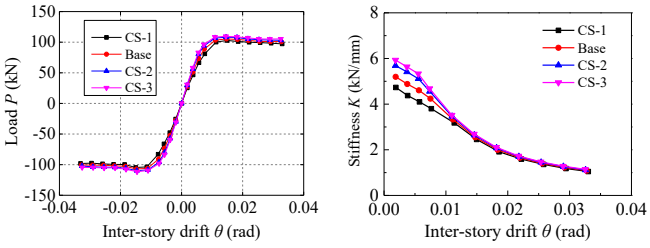

Fig. 17 CS model series results: (a) skeleton curves; (b) stiffness degradation curves

Table 8
Characteristic values of CS model series skeleton curves

Model	Direction	Yield point		Peak point		Failure point	
		θ_y	P_y (kN)	θ_m	P_m (kN)	θ_u	P_u (kN)
CS-1	Positive	0.0076	80.9	0.0149	102.9	0.0330	97.2
	Negative	-0.0074	-82.7	-0.0150	-104.7	-0.0331	-98.1
Base	Positive	0.0075	88.9	0.0147	105.3	0.0327	100.9
	Negative	-0.0075	-90.9	-0.0148	-107.0	-0.0328	-100.5
CS-2	Positive	0.0072	93.2	0.0145	108.1	0.0325	103.1
	Negative	-0.0073	-95.5	-0.0146	-109.9	-0.0326	-102.2
CS-3	Positive	0.0073	96.2	0.0145	109.6	0.0325	105.4
	Negative	-0.0072	-97.2	-0.0146	-111.6	-0.0326	-104.6

5. Calculating the shear capacity of a single MSS-CFSW frame with semi-rigid connections

Wang et al. [7] analyzed the results of cyclic tests conducted on a single MSS-CFSW frame and observed no separation between the CFSW and steel frame. Thus, the connectors can provide a firm connection between the two components to effectively transmit forces. Based on the superposition method, the shear capacity P of a single frame with hinged boundary conditions can be

assumed to comprise two parts: the shear capacity P_f of the single steel frame with hinged boundary conditions and the shear capacity P_w of the CFSW.

In modular steel structures, module units are connected using vertical inter-module semi-rigid connections that constrain the steel frame and improve the unit shear capacity. The shear capacity of a single MSS-CFSW frame considering semi-rigid connections is defined as P_{sr}. Similar to P, P_{sr} includes the shear capacity of a single steel frame with vertical inter-module semi-rigid connections $P_{f,sr}$ and the shear capacity of the CFSW P_w as follows:

$$P_{sr}=P_{f,sr}+P_w \tag{1}$$

Note that $P_{f,sr}$ considers the influence of the vertical inter-module semi-rigid connections, whereas because the CFSW is located inside the steel frame, P_w is unaffected by the vertical inter-module semi-rigid connections.

Referring to the calculation method for the shear capacity of a single steel frame with hinged boundary conditions presented in reference [7], the relationship between the bending moment amplitude and shear in the column section and equilibrium condition of forces can be used to obtain $P_{f,sr}$. The calculation diagram for a single steel frame with vertical inter-module semi-rigid connections is shown in Fig. 18, in which the semi-rigid connections at the tops and bottoms of the columns have been simplified as rotational springs [30]. When a lateral load F acts on the top of a column, the rotational springs rotate with the beam–column joints inside the module, inducing an interaction force between the two components. When conducting a force analysis, each rotational spring can be separated from the steel frame and a reaction moment M_r can be applied at the corresponding beam–column joint in its place. Therefore, the force state of a single steel frame with vertical inter-module semi-rigid connections under the action of F can be considered equivalent to the force state of a single steel frame with hinged boundary conditions under the simultaneous action of F and M_r, as shown in Fig. 18. Thus, the bending moment amplitudes of each section of a single steel frame with hinged boundary conditions must be obtained separately under the action of F and M_r, then superimposed.

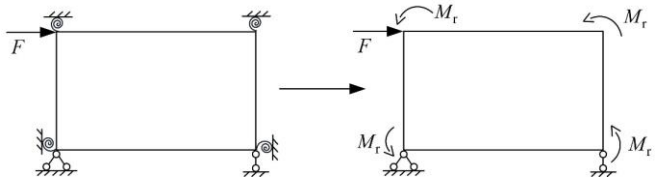

Fig. 18 Calculation diagram of a single steel frame with vertical inter-module semi-rigid connections

Under the action of F, the bending moment in each section reaches its maximum value when the single steel frame with hinged boundary conditions reaches its ultimate state. Strain data from the previous test were analyzed to determine that the single steel frame with hinged boundary conditions reached its ultimate state when part of the beam end section entered plasticity [7]. At this time, the lateral load applied to the single steel frame with hinged boundary conditions is P_f and the bending moments at the ends of the ceiling and floor beams are M_c and M_f, respectively, which can be calculated using Eqs. (28) and (29) in reference [7], respectively. The corresponding bending moment amplitude diagram can be obtained as shown in Fig. 19(a).

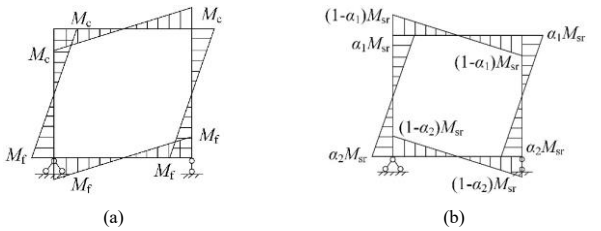

Fig. 19 Bending moment diagram of a single steel frame with hinged boundary conditions: (a) under the action of P_f; (b) under the action of M_{sr}

The bending moment in each section reaches its maximum value when M_r is at its maximum. Thus, the maximum M_r represents the bending moment capacity M_{sr} of the vertical inter-module semi-rigid connection. Fig. 20 shows the calculation diagram for a single steel frame with vertical inter-module semi-rigid connections under the action of M_r, in which i_c, i_{b1}, and i_{b2} denote the linear stiffnesses of the column, ceiling beam, and floor beam, respectively. When the reaction bending moment M_{sr} is applied at joints A, B, C, and D, they will experience rotations θ_A, θ_B, θ_C, and θ_D. Based on the slope–deflection equations, the bending moments at the column and beam ends at joints A, B, C, and D can be respectively obtained by

$$M_{AB}=4i_{b1}\theta_A+2i_{b1}\theta_B \tag{2}$$

$$M_{AC}=4i_c\theta_A+2i_c\theta_C \tag{3}$$

$$M_{BA}=2i_{b1}\theta_A+4i_{b1}\theta_B \tag{4}$$

$$M_{BD}=4i_c\theta_B+2i_c\theta_D \tag{5}$$

$$M_{CD}=4i_{b2}\theta_C+2i_{b2}\theta_D \tag{6}$$

$$M_{CA}=2i_c\theta_A+4i_c\theta_C \tag{7}$$

$$M_{DC}=2i_{b2}\theta_C+4i_{b2}\theta_D \tag{8}$$

$$M_{DB}=2i_c\theta_B+4i_c\theta_D \tag{9}$$

where M_{AB} and M_{AC} are the bending moments at the end of ceiling beam AB and column AC at joint A, respectively; M_{BA} and M_{BD} are the bending moments at the end of ceiling beam AB and column BD at joint B, respectively; M_{CD} and M_{CA} are the bending moments at the end of floor beam CD and column AC at joint C, respectively; and M_{DC} and M_{DB} are the bending moments at the end of floor beam CD and column BD at joint D, respectively.

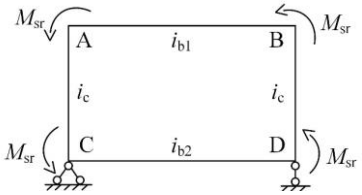

Fig. 20 Calculation diagram for a single steel frame with hinged boundary conditions under the action of M_{sr}

Based on the moments at joints A, B, C, and D, the following moment equilibrium equations can be established:

$$\begin{cases} M_{AB}+M_{AC}+M_{sr}=0 \\ M_{BA}+M_{BD}+M_{sr}=0 \\ M_{CA}+M_{CD}+M_{sr}=0 \\ M_{DB}+M_{DC}+M_{sr}=0 \end{cases} \tag{10}$$

Substituting Eqs. (2)–(9) into Eq. (10), rotations θ_A, θ_B, θ_C, and θ_D can be obtained and subsequently introduced into Eqs. (3) and (7) to derive the maximum bending moment at the top and bottom ends of column AC, respectively, as follows:

$$M_{AC}=-\frac{i_c\left(i_{b1}+2i_{b2}+i_c\right)}{3i_{b1}i_{b2}+\left(2i_{b1}+2i_{b2}+i_c\right)i_c}M_{sr} \tag{11}$$

$$M_{CA}=-\frac{i_c\left(2i_{b1}+i_{b2}+i_c\right)}{3i_{b1}i_{b2}+\left(2i_{b1}+2i_{b2}+i_c\right)i_c}M_{sr} \tag{12}$$

which can be regarded as products of moment distribution coefficients α_1 and α_2, respectively, and M_{sr}, as follows:

$$M_{AC}=-\alpha_1 M_{sr} \tag{13}$$

$$M_{CA} = -\alpha_2 M_{sr} \tag{14}$$

Where

$$\alpha_1 = \frac{i_c\left(i_{b1} + 2i_{b2} + i_c\right)}{3i_{b1}i_{b2} + \left(2i_{b1} + 2i_{b2} + i_c\right)i_c} \tag{15}$$

$$\alpha_2 = \frac{i_c\left(2i_{b1} + i_{b2} + i_c\right)}{3i_{b1}i_{b2} + \left(2i_{b1} + 2i_{b2} + i_c\right)i_c} \tag{16}$$

From the symmetry of the structure and load, the maximum bending moment in column BD can be assumed equal to that in column AC. By combining the moment equilibrium conditions of the joints, the maximum bending moment diagram for a single steel frame with hinged boundary conditions under the action of M_{sr} can be obtained as shown in Fig. 19(b). Based on Figs. 19(a) and (b), the maximum bending moment $M_{col,t}$ at the column top section and maximum bending moment $M_{col,b}$ at the column bottom section are respectively given by

$$M_{col,t} = M_c + \alpha_1 M_{sr} \tag{17}$$

$$M_{col,b} = M_f + \alpha_2 M_{sr} \tag{18}$$

The modular steel frame can be divided into upper and lower parts along the column center; the upper part is analyzed to establish the lateral force equilibrium equation. Considering the relationship between the maximum bending moment and shear in the column, the expression for $P_{f,sr}$ can be obtained as

$$P_{f,sr} = 2 \times \frac{\left(M_{col,t} + M_{col,b}\right)}{h} = \frac{2\left(M_c + \alpha_1 M_{sr} + M_f + \alpha_2 M_{sr}\right)}{h} \tag{19}$$

in which $\alpha_1 = \alpha_2 = 0$ when calculating the shear capacity of a single steel frame with hinged boundary conditions owing to the absence of constraint by semi-rigid connections.

When calculating the shear capacity P_w of the CFSW used in this study, Wang et al. [7] proposed four revisions to the conventional global analysis method to provide the modified global analysis method detailed in Section 6.1 of reference [7]. This method not only considers the presence of horizontal and vertical joints but also targets wallboard units that are more in line with the actual situation. The calculation of P_w is given as follows:

$$P_w = \min\left\{P_1 + P_2 + P_3, P_4 + P_5 + P_6\right\} \tag{20}$$

where P_i is the shear capacity of wallboard unit i, as shown in reference [7].

Table 9 compares the theoretical and simulated shear capacities for each parametric analysis model, indicating that the ratios of the theoretical to simulated shear capacities were between 0.915 and 1.001 with an average value of 0.951 and a standard deviation of 0.023. Thus, the theoretical values agreed well with the simulated values, and the former were generally smaller. This confirms that the calculation method proposed in this paper can effectively determine the shear capacity of a single MSS-CFSW frame with hinged boundary conditions and semi-rigid connections.

The following process can be applied to design the shear capacity of modular steel structures using the derived equation: (1) Determine the type of inter-module connection to be used based on the design requirements. (2) Calculate the horizontal design load to be borne by the single modular steel structure frame. (3) Calculate the inter-module connection rotational stiffness and moment capacity based on the equations provided in the design codes. (4) Based on the preliminarily determined cross-sectional dimensions of the module unit, use the derived equations to calculate the horizontal load that a single frame can resist. If the calculated value is larger than the horizontal design load, the designed cross-sectional dimensions are feasible; otherwise, the cross-sectional dimensions must be improved until the calculated value is greater than the design load.

6. Conclusions

A refined FE model of a single MSS-CFSW frame was established using ABAQUS and the connector unit parameters were determined from the results of shear tests on self-drilling screw connections under shear perpendicular and parallel to the plate edge. The effectiveness of the refined FE modeling method was verified against previous test results, and the influences of the semi-rigid connection and steel frame component stiffnesses on the cyclic behavior of a single frame were investigated. Finally, the semi-rigid connection was considered equivalent to a rotational spring to derive an equation for the shear capacity of a single MSS-CFSW frame. The primary conclusions of this study are as follows:

(1) When the distance from the screws to the plate edge was small, the failure mode and shear capacity of the self-drilling screw connection differed according to the direction of shear (perpendicular or parallel to the plate edge). However, there was no such difference when the distance from the screws to the plate edge was large. In the refined FE model, values were assigned to connector unit parameters in both directions in the CFSW plane according to these results. The numerical simulation results agreed well with the test results.

(2) The connection rotational stiffness and moment capacity were positively correlated with the initial stiffness and shear capacity of the single MSS-CFSW frame, respectively. The maximum increase in initial stiffness was 31.5% and the positive and negative shear capacities increased by 20.2–79.4%. The semi-rigid connections only constrained the steel frame before yielding, after which their influence should not be considered.

(3) As the stiffnesses of the ceiling beam, floor beam, and column increased, the initial stiffness of the single MSS-CFSW frame increased by 8.1–25.8%, 9.7–21.1%, and 9.9–25.4%, respectively, and its shear capacity increased by 14.0–41.0%, 15.8–61.1%, and 2.2–6.5%, respectively. Thus, the influences of these three parameters on the initial stiffness were similar, whereas the floor beam stiffness had a more significant influence on the shear capacity than the other parameters.

(4) The shear capacity of a single MSS-CFSW frame with semi-rigid connections comprises the shear capacities of the steel frame and CFSW. By equating the semi-rigid connections to rotational springs, an equation was derived for the shear capacity of the frame that quantified the contributions of the semi-rigid connections using moment distribution coefficients. The shear capacity of the CFSW was calculated using a previously proposed equation. A comparison of theoretical and simulated values indicated that by calculating the moment distribution coefficient values, the proposed method can effectively determine the shear capacity of a single MSS-CFSW frame with semi-rigid connections or hinged boundary conditions.

Table 9
Comparison between theoretical and simulated shear capacities of parametric analysis models

Model	Direction	Theoretical value			P_{FE} (kN)	P_{sr}/P_{FE}
		$P_{f,sr}$	P_w	P_{sr}		
Base	Positive	54.3	48.2	102.5	105.2	0.974
	Negative	54.3	48.2	102.5	107.0	0.958
CRS-1	Positive	91.9	48.2	140.1	145.0	0.966
	Negative	91.9	48.2	140.1	144.5	0.970
CRS-2	Positive	91.9	48.2	140.1	148.5	0.943
	Negative	91.9	48.2	140.1	150.1	0.933
CRS-3	Positive	91.9	48.2	140.1	148.5	0.943
	Negative	91.9	48.2	140.1	150.2	0.933

CMC-1	Positive	73.1	48.2	121.3	126.6	0.958
	Negative	73.1	48.2	121.3	128.6	0.943
CMC-2	Positive	91.9	48.2	140.1	149.5	0.937
	Negative	91.9	48.2	140.1	148.0	0.947
CMC-3	Positive	129.4	48.2	177.6	187.2	0.949
	Negative	129.4	48.2	177.6	187.8	0.946
CBS-1	Positive	43.7	48.2	91.9	92.1	0.998
	Negative	43.7	48.2	91.9	93.9	0.979
CBS-2	Positive	64.3	48.2	112.5	121.5	0.926
	Negative	64.3	48.2	112.5	123	0.915
CBS-3	Positive	75.2	48.2	123.4	129.9	0.950
	Negative	75.2	48.2	123.4	131.1	0.941
FBS-1	Positive	42.4	48.2	90.6	90.5	1.001
	Negative	42.4	48.2	90.6	92.4	0.981
FBS-2	Positive	73.4	48.2	121.6	128.9	0.943
	Negative	73.4	48.2	121.6	127.5	0.954
FBS-3	Positive	86.7	48.2	134.9	145.8	0.925
	Negative	86.7	48.2	134.9	144.3	0.935
CS-1	Positive	54.3	48.2	102.5	102.9	0.996
	Negative	54.3	48.2	102.5	104.7	0.979
CS-2	Positive	54.3	48.2	102.5	108.1	0.948
	Negative	54.3	48.2	102.5	109.9	0.933
CS-3	Positive	54.3	48.2	102.5	109.6	0.935
	Negative	54.3	48.2	102.5	111.6	0.918
Average						0.951
Standard deviation						0.023

Funding

This study was supported by the Fundamental Research Funds for the Central Universities, grant number XJ2023001801.

Declaration of competing interests

The authors have no conflicts of interest to declare.

References

[1] Zhang P., Design and Mechanical Properties of Multi-storey Steel Module Structure. Master's Dissertation, Tianjin University, Tianjin, 2016.
[2] Ding Y., Deng E.F., Zong L., Dai X.M., Lou N., Chen Y., "Experimental study on seismic performance of corrugated steel plate shear wall in modular container construction", Journal of Building Structures, 39, 110–118, 2018.
[3] Ding Y., Deng E.F., Zong L., Dai X.M., Lou N., Chen Y., "Cyclic tests on corrugated steel plate shear walls with openings in modularized-constructions", Journal of Constructional Steel Research, 138, 675–691, 2017.
[4] Dai X.M., Ding Y., Zong L., Deng E.F., Lou N., Chen Y., "Experimental study on seismic behavior of steel strip reinforced CSPSWs in modular building structures", Journal of Constructional Steel Research, 151, 228–237, 2018.
[5] Liu Y., Chen Z., Liu J., Bai Y., Zhong X., Wang X., "Lateral stiffness evaluation on corner-supported thin walled modular steel structures", Thin-Walled Structures, 157(6), 106967, 2020.
[6] Feng R., Liu S., Y. Qiu Y., "Seismic performance of multi-story modular box buildings, Journal Constructional Steel Research, 168, 106002, 2020.
[7] Wang Q., Su M., Deng Z., Chen R., Chen W., Zhou X., Gong H., Ma L., "Seismic performance and shear capacity of modular steel structures infilled with cold-formed steel walls using a novel connection system", Engineering Structures, 289, 116322, 2023.
[8] Wang Q., Su M., Chen R., Deng Z., Chen W., "Seismic performance and shear capacity of modular steel frames infilled with cold-formed steel walls with openings", Thin-Walled Structures, 187, 110744, 2023.
[9] Khan K., Chen Z.H., Liu J.D., Yan J.B., "Simplified modelling of novel non-welded joints for modular steel buildings", Advanced Steel Construction, 17(4), 412–424, 2021.
[10] Chen H.L., Ke C., Chen C., Li G.Q., "The tensile performance of inter-module connection with a bolt and shear key fitting for modular steel buildings", Advanced Steel Construction, 19(2), 102–111, 2023.
[11] Dai X.M., Zong L., Ding Y., Li Z.X., "Experimental study on seismic behavior of a novel plug-in self-lock joint for modular steel construction:", Engineering Structures, 181, 143–164, 2019.
[12] Lacey A.W., Chen W., Hao H., Bi K., "New interlocking inter-module connection for modular steel buildings: Experimental and numerical studies", Engineering Structures, 198, 109465, 2019.
[13] Sanches R., Mercan O., Roberts B., "Experimental investigations of vertical posttensioned connection for modular steel structures", Engineering Structures, 175, 776–789, 2018.
[14] Yang N., Xia J., Chang H., Zhang L., Yang H., "A novel plug-in self-locking inter-module connection for modular steel buildings", Thin-Walled Structures, 187, 110774, 2023.
[15] Chua Y.S, Liew J.R., Pang S.D., "Modelling of connections and lateral behavior of high-rise modular steel buildings", Journal of Constructional Steel Research, 166, 105901, 2020.
[16] Lacey A.W., Chen W., Hao H., Bi K., "Effect of inter-module connection stiffness on structural response of a modular steel building subjected to wind and earthquake load", Engineering Structures, 213, 110628, 2020.
[17] Wang Q., Su M., "Stability study on sway modular steel structures with semi-rigid connections", Thin-Walled Structures, 161, 107529, 2021.
[18] Huang Z.G., Seismic Behaviors Study on Low-Rise Cold-Formed Thin-Wall Steel Residential Buildings, PhD Dissertation, Xi'an University of Architecture and Technology, Xi'an, 2011.
[19] Xu Y., Experimental Research on Shear Performance of New-type Cold-formed Steel Load Bearing Walls, Master's Dissertation, Southeast University, Nanjing, 2016.
[20] Yu Q., Numerical Simulation on the Shear and Axial Compression Performance of Cold-Formed Steel Shear Walls, Master's Dissertation, Southeast University, Nanjing, 2016.
[21] Buonopane S.G., Bian G., Tun T.H., Schafer B.W., "Computationally efficient fastener-based models of cold-formed steel shear walls with wood sheathing", Journal of Constructional Steel Research, 110, 137–148, 2015.
[22] Hao J., Liu B., Shao D., Wang Y., Li K., Li Y., "Experimental study on shear behavior of screw connections in cold-formed thin-wall steel structures", Journal of Xi'an University of Architecture and Technology (Natural Science Edition), 46, 769–773+779, 2014.
[23] Li Y., Ma R., He H., "Experimental study on behavior of screw connections for cold-formed thin-walled steel and structural OSB boards", Journal of Building Structures, 35, 48–56, 2014.
[24] Ye J., Wang X., Zhao M., "Experimental study on shear behavior of screw connections in CFS sheathing", Journal of Constructional Steel Research, 121, 1–12, 2016.
[25] Han P., Experimental Study on Behavior of Screw Connections in CFS Keel-Sheeting Board, Master's Dissertation, Nanjing: Southeast University; 2018.
[26] Wang Q., Study on Seismic Performance of Semi-rigid Modular Steel Structure Filled with Cold-formed Steel Wall, PhD Dissertation, Xi'an University of Architecture and Technology, Xi'an, 2023.
[27] Zhao M., Behavior of Screw Connections in CFS-sheeting Board, Master's Dissertation, Southeast University, Nanjing, 2015.
[28] Huang R., Research on Hysteretic and Crack Resistance of Steel Frame-ALC Wallboard Structure System, Master's Dissertation, Harbin Institute of Technology, Harbin, 2021.
[29] GB 50017-2017, Standard for Design of Steel Structures, China Building Industry Press, Beijing, 2018.
[30] Wang Q., Su M., "Displacement mode of column-supported modular steel structures with semi-rigid connections", Journal of Building Engineering, 62, 105397, 2022.

Advanced Steel Construction – Vol. 21 No. 4 (2025) 316–326
DOI:10.18057/IJASC.2025.21.4.4

SEISMIC PERFORMANCE OF END-PLATE CONNECTION IN A NARROW-FLANGE H-SHAPED BEAM-COLUMN

Wei-Hui Zhong [1, 2, *], Di Wu [1], Zheng Tan [1, 2], Ying-Zhao Qiu [1], Dong-Ping Yang [1], Chen-Hao Ren [3] and Le Deng [1]

[1] *School of Civil Engineering, Xi'an University of Architecture and Technology, Xi'an 710055, China*
[2] *Key Lab of Structural Engineering and Earthquake Resistance, Ministry of Education, Xi'an University of Architecture and Technology, Xi'an 710055, China*
[3] *Shaanxi Architecture Science Research Institute Company Limited, Xi'an 710082, China*
** (Corresponding author: E-mail: Email: zhongweihui1980@163.com)*

ABSTRACT

To improve the seismic performance of both low-rise and multi-story steel residential structures, and to address the ongoing issue of column protrusion, this paper introduces a cross-shaped end-plate connection joint. This joint is designed for narrow-flange H-beams and has been evaluated through quasi-static tests for failure modes, hysteresis curves, and load-bearing capacity. Experimental findings indicate that this joint serves as a semi-rigid connection, offering exceptional ultimate rotational capacity, energy dissipation, and ductility. These features make it well-suited for use in mid- and low-rise seismic steel frame structures. To deepen our understanding of the joint's seismic performance, a numerical model was established using ABAQUS software. The validity of this modeling approach was confirmed by comparing it with experimental results. Several variables were analyzed for their impact on the joint's seismic performance, including axial compression ratio, column web thickness, skin plate thickness, column-flange reinforcement plate thickness, and beam end-plate thickness. Our analysis reveals that an increase in the axial compression ratio makes the negative slope of the joint's hysteresis curve more pronounced. This suggests that the axial compression ratio should not exceed 0.4. Additionally, the use of skin plates led to a 26.3% increase in joint yield displacement and a 14.9% increase in ultimate displacement. The incorporation of column-flange reinforcement plates boosted both the yield and peak strength by 15.5% and 14.2%, respectively. Consequently, we recommend using skin and reinforcement plate thicknesses that are 0.5 and 0.8 times the thickness of the end-plate, respectively. By carefully selecting the appropriate parameters for these components, this study offers valuable insights and guidelines for the practical implementation of beam-column joints in low-rise and multi-story steel residential structures.

ARTICLE HISTORY

Received: 9 March 2024
Revised: 15 January 2025
Accepted: 6 February 2025

KEYWORDS

Narrow-flange H-shaped Beam column;
End-plate connections;
Seismic performance;
Prefabricated structures

1. Introduction

In the context of a strong push for green, low-carbon, and energy-efficient building structures, steel frame systems and light steel truss systems have gained widespread use in low-rise and multi-story steel residential structures [1]. However, these types of buildings often face challenges, including reduced lateral stiffness of frame columns and the awkward positioning of wide-flange columns that protrude from walls. These issues affect not only aesthetic appeal of the interior spaces but also the efficient use of architectural space [2]. In low and medium-rise steel frame structures, the vertical load-bearing members are subjected to relatively small loads. Utilizing wide-flange H-beam columns in such cases may lead to material wastage and encroachment on the wall, thereby negatively impacting its aesthetics. Therefore, this paper suggests employing narrow-flange load-bearing members in low and medium-rise steel frame structures. To mitigate the problem of protruding columns, narrow-flange columns can be effectively utilized in mid- and low-rise buildings.

To date, the majority of academic research has focused on the seismic performance of wide- and medium-flange beam-column connections in the strong-axis direction. For instance, Wang [3] introduced a detachable end-plate connection with a cruciform structure, finding that factors such as end-plate thickness and the column's width-to-thickness ratio had a significant impact on connection performance. D'Aniello et al. [4] employed finite element analysis to discover that adding stiffening ribs to end plates could substantially improve their strength and stiffness. They also examined the performance of beam-column connections under various conditions. Haghollahi et al. [5] performed experimental research to identify performance trends in connections both with and without stiffening ribs. Van-Long et al. [6] proposed an extended end-plate connection method for linking I-beams to externally wrapped composite columns, using the component method for simulation.

Other scholars have focused on specialized areas. Chen [7] examined beam-column end-plate connections in portal frames and found that thickening the web plates in the connection zone was more beneficial than adding diagonal stiffening ribs. Guo et al. [8] designed and conducted experiments on eight different beam-column end-plate connections, concluding that bolted end-plate connections showed excellent ductility and energy dissipation capacity. Li et al. [9] experimented with externally extended end-plate connections of varying configurations. They found that the relative strengths of bolts, end plates, and column walls directly affected the failure modes of the joints. Yan [10] introduced a linear model for calculating the initial stiffness of semi-rigid connection joints, while Tong [11] presented an enhanced end-plate stiffening technique and developed design formulas for externally extended end-plate stiffeners.

In contrast to wide- and medium-flange beam-column connections, which have larger height-to-thickness ratios, narrow-flange connections display greater stiffness in the weak-axis direction. This leads to notable differences in seismic performance between narrow-flange beam-column connections and their wide- or medium-flange counterparts. While some research exists on narrow-flange connections, studies focusing on their seismic performance in the strong-axis direction are relatively limited. Zhong et al. [12] investigated a specific narrow-flange beam-column end-plate weak-axis connection joint and found that factors such as beam end-plate and skin plate thicknesses significantly affect the joint's seismic performance.

Although numerous scholars have explored the performance of narrow-flange beam-column connections, research specifically targeting their seismic performance in the strong-axis directions remains limited. To address the issue of flange exposure and further investigate the seismic performance of narrow-flange H-section steel beam-column end-plate connections in the strong-axis direction, this paper introduces a cross-shaped joint configuration for narrow-flange H-beam-column connections. We subjected full-scale beam-column connection specimens to quasi-static tests to evaluate their failure modes, hysteresis curves, and overall seismic performance. Utilizing finite element analysis and corroborating the results with experimental data, we ensured the validity of our modeling method. A comprehensive parametric analysis was conducted, focusing on factors such as the axial compression ratio, column web thickness, skin plate thickness, column-flange reinforcement plate thickness, and beam end-plate thickness. This analysis aimed to provide deeper insights into the key parameters affecting the seismic performance of the proposed joint. Based on our findings, we offer design recommendations that serve as a foundational guide for engineering applications.

2. Joint design

2.1. The selection of substructures

In compliance with the Chinese Steel Structure Design Standard GB 50017-2017[13], we designed a two-story steel frame prototype structure featuring a 2 × 2 span configuration. The structure has a floor height of 3 m, a span of 3.9 m, a permanent floor load of 3.1 kN/m^2, and a live load of 2 kN/m^2. We selected the bottom-level central column in the strong-axis direction (BP-5) of the prototype structure as the subject of our study, as illustrated in Fig. 1. The cross-

shaped joint structure was arranged in a double-half-span configuration, comprising a failing column flanked by connected steel beams. Typically, the column's moment of flexural failure occurs at the midpoint of the inter-story height; thus, we chose a length of 2.4 m for the failing column. For the beams, the moment of flexural failure generally occurs around half the beam span, leading us to select a length of 1.6 m for one side of the beam.

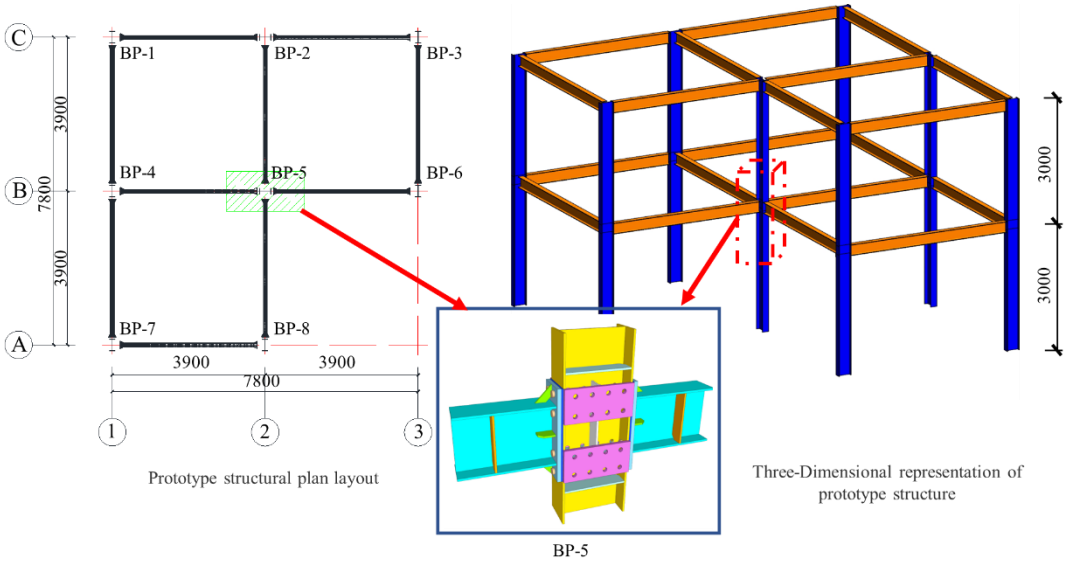

Fig. 1 Prototype steel frame structure

2.2. Experimental specimen design

2.2.1. Joint structural design

This paper proposes a novel structural concept for narrow-flange H-section steel beam-column connections, featuring an extended end-plate bolted joint. The specific configuration of this connection is depicted in Fig. 2. The external extended end-plate design allows for energy dissipation through end-plate deformation, resulting in excellent hysteresis behavior and energy dissipation capacity [14]. Furthermore, the inclusion of stiffening ribs on the beam end-plate enhances both its strength and stiffness, facilitating a more uniform load distribution on the bolts and improving bolt tension distribution.

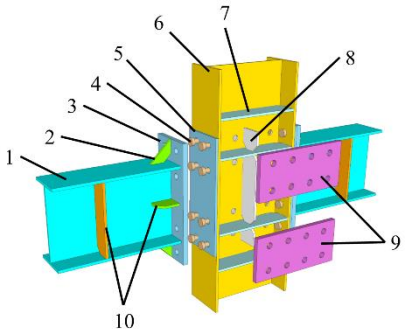

1. Beam; 2. End-plate stiffening rib; 3. End-plate;
4. High-strength bolt; 5. Column-flange reinforcement plate; 6. Column;
7. Column transverse stiffeners; 8. Column longitudinal stiffeners; 9. Skin plate;
10. Beam stiffening rib

Fig. 2 Narrow-flange extension end-plate bolted joint

Adding transverse and longitudinal stiffeners in the joint region not only improves the joint's stiffness and strength but also effectively distributes its load-bearing capacity, markedly enhancing local buckling behavior. Additionally, the incorporation of skin plates in the weak-axis direction fortifies the beam-column joint region. This serves a dual purpose: it both safeguards the joint and preserves the aesthetic integrity of the building walls. The design accommodates connections in the weak-axis direction, with a skin plate thickness equal to that of the beam end-plate.

2.2.2. End-plate and bolt design

In the realm of end-plate connection joint design, Solhmirzaei et al. [15] constructed two bolted end-plate joints and compared their performance against the bolted stiffened end-plate with four bolts reinforcement (BSEEP-16ES) standard recommended by AISC 4-358 [16]. Their investigation showed that the custom-designed joints demonstrated superior seismic resistance capabilities. Tartaglia [17] compared the AISC 358-16 guidelines with European standards, demonstrating that stiffened end-plate joints can ensure the formation of plastic hinges in steel beams under cyclic loading conditions. This research also explored the use of four-row bolted connections for beams with and without stiffening ribs. Following a similar approach, our study employs a four-row bolt configuration for the connections.

In compliance with the Chinese structural technical standard GB 51022-2015 [18], we opted for Grade 10.9 M16 high-strength friction-type bolts with an 18 mm bolt hole diameter. Bolt dimensions were determined based on the tension transmitted through the beam's end flange, as calculated according to the Chinese steel structure design standard GB50017-2017 [13].

2.2.3. Dimension design of specimens

Due to the advantages of ease in both fabrication and experimental loading, our test specimens were designed and constructed as full-scale models. The steel beam and column sections have specifications of HN250 × 125 × 6 × 9 (mm) and HN300 × 150 × 6.5 × 9 (mm) [H-overall depth (d) × flange width (b_f) × web thickness (t_w) × flange thickness (t_f)], and are made of Q235B-grade steel, as depicted in Fig. 3(a).

2.2.4. Skin plate design

Regarding the design of skin plates, Lu [19] proposed a technique involving the use of skin plates to connect steel beams to H-shaped columns in the weak-axis direction. This allows the structural components to fail before the joints do. These skin plates were designed in accordance with the permissible bolt hole spacing values specified in the Chinese steel structure standard GB 50017-2017 [13]. Positioned at the same horizontal level as the edge of the end plates in the column's height direction, the skin plates align flush with the flanges on either side of the column in the width direction. To prevent localized damage to the column's narrow flange, skin plates were introduced in the weak-axis direction to ensure a uniform load distribution and uniform stiffness. The thickness of the upper and lower skin plates is informed by the thickness of both column flanges and the web plate. The thickness of these plates typically falls between the thicknesses of the web plate and the column flanges. For this study, we selected a skin plate thickness of 16 mm, as shown in Fig. 3(b).

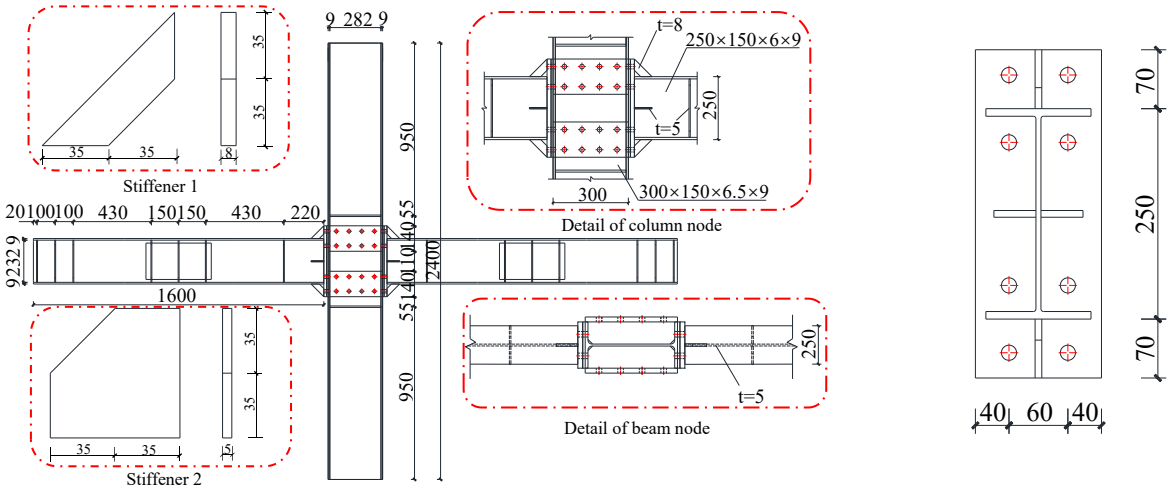

(a) Detailed geometric dimensions of the specimen (b) End-plate size

Fig. 3 Geometric dimension drawing of the specimen

2.3. Joint verification

In this work, we focus on BP-5, as illustrated in Fig. 1. Calculations reveal that the axial compression ratio of BP-5 is approximately 0.2. The following sections present a detailed seismic assessment of this joint:

2.3.1. Seismic structural measures calculation

Designed to withstand a predicted seismic intensity of 8 degrees, the steel frame is categorized as Level III for seismic performance according to the Chinese Building Seismic Design Code GB50011-2010 [20] . The aspect ratios of the frame's columns meet the design criteria, and the verification are shown in Eqs. (1) and (2):

$$l_0 / i_x = 3000/124 = 24.19 \le 100\sqrt{235/f_y} = 100 \tag{1}$$

$$l_0 / i_y = 3000/32.9 = 91.19 \le 100\sqrt{235/f_y} = 100 \tag{2}$$

In accordance with the Chinese Building Seismic Design Code GB50011-2010 [20], we calculated and verified the width-to-thickness ratio limits for various components within the steel frame. The calculations confirm compliance with the code's requirements.

2.3.2. Component verification

To ensure that the beam fails before the column, we increased the column's stiffness and designed its moment capacity to enhance its resistance to failure and bending strength. The aim is to have the beam yield prior to the column, forming plastic hinges at the beam ends, as defined by Eq. (3).

$$\sum W_{pc}\left(f_{yc} - N_p / A_c\right) \ge \eta \sum W_{pb} f_{yb} \tag{3}$$

where w_{Pc} and w_{Pb} signifies the plastic section moduli of the column and beam at the joint, respectively; f_{yc} and f_{yb} denote the yield strengths of the steel used in the column and beam, respectively; N_P represents the axial force in the column for the seismic combination; and A_c is the column's cross-sectional area. Further, η represents the strong column coefficient, with values of 1.15 for the first level, 1.10 for the second level, and 1.05 for the third level.

According to Eq. (3), the computed plastic moment at the column-end exceeds that at the beam-end (189.88 kN·m > 164.34 kN·m), thereby ensuring that the beam fails before the column does.

3. Experimental synopsis

3.1. Material property analysis

Material property testing was carried out in accordance with the relevant Chinese standard GB/T2975-2018 [21], and the resulting steel material performance indicators are detailed in Table 1.

Table 1
Material properties of specimens

Steel member	Yield strength f_y/MPa	Tensile strength f_u/MPa	Elastic modulus E/GPa	Elongation percentage %
Beam web	430	562	207	32
Column web	285	408	208	39
Beam-end reinforcement plate	295	435	185	40
Beams, column flange	242	390	239	43
End-plate, skin plate	298	462	204	53
Beam-end web stiffener ribs	472	585	219	28

3.2. Experimental procedure

3.2.1. Experimental apparatus setup

The experimental loading setup, shown in Fig. 4(a), positioned the test specimen between two gantry frames. A servo actuator was horizontally affixed to the reaction wall. The bottom of the test specimen was connected to a ground beam via a hinge axis. This ground beam was longitudinally placed between the two gantry frames and anchored securely to both sides using anchor bolts. Additional stabilization was provided by four compression beams. A hydraulic jack on the reaction beam applied vertical pressure to the columns, maintaining a strictly downward direction. The column base was linked to the hinge axis to replicate the column's flexural point. At the beam-end, a connection was made through a bracket and linkage, with the opposite end of the linkage fastened to the ground beam, as shown in Fig. 4(b). Lateral supports were installed at the mid-section of both the joint and loading beam to prevent out-of-plane instability during loading, as illustrated in Fig. 4(c).

3.2.2. Experimental loading procedure

The experimental loading approach utilized a hybrid load–displacement method. Initially, a vertical load of 200 kN was applied to the column's top to account for second-order gravity effects. Next, horizontal reciprocating loads were applied to the top of the column. The horizontal cyclic loading had two stages: the first stage involved load-controlled conditions, with the yielding load incrementally distributed over three steps—16, 32, and 48 kN—each subjected to one complete cycle. The second stage was displacement-controlled; after

reaching the yield point, the loading increased in increments of 0.5 times the yield displacement (20 mm) for each level. Each level went through three complete cycles, and the loading continued until specimen failure, as outlined in Fig. 5.

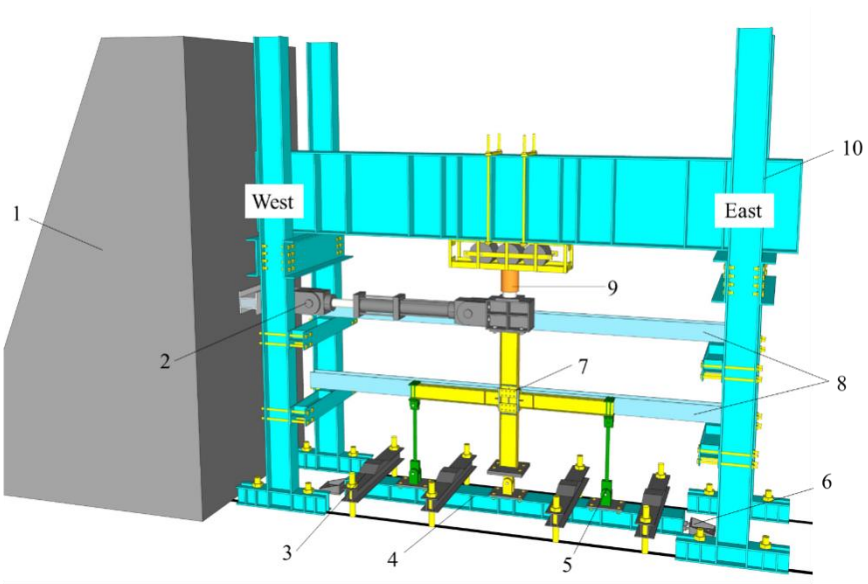

1. Reaction wall; 2. MTS servo actuator; 3 Pressed beam; 4. Floor beams; 5. Chain rod; 6. Anchor bolts; 7. Test piece; 8. Side beams; 9. Jack; 10. Mastry

(a) Test the loading device

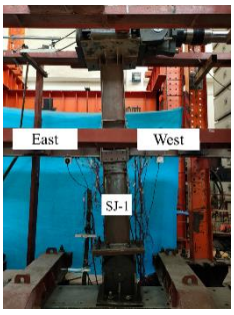

(b) Front of the test device

(c) Side of the test device

Fig. 4 Experimental device

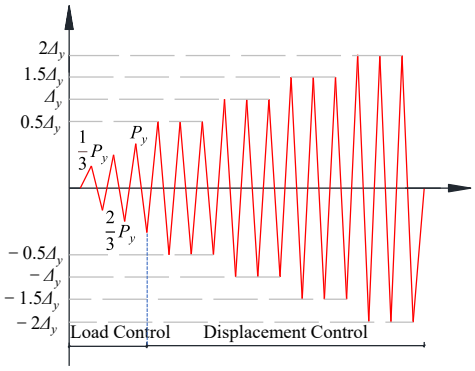

Fig. 5 Experimental loading system

3.3. Sensor placement

The experimental measurement parameters mainly encompassed column-end displacements, beam-column joint rotations, beam-column flange strains, beam-column web strains, and stiffener strains, among others. The arrangement of the displacement sensors is displayed in Fig. 6(a). Relative rotations between the columns and beams were measured and are labeled as W1–W4. Displacement sensors W5 and W7 were situated at the top and bottom of the column, respectively. Sensor W6 was designated to monitor any sliding between the hinge axis and the ground beam.

Strain gauges were used to quantify the strains on the beam flanges, beam webs, column flanges, and beam webs, as illustrated in Fig. 6(b). Due to the specimen's symmetry, only one half is illustrated, with corresponding symmetric measurement points indicated in parentheses.

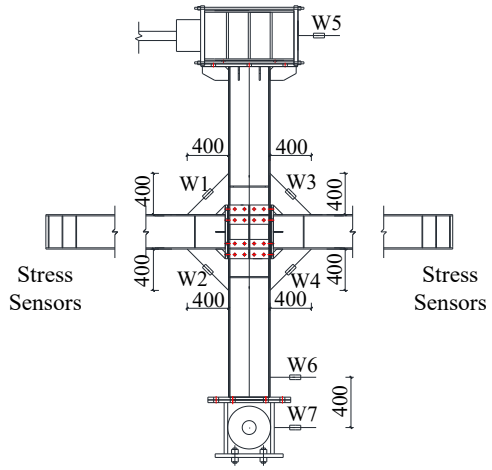

(a) Displacement meter layout drawing

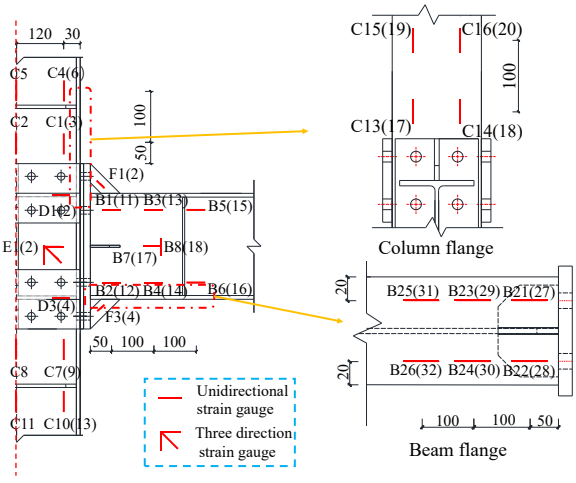

(b) Strain gauge arrangement in the beam and column nodal area

Fig. 6 Measurement point arrangement of beam and column joint data

4. Experimental results and analysis

4.1. Experimental curves and failure modes

The load–displacement hysteresis curve for specimen SJ-1 is depicted in Fig. 7. This curve shows basic symmetry in both the positive and negative directions and exhibits a pronounced pinched shape. A gradual decline in both load-bearing capacity and stiffness indicates that the specimen demonstrated strong plastic deformation and energy dissipation abilities. No evident signs were observed during the early stages of loading. However, at point A (75 mm, 58 kN), significant shear deformation became visible in the nodal region, as captured in Fig. 8(a). At point B (-135 mm, -68 kN), localized buckling manifested in the stiffener at the east side of the beam's end-plate, as shown in Fig. 8(b). upon reaching point C (175 mm, 68 kN), the tension-side end-plate stiffener on the east side detached, illustrated in Fig. 8(c). At point D (-184 mm, -63 kN), a marked increase in end-plate deformation was evident, as shown in Fig. 8(d). Ultimately, when the load reached point E (196 mm, 45 kN), the load-bearing capacity fell below 85% of the peak load, signaling the end of the loading process.

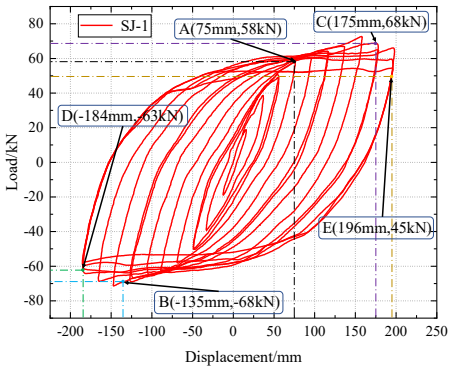

Fig. 7 Load–displacement hysteresis curve

(a) Joint domain shear deformation

(b) End-plate stiffener is locally buckled

(c) End-plate stiffener is disconnected

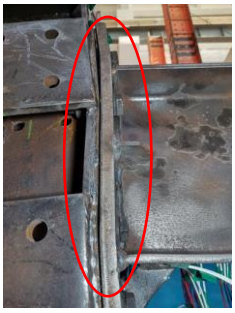

(d) Deformation of the end-plate is significantly increased

Fig. 8 Test phenomenon of specimens

During the experiment, after the stiffener on the end-plate fractured, the end-plate displayed noticeable deformation and showed weld-seam fractures at its junction with the beam flange. This outcome suggests that the end-plate stiffeners effectively augment the stiffness of the end-plate, thereby delaying the occurrence of weld-seam fractures between the end-plate and the beam flange. The inter-story displacement angle at the specimen's point of failure was 0.045 rad, substantially exceeding the 0.02 rad limit for elastic–plastic interlayer displacement angles in rare seismic events, as specified in the Chinese "Code for Seismic Design of Buildings" (GB50011-2010) [20]. This highlights the specimen's exceptional rotational capacity, signaling its superior seismic performance.

4.2. Strain analysis of specimen components

The strain of each member of the specimen joint is shown in Fig 9, the positive value is the tensile stress, the negative value is the compressive stress, and the measurement points are: the steel beam flange is 50mm away from the end plate (Q1), the steel column flange is 100mm away from the end plate (Q2), the skin plate (Q3), the column joint domain (Q4), and the end plate stiffener (Q5).

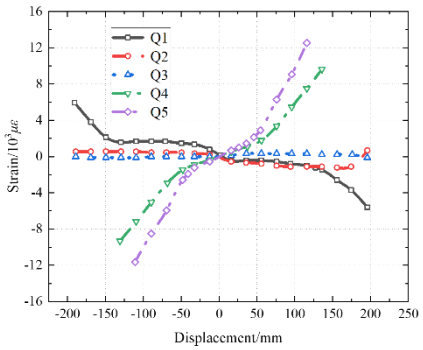

Fig. 9 Displacement–strain curve of the specimen

This study investigated the behavior of various specimen components under different loading conditions. The yielding sequence in the experimental joint unfolded as follows: initial yielding was evident in the end-plate stiffener, followed by shear yielding in the column joint area, and finally, yielding occurred in the beam flange situated 50 mm from the end-plate. Despite its small size, the end-plate stiffener initially exhibited subtle yielding with local buckling becoming conspicuous only after significant plastic deformation had occurred. Following the fracture of the stiffener on the end-plate, a considerable increase in strain was observed in the beam flange, culminating in its eventual yielding. These observations are consistent with the strain data obtained experimentally.

4.3. Skeleton curve analysis

The curve illustrating the bending moment–rotation relationship of the joint offers a comprehensive insight into the mechanical performance of the beam-column joints. As depicted in Fig. 10, the experimental joints transition through distinct phases of elasticity, plasticity, and failure. In the initial stages of loading (phases A–D), the bending moment at the joint increased linearly with the rotation angle. Upon yielding (phases A–B and D–E), the rate of moment growth moderated, and the M–θ curve exhibited significant nonlinearity. During the joint's failure stages (phases B-C and E-F), the load-bearing capacity declined to 85% of the peak load. The ultimate rotation angle of the joint was 0.045 rad, substantially exceeding the 0.03 rad rotational capacity specified by the American LRFD code for special moment-frame joints under cyclic testing [22]. With an initial rotational stiffness of 23,364.78 kN·m, the joint falls within the stiffness classification range of ($0.5EI_b/L_b$, $25EI_b/L_b$) as defined in the code, classifying it as a semi-rigid joint.

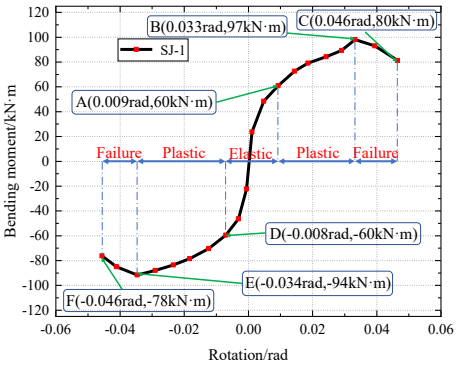

Fig. 10 Skeleton curve

4.4. Stiffness degradation

The secant stiffness K_i serves as an indicator of stiffness degradation in specimens under cyclic loading. Its calculation formula, Eq. (4), is as follows:

$$K_i = \frac{|+F_i|+|-F_i|}{|+X_i|+|-X_i|} \tag{4}$$

where F_i represents the load value at the first-cycle peak during the ith level of loading for the specimen, and X_i corresponds to the displacement value at this peak point.

As computed using Eq. (4), the stiffness degradation curve for the experimental component is presented in Fig. 11. Point A (18 mm, 1.37 kN·mm^{-1}) marks the initial secant stiffness of the joint. As loading progressed, the secant stiffness exhibited a gradual decline. Due to earlier yielding in both the end-plate stiffener and the nodal region, a noticeable dip in stiffness occurred near point B (55 mm, 0.95 kN·mm^{-1}). The stiffness curve showed a consistent reduction, without abrupt changes. When it reached point C (55 mm, 0.95 kN·mm^{-1}), the secant stiffness at the ultimate displacement indicated that the joint maintains relatively stable stiffness characteristics.

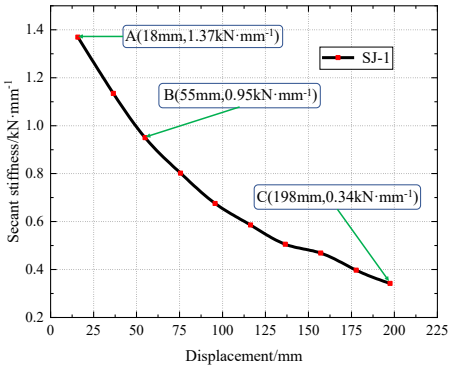

Fig. 11 Stiffness degradation curve of secant line of the specimen

4.5. Energy dissipation capacity of joints

This study also assessed the energy dissipation capacity of the specimens using the equivalent viscous damping coefficient (h_e). The area under the curve is depicted in Fig. 12 and was determined using Eq. (5):

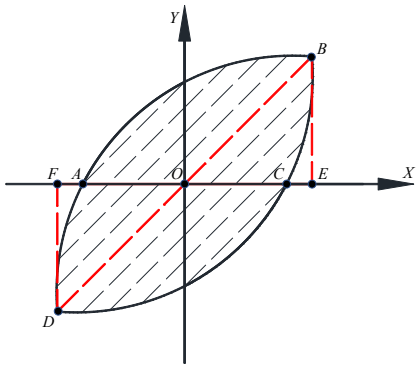

Fig. 12 Calculation of equivalent viscous damping coefficient

$$h_e = \frac{1}{2\pi} \cdot \frac{S_{(ABC+CDA)}}{S_{(OBE+ODF)}} \tag{5}$$

where $S_{(ABC+CDA)}$ represents the area enclosed by the hysteresis loop within one cycle, and $S_{(ABC+ODF)}$ denotes the triangular area corresponding to one cycle.

As illustrated in Fig. 13, the behavior during the initial loading phase, fell within the elastic regime, with the initial equivalent viscous damping coefficient (h_e) positioned at point A (18 mm, 0.09). As the load continued to increase, stress in certain components transitioned to the elastic–plastic range, leading to enhanced energy dissipation. Consequently, h_e increased in a stepwise manner. The maximum h_e for the final test specimen was at point B (198 mm, 0.43), demonstrating that the joint has excellent energy dissipation capacity.

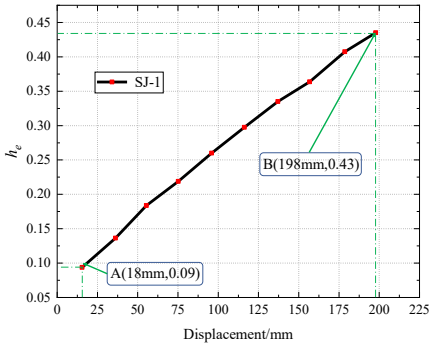

Fig. 13 Equivalent viscous damping coefficient

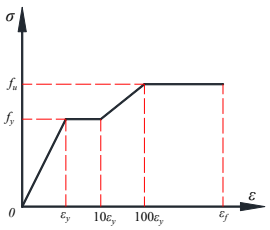

(a) Steel stress–strain curve

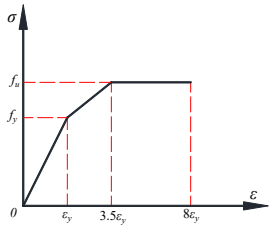

(b) Bolt stress–strain curve

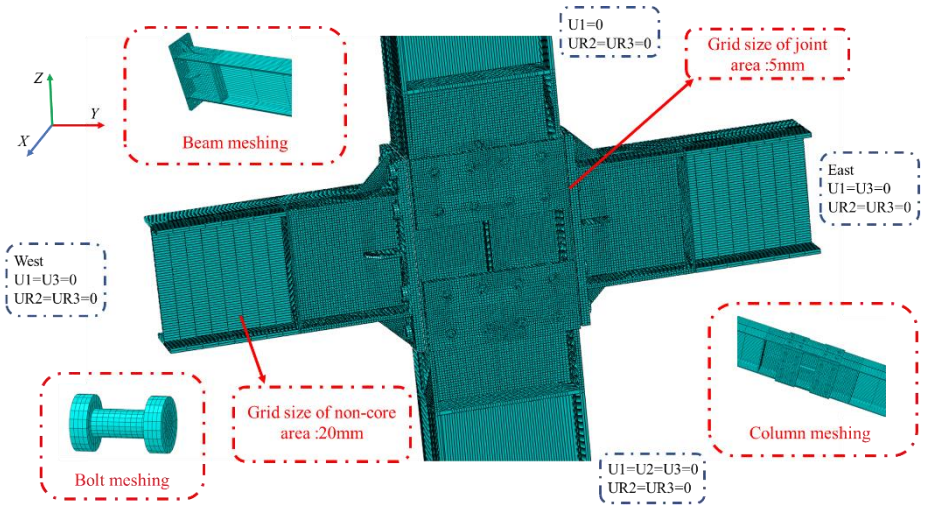

(c) Finite element model and its joint mesh

Fig. 14 Finite element modeling

5. Finite element model analysis

5.1. Establishment of finite element models

This study employed the ABAQUS/Standard static implicit method for finite element analysis on a narrow-flange H-shaped beam-column joint model. The finite element model mirrored the geometric dimensions and boundary conditions of the experimental specimens. To capture the true essence of the experimental data, the model incorporated the behavior of steel under cyclic loading conditions. A dynamic strengthening criterion was applied, and a bilinear constitutive model was chosen to replicate the steel's behavior [23], as shown in Fig. 14(a). In addition, a trilinear constitutive model was used to mimic the behavior of bolts [24], as detailed in Fig. 14(b). The material's Poisson's ratio was set at 0.3, and ductile metal failure criteria were implemented to simulate steel fractures [25]. Parameters such as fracture strain, triaxial stress, and strain rate were defined to simulate the steel fractures within the finite element software. General contact boundary conditions [26] were applied to the interfaces between various elements such as the bolt shaft and bolt hole wall, the nut and connecting end-plate, and column flange, as well as the end-plate and the column flange. In the normal direction, hard contact was defined, and a coefficient of friction of 0.3 was used. This model has not considered the impact of initial defects. Tangential direction contact was defined as Coulomb friction, with friction calculations conducted via the penalty method. Additionally, tie constraints were applied to simulate the welded connections.

The finite element model, complete with boundary constraints, is depicted in Fig. 14(c). In order to more accurately replicate the experimental observations, C3D8R solid elements were used and mesh sensitivity analysis was performed to refine the regions with complex stress patterns.

5.2. Validation of finite element models

Comparison between numerical simulation results and experimental observations including failure modes, hysteresis curves, and skeleton curves are illustrated in Figs. 15 and 16. The model closely matched the experimental findings, particularly in the tearing of the weld joint between the column-flange stiffener plate and the column flange, accompanied by localized buckling at the beam-end. Overall, the finite element simulation results were in strong alignment with the experimental data, capturing the joint's yielding behavior with high accuracy. This discrepancy between the finite element and experimental hysteresis and skeleton curves was below 10%. This level of agreement between the finite element simulation results and the experimental outcomes validates the robustness and accuracy of our finite element modeling approach, confirming its aptness for parameter analysis.

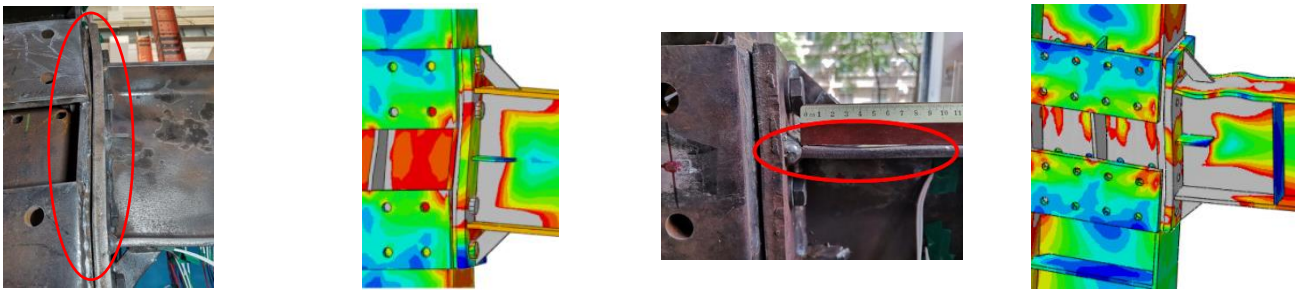

(a) End-plate is bent and deformed

(b) Beam flange is locally buckled

Fig. 15 Comparison of finite element simulation and experimental failure patterns

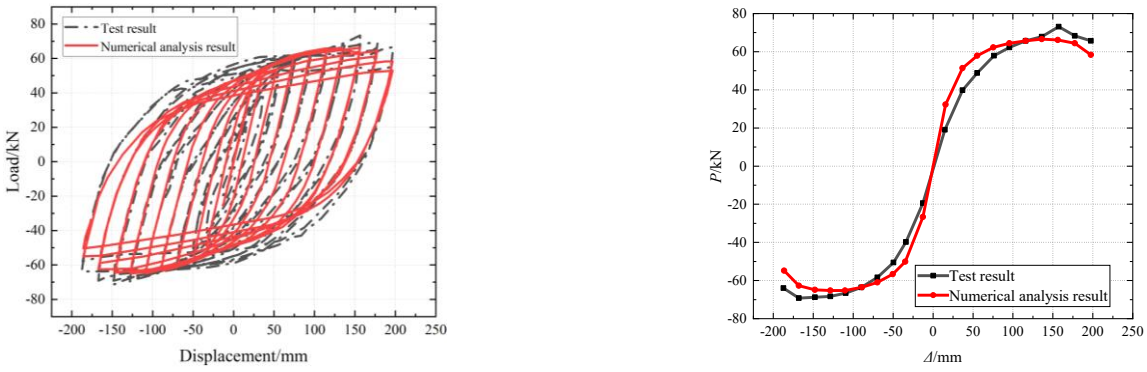

(a) Hysteresis curve

(b) Skeleton curve

Fig. 16 Comparison between finite element and test

6. Parameter analysis

6.1. Selection of test specimen parameters

Expanding on the finite element modeling approach detailed in Section 4.1, we conducted a comprehensive parameter analysis focusing on key variables. These variables included the axial compression ratio (ACR), thickness of the column web (TCW), thickness of the skin plate (TSP), thickness of the column-flange stiffener plate (TFS), and the beam end-plate thickness (BEP). The aim was to investigate their impact on vital performance metrics such as load-carrying capacity, deformability, energy dissipation capacity, and seismic performance. Table 2 presents these parameters, with “BASE” serving as the reference model for comparison.

6.2. Influence of axial compression ratio

The hysteresis curves, skeleton curves, and mechanical performance of the ACR series finite element models are presented in Fig. 17 and Table 3. The ACR series exhibited distinct spindle-shaped hysteresis loops, signaling excellent energy dissipation attributes. Starting with model ACR-2, a negative slope emerged in the hysteresis loop, signaling performance degradation in the frame. This is attributed to increased displacement, which amplifies the second-order effect of P-Δ in the specimens. The negative slope of the joint hysteresis curve is an indication of frame performance degradation.

Upon increasing the ACR, we observed a modest decline in the initial stiffness across the specimens. For instance, for those with an ACR of 0.7, the initial stiffness dipped by 9.7% when compared to the BASE specimen, which has an ACR of 0.2. Therefore, the ACR had a relatively minor influence on the structural stiffness under standard operating conditions. However, its impact on ductility was more conspicuous. Specifically, for the ACR-5 model, the ductility coefficient diminished by 33.5% compared to the BASE specimen. This suggests that the ACR considerably affects both load-bearing and deformation capacities. Accordingly, we recommend stringent control of the ACR during the design stage. For structures expected to experience lateral displacements, it would be prudent to cap the ACR at 0.4 when utilizing this type of joint.

Table 2
Model parameters of each joint

Model number	Axial compression ratio	Column web thickness /mm	Skin plate thickness /mm	Strengthen plate thickness /mm	End-plate thickness /mm
BASE	0.2	6.5	16	8	16
ACR-1	0.3				
ACR-2	0.4				
ACR-3	0.5	6.5	16	8	16
ACR-4	0.6				
ACR-5	0.7				
TCW-1	0.2	8	16	8	16
TCW-2		10			
TSP-1			8		
TSP-2	0.2	6.5	4	8	16
TSP-3			2		
TSP-4			0		
TFS-1				0	
TFS-2				4	
TFS-3	0.2	6.5	16	12	16
TFS-4				16	
TFS-5				20	
BEP-1					12
BEP-2					20
BEP-3	0.2	6.5	16	8	24
BEP-4					28
BEP-5					32

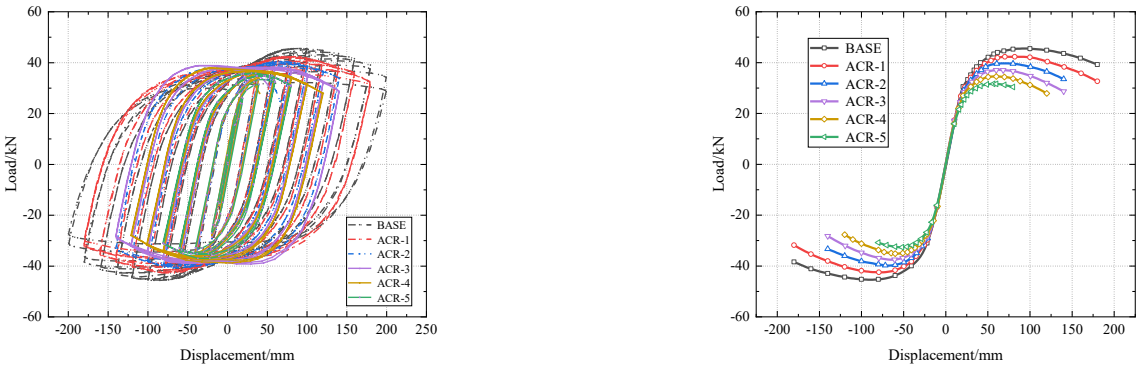

(a) Comparison of ACR series *P–Δ* hysteresis curves

(b) Comparison of ACR series hysteresis skeletons

Fig. 17 Comparison of ACR series hysteresis curve and skeleton

Table 3
Bearing capacity, displacement, and ductility of ACR series specimens

Model number	Initial stiffness kN/mm^{-1}	Yield load P_y/kN	Yield displacement Δ_y/mm	Peak load P_{max}/kN	Limit displacement Δ_u/mm	Ductile coefficient μ
BASE	1.75	37.91	35.02	45.41	181.97	5.19
ACR-1	1.73	35.56	32.56	42.44	158.55	4.87
ACR-2	1.69	33.49	30.42	39.68	138.74	4.56
ACR-3	1.67	31.58	28.48	37.33	121.89	4.28
ACR-4	1.63	29.60	26.63	34.84	109.22	4.10
ACR-5	1.58	27.26	24.40	31.77	81.20	3.32

6.3. Impact of column web thickness

The hysteresis curves, skeleton curves, and mechanical performance of the TCW series and the BASE model are displayed in Fig. 18 and Table 4. Our findings indicate that the BASE and TCW-1 specimens demonstrate strong energy dissipation, evident from their stable and well-defined spindle-shaped hysteresis curves. In contrast, the TCW-2 model, while exhibiting a higher initial load-bearing capacity, shows a quicker decline in that capacity.

A closer look at the TCW series reveals that compared to the BASE model, TCW-1 and TCW-2 experienced yield load increases of 10.31% and 22.95%,

respectively. However, their ultimate displacements diverged by 6.2% and -25.6% from the BASE specimen. This data suggests that an increase in the thickness of TCW leads to compromised ductility at the joints. Consequently, we recommend a column web thickness of 8 mm to maintain adequate joint ductility.

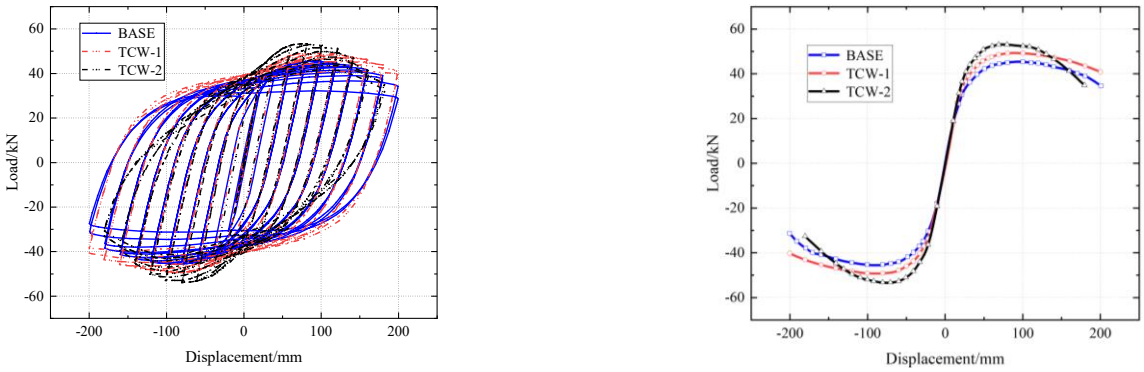

(a) Comparison of TCW series *P–Δ* hysteresis curves

(b) Comparison of TCW series hysteresis skeletons

Fig. 18 Comparison of TCW series hysteresis curve and skeleton

Table 4
Bearing capacity, displacement, and ductility of TCW series specimens

Model number	Initial stiffness kN/mm^{-1}	Yield load P_y/kN	Yield displacement Δ_y/mm	Peak load P_{max}/kN	Limit displacement Δ_u/mm	Ductile coefficient μ
BASE	1.75	37.91	35.03	45.41	181.97	5.19
TCW-1	1.82	41.82	35.29	49.19	193.20	5.47
TCW-2	1.89	46.61	35.96	53.32	144.90	4.03

6.4. Influence of skin plate thickness

Turning to the TSP series, Fig. 19 and Table 5 outline the hysteresis curves, skeleton curves, and mechanical properties of these finite element models. These curves progress through elastic, elastoplastic strengthening, and damage-reduction phases. While the BASE and TSP-1 hysteresis curves with skin plates exhibit a well-defined skin effect and display a relatively stable post-peak performance, the TSP series from TSP-2 onward manifests a more rapid decline in load-bearing capacity. The inclusion of skin plates noticeably boosts the load-bearing potential of the joints.

Upon comparing the BASE and TSP series, we found that the yield loads for TSP-1, TSP-2, TSP-3, and TSP-4 declined by 2.8%, 6.0%, 10.02%, and 22.3%, respectively, when compared to the BASE specimen. Additionally, TSP-4 experienced a drop in yield and ultimate displacement by 26.3% and 14.9%, respectively, when compared with the BASE specimen. Therefore, to balance ductility and load-bearing capability at the joints, we recommend that the thickness of the skin plates should exceed half the thickness of the end-plate.

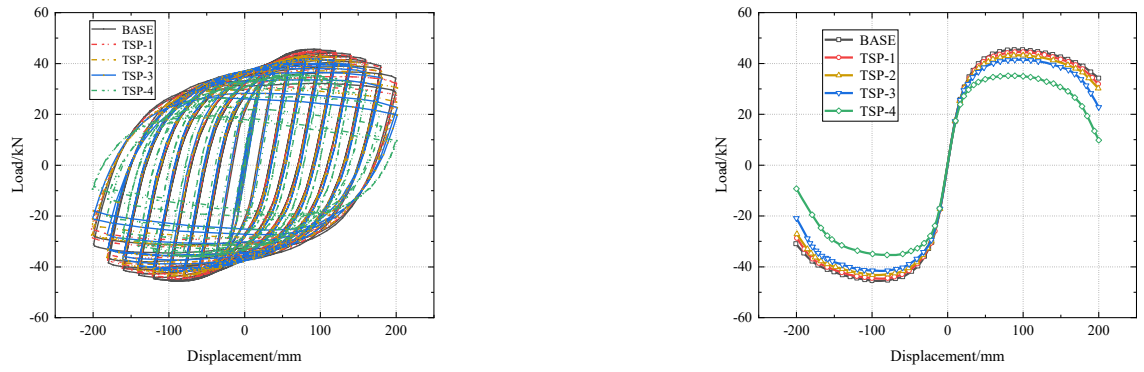

(a) Comparison of TSP series *P–Δ* hysteresis curves

(b) Comparison of TSP series hysteresis skeletons

Fig. 19 Comparison of TSP series hysteresis curve and skeleton

Table 5
Bearing capacity, displacement, and ductility of TSP series specimens

Model number	Initial stiffness kN/mm^{-1}	Yield load P_y/kN	Yield displacement Δ_y/mm	Peak load P_{max}/kN	Limit displacement Δ_u/mm	Ductile coefficient μ
BASE	1.75	37.91	35.03	45.41	181.97	5.19
TSP-1	1.75	36.86	34.55	44.54	180.60	5.25
TSP-2	1.74	35.65	33.38	43.20	180.13	5.40
TSP-3	1.73	34.11	32.04	41.61	173.23	5.41
TSP-4	1.70	29.47	25.80	35.237	154.90	6.00

6.5. Influence of column-flange stiffener plate thickness

The hysteresis curves, skeleton curves, and mechanical properties of the TFS series are delineated in Fig. 20 and Table 6. The finite element analysis reveals that with the exception of TFS-5, hysteresis curves for the various joints approach fullness, indicating a drop in load-bearing capacity after reaching peak loads. Moreover, the rate of this decline remains fairly stable across joints, except for TFS-5.

Through a comparative analysis between the BASE and TFS series, the data show that the yield loads for the TFS series vary by -15.5%, -8.0%, 8.8%, 17.4%, and 24.6% when compared to the BASE specimen. Similarly, peak load variations for the TFS series, in relation to the BASE specimen, are -14.2%, -7.0%, 7.3%, 13.7%, and 18.8%. These numbers signify a boost in load-bearing capacity corresponding with increased thickness of the column-flange strengthening plates.

As for yield displacements, the TFS series exhibits variations of -8.9%, -5.0%, 5.1%, 8.7%, and 10.0% compared to the BASE specimen. The ultimate displacements of the TFS series show variations of -4.7%, -2.5%, 3.5%, 0.3%, and -20.6% relative to the BASE specimen. These findings reveal enhanced deformability with increasing thickness of the column-flange stiffener plates. To balance this improvement with other performance metrics, it is recommended that the thickness of the stiffener plates not exceed 0.8 times that of the end-plate.

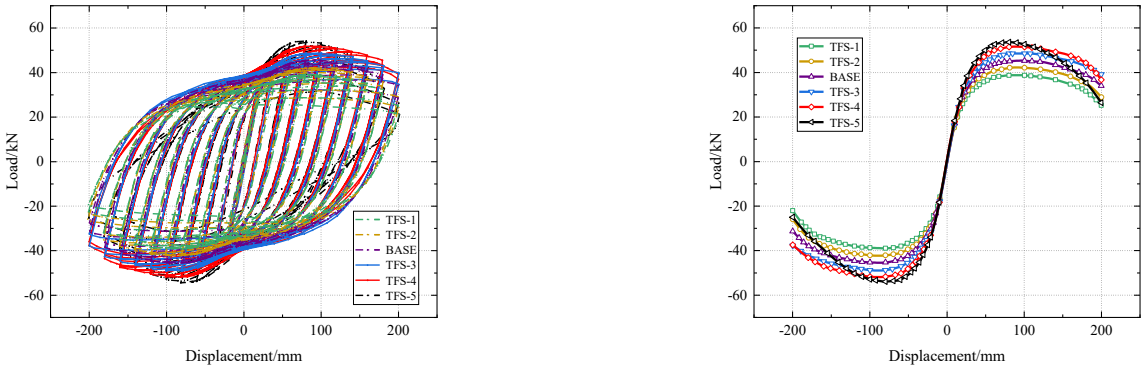

(a) Comparison of TFS series *P–Δ* hysteresis curves

(b) Comparison of TFS series hysteresis skeletons

Fig. 20 Comparison of TFS series hysteresis curve and skeleton

Table 6
Bearing capacity, displacement, and ductility of TFS series specimens

Model number	Initial stiffness kN/mm^{-1}	Yield load P_y/kN	Yield displacement Δ_y/mm	Peak load P_{max}/kN	Limit displacement Δ_u/mm	Ductile coefficient μ
TFS-1	1.62	32.04	31.91	38.94	173.37	5.43
TFS-2	1.70	34.87	33.29	42.23	177.51	5.33
BASE	1.75	37.91	35.03	45.41	181.97	5.19
TFS-3	1.79	41.25	36.83	48.73	188.33	5.11
TFS-4	1.83	44.50	38.08	51.66	182.49	4.79
TFS-5	1.86	47.24	38.55	53.96	144.57	3.75

6.6. Influence of beam end-plate thickness

To investigate the seismic performance of the joint under different end plates, the variable parameter test is carried out under different end plate thicknesses, and the results are as follows:

Turning to the BEP series, Fig. 21 and Table 7 outline their hysteresis curves, skeleton curves, and mechanical properties. Our findings reveal that as end-plate thickness increases, shear deformation in the joint region tends to diminish. For the BEP series, specimens 1–3 and the BASE specimen show complete hysteresis patterns, accompanied by a relatively stable decline in load-bearing capacity. On the contrary, BEP-4 and BEP-5, while displaying enhanced load-bearing capacities, also exhibit pinching phenomena in their hysteresis curves.

Comparing the BASE and BEP series reveals that yield loads in the BEP series specimens exhibit variations of -8.3%, 11.4%, 20.9%, 27.6%, and 28.4%. In terms of ultimate displacements, these variations range from -2.0%, 2.2%, 6.1%, 2.3%, and -27.7%. The data suggest that increased BEP thickness enhances the structure's deformability. Consequently, we recommend an end-plate thickness equal to twice the column-flange thickness.

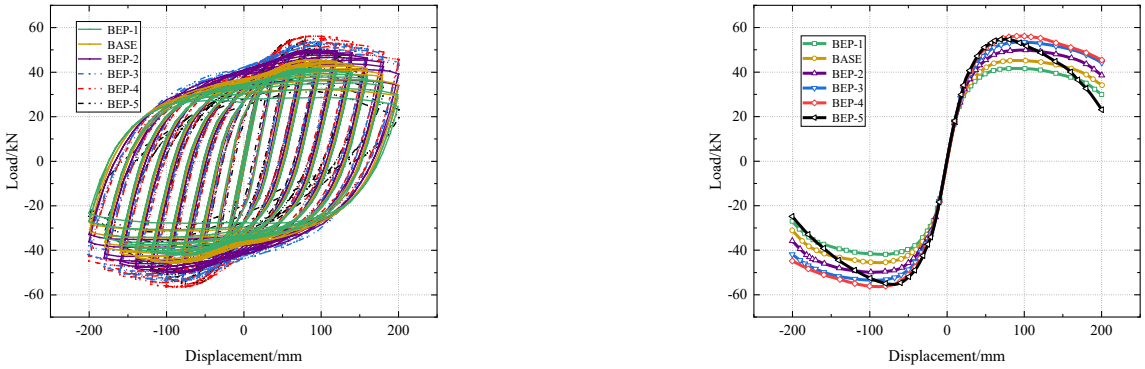

(a) Comparison of BEP series *P–Δ* hysteresis curves

(b) Comparison of BEP series hysteresis skeletons

Fig. 21 Comparison of BEP series hysteresis curve and skeleton

Table 7
Bearing capacity, displacement, and ductility of BEP series specimens

Model number	Initial stiffness kN/mm^{-1}	Yield load P_y/kN	Yield displacement Δ_y/mm	Peak load P_{max}/kN	Limit displacement Δ_u/mm	Ductile coefficient μ
BEP-1	1.71	34.78	32.23	41.76	178.27	5.53
BASE	1.75	37.91	35.03	45.41	181.97	5.19
BEP-2	1.79	42.24	38.33	49.94	185.91	4.85
BEP-3	1.81	45.84	40.48	53.45	193.07	4.77
BEP-4	1.83	48.39	41.91	56.25	186.17	4.44
BEP-5	1.85	48.66	39.20	54.86	131.58	3.35

7. Conclusion

In summary, this study executed both experimental and numerical simulations to investigate the seismic behavior of a narrow-flange H-shaped beam-column structure equipped with endplates. Notably, the finite element models closely mirrored the experimental data, enabling in-depth parametric analyses of critical joint components. A refined resilience model was subsequently established, drawing from a wide array of finite element analyses. The conclusions are as follows:

(1) Experimental data showed that the hysteresis curve of the studied joint takes on a predominantly full, spindle-shaped form. The maximum equivalent viscous damping coefficient reached 0.43, underlining excellent energy dissipation performance. With peak loads of 73 kN, ultimate displacements of 198 mm, and a ductility coefficient exceeding 3.6, the joint demonstrates both strong load-bearing and ductile deformation capabilities. It is thus well-suited for use in mid-to-low-rise steel frame structures.

(2) There exists a negative correlation between the load-bearing capacity of the joints and the ACR. Specifically, as the ACR rises, the hysteresis curve exhibits a steeper negative slope. Therefore, it is advised that the ACR not surpass 0.4. When TCW thickness remains at or below 8 mm, the hysteresis curve exhibits well-defined features, maintaining stable load-bearing capacity and effective energy dissipation. As such, a column web thickness of 8 mm in the joint region is recommended.

(3) Increasing TSP thickness in the joint region benefits both the initial rotational stiffness and the energy dissipation capacity of the joint. Conversely, augmenting the thickness of the column-flange stiffener plate has the effect of diminishing the joint's initial rotational stiffness. To strike a balance between robust load-bearing capacity and optimized performance, we recommend a skin plate thickness that is 0.5 of the end-plate thickness. Additionally, the thickness of the strengthening plates should not exceed 0.8 times that of the end-plate.

(4) As the thickness of the end-plate increases, so does the joint's load-bearing capacity. However, there is a caveat: when the BEP thickness becomes overly substantial, the failure mechanisms transitions to BEP buckling. This change leads to only a marginal improvement in load-bearing capacity and a sharp decline in the structure's resilience to damage. To mitigate this, it is advisable to set the end-plate thickness at double the beam flange thickness.

Declaration of competing interest

The authors declare that they have no known competing financial interests or personal relationships that could have appeared to influence the work reported in this paper.

Acknowledgments

The National Natural Science Foundation of China provided funding for this research (Nos. 52408211, 52178162) and China Postdoctoral Science Foundation Funded Project (No. 2024MD764004). The authors also wish to express their gratitude for the financial support received from the scientific research plan projects of Shaanxi Education Department (Nos. 20JY033, 20JK0713).

References

[1] Hao J.P., Sun X.L., Xue Q., et al., “Research and Applications of prefabricated Steel structure building Systems”, Engineering Mechanics, 34(01), 1-13, 2017. (in Chinese)
[2] Zhou X.H., Wang Y.H., “Status, problems and countermeasures of industrialization development of steel structural residence in China”, Journal of Civil Engineering, 52(01), 1-7, 2019. (in Chinese)
[3] Wang J., Brian U., Thai H.T., et al., “Behaviour and design of demountable beam-to-column composite bolted joints with extended end-plates”, Journal of Constructional Steel Research, 144, 221-235, 2018.
[4] D'Aniello M., Tartaglia R., Costanzo S., et al., “Seismic design of extended stiffened end-plate joints in the framework of Eurocodes”, Journal of Constructional Steel Research, 218, 512-527, 2017.
[5] Haghollahi A., Jannesar R., “Cyclic Behavior of Bolted Extended End-Plate Moment Connections with Different Sizes of End Plate and Bolt Stiffened by a Rib Plate”, Civil Engineering Journal, 4(01), 200-211, 2018.
[6] Hoang V.L., Jaspart J.P., Demonceau J.F., “Hammer head beam solution for beam-to-column joints in seismic resistant building frames”, Journal of Constructional Steel Research, 103, 49-60, 2014.
[7] Chen S.F., “The Strength and stiffness of bolted connection in Portal Frame”, Steel structure, 15(01), 6-11, 2000. (in Chinese)
[8] Guo B., Gu Q., Liu F., “Experimental study on hysteretic behavior of beam-column end-plate joints”, Journal of Building Structure, 23(03), 8-13, 2002. (in Chinese)
[9] Li G.Q., Duan L., Lu Y., “Experimental and theoretical study of bearing capacity for extended endplate connections between rectangular tubular columns and H-shaped beams with single direction bolts”, Journal of Building Structure, 36(09), 91-100, 2015. (in Chinese)
[10] Wang Y., Li H.J., Li J.F., et al., “Analysis of initial stiffness and structural internal forces of semi-rigid beam-column joint connection”. Engineering Mechanics, 20(06), 65-69, 2003. (in Chinese)
[11] Tong G.S., Zhao W., “Design Approach of Stiffeners in Extended End Plate Connections and Finite Element Analysis”, Journal of Shenyang Jianzhu University (Natural Science), 21(06), 616-620, 2005. (in Chinese)
[12] Zhong W.H., Zhao M.J., Zhou L., et al., “Seismic performance of a narrow flange H-beam-to-column full-bolt end-plate weak-axis connection”. Structures, 46, 637-653, 2022.
[13] “Standards for design of steel structures: GB 50017—2017”, Beijing: China Architecture & Building Press, 2017. (in Chinese)
[14] Guo B., Guo B.S., Zhang H.W., “M-θ relations for extended end-plate beam-column bolted connections”, Journal of Shandong Institute of Arch and Eng, 16(03), 1-5, 2001. (in Chinese)
[15] Solhmirzaei A., Tahamouli R.M., Hosseini H.B., “A new detail for the panel zone of beam-to-wide flange column connections with endplate”, Structures, 34, 1108-1123, 2021.
[16] AISC (American Institute of Steel Construction). Prequalified connections for special and intermediate steel moment frames for seismic applications. AN-SI/AISC 358–16, Chicago, IL, 2016.
[17] Tartaglia R., D'Aniello M., Gian A.R., et al., “Full strength extended stiffened end-plate joints: AISC vs recent European design criteria”, Engineering Structures, 159, 155-171, 2018.
[18] Technical code for steel structure of light-weight building with gabled frames GB 51022—2015 [S] Beijing: China Architecture & Building Press, 2017. (in Chinese)
[19] Lu L.F., Li C.C., Liu Z.L., et al., “Finite element analysis of the strengthen-joint region connection of I-shaped columns for the strong axis”, Advanced Civil, Urban and Environmental Engineering, 157, 123-131, 2014.
[20] “Earthquake resistant design code GB 50011-2010”, Beijing: China Architecture & Building Press, 2016. (in Chinese)
[21] “Steel and steel products—Location and preparation of samples and test pieces for mechanical testing GB/T 2975-2018”, Beijing: Standards Press of China,2018. (in Chinese)
[22] FEMA-267A. Interim Guideline: Advisory No. 1, Supplement to FEMA-267A[R]. Rep. SAC Joint Venture, Sacramento, California, 1997.
[23] Tan Z., Zhong W.H., Tian L.M., et al., “Quantitative assessment of resistant contributions of two-bay beams with unequal spans”, Engineering Structures, 242, 112-445, 2021.
[24] Zhong W.H., Tan Z., Tian L.M., et al., “Collapse resistance of composite beam-column assemblies with unequal spans under an internal column-removal scenario”, Engineering Structures, 206, 110-143, 2020.
[25] Tan Z., Zhong W.H., Gao Y., et al., “Collapse behavior of unequal-span multistory composite frames under the scenario of removing an internal column”, Journal of Structural Engineering, 150(12), 04024173, 2024.
[26] ABAQUS, Analysis User’s Manual, 6.17, ABAQUS, Inc., Dassault Systemes, USA, 2017.

Advanced Steel Construction – Vol. 21 No. 4 (2025) 327–335
DOI:10.18057/IJASC.2025.21.4.5

NUMERICAL MODELLING AND DESIGN OF SQUARE CONCRETE-FILLED QN1803 STAINLESS STEEL TUBULAR STUB COLUMNS UNDER AXIAL COMPRESSION

Yao-Hui Chi [1], You-Tian Wang [2,*], Le-Tian Hai [3], Xiang Zeng [4], Bo-Wen Chen [5] and Bo-Shan Chen [4]

[1] *College of Harbour and Coastal Engineering, Jimei University, Xiamen, China*
[2] *Department of Building and Real Estate, The Hong Kong Polytechnic University, Hong Kong SAR, China*
[3] *Research Institute of Urbanization and Urban Safety, School of Civil and Resource Engineering, University of Science and Technology Beijing, Beijing, China*
[4] *School of Civil Engineering and Architecture, Hainan University, Haikou, China*
[5] *School of Civil Engineering and Architecture, Guangxi University, Nanning, China*
* *(Corresponding author: E-mail: youtian.wang@polyu.edu.hk)*

ABSTRACT

A new generation of concrete-filled steel tubular (CFST) columns with steel tubes manufactured from QN1803 high-strength stainless steel (HSSS) was developed, which has the potential to be used extensively in demanding marine environments, and such newly developed material QN1803 offers notable advantages over traditional stainless steel including lower material cost and higher yield strength. However, no work or design rules were available for such concrete-filled QN1803 stainless steel stub columns. This study reports the results of a comprehensive numerical analysis aimed at developing new calculation formulas for concrete-filled QN1803 stainless steel square stub columns under axial compression. A nonlinear finite element (FE) model was established and validated against the existing experimental data reported by many researchers. An extensive parametric analysis comprising 460 FE models was undertaken using the validated FE models to investigate the axial loading response of CFST stub columns with QN1803 stainless steel tubes. The variables examined in the parametric analysis include the different stainless steel, wall thicknesses of the steel tube and concrete strengths. The results suggested that the ultimate bearing strength of CFST QN1803 stub columns increased by 25.3%, compared to corresponding S30408 members. The study further utilized the parametric analysis results to assess the accuracy of existing design criteria, including the Eurocode (EN 1994−1-1) (2004), American Specification (ANSI/AISC) (2022), and Australian/New Zealand standard (AS/NZS) (2017). The comparison results indicated that the existing design criteria tended to underestimate the ultimate strength of CFST stub columns with QN1803 tubes relative to the numerical results. Finally, new calculation formulas were proposed by modifying the current design standards, offering accurate and reliable predictions for these new CFST columns.

ARTICLE HISTORY

Received: 15 December 2024
Revised: 5 June 2025
Accepted: 7 June 2025

KEYWORDS

Concrete-filled QN1803 stainless steel tube;
Axial compression;
Square stub columns;
Numerical analysis;
Proposed calculation formulas

1. Introduction

The concrete-filled steel tubular (CFST) columns are extensively applied in demanding marine environments, including the monopile foundations of offshore wind turbines and submerged floating tunnels [1]. In environments marked by high salinity and humidity, these structures are particularly susceptible to corrosive conditions [2-4]. Therefore, enhancing the corrosion resistance of the exterior steel tubes is essential for ensuring the structural integrity and safety [5-8]. To address this, recent innovative progress in the field of composite structures is to replace carbon steel with stainless steel (SS) as the external column tubes [9,10]. Compared to carbon steel, stainless steel offers additional benefits such as aesthetics, sustainability, recyclability, and ease of maintenance [11-13]. However, their high cost and low strength have limited their applications. Recently, the introduction of a new generation of high-strength stainless steel (HSSS), designated as QN1803, has expanded their application in the steel tubes of concrete-filled steel tubular (CFST) columns. This new material offers improved corrosion resistance in comparison with S30408 while reducing cost and providing significantly higher yield strength [14-19]. Despite these advantages, no design criteria are currently available for such CFST members with QN1803 HSSS tubes under axial loads.

Many researchers [20-22] have conducted in-depth discussions and extensive studies on the performance and design of CFST members with carbon steel tubes. Examples of such research include Uy et al. [23,24], Han et al. [25-27], Tao et al. [28], Bradford et al. [29] and Teng et al. [30]. They found that CFST members offer higher bearing capacity, improved ductility, enhanced long-term serviceability performance and greater energy absorption in comparison with traditional reinforced concrete and steel columns.

In terms of concrete-filled steel stainless steel tubular (CFSST) structures, many studies have been reported in the literature [31-36]. In 2004, Roufegarinejad et al. [37] first introduced the concept of CFST members incorporating the SS tubes. In an early investigation, Young and Ellobody [38] conducted a comprehensive series of experiments to examine how variables such as tube shape, wall thickness of tube, and strength of concrete affect the axial loading response of CFSST columns. Their research led to the formulation of revised design recommendations. Lam and Gardner [39] conducted a comprehensive investigation into the axial loading response of CFSST stub columns with circular and square cross-sections under axial loads. Their findings revealed that existing design specifications for carbon steel tend to be highly conservative. He et al. [40] performed comprehensive experimental and FE analyses on CFSST columns constructed with EN 1.4420 SS tubes, thoroughly investigating their axial loading response. Building on these findings, they updated the current design standards and introduced new design criteria. Tao et al. [41] introduced a simplified model that employs numerical methods to determine the ultimate strength of short square CFSST stub columns. In a recent investigation, Azad et al. [42-44] carried out experiments to study the impact of compression, bending, and combined loading on the structural performance of CFSST members. It was found that the existing codes cannot provide precise predictions for such CFSST columns. However, all the aforementioned research only focused on CFST members with steel tubes manufactured from traditional SS.

In parallel with these developments, recent advancements in stainless steel–concrete composite structures have introduced novel fabrication and material integration strategies. For stainless steel components, additive manufacturing (AM, also referred to as 3D printing) has emerged as a promising technique, offering improved dimensional control, material efficiency, and the ability to fabricate complex geometries without welding [45-47]. In terms of hybrid structural systems, recent research has explored several advanced forms beyond conventional CFSST columns, such as hollow double-skin stainless steel composite sections and stiffened stainless steel tubular members [33]. Among them, concrete-filled double-skin steel tubular (CFDST) sections, consisting of an inner and outer steel tube with infilled concrete, have received growing attention. CFDST columns with stainless steel outer tubes offer notable advantages over their CFSST counterparts, including enhanced strength-to-weight ratios and corrosion resistance, as well as a reduction in concrete core volume that facilitates more efficient use of materials [48].

While these studies have expanded the structural typologies of stainless steel–concrete composites, research concerning the application of newly developed high-strength QN1803 stainless steels in such systems remains limited. Recent studies [49,50] have shown that QN1803 high-strength stainless steel exhibits notable differences in material properties, including yield strength, strain hardening behavior, and ductility, compared to conventional structural steels. These differences may significantly influence the axial behavior of composite columns when QN1803 is used as the outer tube material. As a result, existing design provisions developed for mild steel composite members may not be directly applicable, and the accuracy of prevailing design codes [51-53] requires re-evaluation for such innovative CFSST systems.

This investigation presents a comprehensive numerical analysis aimed at developing new calculation formulas for concrete-filled QN1803 HSSS square stub columns under axial loads. This study seeks to build upon and extend the findings of previous research [54] by incorporating the QN1803 HSSS tubes into CFST members using numerical methods. The proposed FE modelling method was calibrated using existing test data of traditional CFSST columns. To further explore and provide design guidance for CFST stub columns under axial compression, incorporating QN1803 HSSS tubes, an extensive parametric analysis was therefore performed using the calibrated FE modelling method. The impacts of the wall thickness of the steel tubes and the infilled concrete strength on the axial loading response of such CFST members were evaluated. The parametric analysis results were compared against strength predictions provided by prevailing building standards, including the EN 1994-1-1 [51], AS/NZS 5100 [52] and ANSI/AISC 360-22 [53]. Finally, new calculation equations were subsequently recommended through modifying the existing design provisions based on the modelling results, which can provide accurate and reliable predictions for such new CFST members.

2. Summary of experimental study [44,49]

2.1. Stub column tests

A total of 21 test data were collected and summarized in this section for validating the models. Among them, nine CFSST square stub columns were tested by Dai et al. [54] previously, and the remaining 12 test data were reported by He et al. [40], Young and Ellobody [38], Lam and Gardner [39]. Dai et al. [54] performed experiments on short columns utilizing a hydraulic axial testing machine. They precisely measured axial displacements with the aid of two LVDT devices, as depicted in Fig. 1. The columns were placed under a loading condition where they were supported at the top with a pinned connection and fixed support at the bottom. It is noteworthy that the sample tubes were constructed by welding four SS plates, either austenitic or duplex, into a box-shaped section. Regarding the loading method, Young and Ellobody [38], He et al. [40], and Dai et al. [54] used displacement-controlled loading, while Lam and Gardner [39] employed load-controlled loading at 3kN/min. For a more comprehensive overview of the short column tests, refer to the study [54].

(a) Photo of experimental configuration

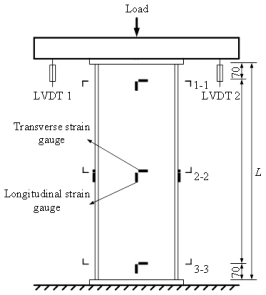

(b) Schematic view

Fig. 1 Stub column tests reported by Dai et al. [54]

2.2. Tensile coupon tests

A total of six tensile coupons were examined by Chen et al. [49] in a previous investigation, and the mechanical properties of QN1803 HSSS was obtained. The tensile test data, summarized in Table 1, are available for conducting parameter analysis.

Table 1
Material properties [44]

Coupon ID	Thick-ness t_w/mm	Young's modulus E/GPa	0.2% proof stress $\sigma_{0.2}$/MPa	Ultimate stress σ_u/MPa
304D-T4-1	3.70	196.0	481.1	767.0
304D-T4-2	3.67	198.5	480.4	777.4
304D-T4-3	3.70	195.8	470.6	776.6
304D-T12-1	11.75	198.0	411.0	736.1
304D-T12-2	11.79	199.5	418.8	734.5
304D-T12-3	11.73	199.8	429.1	739.7

(a) Setup of tensile cotest

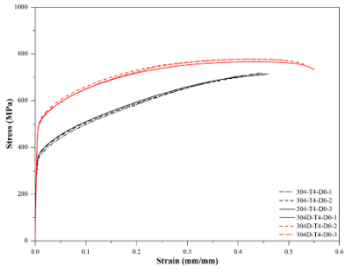

(b) Stress-strain curves of QN1803

Fig. 2 Tensile coupon tests reported by Chen et al. [49]

A tensile test was performed using a 300 kilonewton machine, adhering to the ISO 6892-1 [55] standard. The experimental setup is presented in Fig. 2(a). Test specimens, extracted from the original, untested material, were aligned with the rolling direction of the material. For each thickness, three uniformly sized coupons were prepared. The stress-strain behavior of QN1803 is depicted in Fig. 2(b), demonstrating that its yield strength exceeds 400 MPa, confirming its classification as HSSS. The study revealed that the yield strength of QN1803 surpasses 400 MPa, marking a significant increase in comparison with S30408. A composition investigation revealed that QN1803 HSSS had a nickel content ranging from 1.5% to 2.2%, while the regularly used S30408 and S22053 have nickel contents of 8% to 11% and 4.5% to 6.5%, respectively. The above comparisons highlight that QN1803 differ significantly from S30408 in both chemical composition and material properties. The work of Chen et al. [49] illustrates comprehensive details of the experimental plan.

3. Establishment and verification of numerical models

3.1. General

To replicate the axial loading response of CFST members, a nonlinear finite element model was constructed using the ABAQUS software [56], a widely used finite element analysis software. The experimental data reported by many researchers and additional studies [38-40,54] were used for validation. Comprehensive details on the model's development and validation will be presented next.

3.2. Modelling of material properties

The stress-strain (σ−ε) behavior of SS is characterized in the numerical models using a two-stage Ramberg-Osgood equation, as expressed in Eq. (1). Previous research [42-44] has demonstrated the efficacy of this formulation in accurately representing the nonlinear response of SS in concrete-filled steel tube columns.

$$\varepsilon = \begin{cases} \frac{\sigma}{E} + 0.002(\frac{\sigma}{\sigma_{0.2}})^n & \sigma \le \sigma_{0.2} \\ 0.002 + \frac{\sigma_{0.2}}{E} + \frac{\sigma-\sigma_{0.2}}{E_{0.2}} + \varepsilon_u(\frac{\sigma-\sigma_{0.2}}{\sigma_u-\sigma_{0.2}})^m & \sigma > \sigma_{0.2} \end{cases} \quad (1)$$

where ε_u is the strain corresponding to the ultimate stress σ_u, n and m are the material constants in the Ramberg–Osgood equation, representing the strain-hardening characteristics of the material.

The engineering stress (σ)-strain (ε) data were transformed into true stress (σ_{true})-strain (ε_{true}) curves using Eqs. (2) and (3). This method addresses the nonlinear responses and geometric transformations of materials under deformation, thereby enhancing the precision of the numerical models utilized in this study.

$$\sigma_{true} = \sigma(1+\varepsilon) \quad (2)$$

$$\varepsilon_{true} = ln(1+\varepsilon) - \sigma_{true}/E \quad (3)$$

The performance of concrete is simulated adopting the concrete damage plasticity model in ABAQUS [56]. This model involves defining multiple parameters, including the dilation angle, flow potential eccentricity, uniaxial-to-biaxial compressive strength ratio, tensile-to-compressive meridian stress deviator ratio, and the viscosity parameter. Based on guidelines provided in the literature [54], these values are specified as 30°, 0.1, 1.16, 0.667, and 0, respectively. The elastic modulus of the concrete (E_c) is calculated using Eq. (4) [54], and the Poisson's ratio is consistently assigned a value of 0.2.

$$E_c = 4700\sqrt{f_c'} \quad (4)$$

where f_c' is the cylinder compressive strength.

For CFSST members under compression, the confinement effect of the SS tubes induces triaxial stress states in the concrete core, resulting in mechanical behavior comparable to that of carbon steel CFST members under equivalent loading conditions. The finite element analysis employed the concrete confinement model developed by Tao et al. [41], assuming linear tensile behavior in concrete up to its tensile strength, approximated as 0.1 f_c'. Beyond this threshold, the nonlinear tensile stress-strain relationship is characterized by the fracture energy (G_F), calculated using Eq. (5).

$$G_F = (0.0469d_{max}^2 - 0.5d_{max}+26)\left(\frac{f_c'}{10}\right)^{0.7} \quad (5)$$

3.3. Finite element type and meshing

In modeling the external steel tube and concrete core, the eight-node solid element (C3D8R) from the ABAQUS element library was utilized [57-60]. This element is well-suited for simulating the behavior of both materials due to its capability to accurately capture the interaction between them, as illustrated in Fig. 3. To ensure a balance between computational accuracy and efficiency, an investigation of mesh sensitivity was conducted. Three mesh densities were examined, corresponding to global seed sizes of 1/10, 1/15, and 1/20 of the section width. The results showed that the mesh with a seed size of 1/10 of the section width slightly overestimated the ultimate axial strength (by approximately 3%), whereas the results obtained with 1/15 and 1/20 of the section width were nearly identical. Therefore, a global seed size of 1/15 of the section width was adopted for all subsequent finite element models.

3.4. Modelling of boundary and loading conditions

The interaction and boundary conditions between the tube and the core concrete were modeled using face-to-face contact. To account for potential separation after initial engagement, a hard contact approach was adopted for the normal direction. In the tangential direction, a penalty friction model was implemented to simulate sliding behavior at the steel-concrete interface. A small sliding formulation was adopted, considering the limited slippage observed under axial compression. The friction coefficient was set to 0.25, consistent with values recommended in previous studies [54]. The robustness of this assumption was confirmed by additional simulations with higher friction coefficients (0.4 and 0.6), which showed negligible influence on the axial load–displacement response. As depicted in Fig. 4, two reference points, RP1 and RP2, were created and linked to the nodes located at each end of the cross-section. For RP1, boundary conditions were set to restrict movement in all directions. Conversely, RP2 was permitted to move freely along the z-direction but was restricted in all other directions.

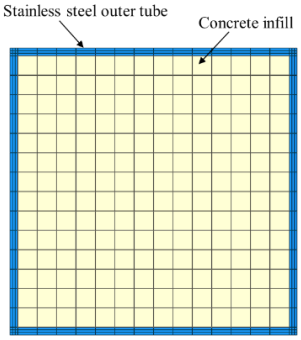

Fig. 3 Mesh configuration of FE models

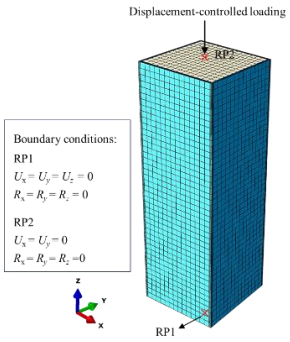

Fig. 4 Boundary conditions

3.5. Initial geometric shapes and residual stress

Initial geometric imperfections and residual stresses can significantly affect the local buckling behavior and ultimate strength of hollow steel sections. However, for concrete-filled steel tubular (CFST) stub columns, the presence of concrete core effectively restrains local out-of-plane deformations and reduces the influence of these initial imperfections. Tao et al. [41] demonstrated that this confinement not only suppresses local buckling but also plays a role analogous to that of initial geometric imperfections, thereby diminishing their influence on compressive behavior. This mitigation mechanism has also been validated in concrete-filled stainless steel tubular columns. Specifically, Han et al. [33] concluded that for short CFSST members, the effects of initial geometric imperfections and residual stresses are significantly reduced due to the stabilizing effect of the concrete infill.

Based on these findings, and considering that the QN1803 stainless steel tubes used in this study were filled with concrete and tested as stub columns, the exclusion of initial geometric imperfections and residual stresses in the finite element modeling is deemed reasonable.

Table 2
Summarized test data of CFST stub columns from literature

Source	Specimen ID	Tube material	$B \times t$ (mm)	L (mm)	f_y (MPa)	f_c' (MPa)	$N_{u,test}$ (kN)
Dai et al. [54]	A-t8C50	304	296×7.8	840	293	38.1	6290
	A-t10C50		300×9.9	840	287	38.1	7113
	A-t12C50		304×11.9	842	301	38.1	7924
	A-t8C70		296×7.8	840	293	56.6	6743
	A-t10C70		300×9.9	840	287	56.6	7947
	A-t12C70		304×11.9	840	301	56.6	8575
	A-t8C80		296×7.8	841	293	64.9	7436
	A-t10C80		300×9.9	839	287	64.9	8430
	A-t12C80		304×11.9	840	301	64.9	9257
Young and Ellobody [38]	SHS1C40	EN 1.4462	150×5.8	450	497	46.6	2768.1
	SHS1C60		150×5.8	450	497	61.9	2972.0
	SHS1C80		150×5.8	450	497	83.5	3019.9
Lam and Gardner [39]	SHS100×100×2-C30	Not provided	100×2.2	300	385	30	534
	SHS100×100×2-C60		100×2.0	300	385	53	687
	SHS100×100×2-C100		100×2.2	300	385	74	836
He et al. [40]	SHS100×100×3-C40	High-chromium grade EN 1.4420	99×3.0	299	365	49.1	830
	SHS100×100×3-C60		100×3.0	299	365	68.1	1004
	SHS100×100×3-C80		100×3.0	299	365	86.4	1162
	SHS120×120×5-C40		120×5.0	358	317	49.1	1373
	SHS120×120×5-C60		120×5.0	359	317	68.1	1566
	SHS120×120×5-C80		120×5.0	357	317	86.4	1840

3.6 Validation of numerical models

Table 2 presents a comparison of 21 laboratory test findings for CFSST members, as reported by Dai et al. [54], He et al. [40], Young and Ellobody [38], and Lam and Gardner [39]. Table 3 compares the ultimate strength estimated by numerical analysis ($N_{u,FE}$) with laboratory testing ($N_{u,test}$) [38-40,54], revealing an average $N_{u,test}/N_{u,FE}$ ratio of 0.95 with a coefficient of variation (COV) of 0.034 . Fig. 5 plots the relationship between load and axial displacement, as obtained from both laboratory testing [38-40,54] and numerical analysis. The analysis reveals that all curves exhibit strong agreement regarding ultimate strength. Nonetheless, some finite element curves display slightly greater initial stiffness in comparison with the experimental curves. This discrepancy is likely attributable to localized slipping between the loading support and the sample during testing. Fig. 6 presents the deformed configurations captured during experimental testing and finite element (FE) modeling for specimen A-t10C80. The experimental observations identified local buckling failure predominantly in the midsection of the steel tube, a phenomenon closely mirrored by the numerical simulation outcomes.

Consequently, the FE models are capable of estimating the axial loading response of CFSST members for both their ultimate strength and failure characteristics, which is supported by the negligible average difference [61-63].

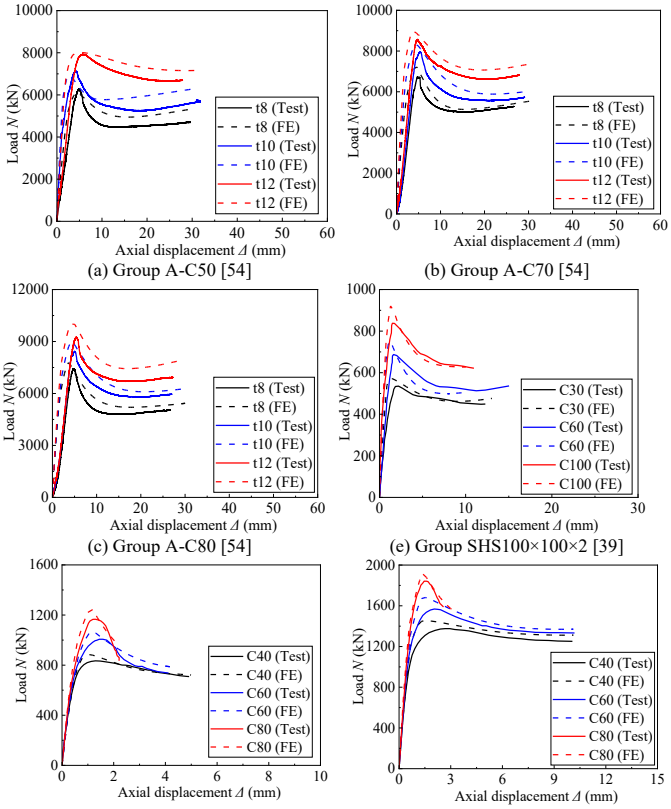

(a) Group A-C50 [54] (b) Group A-C70 [54]

(c) Group A-C80 [54] (e) Group SHS100×100×2 [39]

(g) Group SHS 100×100×3 [40] (h) Group SHS 120×120×5 [40]

Fig. 5 Typical comparisons of test and FE load-axial displacement curves

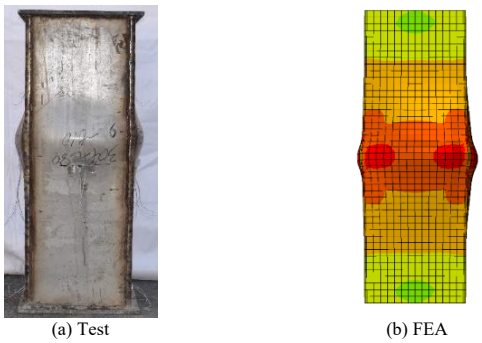

(a) Test (b) FEA

Fig. 6 Comparisons of test and FE failure modes for specimen A-t10C80 [54]

4. Parametric analysis for CFST columns with QN1803 tube

4.1. General

Following comprehensive validation of the FE model, an extensive parametric study comprising 460 models was conducted to assess the axial loading response of CFST stub column constructed with QN1803. The crucial variables examined in this investigation included the different stainless steel, wall thicknesses of the tube and concrete strengths. Table 4 details the critical parameters employed in the parametric research.

To assess how different types of stainless steel affect the load-bearing capacity of CFSST stub columns, both QN1803 and S30408 were considered as steel tubes. Noting that the mechanical properties for QN1803 and S30408 are derived from tensile tests performed by Chen et al. [49], with further details provided in Section 2.2. The steel tubes were designed to have a width (B) of 200 mm and a length (L) of 600 mm to ensure the local buckling behaviour of composite stub columns. This slenderness ratio has been widely adopted in previous CFST and CFSST studies for investigating confined local failure mechanisms [38-41]. Also, five different grades of concrete were examined in the parametric research, and the cylinder compressive strengths (f_c') were 23.7 MPa, 31.6 MPa, 39.5 MPa, 47.4 MPa, and 55.3 MPa. The constitutive laws for these concrete grades are established using the concrete damage plasticity model, as outlined in Section 3.2. The thickness (t) varies between 1 mm and 10 mm. The selected values of section width (B) and wall thickness (t) were designed to cover a broad range of width-to-thickness ratios, thereby encompassing compact, noncompact, and slender section profiles according to the classification of squarer hollow sections (SHS) in ANSI/AISC 360-22 [53]. The subsequent chapters will provide an in-depth analysis of how variations in SS types, wall thickness, and concrete strength influence the overall strength of CFSST members.

4.2. Impact of different stainless steel

Fig. 7(a) demonstrates the impact of different stainless steels on the axial behavior of CFSST stub columns. The comparison findings suggested that the CFST stub columns with QN1803 HSSS tube exhibit higher strength by 25.3% in comparison with S30408 columns. Additionally, Fig. 7(b) illustrates the load-displacement curves normalized for comparison, in which the normalized load value (N_{nor}) has been adopted in the form of $N/(\sigma_{0.2}A_s + A_c f_c')$ and the normalized displacement value (Δ_{nor}) have been taken as Δ/H. The findings reveal that both specimens can exceed a normalized load of 1.0, achieving a similar peak load of approximately 1.07. However, after reaching peak load, the specimen fabricated with QN1803 HSSS exhibits greater post-peak strength compared to S30408 columns.

4.3. Impact of tube thicknesses

Fig. 8 displays the N-Δ and N_{nor}-Δ_{nor} curves for typical short steel-concrete composite column with QN1803 HSSS tubes, where all columns have a consistent steel tube width of 200 mm and a concrete compressive strength of 47.4 MPa. The SS tubes come in various thicknesses, including 1 mm, 3 mm, 6 mm, 8 mm, and 10 mm. As observed from Fig. 8(a), the ultimate bearing strength of these columns significantly improves as the thickness of the steel tubes increases. The enhancement in load-bearing capacity primarily results from the increased thickness of the tubes, which enlarges the cross-sectional

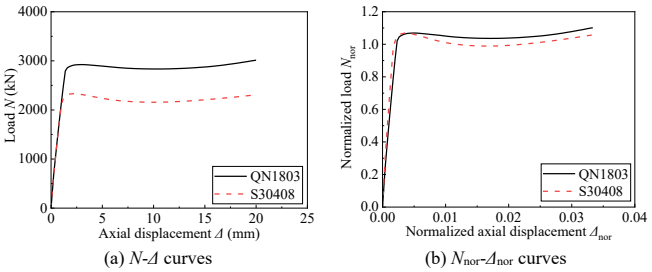

(a) N-Δ curves (b) N_{nor}-Δ_{nor} curves

Fig. 7 Impact of stainless steel type on square CFSST stub columns

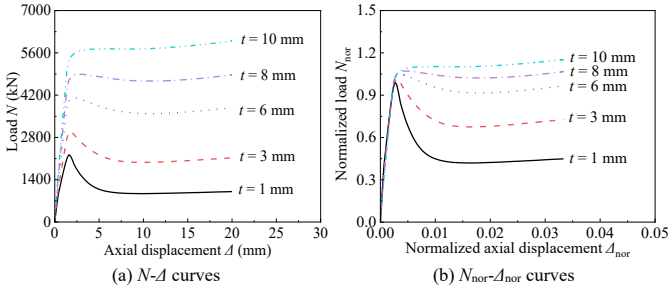

(a) N-Δ curves (b) N_{nor}-Δ_{nor} curves

Fig. 8 Impact of outer tube thicknesses on square CFSST stub columns

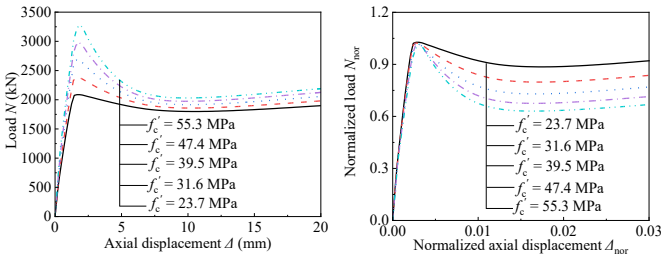

(a) N-Δ curves (b) N_{nor}-Δ_{nor} curves

Fig. 9 Impact of concrete strength on square CFSST stub columns

area and consequently provides more substantial confinement for the internal concrete fill. The increase in the sectional area of the tube results in a rise in the confinement factor, ξ, defined as $A_s\sigma_{0.2}/A_cf_{ck}$. A larger cross-sectional area A_s corresponds to a higher ξ value, thus strengthening the confinement imposed on the concrete. Noting that f_{ck} represents the characteristic strength of concrete, defined as $0.67f_{cu}$ in accordance with EN 1992-1-1 [64].

4.4 Impact of concrete strengths

Fig. 9 illustrates the impact of the axial loading response of the infilled concrete (f_c') on the load-bearing capacity of short steel-concrete composite columns constructed with QN1803 HSSS tubes. The analysis also compares the N-Δ and N_{nor}-Δ_{nor} curves. The specimens comprised steel tubes with a 200 mm diameter and 5 mm wall thickness, with concrete strengths varying from 23.7 MPa to 55.3 MPa. As seen in Fig. 9(a), the ultimate bearing capacity of these CFST stub columns increases significantly as the concrete strength rises. However, maintaining a constant thickness for the SS tube while enhancing the concrete strength reduces the level of confinement provided to the concrete core. This reduction in confinement effectiveness lowers the confinement factor ξ and, consequently, decreases the normalized load capacity at higher strain levels, as illustrated in Fig. 9(b).

5. Evaluation of current design rules

5.1. General

As previously noted, there are currently no design codes specifically addressing steel-concrete composite columns with QN1803 tubes subjected to axial loads. The existing design criteria, including Eurocode EN 1994–1-1 [51], Australian Standard AS/NZS 5100 [52] and American Specification ANSI/AISC 360-22 [53], were summarised and evaluated in this section, although they were recommended for conventional CFST members.

Table 5 summarizes the slenderness limits and material strength parameters as specified by current design codes [46-48]. Despite the slenderness limits of studied CFSST stub columns generally exceeding the limits, the objective of this investigation is to evaluate the potential for extending the applicability of these design criteria [51-53].

5.2. Evaluation of design criteria outlined in EN 1994-1-1 [51]

Eurocode EN 1994-1-1 [51] specifies a slenderness limit of $B/t \le 52\sqrt{\frac{235}{\sigma_{0.2}}}$ for the steel tube of CFST members. Exceeding this limit necessitates the consideration of local buckling, which can be addressed using either the Effective Thickness Method (ETM) [65] or the Continuous Strength Method (CSM) [66]. Table 5 presents the adjusted local slenderness limits for the CFST cross-section $B/t \le 52\sqrt{\frac{235}{\sigma_{0.2}}\frac{E}{210000}}$, which considered the distinct material properties of QN1803 and S30408 in comparison with carbon steel.

The axial capacity (N_{EC4}) of CFST square columns can be determined using Eq. (6). For those specimens that exceed the recommended slenderness limit, Eqs. (7) and (8) from EN 1993-1-4 [65] were employed to calculate the reduction factor (ρ_{EC}). This approach allows for the estimation of the ultimate bearing strength of CFST members featuring slender SS tubes.

$$N_{EC4} = \rho_{EC}A_s\sigma_{0.2} + A_cf_c' \tag{6}$$

$$\rho_{EC} = \frac{0.772}{\bar{\lambda}_p} - \frac{0.079}{\bar{\lambda}_p{}^2} \quad \text{but} \le 1.0 \tag{7}$$

$$\bar{\lambda}_p = \frac{\frac{\bar{b}}{t}}{28.4\varepsilon_{EC}\sqrt{k}} \tag{8}$$

Where $\bar{b}$ is the flat element width for webs and flanges of SHS, which can be taken as B - $3t$, k is the buckling factor, which was taken as 4.

Fig. 10 contrasts the axial strength obtained from the finite element findings ($N_{u,FE}$) with the predicted strength from EN 1994-1-1 [64]. The ratio $N_{u,FE}/N_{EC4}$ is plotted against the modified slenderness ratio of the steel tube $(B/t)/\varepsilon_{EC4}$, where ε_{EC4} is defined as $\sqrt{\frac{235}{\sigma_{0.2}}\frac{E}{210000}}$. The mean values and COV of $N_{u,FE}/N_{EC4}$ for CFST stub columns with QN1803 steel tubes are 1.20 and 0.106, respectively, as presented in Table 6. Both Table 6 and Fig. 10 illustrate that the EN 1994-1-1 [51] design criteria for CFST members yield conservative predictions when applied to stubs incorporating QN1803 or S30408 steel tubes.

5.3. Evaluation of design criteria outlined in AS/NZS 5100 [52]

AS/NZS 5100 [52] utilizes a method for estimating the ultimate bearing strength of CFST members that closely resembles the approach outlined in EN 1994-1-1 [51]. The only difference is the calculation method for estimating the specified slenderness limit. The slenderness limit for the steel tube of CFST members was calculated by $b/t \le 45\sqrt{\frac{250}{\sigma_{0.2}}\frac{E}{200000}}$, which also considers the difference in material properties of QN1803 and S30408.

The ultimate bearing strength of CFST stub column with SHS under axial loads (N_{AS}) is calculated by Eq. (9). Similarly, for those specimens that exceed the recommended slenderness limit, the reduction coefficient (ρ_{AS}) was determined using the following Eqs. (10)-(11).

$$N_{AS} = \rho_{AS}A_s\sigma_{0.2} + A_cf_c' \tag{9}$$

$$\rho_{AS} = \frac{1-\frac{0.22}{\lambda_{AS}}}{\lambda_{AS}} \quad \text{but} \le 1.0 \tag{10}$$

$$\lambda_{AS} = \frac{\frac{1.052b}{t}}{\sqrt{k}}\sqrt{\frac{F_n}{E}} \tag{11}$$

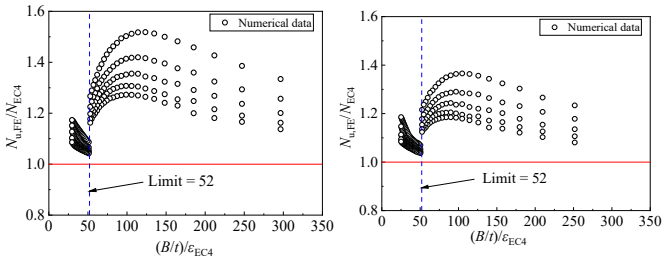

(a) QN1803 (b) S30408

Fig. 10 Evaluation of ultimate strengths obtained from parametric research with resistance predictions by EN 1994–1-1 [51]

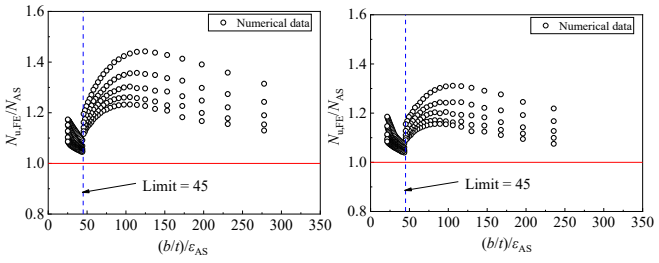

(a) QN1803 (b) S30408

Fig. 11 Evaluation of ultimate strengths obtained from parametric research with resistance predictions by AS/NZS 5100 [52]

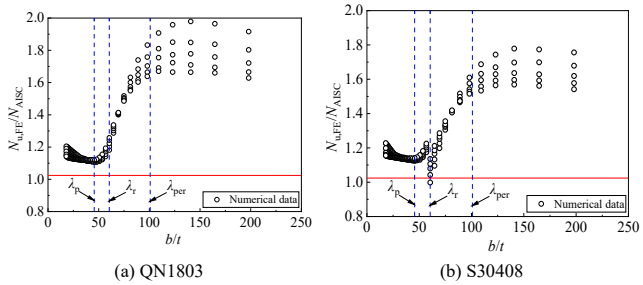

(a) QN1803 (b) S30408

Fig. 12 Evaluation of ultimate strengths obtained from parametric research with resistance predictions by ANSI/AISC 360-22 [53]

Table 3
Evaluation of the ultimate load from laboratory tests and FE studies

Source	Specimen ID	$N_{u,test}$ (kN)	$N_{u,FE}$ (kN)	$N_{u,test}/N_{u,FE}$
Dai et al. [54]	A-t8C50	6290	6084	1.03
	A-t10C50	7113	6888	1.03
	A-t12C50	7924	8016	0.99
	A-t8C70	6743	7215	0.93
	A-t10C70	7947	8320	0.96
	A-t12C70	8575	8939	0.96
	A-t8C80	7436	7774	0.96
	A-t10C80	8430	8971	0.94
	A-t12C80	9257	10000	0.93
Young and Ellobody [38]	SHS1C40	2768.1	2842	0.97
	SHS1C60	2972.0	3112	0.96
	SHS1C80	3019.9	3226	0.94
Lam and Gardner [39]	SHS100×100×2-C30	534	572	0.93
	SHS100×100×2-C60	687	752	0.91
	SHS100×100×2-C100	836	920	0.91
He et al. [40]	SHS100×100×3-C40	830	886	0.94
	SHS100×100×3-C60	1004	1066	0.94
	SHS100×100×3-C80	1162	1244	0.93
	SHS120×120×5-C40	1373	1454	0.94
	SHS120×120×5-C60	1566	1681	0.93
	SHS120×120×5-C80	1840	1910	0.96
Mean				0.95
COV				0.034

Table 4
Summary of key parameters adopted in the parametric research

Stainless steel type	D (mm)	L (mm)	t (mm)	f_c' (MPa)
QN1803, S30408	200	600	t = 1 mm to 10 mm, step 0.2 mm	23.7, 31.6, 39.5, 47.4, 55.3

Table 5
Scope of application based on cross-sectional dimensions and material strength in current design standards

Design codes	Maximum cross-sectional slenderness		f_y (MPa)	f_c' (MPa)
	Original limit	Normalized slenderness limit		
EN 1994-1-1 [51]	$\frac{B}{t} \le 52\sqrt{\frac{235}{f_y}}$	$\frac{B}{t} \le 52\sqrt{\frac{235}{\sigma_{0.2}}\frac{E}{210000}}$	235–460	20–50
AS/NZS 5100 [52]	$\frac{b}{t} \le 45\sqrt{\frac{250}{f_y}}$	$\frac{b}{t} \le 45\sqrt{\frac{250}{\sigma_{0.2}}\frac{E}{200000}}$	230–400	25–65
ANSI/AISC 360-22 [53]	$b/t \le 5\sqrt{\frac{E}{f_y}}$	$\frac{b}{t} \le 5\sqrt{\frac{E}{\sigma_{0.2}}}$	≤525	21–70

Table 6
Comparisons of ultimate loads obtained from parametric research with predictions from current codes

No. of data: 460		EN 1994-1-1 [51]	AS/NZS 5100 [52]	ANSI/AISC 360-22 [53]
		$N_{u,FE}/N_{EC4}$	$N_{u,FE}/N_{AS}$	$N_{u,FE}/N_{AISC}$
QN1803	Mean	1.20	1.18	1.26
	COV	0.106	0.085	0.184
S30408	Mean	1.14	1.13	1.23
	COV	0.072	0.056	0.138

Table 7
Comparisons of ultimate loads obtained from parametric research with predictions from current codes (with k =10.46)

No. of data: 460		EN 1994-1-1 [51]	AS/NZS 5100 [52]	Proposed modification based on EN 1994-1-1 [51]	Proposed modification based on AS/NZS 5100 [52]
		$N_{u,FE}/N_{EC4}$^	$N_{u,FE}/N_{AS}$^	$N_{u,FE}/N_{EC4}$*	$N_{u,FE}/N_{AS}$*
QN1803	Mean	1.12	1.11	1.01	1.01
	COV	0.065	0.053	0.064	0.058
S30408	Mean	1.09	1.08	1.01	1.00
	COV	0.042	0.036	0.050	0.044

Fig. 11 a comparative analysis between the ultimate load ($N_{u,FE}$) obtained from the parametric research and the ultimate load (N_{AS}) calculated by AS/NZS 5100 [52]. The ratio $N_{u,FE}/N_{AS}$ is plotted against the modified local slenderness ratio $(b/t)/\varepsilon_{AS}$. The mean values and COV of $N_{u,FE}/N_{AS}$ for CFST stub columns with QN1803 steel tubes are 1.18 and 0.085, respectively, as presented in Table 6. This indicates that the design criteria, as specified in AS/NZS 5100 [52] tend to underestimate the axial capacity of CFST members with QN1803 HSSS tubes.

5.4. Evaluation of design criteria outlined in ANSI/AISC 360-22 [53]

This study employs the design approach outlined in ANSI/AISC 360-22 [53] to assess the load-bearing capacity (N_{AISC}) of CFST short columns utilizing QN1803 and S30408 SS tubes. The ANSI/AISC 360-22 [53] design guidelines suggest categorizing concrete-filled short columns with carbon steel tubes into three classifications according to the b/t ratio of the steel tubes.

According to ANSI/AISC 360-22 [53], the cross-sectional strength (N_{AISC}) of the CFST specimens is calculated by Eq. (12). When a compact steel tube is used ((i.e. b/t falls below the limiting width-to-thickness ratio (λ_p), the tube can achieve its yield-bearing capacity (A_sf_y), with the concrete reaching a compressive strength of $0.85f_c'$. For non-compact steel tubes (i.e., b/t exceeds λ_p but does not exceed λ_r), the steel tube can still reach its yield-bearing capacity (A_sf_y), but the confinement induced on the concrete fill is diminished. In this scenario, the design utilized a compressive strength range for the confined concrete between $0.7f_c'$ and $0.85f_c'$. For slender steel tubes, where the b/t exceeds the critical value (λ_r) but remains below the maximum allowable ratio (λ_{per}), the steel tubes do not achieve their yield strength (A_sf_y). This results in diminished confinement for the concrete infill. Consequently, the design adopts a confined concrete compressive strength of $0.7f_c'$.

$$N_{AISC} = \begin{cases} A_s f_y + 0.85 A_c f_c' & \lambda \le \lambda_p \\ P_p - \frac{P_p - P_y}{(\lambda_r - \lambda_p)^2}(\lambda - \lambda_p)^2 & \lambda_p < \lambda \le \lambda_r \\ A_s f_{cr} + 0.7 A_c f_c' & \lambda_r < \lambda \le \lambda_{per} \end{cases} \quad (12)$$

In Eq. (12), the values of P_p and P_y are calculated using Eqs. (13) and (14) respectively. The critical buckling stress of the outer tube, denoted as f_{cr}, is derived using Eq. (15).

$$P_p = A_s\sigma_{0.2} + 0.85A_cf_c' \quad (13)$$

$$P_y = A_s\sigma_{0.2} + 0.7A_cf_c' \quad (14)$$

$$f_{cr} = \frac{9E_s}{\lambda^2} \quad (15)$$

Fig. 12 compares the ultimate load ($N_{u,FE}$) obtained through the parametric analysis with the corresponding NAISC values predicted using ANSI/AISC 360-22 [53]. The ratio $N_{u,FE}/N_{AISC}$ is plotted against the b/t of the steel tube. The mean values and coefficient of variation (COV) of $N_{u,FE}/N_{AISC}$ for the investigated specimens with QN1803 steel tubes are 1.26 and 0.184, respectively, as presented in Table 6. The comparison findings indicate that ANSI/AISC 360-22 [53] tends to underpredict the ultimate bearing strength of CFST members. The primary cause of this conservatism is the underestimation of the SS tube's strain-hardening effect. A similarly conservative trend is observed for stub columns with local slenderness exceeding λ_r, indicating that the slenderness limits set by ANSI/AISC 360-22 [53] may be overly restrictive, which should be evaluated carefully.

6. Proposed new calculation formulas

6.1. General

New calculation formulas were recommended by modifying the EN 1994-1-1 [51] and AS/NZS 5100 [52] in this section, and a correction factor η on the basis of k=10.67 was introduced, which considered the restraint effect of steel tubes on concrete and the strain hardening of SS. The formulas for the correction factor η were developed through regression analysis, utilizing data from 460 parametric studies. It should be noted that the buckling coefficient k given in EN 1994-1-1 [51] and AS/NZS 5100 [52] should be adjusted from 4 to 10.67 when determining the effective area of the steel tube. This adjustment is supported by a theoretical study by Bradford et al. [67], which indicated that k should be 10.67, approximately 2.67 times greater than the unfilled case, using the Rayleigh-Ritz method. This approach has also been adopted in previous studies on CFSST columns, such as Dai et al. [68,69], where k=10.67 was applied for calculating the local stability of stainless steel tubes. As presented in Figs. 13 and 14, the strength predictions (k = 10.67) calculated by EN 1994-1-1 [51] and AS/NZS 5100 [52] are compared with the parametric research findings. It could be found that the average ratios of $N_{u,FE}/N_{EC4}$ and $N_{u,FE}/N_{AS}$ are 1.12 and 1.11, respectively, indicating that the revised calculation formulas could provide more precise estimates for determining the ultimate bearing strength of CFSST members, when k is assumed to be 10.67.

The proposed correction factor η adopts a bilinear form, expressed as η = a + b $\rho\,\xi_o$, where ρ is the reduction factor accounting for local buckling and ξ_o is the confinement effect. For stainless steel tubes, the presence of strain hardening allows the steel to maintain significant post-yield strength, which may result in an actual contribution exceeding $\rho\,A_sf_y$, as assumed in conventional design formulations. This extended resistance not only increases the steel tube's direct axial contribution but also enhances its ability to provide continuous lateral confinement to the concrete core. Therefore, the constant term a reflects the amplified confinement effect attributed to the sustained strength of stainless steel beyond yielding, while the term b $\rho\,\xi_o$ captures the additional axial resistance arising from strain hardening and its interaction with local buckling. This formulation provides a physically informed enhancement to existing design provisions, particularly for CFST members incorporating high-strength stainless steel tubes. The detailed expressions and validation of η-based design formulas for both EN 1994-1-1 [51] and AS/NZS 5100 [52] are presented in the following sections.

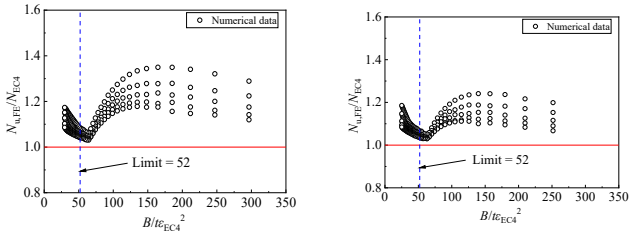

(a) QN1803 (b) S30408

Fig. 13 Evaluation of ultimate strengths obtained from parametric research with resistance predictions by EN 1994–1-1 [51] (with k = 10.67)

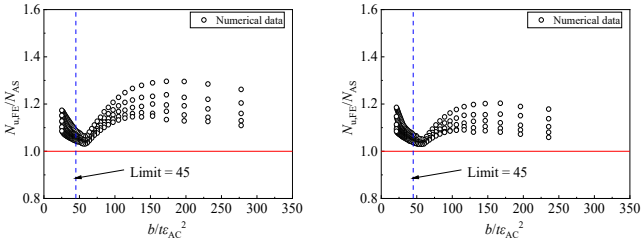

(a) QN1803 (b) S30408

Fig. 14 Evaluation of ultimate strengths obtained from parametric research with resistance predictions by AS/NZS 5100 [52] (with k = 10.67)

6.2. New calculation formulas based on modified EN 1994–1-1 [51]

In this investigation, new calculation formulas were recommended using the correction factor ηEC on the basis of modified EN 1994- [51]. The ultimate bearing strength of CFST square stub columns under axial loads (N_{EC4}^*) could be estimated by Eq. (16), and the correction factor (η_{EC}) could be calculated by Eqs. (17)-(18).

Table. 7 presents a comparison between the axial strength acquired from the parametric research and the strength predicted by modified EN 1994-1-1[51]. The mean ratios of the $N_{u,FE}$ to the predicted design strengths (N_{EC}^*) are 1.01 for both QN1803 and S30408. The associated coefficients of variation (COVs) are 0.064 for QN1803 and 0.050 for S30408. Fig.15 demonstrates that the newly recommended calculation formulas in this work offer more precise predictions for estimating the axial load-bearing capability of new CFSST members.

$$N_{EC4}^* = \eta_{EC} A_c f_c' \tag{16}$$

$$\eta_{EC} = \begin{cases} 1.12 + 1.11\rho_{EC}\xi_o & \text{for QN1803 CFST stub columns} \\ 1.04 + 1.14\rho_{EC}\xi_o & \text{for S30408 CFST stub columns} \end{cases} \tag{17}$$

$$\xi_o = \frac{A_s \sigma_{0.2}}{A_c f_c'} \tag{18}$$

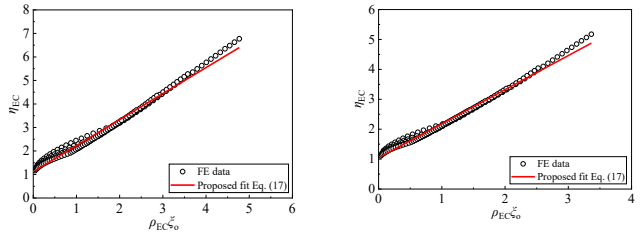

(a) QN1803 CFSST stub columns (b) S30408 CFSST stub columns

Fig. 15 Back calculated η_{EC} based on the ultimate load derived from parametric research varying with the $\rho_{EC}\xi_o$ and proposed algebraic characterizations

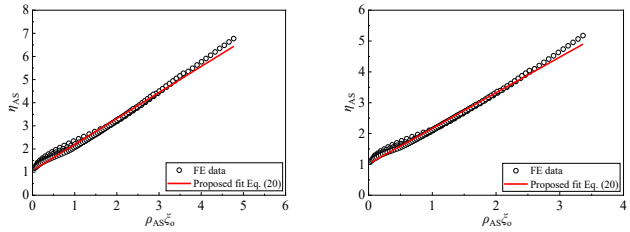

(a) QN1803 CFSST stub columns (b) S30408 CFSST stub columns

Fig. 16 Back calculated ηAC based on the ultimate load derived from parametric research varying with the ρACξo and proposed algebraic characterizations

6.3. New calculation formulas based on modified AS/NZS 5100 [52]

New calculation formulas were also recommended by modifying AS/NZS 5100 [52] in this investigation. Table 7 compares the axial strength from the parametric research ($N_{u,FE}$) with the strength predicted by the modified AS/NZS 5100 (N_{AS}^*), as indicated in Eqs. (19) and (20). The modified equations reveal average $N_{u,FE}/N_{AS}^*$ ratios of 1.01 and 1.00 for QN1803 and S30408, with associated coefficients of variation of 0.058 and 0.044. This demonstrates that the new calculation formulas recommended in this investigation could significantly enhance the precision of predictions for assessing the load-bearing capacity of CFSST members, as indicated in Fig. 16.

$$N_{AS}^* = \eta_{AS} A_c f_c' \tag{19}$$

$$\eta_{AS} = \begin{cases} 1.07 + 1.12\rho_{AS}\xi_o & \text{for QN1803 CFST stub columns} \\ 1.02 + 1.15\rho_{AS}\xi_o & \text{for S30408 CFST stub columns} \end{cases} \tag{20}$$

7. Conclusions

This study presents a thorough numerical analysis aimed at establishing new calculation formulas for CFST QN1803 SS square stub columns under axial loading. The key findings of this research are summarized as follows:

(1) A nonlinear finite element model was developed and validated against experimental data from various researchers. The validation process confirmed good consistency between the FE predictions and the experimental findings.

(2) Following the validation, an extensive parametric study involving 460 FE models was performed to analyze the axial loading response of CFST stub columns with QN1803 SS tubes. Key parameters investigated included variations in SS grades, steel tube wall thicknesses, and concrete strengths. The findings indicated that the ultimate bearing strength of CFST QN1803 stub columns increased by an average of 25.3% in comparison with S30408 members. Increasing the thickness of the steel tubes enhanced the ultimate bearing strength due to the larger cross-sectional area, which intensified the confinement on the internal concrete infill. Additionally, increasing the concrete strength boosted the ultimate bearing strength, although this reduced the confinement effect, leading to a drop in normalized load at higher strain levels.

(3) The ultimate bearing strength derived from the parametric research was compared to the design strength predicted by EN 1994–1-1 [51], AS/NZS 5100 [52] and ANSI/AISC 360-22 [53]. The comparison findings indicated that the existing design criteria tended to underestimate the ultimate strength of CFST stub columns with QN1803 tubes relative to the numerical results.

(4) This study recommends new calculation formulas for the compressive resistance by modifying the design equations in EN 1994-1-1 [51] and AS/NZS 5100 [53], and new parameters (η_{EC} and η_{AS}) were introduced in the new calculation methods for considering the strain hardening effects of steel tubes and the confinement effects of the SS tube on the infilled concrete. New calculation formulas recommended in this investigation demonstrated accurate and reliable predictions for the ultimate bearing strength of these new CFST members. The proposed axial strength formulations for CFSST stub columns also provide a theoretical basis for extending the design methodology to slender members or to CFST columns under combined loading conditions such as axial–bending or axial–torsional actions.

Acknowledgements

This work is supported by the Natural Science Foundation of Fujian Province, China (Grant No. 2022J01816)

References

[1] Li, G. C., Chen, B. W., Yang, Z. J., Ge, H. B., & Li, X. (2021). Axial behavior of high-strength concrete-filled high-strength square steel tubular stub columns. Adv Steel Constr, 17(2), 158-168.
[2] Wang, Y., Uy, B., Li, D., Thai, H. T., Mo, J., & Khan, M. (2023). Behaviour and design of coupled steel-concrete composite wall-frame structures. Journal of Constructional Steel Research, 208, 107984.
[3] Wang, Y., Khan, M., Uy, B., Katwal, U., Tao, Z., Thai, H. T., & Ngo, T. (2024, June). Long-term performance of steel-concrete composite wall panels under axial compression. In Structures (Vol. 64, p. 106606). Elsevier.
[4] Wang, Y., Khan, M., Li, D., Uy, B., Thai, H. T., & Ngo, T. (2023). A review on long-term behaviour of steel-concrete composite structures. Ce/papers, 6(3-4), 268-275.
[5] Feng, R., Wu, C., Chen, Z., Roy, K., Chen, B., & Lim, J. B. (2020). An experimental study on stainless steel hybrid tubular joints with square braces and circular chord. Thin-Walled Structures, 155, 106919.
[6] Feng, R., Tang, C., Roy, K., Chen, Z., Chen, B., & Lim, J. B. (2020). An experimental study on stress concentration factors of stainless steel hybrid tubular K-joints. Thin-Walled Structures, 157, 107064.
[7] Fang, Z., Roy, K., Padiyara, S., Chen, B., Raftery, G. M., & Lim, J. B. (2023, January). Web crippling design of cold-formed stainless steel channels under interior-two-flange loading condition using deep belief network. In Structures (Vol. 47, pp. 1967-1990). Elsevier.
[8] Feng, R., Tang, C., Chen, Z., Roy, K., Chen, B., & Lim, J. B. (2021). A numerical study and proposed design rules for stress concentration factors of stainless steel hybrid tubular K-joints. Engineering Structures, 233, 111916.
[9] Yan, J. B., Zhang, B., Feng, J. Y., Du, Y. S., Luo, Y. B., & Shi, Y. D. (2022). Low-temperature compression behaviour of circular stub stainless-steel tubular columns. Advanced Steel Construction, 18(3), 670-678.
[10] Fan, S. G., Ding, R. M., Han, Y. L., Chen, M. H., Liu, C. L., & Tao, Y. L. (2020). Experimental study on bearing capacity of austenitic stainless steel lipped channel columns. Advanced Steel Construction, 16(1), 65-76.
[11] Li, D., Uy, B., Aslani, F., & Hou, C. (2019). Behaviour and design of spiral-welded stainless steel tubes subjected to axial compression. Journal of Constructional Steel Research, 154, 67-83.
[12] Wang, Y., Chen, B., Wang, J., Luo, L., Li, B., Ye, Q., & Hai, L. (2025). Effect of web openings on the patch-loading resistance of QN 1803 high-strength stainless steel plate girders. Thin-Walled Structures, 113065.
[13] Wang, Y., Chen, B., Dai, P., Chen, Y., Zhang, Z., Lu, P., & Huang, C. (2025, August). Design recommendations for perforated S32001 high-strength stainless steel girders under concentrated loading. In Structures (Vol. 78, p. 109295). Elsevier.
[14] Wang, Y., Chen, B., Dai, P., Wang, Y., Song, Y., Jiang, K., & Hai, L. (2025). Experimental and numerical study on lateral-torsional buckling of welded QN1803 high-strength stainless steel I-girders. Thin-Walled Structures, 212, 113190.
[15] Chen, B., Wang, Y., Xing, Z., Lim, J. B., & Hai, L. (2024). Material properties and shear behaviour of QN1803 high-strength stainless steel plate girders. Engineering Structures, 301, 117209.
[16] Chen, B., Wang, Y., Xu, D., Yuan, H., & Yan, L. (2023). Finite element analysis and proposed design rules for 304D high-strength stainless steel I-shaped members in shear. Journal of Constructional Steel Research, 204, 107861.

[17] Chen, B., Dai, Y., Wang, Y., Wang, Y., Song, Y., Luo, L., & Hai, L. (2025). Patch-loading resistance of QN1803 and S32001 high-strength stainless steel plate girders: Experimental study and numerical simulation. Thin-Walled Structures, 206, 112681.
[18] Chen, B., Wang, Y., Wang, Y., Luo, L., Li, B., Lim, J. B., & Dai, Y. (2024). New design recommendations for QN1803 high-strength stainless-steel plate girders with web openings in shear. Journal of Constructional Steel Research, 221, 108907.
[19] Foshan Goldeco Stainless Steel Co. Ltd. Guangdong, China, 2022. https://www.goldecosteel.com/304d-stainless-steel.htm
[20] Song, Y., Li, J., & Chen, Y. (2019). Local and post-local buckling of normal/high strength steel sections with concrete infill. Thin-Walled Structures, 138, 155-169.
[21] Giakoumelis, G., & Lam, D. (2004). Axial capacity of circular concrete-filled tube columns. Journal of constructional steel research, 60(7), 1049-1068.
[22] Liew, J. R., & Xiong, D. X. (2012). Ultra-high strength concrete filled composite columns for multi-storey building construction. Advances in Structural Engineering, 15(9), 1487-1503.
[23] Uy, B. (1998). Local and post-local buckling of concrete filled steel welded box columns. Journal of constructional steel research, 47(1-2), 47-72.
[24] Uy, B. (2008). Stability and ductility of high performance steel sections with concrete infill. Journal of Constructional Steel Research, 64(7-8), 748-754.
[25] Han, L. H., Li, W., & Bjorhovde, R. (2014). Developments and advanced applications of concrete-filled steel tubular (CFST) structures: Members. Journal of constructional steel research, 100, 211-228.
[26] Han, L. H., Zhao, X. L., & Tao, Z. (2001). Tests and mechanics model for concrete-filled SHS stub columns, columns and beam-columns. Steel and Composite Structures, an International Journal, 1(1), 51-74.
[27] Han, L. H. (2002). Tests on stub columns of concrete-filled RHS sections. Journal of constructional steel research, 58(3), 353-372.
[28] Tao, Z., Song, T. Y., Uy, B., & Han, L. H. (2016). Bond behavior in concrete-filled steel tubes. Journal of Constructional Steel Research, 120, 81-93.
[29] Bradford, M. A., Loh, H. Y., & Uy, B. (2002). Slenderness limits for filled circular steel tubes. Journal of Constructional Steel Research, 58(2), 243-252.
[30] Teng, J. G., Wang, J. J., Lin, G., Zhang, J., & Feng, P. (2021). Compressive behavior of concrete-filled steel tubular columns with internal high-strength steel spiral confinement. Advances in Structural Engineering, 24(8), 1687-1708.
[31] Lam, D., Yang, J., & Dai, X. (2019, October). Finite element analysis of concrete filled lean duplex stainless steel columns. In Structures (Vol. 21, pp. 150-155). Elsevier.
[32] Dai, P., Yang, L., Wang, J., & Zhou, Y. (2020). Compressive strength of concrete-filled stainless steel tube stub columns. Engineering Structures, 205, 110106.
[33] Han, L. H., Xu, C. Y., & Tao, Z. (2019). Performance of concrete filled stainless steel tubular (CFSST) columns and joints: Summary of recent research. Journal of Constructional Steel Research, 152, 117-131.
[34] Uy, B., Tao, Z., & Han, L. H. (2011). Behaviour of short and slender concrete-filled stainless steel tubular columns. Journal of Constructional Steel Research, 67(3), 360-378.
[35] Ellobody, E. (2007). Nonlinear behavior of concrete-filled stainless steel stiffened slender tube columns. Thin-Walled Structures, 45(3), 259-273.
[36] Hassanein, M. F. (2010). Numerical modelling of concrete-filled lean duplex slender stainless steel tubular stub columns. Journal of constructional steel research, 66(8-9), 1057-1068.
[37] Roufegarinejad, A., Uy, B., Bradford, M. A., Deeks, A. J., & Hao, H. (2005). Behaviour and design of concrete filled steel columns utilising stainless steel cross sections under combined actions. In Developments in Mechanics of Structures and Materials: Proceedings of the 18th Australasian Conference on the Mechanics of Structures and Materials, Perth, Australia, 1-3 December 2004.
[38] Young, B., & Ellobody, E. (2006). Experimental investigation of concrete-filled cold-formed high strength stainless steel tube columns. Journal of Constructional Steel Research, 62(5), 484-492.
[39] Lam, D., & Gardner, L. (2008). Structural design of stainless steel concrete filled columns. Journal of Constructional Steel Research, 64(11), 1275-1282.
[40] He, A., Wang, F., & Zhao, O. (2019). Experimental and numerical studies of concrete-filled high-chromium stainless steel tube (CFHSST) stub columns. Thin-Walled Structures, 144, 106273.
[41] Tao, Z., Uy, B., Liao, F. Y., & Han, L. H. (2011). Nonlinear analysis of concrete-filled square stainless steel stub columns under axial compression. Journal of Constructional Steel Research, 67(11), 1719-1732.
[42] Azad, S. K., Li, D., & Uy, B. (2020). Axial slenderness limits for duplex and lean duplex stainless steel-concrete composite columns. Journal of Constructional Steel Research, 172, 106175.
[43] Azad, S. K., Li, D., & Uy, B. (2020). Axial slenderness limits for austenitic stainless steel-concrete composite columns. Journal of Constructional Steel Research, 166, 105856.
[44] Azad, S. K., Li, D., & Uy, B. (2021). Compact and slender box concrete-filled stainless steel tubes under compression, bending, and combined loading. Journal of Constructional Steel Research, 184, 106813.
[45] Buchanan, C., & Gardner, L. (2019). Metal 3D printing in construction: A review of methods, research, applications, opportunities and challenges. Engineering Structures, 180, 332-348.
[46] Huang, Y., Yang, L., Liu, M., & Xu, K. (2025). Numerical study and design of WAAM stainless steel SHS stub columns under axial compression. Journal of Constructional Steel Research, 227, 109419.
[47] Huang, Y., Yang, L., & Xin, Q. (2023). Novel geometrical model and design mechanical parameters for CMT-WAAM stainless steel. Journal of Constructional Steel Research, 210, 108071.
[48] Ban, H., Zeng, Z., Zhang, L., Wang, F., Yun, X., & Dai, P. (2025). Numerical analysis and design of concrete-filled double skin CHS with 316L+ Q355 stainless-clad bimetallic steel outer tubes under axial compression. Engineering Structures, 329, 119796.
[49] Chen, B., Wang, Y., Xing, Z., Lim, J. B., & Hai, L. (2024). Material properties and shear behaviour of QN1803 high-strength stainless steel plate girders. Engineering Structures, 301, 117209.
[50] Chen, B., Wang, Y., Xu, D., Yuan, H., & Yan, L. (2023). Finite element analysis and proposed design rules for 304D high-strength stainless steel I-shaped members in shear. Journal of Constructional Steel Research, 204, 107861.
[51] EN 1994–1-1:2004. Eurocode 4: Design of composite steel and concrete structures - Part 1-1: General rules and rules for building. European Committee for Standardization, Brussels;2004.
[52] AS/NZS 5100.6:2017. Bridge design, Part 6: steel and composite construction, Australian/New Zealand Standards, Sydney, Australia; 2017.
[53] ANSI/AISC 360-22. Specification for structural steel buildings. American Institute of Steel Construction (AISC), Chicago;2022.
[54] Dai, P., Yang, L., Wang, J., Ning, K., & Gang, Y. (2022). Compressive behavior of concrete-filled square stainless steel tube stub columns. Steel and Composite Structures, 42(1), 91-106.
[55] ISO 6892-1: 2009. Metallic Materials − Tensile Testing − Part 1: Method of Test at Room Temperature. International Organization for Standardization, Geneva, Switzerland, 2009.
[56] ABAQUS. Analysis user's manuals and example problems manuals, version 2021 Providence, Rhode Island: Abaqus Inc.; 2021.
[57] Wang, Y., Khan, M., Uy, B., Lim, L., Thai, H. T., & Ngo, T. (2025). Behaviour, design and performance of steel-concrete composite walls in fire. Journal of Constructional Steel Research, 227, 109408.
[58] Mo, J., Uy, B., Li, D., Thai, H. T., & Wang, Y. (2022). Behaviour and design of composite walls under axial compression. Journal of Constructional Steel Research, 199, 107635.
[59] Mo, J., Uy, B., Li, D., Thai, H. T., & Wang, Y. (2023). Behaviour and design of composite walls under lateral loading and combined loading. Journal of Constructional Steel Research, 210, 108087.
[60] Li, D., Uy, B., Mo, J., Wang, Y., & Thai, H. T. (2023). Behaviour and design of steel and composite beam connections to composite walls. Journal of Constructional Steel Research, 206, 107915.
[61] Zhu, L., Jiang, Y., Liu, Z., Wang, Y., Wang, W., & Chen, B. (2024, July). Web crippling behaviour of high-strength aluminium alloy channel-shaped members with strengthened web holes: Numerical study and new design rules. In Structures (Vol. 65, p. 106690). Elsevier.
[62] Tahmasebinia, F., Wang, Y., Wu, S., Ho, J., Shen, W., Ma, H., ... & Marroquin, F. A. (2021). Advanced structural analysis of innovative steel–glass structures with respect to the architectural design. Buildings, 11(5), 208.
[63] Gao, L., Wang, Y., Wang, J., Yuan, J., Chen, B., & Bai, L. (2025). Experimental and numerical investigation on global-stability of welded BS700 high-strength steel beams. Journal of Constructional Steel Research, 227, 109373.
[64] EN 1992-1-1, Eurocode 2, Design of Concrete Structures – Part 1-1: General Rules and Rules for Buildings, CEN, Brussels, 2004.
[65] EN 1993-1-4: 2006+A1: 2015. Eurocode 3: Design of Steel Structures - Part 1–4: General Rules- Supplementary Rules for Stainless Steels. European Committee for Standardization (CEN), Brussels;2015.
[66] Gardner, L., Yun, X., & Walport, F. (2023). The continuous strength method–review and outlook. Engineering Structures, 275, 114924.
[67] Bradford, M. A., Wright, H. D., & Uy, B. (1998). Local buckling of the steel skin in lightweight composites induced by creep and shrinkage. Advances in Structural Engineering, 2(1), 25-34.
[68] Dai, P., Yang, L., Yun, X., Wang, F., & Zhang, L. (2024). Experimental study of concrete-filled stainless steel tubular stub columns with circular and square cross-sections subjected to combined compression and bending. Engineering Structures, 305, 117773.
[69] Dai, P., Yang, L., Zhang, L., & Ban, H. (2025, August). Structural behaviour and design of concrete-filled stainless steel tubular stub columns with circular and square cross-sections subjected to combined compression and bending. In Structures (Vol. 78, p. 109162). Elsevier.

Advanced Steel Construction – Vol. 21 No. 4 (2025) 336–345
DOI: 10.18057/IJASC.2025.21.4.6

NUMERICAL SIMULATION OF THE STAINLESS STEEL RHS MEMBER UNDER CYCLIC LOADING, IDENTIFICATION OF MATERIAL MODEL PARAMETERS, AND COMPARISON WITH HSS STEELS

Tomáš Dvořák *, Petr Hradil and Jiří Kala

Institute of Structural Mechanics, Faculty of Civil Engineering, Brno University of Technology, Czech Republic
** (Corresponding author: E-mail: Tomas.Dvorak11@vut.cz)*

ABSTRACT

This study examined the cyclic behavior of stainless steel through a combination of experimental tests and numerical simulations. The study began with a comprehensive analysis of material properties and experimental configurations, which provided a solid foundation for developing a robust finite element (FE) model.
A new simplified material model inspired by Ramberg-Osgood was developed for easy use in practical tasks. For example, the ANSYS software only offers the original Ramberg-Osgood model for monotonic loading and Chaboche model is not as easy to calibrate as the Ramberg-Osgood model which is defined by parameters which can be easily retrieved from coupon tests. The combination of the validation against experimental data and material model parameters identification using sensitivity analysis and mathematical metamodel confirmed that the model accurately reflects the material's performance under cyclic loading conditions.
Further comparisons with high strength steels (HSS) underscore the superior performance of stainless steel when subjected to cyclic loading. These findings underscore the advantages of stainless steel in structural applications requiring high ductility, strain hardening, and resistance to cyclic loading.
In conclusion, this research validates the effectiveness of the simplified material model and underlines the increasing use of stainless steel in contemporary structural engineering. Its distinct properties make it a valuable material, especially in many times repeated loading, where performance under cyclic loading is critical.

ARTICLE HISTORY

Received: 21 January 2025
Revised: 25 June 2025
Accepted: 26 June 2025

KEYWORDS

Stainless steel;
High strength steel;
Cyclic loading;
Ductility;
Parameter identification;
Metamodel of Optimal Prognosis

1. Introduction

Carbon steel has been historically the most prevalent material used in civil engineering constructions. In recent decades, stainless steel has been increasingly employed in certain industries due to its much improved chemical and biological resistance, strength, and favorable mechanical features. Above all, stainless steel high ductility, strain hardening, and fire resistance all possess distinct benefits compared to common carbon steel. Consequently, stainless steel is becoming more and more a fitting construction material for such tasks as seismic engineering. [1], [2], [3]. In [4], Chen et al. performed a series of experiments and numerical simulations to verify the applicability of prEN 1993-1-4(EC3) [5] code relations for dynamically loaded stainless steel H cross-sections. As expected, the standard provides conservative values, while the methodology modified by the authors got on the dangerous side under certain circumstances.

While the monotonic loading behavior of stainless steel is well-documented, the investigation into its response under cyclic loading conditions is relatively recent but rapidly expanding [3], [6]. Research efforts have been directed toward understanding the performance of stainless steel grades (e.g., austenitic, duplex) under both axial [7] and bending [8] cyclic loads. Numerous experimental studies have been conducted on both material coupons and full-scale structural members to characterize their cyclic response. These experimental studies have been extensively complemented by numerical simulations utilizing the finite element (FE) method, which incorporates appropriate advanced material models (e.g., Chaboche, Armstrong-Frederick, two-surface plasticity models) to accurately predict behavior under complex cyclic loading conditions [9], [10].

Luo et al. in [11] conducted a series of experiments at medium and high levels of plastic stress on elements including the weld and the heat-affected region. Based on the results, they calibrated the Chaboche model. The authors stated that its accuracy is strongly influenced by the correspondence of the loading and simulated levels of plastic strain. The authors [12] approach the problem in a similar way, extending the study to a wide range of steel grades. On the contrary, the study [13] is very closely devoted to a detailed description of the differences in the response to cyclic loading based on the change in the chemical composition of stainless steels. By reducing the nickel content, the new QN1803 stainless steel has greater strength at a lower cost than the widely used S30408 stainless steels. The study notes a significantly better response to the cyclic loading of both stainless steels than conventional steels of comparable strength classes.

In [14], improved Voce-Chaboche constitutive relations are described. The added combination of isotropic and kinematic hardening schemes can better describe the transition to the first plastic cycle.

The authors [15] also deal with the Chaboche model with a combined hardening surface. The authors describe a simplified procedure for calibrating the parameters. Using 171 response experimental curves, they designed a four-stage statistically based prediction method that should be able to replace classical calibration.

The thesis [16] deals with the revision of the Chaboche model. A viscous parameter is added, which is ignored in the classical model in order to better describe the variable plastic modulus in stress-controlled cycling and the continuously increasing strain in stress-controlled cycling. By adding parameters, it is possible to better describe the response, but at the cost of difficulty obtaining the supplied input parameters by means of non-standard tests. Parameters are also added in [17]. The described model does not consider some parameters, simplifies others – it introduces a linear relationship between the coefficient and the effective/equivalent stress.

In [18], Kaleva et al. perform an extensive comparison of the Ottosen-Stenström-Ristinmaa and Lemaitre-Chaboche models for application to the high-cycle fatigue model. They confirm that some parameters cannot be identified directly experimentally. Based on their observations, a high agreement in the response of both models was found.

A lot of attention is paid to the effort to streamline the finding of input parameters of material models. In [19], the method of modification of the cyclic experimental loading is used. Authors [20] and [21] follow the path of optimization and subsequent training of genetic algorithms that should generate input parameters of the material models.

Though these advancements have been achieved, uses of sophisticated material models in commercial FE softwares to continue to present difficulties for practical engineering use because they are too complex, expensive to calculate, and difficult to calibrate material model parameters. There is a fundamental need for material models that are sufficiently accurate but not too computationally expensive and simple to apply and used by engineers for design and analysis.

This research complements this gap by examining the use of a newly developed simplified material model specifically for use in engineering, designed to accurately model the response of cyclic loading on stainless-steel members. A compromise between accuracy and simplicity, which is typically not available in any current commercial analysis packages for cyclic loading analysis, the model is derived from the popular Ramberg-Osgood formulation. The outcomes thus obtained via this reduced material model are then precisely compared with comparative experimental loading test, thus providing validation.

The methodology begins with the creation of a numeric FE model, experimentally validated with the help of loading test [22]. For reliability

verification of the proposed material model, the numeric model is investigated through a serious sensitivity analysis. In the sensitivity analysis, the impact of the input parameters of the newly proposed material model on the overall numeric simulation response is investigated. These most sensitive parameters are then optimized to generate the best possible agreement between the experimental results and the model predictions.

Finally, to also highlight the actual benefits of stainless steel in safety-critical application, a comparison study is done. Numerical calculations with the simplified material model of stainless steel are compared with those of high strength steels (HSS), specifically in the case of cyclic loading cantilever beams. The distinguishing cyclic performance and structural response characteristics of these two materials are identified, noting the superior capacity of stainless steel to resist repeated loading. This contrast also indicates the increasing utility of stainless steel as a preferred material for structural applications involving high ductility, significant strain hardening, and improved resistance to cyclic loading and fatigue.

2. Experiment

The experiment was conducted at the University of Studi. A study of nine cold-formed rectangular stainless-steel members subjected to cyclic loading was carried out [22]. For purposes of this article, one test configuration was selected. The Cantilever beam is made from EN 1.4301 austenitic stainless steel, cold formed cross-section 120×80×6 mm with a total length of 1730 mm and effective length of 1650 mm, see Fig. 2 (a).

2.1. Material properties

The mechanical properties of the material were further determined by experiments carried out at the Universitat Politècnica de Catalunya [23]. A series of tensile coupon tests were carried out on both the flat and the corner parts of the cross-sections to take into account the increased tensile strength of the corner parts due to the cold forming process. Obtained material parameters and stress-strain curves are shown in Table 1 and Fig. 1. E is the Young's modulus, $\sigma_{0.2}$ is the strength at the strain 0.2%, σ_u is the ultimate strength, ε_u is the strain at ultimate strentgh, n is strain hardening parameter, and m is second strain hardening parameter.

Table 1
Material parameters [23]

Parameter	Unit	Flat part	Corner part
E	MPa	185 778	185 360
$\sigma_{0.2}$	MPa	479	635
σ_u	MPa	679	840
ε_u	m/m	0.39	0.34
n	-	7.05	5.40
m	-	2.55	7.89

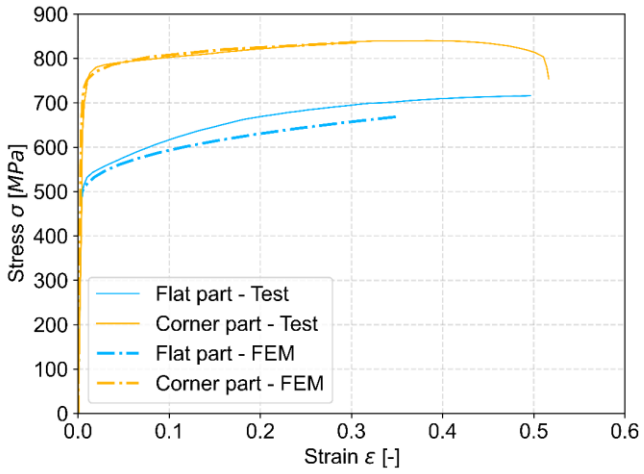

Fig. 1 Stress-strain diagram for flat and corner cupons (solid lines) and for the material model (dash dot)

2.2. Test configuration

The test configuration is shown in Fig. 2 (a). The beam was subjected to cyclic loading for testing bending around the major axis. The bottom end of the beam was embedded to the floor and the top end was loaded by a hydraulic actuator. The actuator is hinged on both sides to prevent bending moments and vertical forces. The bottom end was made from flange and stiffeners, which were welded to the beam. The flange is fixed to the ground by four bolts. Loading protocol is shown in Fig. 2 (b). The record of the load test is shown in Fig. 2 (c), where u is the displacement of the top of the beam where the actuator is hinged, and the force reaction is the force in the actuator.

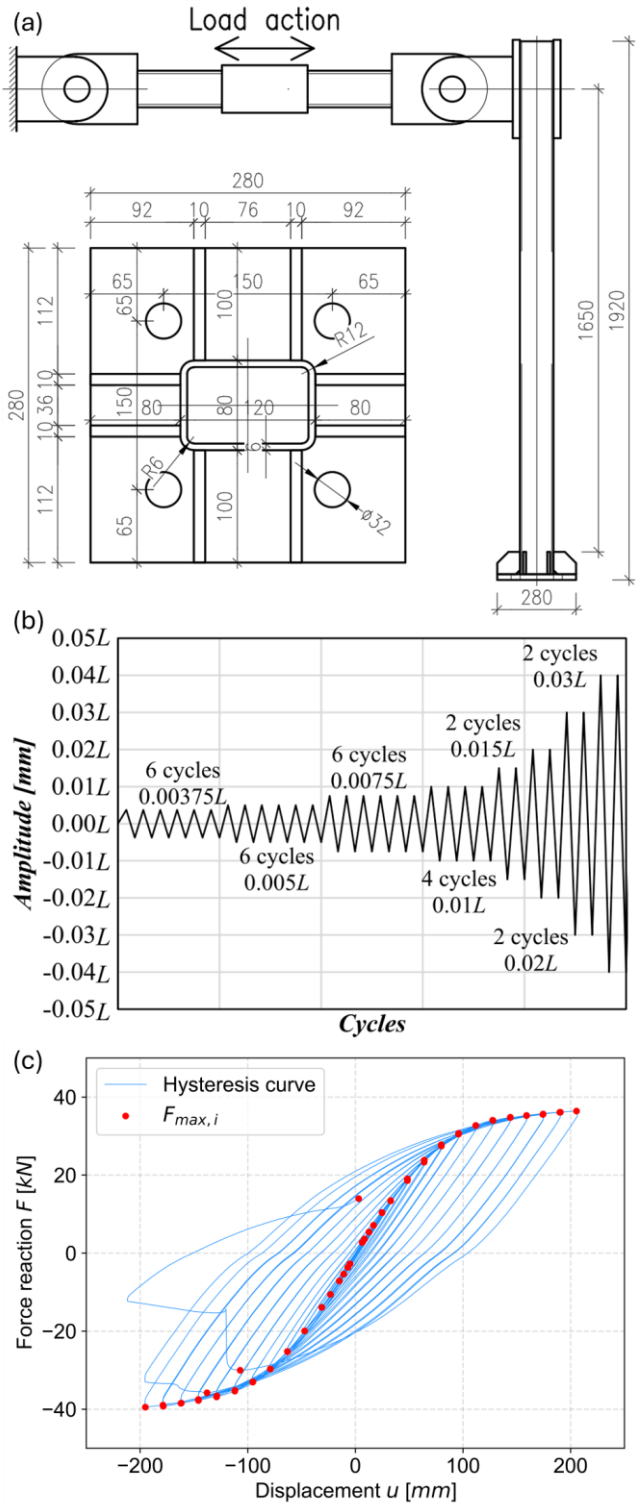

Fig. 2 (a) Experiment (loading test) configuration, (b) Loading protocol [4] and (c) Record of the load test – Hysteresis curve

3. Numerical model

The Finite Element method was used for the numerical simulation of the loading test. To solve the static response, a 3D FE shell model was constructed with a nonlinear elastoplastic material model with kinematic hardening, which properly simulates the Bauschinger effect while cyclic loading [6], [7]. Detailed information about the material model and FE model is described in the subchapters below.

3.1. Material model

The nonlinear elastoplastic material model with kinematic hardening was used to describe the material behavior under cyclic loading. The material model is based on Nadai and Ramberg-Osgood theory [24]. This theory was many times modified e.g. [25]. For current work was used the material model defined by equations (1-5) with linear elastic branch and nonlinear plastic branch with linear unloading branch. Stress-strain diagram is shown in Fig. 3.

$$\varepsilon = \varepsilon_{el} + \varepsilon_{pl} \tag{1}$$

$$\varepsilon_{el} = \frac{\sigma}{E} \tag{2}$$

$$\varepsilon_{pl} = \frac{\sigma-\sigma_y}{E_y} + \varepsilon_u \left(\frac{\sigma-\sigma_y}{\sigma_u-\sigma_y}\right)^m, \quad \sigma > \sigma_y \tag{3}$$

$$\varepsilon = \begin{cases} \frac{\sigma}{E}, & \sigma \le \sigma_y \\ \frac{\sigma}{E} + \frac{\sigma-\sigma_y}{E_y} + \varepsilon_u \left(\frac{\sigma-\sigma_y}{\sigma_u-\sigma_y}\right)^m, & \sigma > \sigma_y \end{cases} \tag{4}$$

$$E_y = \frac{E}{1+0.002n\frac{E}{\sigma_y}} \tag{5}$$

Where ε is total strain, ε_{el} is elastic strain, ε_{pl} plastic strain, σ actual stress, σ_y yield strength, σ_u ultimate strength, n strain hardening parameter, m second strain hardening parameter and E_y is a tangent modulus of the stress strain curve at the yield strength.

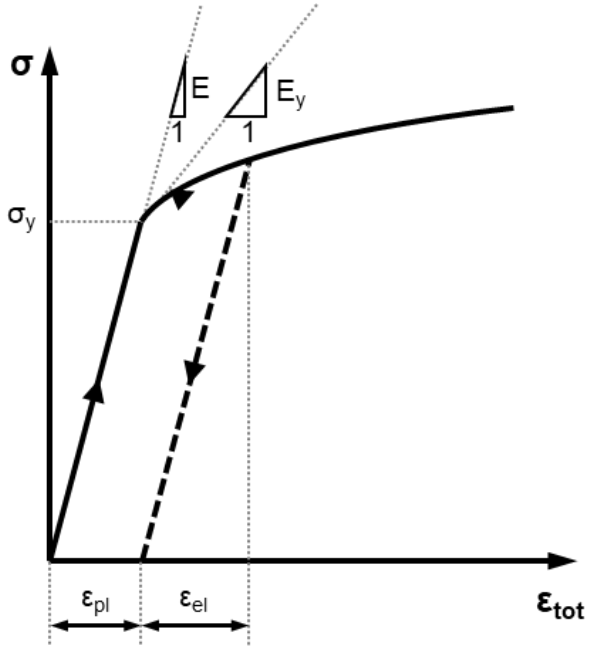

Fig. 3 Nonlinear elastoplastic stress-strain diagram of the simplified material model

Input of the stress-strain relationship is carried out using the true stress. The relationships between the engineering stresses obtained from the experiment and the true stresses used in numerical simulations are shown in the equations (6-7).

$$\sigma_{TRUE} = \sigma_{ENG}(1+\varepsilon) \tag{6}$$

$$\varepsilon_{TRUE} = \ln(1+\varepsilon) \tag{7}$$

The use of a linear elastic branch is a simplification in compared to [24] and the stress-strain relationship specified in EN 1993-1-4, which consider a nonlinear elastic branch and the plastic strains formation at stresses under proof stress. The stress-strain relationship according to Annex C of EN 1993-1-4 and prEN 1993-1-14 [26] is defined by equations (5, 8-11), this stress strain diagram was also used by [27] in case of stainless steel CHS members.

$$\varepsilon = \begin{cases} \frac{\sigma}{E} + 0.002\left(\frac{\sigma}{f_y}\right)^n, & \sigma \le f_y \\ 0.002 + \frac{f_y}{E} + \frac{\sigma-f_y}{E_y} + \varepsilon_u\left(\frac{\sigma-f_y}{f_u-f_y}\right)^m, & \sigma > f_y \end{cases} \tag{8}$$

$$n = \frac{\ln(20)}{\ln\left(\frac{f_y}{R_{p0.01}}\right)} \tag{9}$$

$$\varepsilon_u = 1 - \frac{f_y}{f_u} \tag{10}$$

$$m = 1 + 3.5\frac{f_y}{f_u} \tag{11}$$

Where ε is total strain, σ actual stress, f_y yield strength, f_u ultimate strength, ε_u strain at ultimate strength, n strain hardening parameter, m second strain hardening and $R_{p0.01}$ is stress at plastic strain 0.01%.

Simplification has been used for ease of use in practical problems, both in specifying the material model and in evaluating stresses and clearly identifying elastic and plastic deformations.

3.2. Numerical FE model

The FE model was modelling using linear shell elements with six degrees of freedom at each node. The SHELL181 element type is suitable for thin shell structures, large strain nonlinear applications, and change in shell thickness. Element formulation is based on logarithmic strain and true stress measures. [12]

The finite element mesh is mostly composed of 4-node finite elements and combination of 4-node and 3-node elements in the regions of mesh refinement. The spatial regions are formed by a mapped mesh of 4-node elements. In the region of high stress gradient, the finite element mesh is condensed to a finite element size of 5 mm. Above this part, the transition region consists of a combination of 4-node and 3-node elements. The remainder of the beam is made up of a mapped mesh of element size 20 mm. The finite element mesh of the stiffeners and flanges is made up of a free mesh of sizes in the approximate range of 5-25 mm.

The model was supported at nodes in the center of the holes in the flange. The bolts were replaced by boundary conditions that constrain the node displacement in all directions with free rotational degrees of freedom. These nodes were coupled to the holes edge by contact pair elements CONTA177 + TARGET170 using the MPC (Multi-point constraint) algorithm. [12]

The displacement of the top of the beam is realized by a node at the end position of the actuator. This node is also coupled to the beam by the contact pair elements CONTA174 + TARGET170 using the MPC algorithm. The boundary condition of this node is only a constrained (prescribed) displacement in the loading direction (x direction – about the major axis of the cross-section), other degrees of freedom are free.

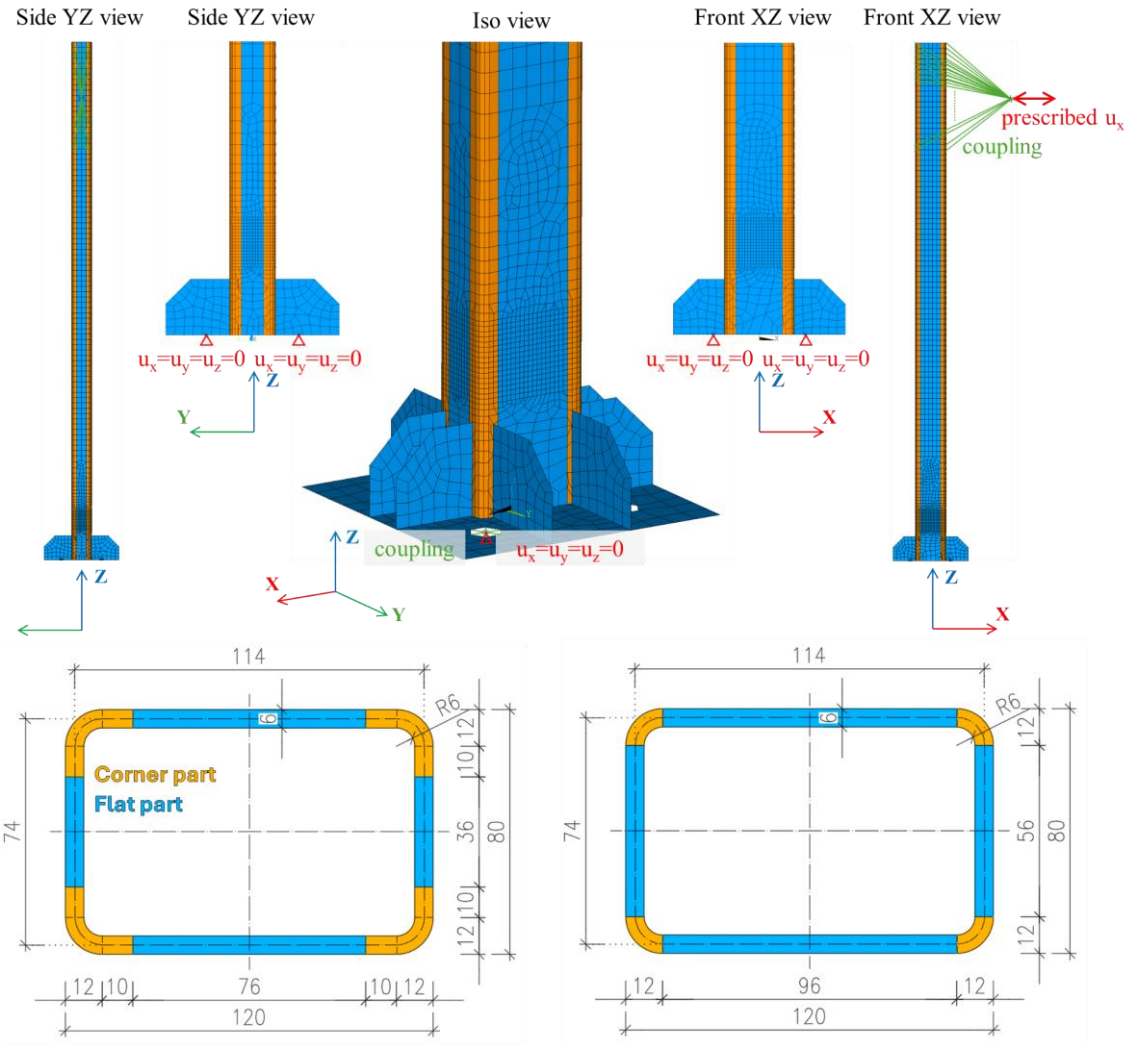

Fig. 4 FE mesh, boundary conditions, material model assignment and cross-section with and without corner area extension

The material model assignment to the finite elements is shown in Fig. 4. The material model for the corner part is assigned to the extended corner part of the section according to the cold forming process of the RHS section manufacture. The distance of the extension is chosen according to previous research. Values of the extension range from the thickness t up to 2t [25], for this work was used extension of $0.5\pi r_i$ [28], where ri is the inner radius. The extension of 10 mm is shown in Fig. 4.

The initial material model input parameters were retrieved by fitting the stress-strain diagrams from coupon tests [23]. The initial material model input parameters are given in Table 1 and the fitted stress-strain diagrams are plotted and compared with measured stress-strain curves in Fig. 1.

The numerical model was subjected to a sensitivity study of model to verify the model and check various influences on the results. In the study, the influence of support stiffness (rigid/deformable), finite element mesh size (2 times finer), corner extension (see Fig. 4), finite element integration method (full/reduced) and finite element type (linear/quadratic) were investigated.

This verification was carried out for the monotonic loading test. An overview of the test study is given in Table 2. A comparison of the results is shown in Fig. 5. From the load-displacement curves it can be seen that the stiffness of the support, the mesh element size, the integration method and the element type have an insignificant effect. The effect of the corner extension will be investigated further in subsequent chapters by optimizing the material parameters.

Table 2
Optimized values of the material model parameters.

Model	Supports	Mesh	Corners	FE integration	Element type
00 – Reference	*Rigid*	*Ref.*	*No extended*	*Full*	*Linear (SHELL181)*
01 – Support stiffness	***Deformable***	*Ref.*	*No extended*	*Full*	*Linear (SHELL181)*
02 – Mesh size	*Rigid*	***Finer***	*Ne extended*	*Full*	*Linear (SHELL181)*
03 – Corner extension	*Rigid*	*Ref.*	***Extended***	*Full*	*Linear (SHELL181)*
04 – Integration method	*Rigid*	*Ref.*	*No extended*	***Reduced***	*Linear (SHELL181)*
05 – Element type	*Rigid*	*Ref.*	*No extended*	*Full*	***Quadratic (SHELL281)***

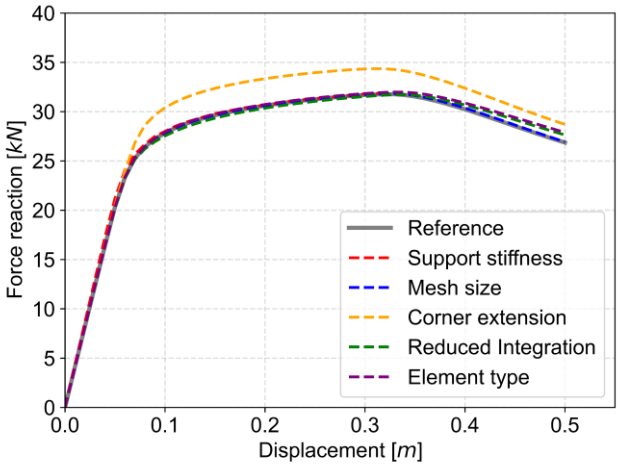

Fig. 5 Load-displacement curves of the influence study

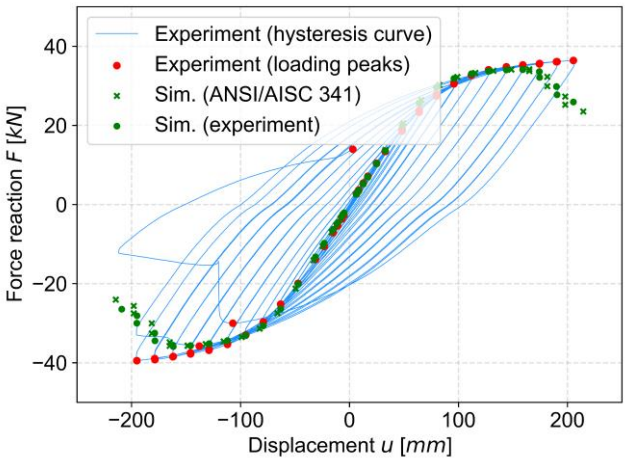

Fig. 6 Comparison of the load steps

3.3. Numerical simulation and results

The numerical simulations were controlled by the prescribed displacement of the node replacing the actuator, see Fig. 2 (a) and Fig. 4.

The beam was cyclically loaded according to ANSI/AISC 341 [14] in relation to the experimental load test [4], where the prescribed displacements weren't exactly achieved. The record of the experimental loading test is shown in Fig. 6 with a comparison of the load stepping according to ANSI/AISC 341. In the simulation test, the beam was loaded for a total of 96 cycles.

The calculation was carried out for two variants. One variant without extended corners and one variant with extended corners, see Fig. 4. The input material model parameters were used as described in Table 1. The results of these two numerical simulations are shown using load-displacement hysteresis curves in Fig. 7 (a, b). The hysteresis curve is the record of the displacement and force at the node, which replaces the actuator in the numerical simulation. For a clearer view, the results are also shown using the peak values where the load changes the direction, see Fig. 7 (c, d). From the result can be seen, that a better response is obtained using the FE model with an extended corner part. This model was further used for sensitivity analysis and optimization of material model input parameters to achieve a more accurate response to cyclic loading.

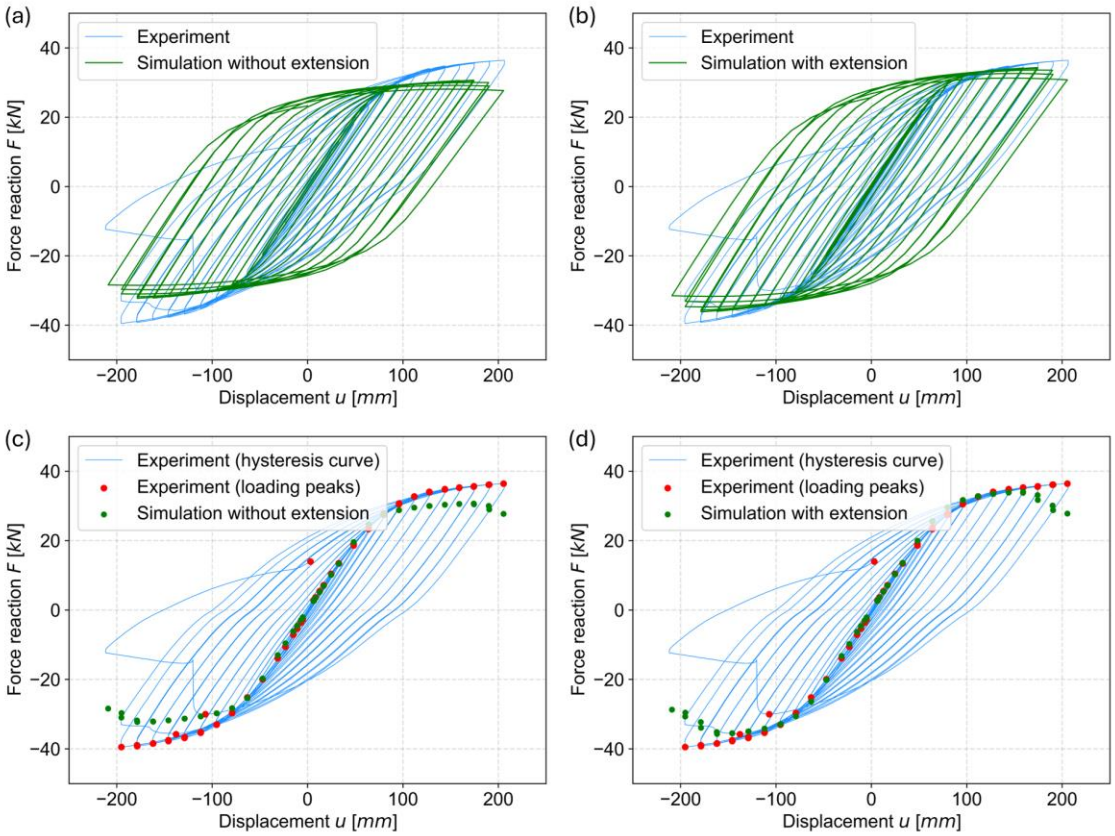

Fig. 7 Load-displacement hysteresis curves with original material model parameters (a), (c) for model without cross-section corner extension and (b), (d) for model with cross-section corner extension

4. Sensitivity analysis and optimization of the material model parameters

Optimization was carried out to achieve a more accurate response from the numerical model. The optimization was performed for the input parameters of the material model.

To save computational time, the optimization was performed using a surrogate mathematical metamodel – MOP (Metamodel of Optimal Prognosis) that was constructed using approximations of the responses of the set of numerical simulations [29]. The mathematical model approximates and replaces the numerical model for pre-selected responses that it can be predicted based on

the input parameters.

4.1. Mathematical metamodel and sensitivity analysis

The mathematical metamodel was created by combining several approximation models for individual responses. Possible approximation models were Linear Regression, Moving Least Squares, and Isotropic Kriging [30]. The choice of the approximation model depended on the value of the *CoP* (Coefficient of optimal prognosis), which quantifies the quality of the approximation by the equation (12) as follow:

$$CoP = 1 - \frac{SS_E^{Prediction}}{SS_T} \tag{12}$$

where SSEPrediction is the sum of the squared prediction errors and SST is equivalent to the total variation. The value of this coefficient ranges from 0 to 1.0, with 1.0 representing a perfect approximation. A further description can be found in [30].

The metamodel contains 12 input parameters, which are the input parameters of the material model for the flat and corner parts of the cross-section. The input parameters are given in Table 3 with the initial values and upper and lower bounds. The responses of the metamodel were the load forces at the end of the selected load steps during the numerical simulation of the load test.

To create the metamodel, 150 numerical simulations of the load test were performed at first step. The input parameters of these simulations were generated using Advanced Latin Hypercube Sampling. At the second step, the AMOP (Adaptive Metamodel of Optimal Prognosis) was performed to achieve higher values of the CoP. There were made 650 simulations at all to create the MOP.

An overview of the MOP is provided by the CoP matrix shown in Fig. 9 (a, b), where the *CoP* values of each response approximation are shown in the right column. The remaining columns show the sensitivities of the input parameters to each response. A clearer representation of some selected responses and sensitivities is shown in Fig. 9 (c–h). The CoP matrix clearly shows the high sensitivity (high importance) of the elastic modulus in the early stages of the loading. At later stages, the sensitivity of the elastic modulus decreases, and the sensitivity of the yield and ultimate stresses increases. The parameters of the corner parts are more sensitive than those of the flat part. The sensitivities of the parameters *n_1* and *n_2* are small, and the sensitivities of the *eps_u_1* and *eps_u_2* are unimportant within the given sensitivity analysis boundaries (see Table 2). To validate the unimportant parameters, two further analyses were performed, and the results confirmed their unimportance, see load displacement diagram in Fig. 8. With increasing plastic strains, minor differences occur at later stages, but these are negligible for current analysis. If loading were to continue to later stages, the influence of the *eps_u* parameters would be greater.

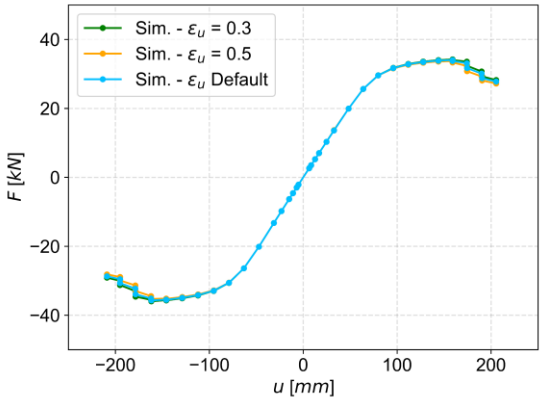

Fig. 8 Load-displacement diagram of *eps_u* influence study

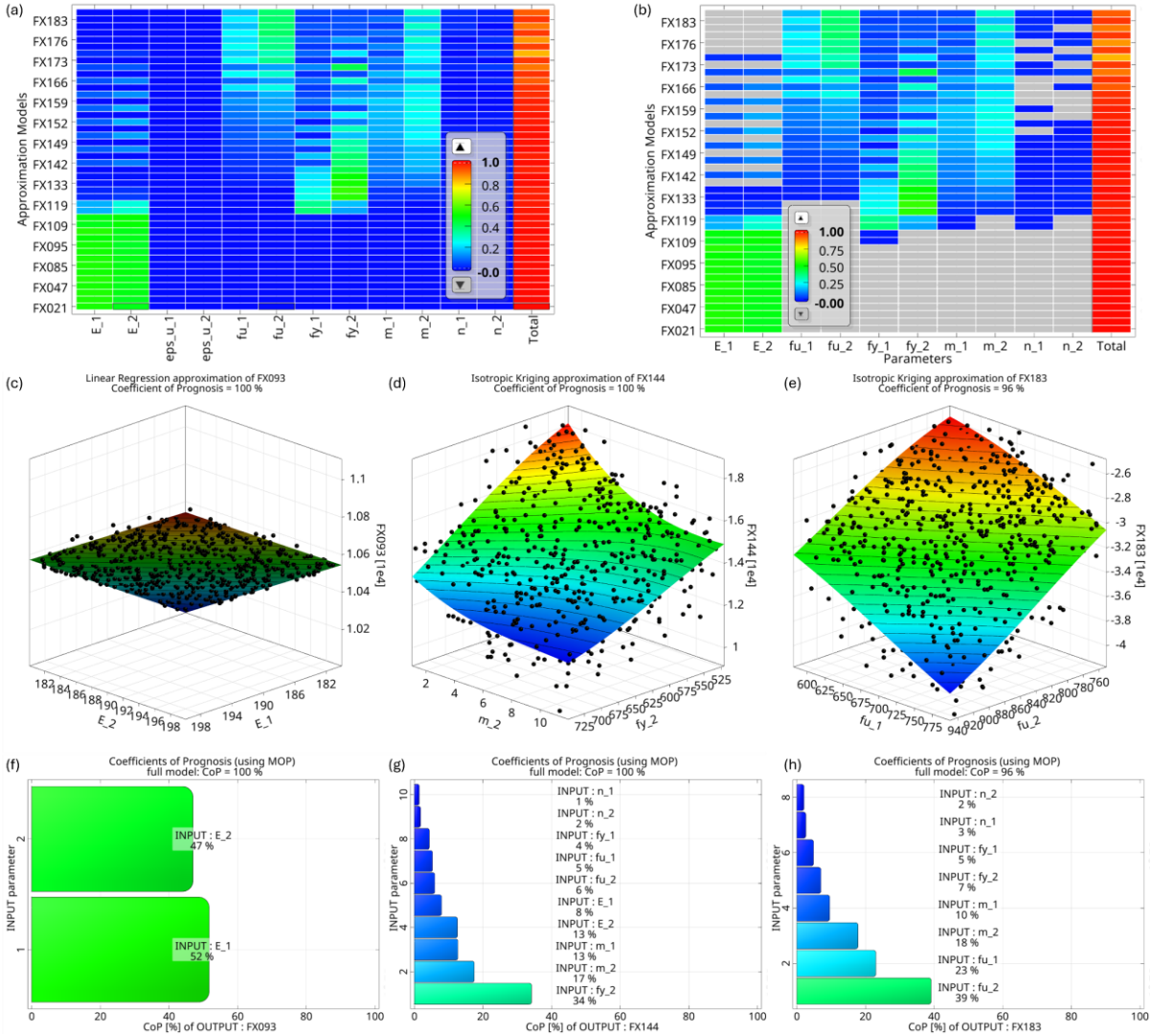

Fig. 9 (a) Full CoP Matrix, (b) Filtered CoP Matrix, (c–h) CoP of the selected responses and sensitivity of its input parameters

4.2. Optimization

The optimization was performed by minimizing the objective function. The objective function was the sum of the differences in the measured forces at the selected load levels between the experiment and the mathematical metamodel prediction. See equation (13).

$$f_{obj} = \sum_{k=1}^{n} \Delta_k = \sum_{k=1}^{n} \left| F_{k,exp} - F_{k,pred} \right|, \quad (13)$$

where $F_{k,exp}$ are the measured forces from the experiment and $F_{k,pred}$ are the predicted forces by the mathematical metamodel.

The advantage of using the mathematical metamodel is low computational cost and therefore the possibility of using more optimization methods. At this work, optimization was performed using the Non-Linear Programming by Quadratic Lagrangian (NLPQL), the Adaptive Response Surface Method (ARSM), and the Evolutionary Algorithms (EA) which are suitable for optimization with one objective function [30].

Optimization was performed with all input parameters except the *eps_u_1* and *eps_u_2*, which were determined as unimportant by the sensitivity analysis, see Fig. 9 (a). The upper and lower bounds of the parameters value range remain the same as for the mathematical metamodel, see Table 3.

Optimized values of the material model input parameters converge to similar values. Optimized values from optimization using ARSM are listed in Table 3 and the stress-strain diagrams of the material model is plotted in Fig. 10.

Table 3
Optimized values of the material model parameters.

Input parameters		Unit	Lower bound	Upper bound	Ref. value	Optimized
E	*E_1*	GPa	180	200	185.8	180
$\sigma_{0.2}$	*fy_1*	MPa	400	560	479	440
σ_u	*fu_1*	MPa	650	800	679	750
ε_u	*eps_u_1*	m/m	0.3	0.5	0.39	-
n	*n_1*	-	1	16	7.05	7.2
m	*m_1*	-	1	16	2.55	10.6
E	*E_2*	GPa	180	200	185.4	180
$\sigma_{0.2}$	*fy_2*	MPa	520	750	635	550
σ_u	*fu_2*	MPa	750	950	840	900
ε_u	*eps_u_2*	m/m	0.25	0.45	0.34	-
n	*n_2*	-	1	16	5.4	3.0
m	*m_2*	-	1	16	7.89	12.1

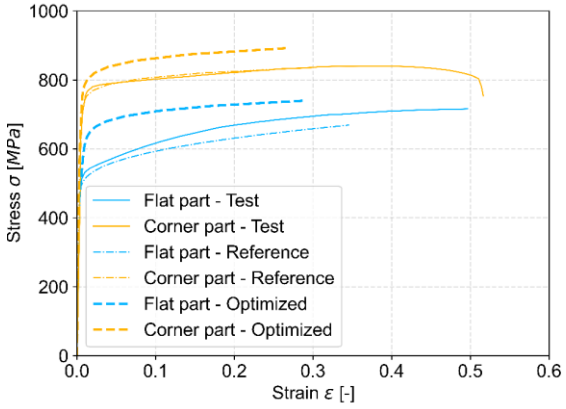

Fig. 10 Stress-strain diagram of the material with the optimized values

4.3. Verification of the metamodel

The verification was performed to check the quality of the mathematical metamodel. The numerical simulation results were compared with the prediction of the mathematical metamodel. The calculations and predictions were performed with the optimal input parameters of the material model listed in Table 3 . The comparison of the numerical simulation and the experimental measurements is shown in Fig. 11 (a). The comparison with the mathematical metamodel is shown in Fig. 11 (b).

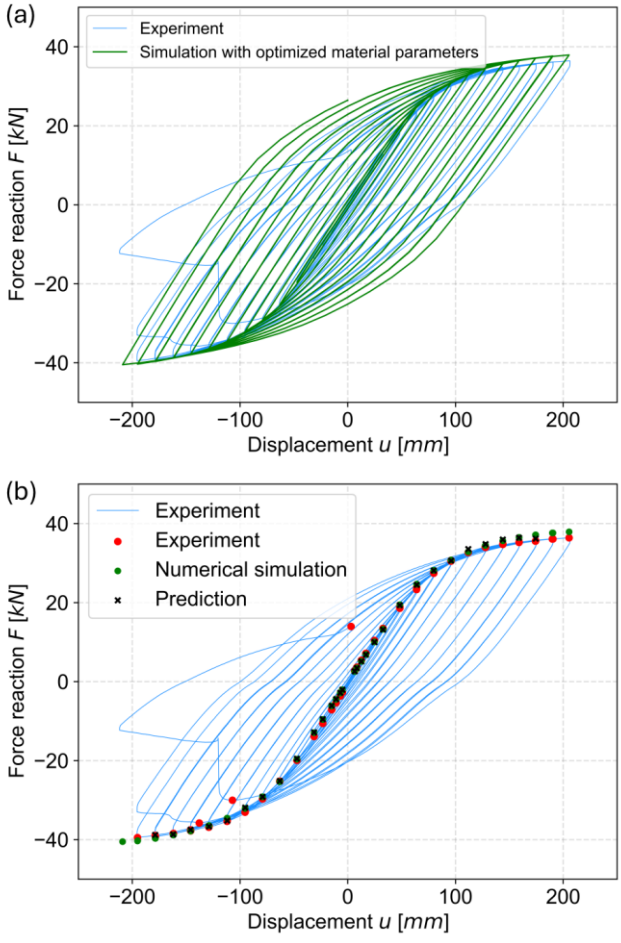

Fig. 11 (a) Numerical simulation with optimized input parameters of the material model

(b) Comparison of the experiment, metamodel prediction, and numerical simulation

5. Comparison with HSS steels

To compare the response under cyclic loading between carbon and stainless steels, a series of numerical simulations were carried out using high strength constructional steel, see Table 4 for material parameters and Fig. 12 with plotted stress-strain diagrams in true stress. The ultimate strain is determined by the equation (14).

Table 4
Nominal values of yield and tensile strengths and minimum percentage elongation after fracture of High strength steels according to EN 10025-6 [31].

Type	f_y N/mm^2	f_u N/mm^2	A %
S460	460	550	17
S500	500	590	17
S550	550	640	16
S620	620	700	15
S690	690	770	14
S890	890	940	11

$$\varepsilon_u = \left(1 - \frac{f_y}{f_u}, A\right) \tag{14}$$

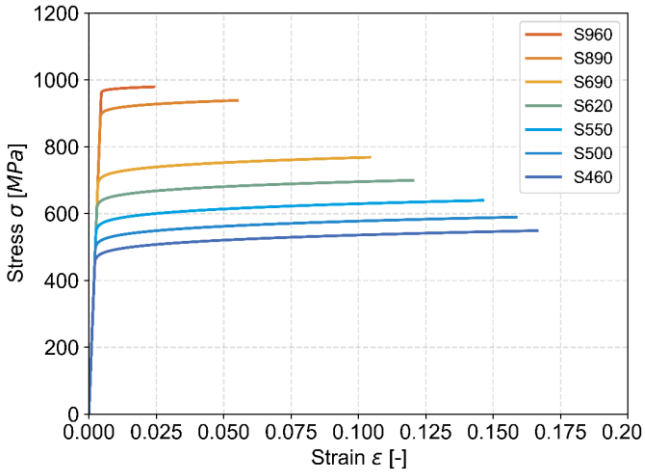

Fig. 12 Stress-strain diagram (true stress) according to EN 10025-6 and prEN 1993-1-14

The comparison is made using several methods. Load-displacement curves are shown in Fig. 13 (a). The results with HSS are directly compared with stainless steel represented by load test results and numerical simulation with optimized material model parameters. The comparison in the Fig. 13 (b) is made by directly normalizing the load-displacement curve by yield strength. Both comparisons show a non-decreasing curve of stainless steels compared to high strength steels. In addition, stainless steel shows a much higher F/f_y ratio

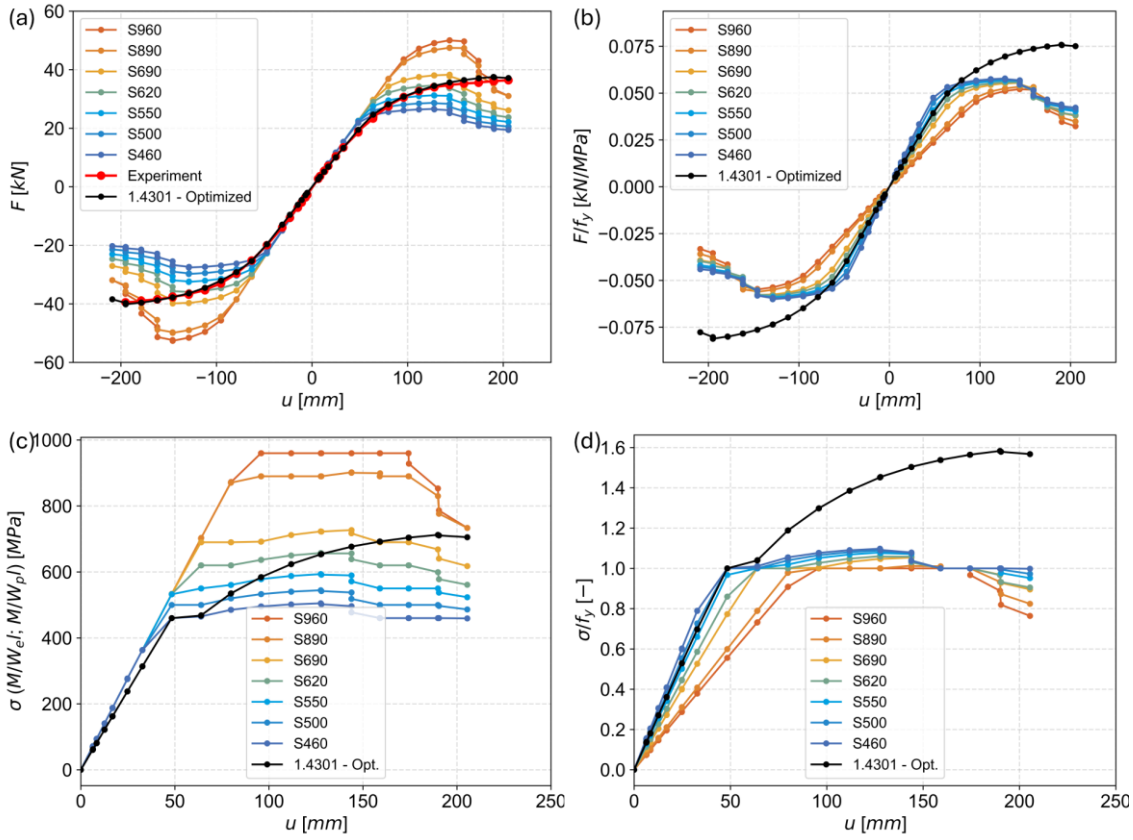

Fig. 13 Simulations results with the HSS in compare with the numerical simulation with optimized material model parameters. (a) Load-displacement curve, (b) Load displacement curve normalized by the yield strength, (c) Normal stresses at critical section (at embedment) calculated using equation (15), (d) Normalized normal stresses at critical section (at embedment) calculated using equation (16)

In Fig. 13 (c), the comparison is made using the normal stress in the critical section above the embedment. The stress is determined by an approximate method by considering a linear elastic-perfect plastic stress distribution in the plane of the section. The stress calculation is given by the equation (15). Next comparison (Fig. 13 (d)) is made using normalized values of previously calculated normal stresses which are normalized by yield strength and ultimate strength. The calculation of the normalized values is shown in the equation (16). However, the plotted stresses are not real stresses, but a quantifier/indicator of section utilization. At the same time, there is no real stress drop, which can be seen in Fig. 13 (b), it is the loss of section bearing capacity due to local buckling of the cross-section above the embedment shown in Fig. 14.

$$\sigma = \begin{cases} \frac{M}{W_{el}}, & \frac{M}{W_{el}} \le f_y \\ f_y, & \frac{M}{W_{pl}} \le f_y \\ \frac{M}{W_{pl}}, & \frac{M}{W_{pl}} \le f_u \\ \frac{M}{W_{pl}}, & \frac{M}{W_{pl}} > f_u \end{cases} \quad (15)$$

$$\sigma/f_y = \begin{cases} \frac{M}{W_{el}}/f_y, & \frac{M}{W_{el}} \le f_y \\ \frac{f_y}{f_y} = 1, & \frac{M}{W_{pl}} \le f_y \\ \frac{M}{W_{pl}}/f_u, & \frac{M}{W_{pl}} \le f_u \\ \frac{M}{W_{pl}}/f_u, & \frac{M}{W_{pl}} > f_u \end{cases} \quad (16)$$

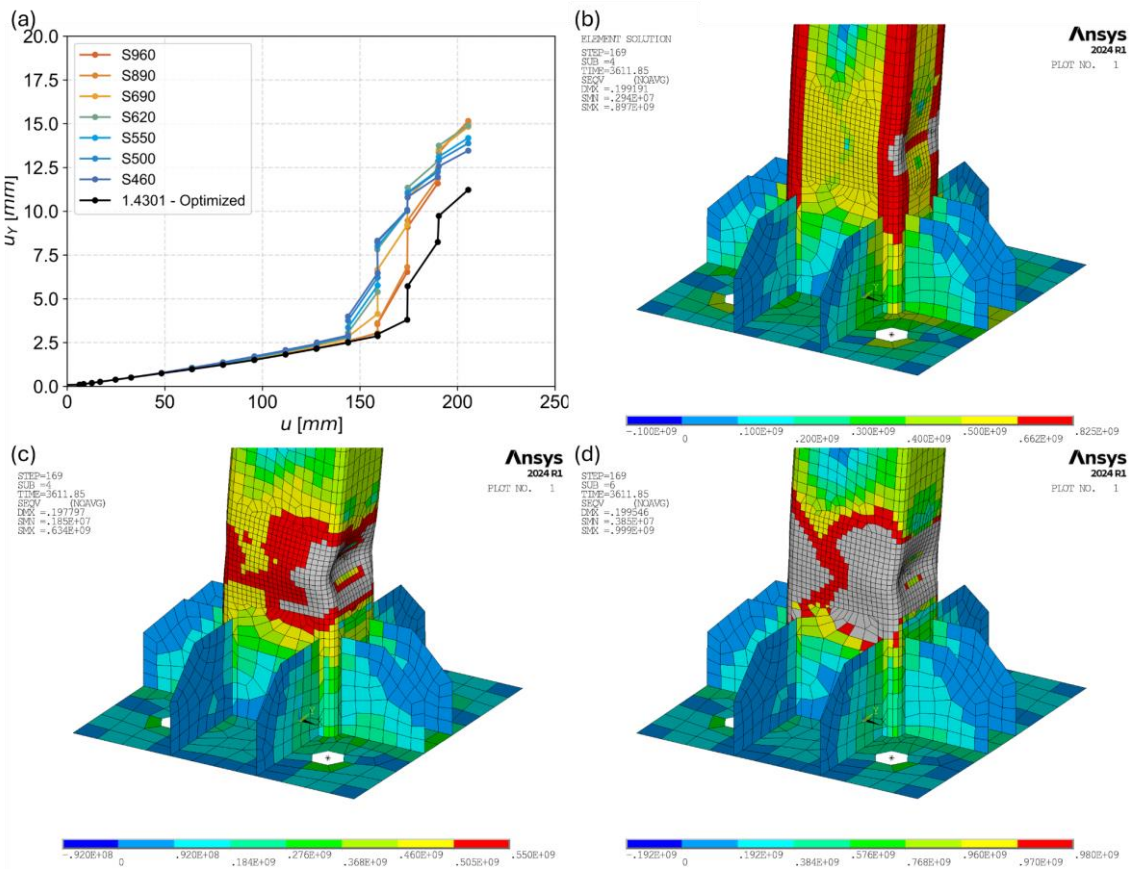

Fig. 14 (a) Transverse deformation of the cross-section. Equivalent stress above embedment. Step 169 at top displacement 175 mm. (b) 1.4301 – Opt., (c) S460, and (d) S980

The final comparison is the transverse deformation of the section above the embedment during loading, see Fig. 14 (a). Stainless steel exhibits lower transverse deformations at higher loads, while at lower loads the transverse deformations are comparable. The transverse deformation and local buckling above the embedment are shown in Fig. 14 (b–d).

6. Discussion

The superior performance of stainless steel compared to high strength steels (HSS) under cyclic loading conditions has notable implications for structural design, particularly under many times repeated loading. The ability of stainless steel to maintain its strength and ductility under repeated loading makes it a viable option for structures where resilience and durability are critical. This study supports the use of stainless steel in applications where materials are subjected to high cyclic loads, such as in bridges, high-rise buildings, and infrastructure in earthquake-prone areas.

7. Conclusion

This study systematically investigated the cyclic behavior of stainless steel through both experimental and numerical approaches, offering insights into the material's performance under cyclic loading conditions. The research began with a detailed examination of the material properties and experimental setup, laying the groundwork for developing a robust numerical FE model.

The simplified material model was developed, and its material model parameters were optimized using sensitivity analysis and MOP. The material model was validated against experimental data and was found to be effective in predicting the response of stainless steel under cyclic loading. The numerical model with the simplified material model qualitatively simulated the experiment and proved to be an appropriate choice for modelling the cyclic behavior of stainless steel, whereas ANSYS only offers the Ramberg-Osgood model for monotonic loading.

Moreover, the simplified model appears to be a very good alternative to the Chaboche model because it is defined by fewer input parameters that can be more intuitively determined and identified from laboratory tests. The yield strength, ultimate strength and ultimate strain are clearly given and then it is practically sufficient to identify the strain hardening parameters *m* and *n*. Therefore, this simplified model is very suitable for practical use in nonlinear calculations of the steel structures under cyclic or repetitive loading.

Additionally, the study extended the comparison to high strength steels (HSS), demonstrating that stainless steel exhibits superior effectiveness in scenarios involving cyclic loading. The findings underscore the potential of stainless steel as a preferred material in structural applications where ductility, strain hardening, and resistance to cyclic loading are required.

In conclusion, this research not only validates the effectiveness of the simplified material model but also reinforces the growing importance of stainless steel in modern structural engineering, particularly in dynamic and seismic environments.

Acknowledgements

The authors gratefully acknowledge funding support from the Czech Science Foundation (No. GA23-04712S) and the Brno University of Technology (No. FAST-S-24-8503).

References

[1] Y. Li, C.-C. Lee, and Y. Cai, “Recent Research Advances in High-Performance Steel Tubular Members: Material Properties, Stub Columns, and Beams,” Buildings, vol. 13, no. 11, p. 2713, Oct. 2023, doi: 10.3390/buildings13112713.

[2] C. Ding, “Properties of stainless steel and its application in construction,” Applied and Computational Engineering, vol. 59, no. 1, pp. 51–56, May 2024, doi: 10.54254/2755-2721/59/20240748.

[3] K. H. Nip, L. Gardner, C. M. Davies, and A. Y. Elghazouli, “Extremely low cycle fatigue tests on structural carbon steel and stainless steel,” J Constr Steel Res, vol. 66, no. 1, pp. 96–110, Jan. 2010, doi: 10.1016/j.jcsr.2009.08.004.

[4] Z. Chen, J. Yao, B. Zheng, and G. Shu, “Classification and ultimate capacity of duplex stainless steel H-section under cyclic loading,” J Constr Steel Res, vol. 218, p. 108725, Jul. 2024, doi: 10.1016/j.jcsr.2024.108725.

[5] CEN, “Eurocode 3 - Design of steel structures - Part 1-4: General rules - Supplementary rules for stainless steels,” 2006, European Committee for Standardization, Brussels.

[6] A. Ene, I. Both, O. Abrudan, A. Stratan, H. F. Dașcău, and N. A. Sîrbu, “Experimental Investigation of Monotonic and Cyclic Behaviour of High-Performance Steels,” Key Eng Mater, vol. 953, pp. 13–20, Aug. 2023, doi: 10.4028/p-K0XkeD.

[7] F. Zhou, C. Fang, and Y. Chen, “Experimental and numerical studies on stainless steel tubular members under axial cyclic loading,” Eng Struct, vol. 171, pp. 72–85, Sep. 2018, doi: 10.1016/j.engstruct.2018.05.093.

[8] C. Fang, F. Zhou, and C. Luo, “Cold-formed stainless steel RHSs/SHSs under combined compression and cyclic bending,” J Constr Steel Res, vol. 141, pp. 9–22, Feb. 2018, doi: 10.1016/j.jcsr.2017.11.001.

[9] M. Subasic et al., “Experimental investigation and numerical modelling of the cyclic plasticity and fatigue behavior of additively manufactured 316 L stainless steel,” Int J Plast, vol. 176, p. 103966, May 2024, doi: 10.1016/j.ijplas.2024.103966.

[10] R. Halama, J. Fumfera, P. Gál, T. Kumar, and A. Markopoulos, “Modeling the Strain-Range Dependent Cyclic Hardening of SS304 and 08Ch18N10T Stainless Steel with a Memory Surface,” Metals (Basel), vol. 9, no. 8, p. 832, Jul. 2019, doi: 10.3390/met9080832.

[11] J. Luo, S. Li, L. Mao, and G. Shi, “Constitutive model of duplex stainless steel S22053 and its weld under cyclic large plastic strain loading,” J Constr Steel Res, vol. 205, p. 107882, Jun. 2023, doi: 10.1016/j.jcsr.2023.107882.

[12] L.-T. Hai, G.-Q. Li, Y.-B. Wang, and Y.-Z. Wang, “A fast calibration approach of modified Chaboche hardening rule for low yield point steel, mild steel and high strength steels,” Journal of Building Engineering, vol. 38, p. 102168, Jun. 2021, doi: 10.1016/j.jobe.2021.102168.

[13] L. Hai, B. Chen, P. Dai, H. Ban, Y. Wang, and H.-T. Li, “Cyclic plastic behavior of austenite stainless steel QN1803 and S30408: Experiment and constitutive modeling,” Constr Build Mater, vol. 473, p. 141083, Apr. 2025, doi: 10.1016/j.conbuildmat.2025.141083.

[14] W. Shao, L. Yuan, and J. Yan, “Modeling the reeling process of offshore pipelines: A theoretical framework based on updated Voce-Chaboche model,” Ocean Engineering, vol. 332, p. 121383, Jul. 2025, doi: 10.1016/j.oceaneng.2025.121383.

[15] L. Hai, Y. Wang, H. Ban, G. Li, and X. Du, “A simplified prediction method on Chaboche isotropic/kinematic hardening model parameters of structural steels,” Journal of Building Engineering, vol. 68, p. 106151, Jun. 2023, doi: 10.1016/j.jobe.2023.106151.

[16] R. Du, X. Zhang, H. Wang, X. Liu, and Y. Wei, “A revised Chaboche model from multiscale approach to predict the cyclic behavior of type 316 stainless steel at room temperature,” Int J Fatigue, vol. 167, p. 107303, Feb. 2023, doi: 10.1016/j.ijfatigue.2022.107303.

[17] H. Ramezansefat and S. Shahbeyk, “The Chaboche hardening rule: A re-evaluation of calibration procedures and a modified rule with an evolving material parameter,” Mech Res Commun, vol. 69, pp. 150–158, Oct. 2015, doi: 10.1016/j.mechrescom.2015.08.003.

[18] O. Kaleva, H. Orelma, and D. Petukhov, “Parameter estimation of a high-cycle fatigue model combining the Ottosen-Stenström-Ristinmaa approach and Lemaitre-Chaboche damage rule,” Int J Fatigue, vol. 147, p. 106153, Jun. 2021, doi: 10.1016/j.ijfatigue.2021.106153.

[19] S. Liu, G. Liang, and Y. Yang, “A strategy to fast determine Chaboche elasto-plastic model parameters by considering ratcheting,” International Journal of Pressure Vessels and Piping, vol. 172, pp. 251–260, May 2019, doi: 10.1016/j.ijpvp.2019.01.017.

[20] A. H. Mahmoudi, H. Badnava, and S. M. Pezeshki-Najafabadi, “An application of Chaboche model to predict uniaxial and multiaxial ratcheting,” Procedia Eng, vol. 10, pp. 1924–1929, 2011, doi: 10.1016/j.proeng.2011.04.319.

[21] K. Ning, L. Yang, and O. Zhao, “Advanced cyclic constitutive model and parameter calibration method for austenitic stainless steel,” J Constr Steel Res, vol. 222, p. 108981, Nov. 2024, doi: 10.1016/j.jcsr.2024.108981.

[22] I. González-de-León, E. Nastri, I. Arrayago, R. Montuori, V. Piluso, and E. Real, “Experimental study on stainless steel tubular members under cyclic loading,” Thin-Walled Structures, vol. 181, p. 109969, Dec. 2022, doi: 10.1016/j.tws.2022.109969.

[23] I. Arrayago, I. González-de-León, E. Real, and E. Mirambell, “Tests on stainless steel frames. Part I: Preliminary tests and experimental set-up,” Thin-Walled Structures, vol. 157, p. 107005, Dec. 2020, doi: 10.1016/j.tws.2020.107005.

[24] Ramberg W and Osgood WR, “Description of stress–strain curves by three parameters,” 1943, National Advisory, Washington, DC.

[25] M. Ashraf, L. Gardner, and D. A. Nethercot, “Finite element modelling of structural stainless steel cross-sections,” Thin-Walled Structures, vol. 44, no. 10, pp. 1048–1062, Oct. 2006, doi: 10.1016/j.tws.2006.10.010.

[26] CEN, “Eurocode 3: Design of Steel Structures - Part 1-14: Design by Finite Element Analysis,” 2023, Brussels.

[27] D. Jindra, Z. Kala, and J. Kala, “Buckling curves of stainless steel CHS members: Current state and proposed provisions,” J Constr Steel Res, vol. 198, p. 107521, Nov. 2022, doi: 10.1016/j.jcsr.2022.107521.

[28] N. Abdel-Rahman and K. S. Sivakumaran, “Material Properties Models for Analysis of Cold-Formed Steel Members,” Journal of Structural Engineering, vol. 123, no. 9, pp. 1135–1143, Sep. 1997, doi: 10.1061/(ASCE)0733-9445(1997)123:9(1135).

[29] J. Will and T. Most, “Metamodell of optimized Prognosis (MoP) -an Automatic Approach for User Friendly Parameter Optimization,” 2009.

[30] Inc. ANSYS, “Methods for Multi-Disciplinary Optimization and Robustness Analysis,” Jan. 2024, ANSYS, Inc., Canonsburg: Release 2024 R1.

[31] CEN, “EN 10025: Hot rolled products of structural steels. Part 6: Technical delivery conditions for flat products of high yield strength structural steels in the quenched and tempered condition,” 2019, Brussels.

Advanced Steel Construction – Vol. 21 No. 4 (2025) 346–356
DOI:10.18057/IJASC.2025.21.4.7

STUDY ON COMPRESSIVE BEHAVIOR OF LASER-ARC WELDED TUBE-IN-TUBE S355 STEEL COLUMNS

Ming-Yang Li [1], De-Hong Huang [2], Zi-Yi Zeng [3], Yao-Peng Liu [2,*] and Siu-Lai Chan [2, 4]

[1] *School of Civil Engineering, Southwest Jiaotong University, Chengdu, China*
[2] *School of Civil Engineering and Transportation, South China University of Technology, Guangzhou 510641, China*
[3] *Department of Civil and Environmental Engineering, The Hong Kong Polytechnic University, Hong Kong, China*
[4] *State Key Laboratory of Subtropical Building and Urban Science, South China University of Technology, Guangzhou 510641, China*
* *(Corresponding author: E-mail: yaopengliu@scut.edu.cn)*

ABSTRACT

This paper presents an experimental and numerical study on the axial compression behavior of laser-arc hybrid welded tube-in-tube steel columns made of S355. Three different cross-sectional configurations, i.e. square-in-square (SS), circular-in-square (SC) and conventional square hollow section (S), were investigated through monotonic tension tests and axial compression tests. Digital Image Correlation (DIC) was employed to analyze deformation patterns. Results demonstrate that the ductility of composite SS and SC columns has been significantly improved compared to single hollow-section columns, effectively delaying local buckling and mitigating strength degradation. Moreover, numerical simulations using finite element method (FEM) were conducted and validated against experimental results. Parametric studies were conducted to evaluate the influence of column slenderness on axial load-bearing capacity, highlighting that current design codes (EN 1993-1-1:2022 and GB 50017-2017) provide conservative predictions. Findings suggest adopting the class a_0 curve from EN 1993-1-1:2022 or the class a curve from GB 50017-2017 for the design of such composite columns. This study provides essential data and practical guidance for the structural application of laser-arc welded tube-in-tube composite columns.

ARTICLE HISTORY

Received: 12 November 2024
Revised: 20 February 2025
Accepted: 1 March 2025

KEYWORDS

Laser-arc hybrid welding;
Tube-in-tube steel column;
Finite element method;
Compressive behavior;
Initial geometric imperfections

1. Introduction

Modular construction has gained increasing attention and application both domestically and internationally due to its advantages of fast construction speed, high engineering quality, low labor consumption, energy efficiency, and environmental protection[1, 2]. However, due to spatial constraints, the cross-sectional dimensions of modular construction members are limited. To overcome these limitations, this study proposes two new types of steel column cross-sections: square hollow section column nested within square hollow section column and circular hollow section column nested within square hollow section column, both formed through laser-arc hybrid welding.

Currently, scholars have conducted relatively limited research on hollow section columns. Wang et al. [3] conducted material tensile tests and local buckling tests on RHS/SHS stub column specimens of varying strengths and evaluated existing design provisions in the Eurocode 3 for such structural columns. Ma et al. [4] provided a comprehensive review on high-strength steel hollow sections, highlighting gaps in design rules. Yang et al. [5] proposed a new equation for deriving the cross-sectional slenderness of SHS and RHS considering the influence of corner radius. Li et al. [6] studied flexural and interactive buckling of 7A04-T6 high-strength aluminium RHS columns, offering improved design methods based on test and FE results. Zhu et al. [7] studied the behavior and design of hot-rolled carbon steel circular hollow sections (CHS) under the effect of moment gradients. Lin et al. [8] conducted a numerical study on high-strength steel welded box columns and proposed new column curves incorporating yield strength and width-to-thickness ratio to improve design accuracy beyond existing codes. Yan et al. [9] conducted low-temperature compression tests and simulations on stainless-steel tubular stub columns, revealing enhanced strength but reduced ductility with decreasing temperature. Meng et al. [10] investigated the buckling behavior of axial compressive hollow sections members, encompassing CHS, SHS, and RHS sections. Wang et al. [11, 12] conducted experimental and numerical studies on S890 and S960 CHS members under combined and eccentric loading, and evaluated the applicability of existing design codes, highlighting their varying accuracy for different section classes. Yin et al. [13] conducted tests and simulations on cold-formed HSS SHS columns, and proposed modified buckling curves for design.

Some studies have been conducted by researchers on the axial compressive performance and design methods of composite cross-sections. Li et al. [14] conducted experimental and numerical investigations on the local buckling behavior of cold-formed steel built-up box-section columns and revealed the built-up interaction mechanism between C- and U-section components. Zhao et al. [15] proposed a new type of cold-formed stainless-steel spliced rectangular tubular column and demonstrated through tests and FE analysis that V-shaped stiffeners significantly enhance its axial and compression-bending capacities. However, systematic research on structural members with square-circular composite cross-sections remains relatively limited.

Traditional arc welding techniques, while widely used in structural fabrication, suffer from several well-recognized limitations, including high heat input, significant welding deformation, large heat-affected zones (HAZ), and low welding efficiency [16–21]. These drawbacks are particularly detrimental when applied to thick-section or high-performance steels, where dimensional control and material integrity are critical. For example, Sokolov et al. [22, 23] observed that conventional welding methods tend to induce excessive thermal distortion and broad HAZs in thick S355 structural steel, adversely affecting dimensional precision and mechanical performance. Similarly, Zhong et al. [24] emphasized that traditional fusion welding introduces considerable membrane residual stresses and geometric imperfections in stainless steel T-sections, which may compromise structural stability.

In contrast, laser welding presents a high-precision, high-efficiency alternative, offering numerous advantages such as lower total heat input, narrower HAZ, reduced residual stresses, minimized distortion, and higher welding speeds [25–28]. These benefits stem from its concentrated energy delivery and non-contact nature. In addition, laser welding enables deep penetration and excellent process control, which is especially advantageous in joining thick or high-strength steel sections. For instance, Zhang et al. [17] demonstrated that with a 10 kW fiber laser, full penetration welding of thick stainless steel was achievable at high speeds, while also identifying the keyhole dynamics responsible for surface underfill defects, a challenge that is otherwise exacerbated in conventional methods.

Moreover, laser welding is readily integrable with robotic platforms, promoting automation and manufacturing repeatability. Sokolov and Salminen [29] conducted comparative trials and confirmed that laser welding maintains superior weld quality even under variable edge preparation conditions, underscoring its industrial robustness.

Building upon the merits of individual welding methods, laser-arc hybrid welding (LAHW) has emerged as a promising technique that combines the high precision and penetration of laser welding with the good gap-bridging ability and process stability of arc welding. Several researchers have explored the synergistic mechanisms of LAHW. Zhang et al. [26] quantified the "synergy effect" in LAHW of aluminum alloys using plasma spectroscopy, confirming that laser energy enhances arc stability and increases the material's laser absorptivity, while the arc assists with broadening the fusion zone and improving melt flow. Likewise, Yin et al. [16] demonstrated that in LAHW of low-strength high-toughness steel, the increased cooling rate due to the combined heat source promoted the formation of bainite and fine acicular ferrite in the weld metal, thereby enhancing both hardness and low-temperature

toughness.

In light of the limited research in the existing literature on the application of LAHW to square and circular hollow section (SHS/CHS) members, as well as composite steel members, this study aims to investigate the axial compressive performance of ultra-high-power LAHW composite section steel columns, with the goal of providing experimental data and theoretical support for the practical engineering application of such novel structural systems.

In this research, axial compression tests were first conducted on laser-welded composite section columns to obtain their structural response under axial loads, including load–displacement curves, deformation and failure modes, as well as global buckling behavior. The comparison between the influences of different internal tube configurations on load-bearing capacity and failure mechanisms was performed. Subsequently, a finite element model was developed in ABAQUS and validated against the experimental results. A parametric study was then performed to investigate the influence of slenderness ratio on the axial capacity of columns with the two composite section types. Finally, by comparing the simulation results with predictions from Chinese specification (GB 50017-2017 [30]) and European specification (EN 1993-1-1:2022 [31]), the applicability of each code to these composite sections was evaluated, and corresponding design recommendations were proposed.

2. Experimental study

2.1. Specimen preparation and experimental procedure

This experimental investigation comprises tensile coupon tests and axial compression tests on steel columns with various cross-sectional configurations. The columns, fabricated using ultra-high-power LAHW, were made of grade S355J0 steel.

2.1.1. Monotonic tension test

To investigate the material properties of the steel used in this study, monotonic tension tests were conducted. Given that the tested hollow section columns tested had a wall thickness of 10 mm, the tensile specimens were also prepared with the same thickness. As illustrated in **Fig. 2**(c), the specimens were designed and fabricated in accordance with ISO 6892-1:2019 [32], and were cut from the same batch of steel using a wire cutting process. All specimens complied with the specified dimensional and quality requirements. The experimental procedure followed the guidelines of ISO 15609-1:2019 [33], and the tests were carried out using an electro-hydraulic servo fatigue testing machine, as shown in **Fig. 2**(a).

2.1.2. Column specimens and test setup

The axial compression tests included three types of steel column cross-sections, two of which were composite sections. The composite cross-sections consisted of one square hollow section nested within another square hollow section (SS), and one circular hollow section nested within a square hollow section (SC). The third type was a conventional square hollow section (S). For each section type, four identical specimens were fabricated using LAHW, resulting in a total of 12 test specimens. The section dimensions — including outer column diameter (d_1), outer column thickness (t_1), inner column diameter (d_2), inner column thickness (t_2), cross-sectional area (A), specimen length (L), and effective buckling length (L_{cr}) — are summarized in **Table 1**. Cross-sectional configurations and weld locations are illustrated in **Fig. 1**. The specimen labeling follows a consistent format, e.g., 'SS-1' denotes the first specimen of the SS column group.

Table 1
Geometric dimensions of the test specimens

Type	d_1 (mm)	d_2 (mm)	t_1 (mm)	t_2 (mm)	A (mm^2)	L (mm)	L_{cr} (mm)
SS	200	143	10	10	120.5	1200	1840
SC	200	178	10	10	124.4	1200	1840
S	200	/	10	/	76	1200	1840

Note : $L_{cr} = L + 640$mm

The loading setup is shown in **Fig. 3**(a). An electro-hydraulic 1500-ton testing machine was used to apply axial compressive loading, with a loading rate of 1 mm/min. Once the applied load dropped to 80% of the peak load, the test was terminated and the load was removed. A knife hinge as shown in **Fig. 3**(c) is arranged at each end of the test specimen, which allowed the in-plane rotation about only one axis, with 320mm hinge offset per end.

Fig. 4 shows strain gauges positioned at three column heights (3L/8, L/2, 5L/8) and both ends. Composite-section columns required dual gauges straddling the mid-length weld seam, while square hollow sections used single gauges. LVDTs monitored deformations: DT1–DT2 (in-plane lateral), DT3 (out-of-plane), DT4–DT5 (axial), and DT6–DT9 (end rotations via knife hinges).

The deformation of the steel columns was monitored using 2D-DIC technology during the experiment as shown in **Fig. 3**(b). The surface of the steel column specimens without attached strain gauges was designated as the 2D-DIC measurement area. This surface received a uniform coat of matte white paint followed by the application of a black speckle pattern using hydro transfer printing to enable digital image correlation analysis.

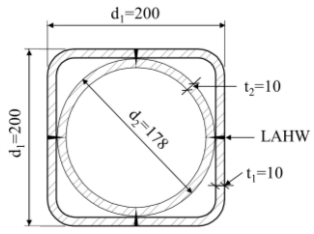

(a) Type SS

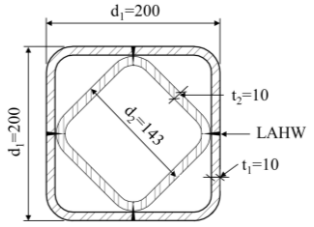

(b) Type SS

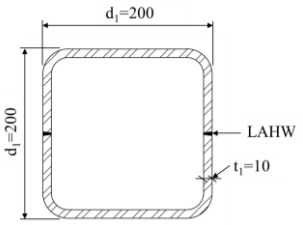

(c) Type S

Fig. 1 Cross-sections of Steel Columns: Types SS, SC and S

2.1.3. Measurement of initial geometric imperfections

The initial geometric imperfections on both sides of the member along the weak axis direction were measured using a combination of vernier calipers, a spirit level, a plumb line, and the string-line method, following the approach proposed by Li[6], as illustrated in **Fig. 5**. A plumb line was first suspended from the end plate. The distances from the column surface to the plumb line were then measured at the top, bottom positions to define the virtual reference plane, as indicated by the blue dashed line in **Fig. 5**. The initial geometric imperfections were measured at the mid-height, 1/4, and 3/4 height positions along the column. At each location, measurement points were placed on two opposing faces of the column, spaced at 140 mm intervals. The deviations between the measured values and the ideal (imperfection-free) positions were calculated based on geometric relationships, yielding values denoted as Δv_{ai}, Δv_{bi}, Δv_{ci} and Δv_{di}, as shown in **Fig. 5**. The maximum value among Δv_1, Δv_2, and Δv_3 was taken as the initial geometric imperfection of the specimen, denoted as v_0. The calculation formulas for Δv_1, Δv_2, and Δv_3 are show in Eq. (1), and the results are summarized in the accompanying table.

$$\Delta v_i = (\Delta v_{ai} + \Delta v_{bi} + \Delta v_{ci} + \Delta v_{di})/4 \quad (1)$$

where i =1, 2, 3.

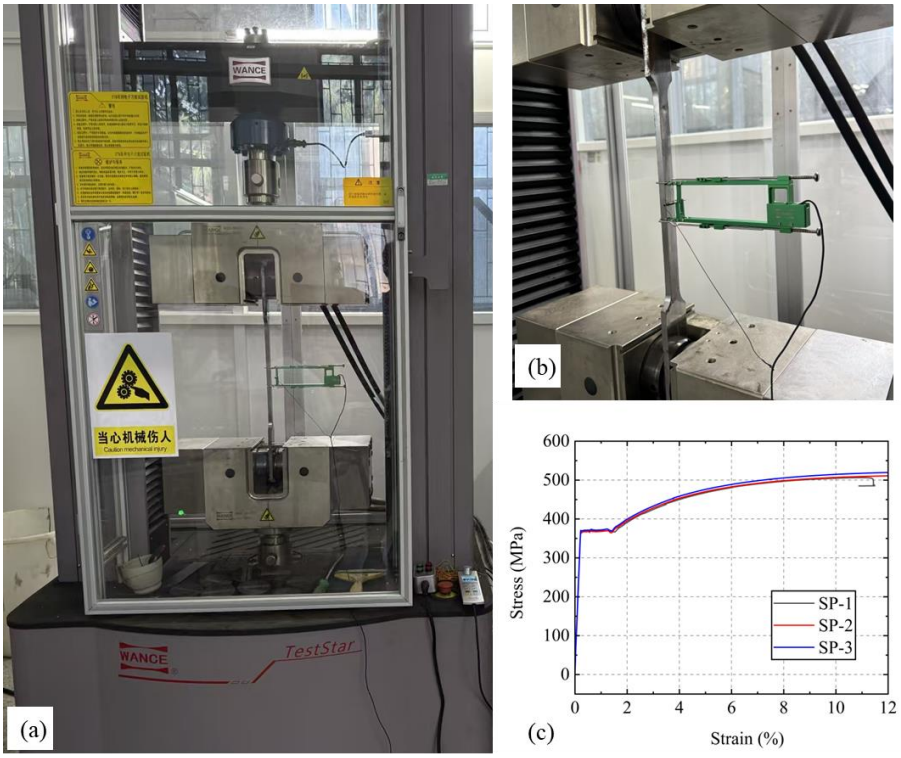

Fig. 2 Experimental setup of monotonic tension tests: (a) Test device; (b) The extensometer set up; (c) Stress-strain curve of monotonic tension tests;

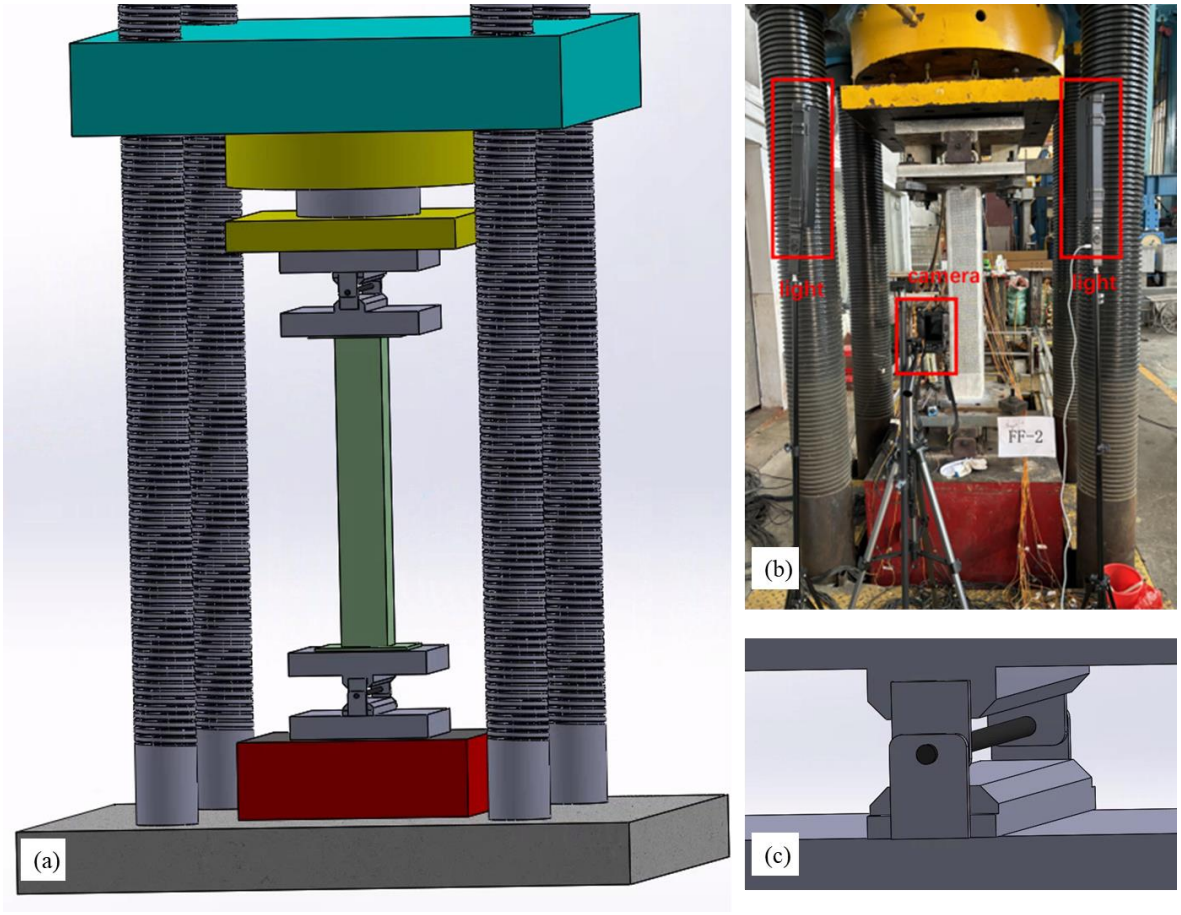

Fig. 3 Experimental setup of compressive test: (a) 1500 ton. loading machine; (b) 2D-DIC monitor; (c) Knife hinge

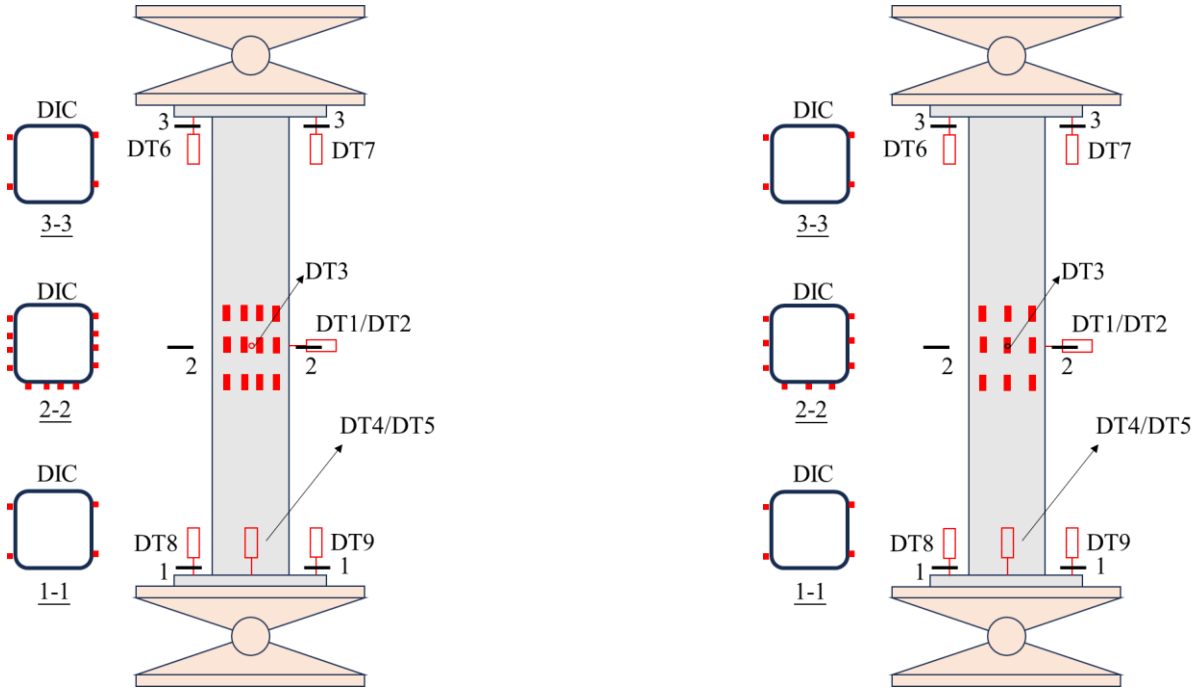

(a) Type SS and SC (b) Type S

Fig. 4 Layout of measurement points for compressive members

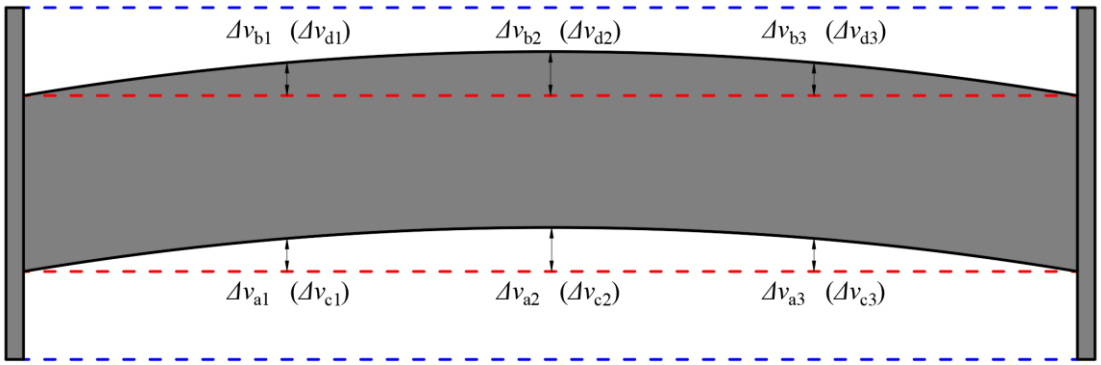

Fig. 5 Measurement procedure of initial geometric imperfections

The initial eccentricities at the top (e_{0t}) and bottom (e_{0b}) of the specimens were calculated retrospectively based on the strain gauge readings at the column ends and the applied axial load, following Eq. (2). To ensure that all specimens were subjected to elastic and stable axial compression, the readings corresponding to a vertical load of 0.15 N_u were used in the calculations, where N_u denotes the axial compressive strength of the specimen. The specific formulas for calculating the end eccentricities are provided below, and the results are summarized in **Table 3**.

$$e_0 = \frac{\varepsilon_1+\varepsilon_2-\varepsilon_3-\varepsilon_4}{4} \cdot \frac{EW}{0.15N_u} \tag{2}$$

In Eq. (2), e_0 denotes the end eccentricity of the column; ε_1 to ε_4 represent the absolute values of the strains measured by the four strain gauges installed at the column end; E is the experimentally measured Young's modulus; W is the measured section modulus of the specimen; and N_u is the axial compressive strength of the specimen.

In summary, the equivalent initial geometric imperfection can be calculated using $e = v_0 + (e_{0b} + e_{0t})/2$, and the results are presented in **Table 3**.

2.2. Experimental results and discussion

2.2.1. Results of Monotonic tension test

Through monotonic tension tests on three standard material specimens, the stress–strain curves shown in **Fig. 2**(c) were obtained. The Young's modulus (E), yield strength (σ_y), ultimate tensile strength (σ_u), and elongation after fracture (δ) of the steel are summarized in **Table 2**. The results indicate that the yield strength (σ_y) of the S355J0-grade steel used in this study was measured to be 367.8 MPa, the ultimate tensile strength (σ_u) was measured to be 510.04 MPa, and the average elongation after fracture is 38.4%. These material properties were subsequently used in the numerical simulations and parameter analysis.

Table 2
Results of monotonic tension tests

Specimens	E (N/mm^2)	σ_y (MPa)	σ_u (MPa)	δ (%)
Sp-1	200399.06	369.04	506.28	36.4
Sp-2	204331.7	366.27	512.32	38.3
Sp-3	195757.38	368.07	511.53	40.2
Average	200162.71	367.8	510.04	38.4

Table 3
Initial geometric imperfections of test specimens

Specimen	Global geometric imperfections				Initial eccentricity		*e*/*L*(‰)
	Δv_1 (mm)	Δv_2 (mm)	Δv_3 (mm)	v_0 (mm)	e_{0b} (mm)	e_{0t} (mm)	
SS-1	0.114	0.18	0.1625	0.180	1.32×10^{-5}	-4.2×10^{-6}	0.150
SS-2	0.271	0.355	0.326	0.355	-1.1×10^{-6}	1.09×10^{-6}	0.296
SS -3	0.315	0.333	0.130	0.334	5.05×10^{-8}	3.41×10^{-6}	0.277
SS -4	0.294	0.248	0.260	0.294	-5.2×10^{-6}	-4.7×10^{-6}	0.294
SC-1	0.179	0.194	0.185	0.194	-2.2×10^{-5}	-7.2×10^{-6}	0.162
SC -2	0.245	0.189	0.326	0.326	-7.4×10^{-6}	-1.1×10^{-6}	0.272
SC -3	0.496	0.491	0.328	0.496	-4.6×10^{-6}	-4.2×10^{-6}	0.414
SC -4	0.180	0.166	0.21	0.210	-3.9×10^{-7}	-1.0×10^{-5}	0.175
S-1	0.341	0.331	0.261	0.341	-5.7×10^{-6}	/	0.2845
S-2	0.155	0.066	0.186	0.186	-6.6×10^{-7}	-2.8×10^{-6}	0.155
S-3	0.231	0.152	0.240	0.240	-1.7×10^{-6}	6.8×10^{-7}	0.200
S-4	0.131	0.228	0.224	0.228	-3.2×10^{-6}	-4.3×10^{-6}	0.190

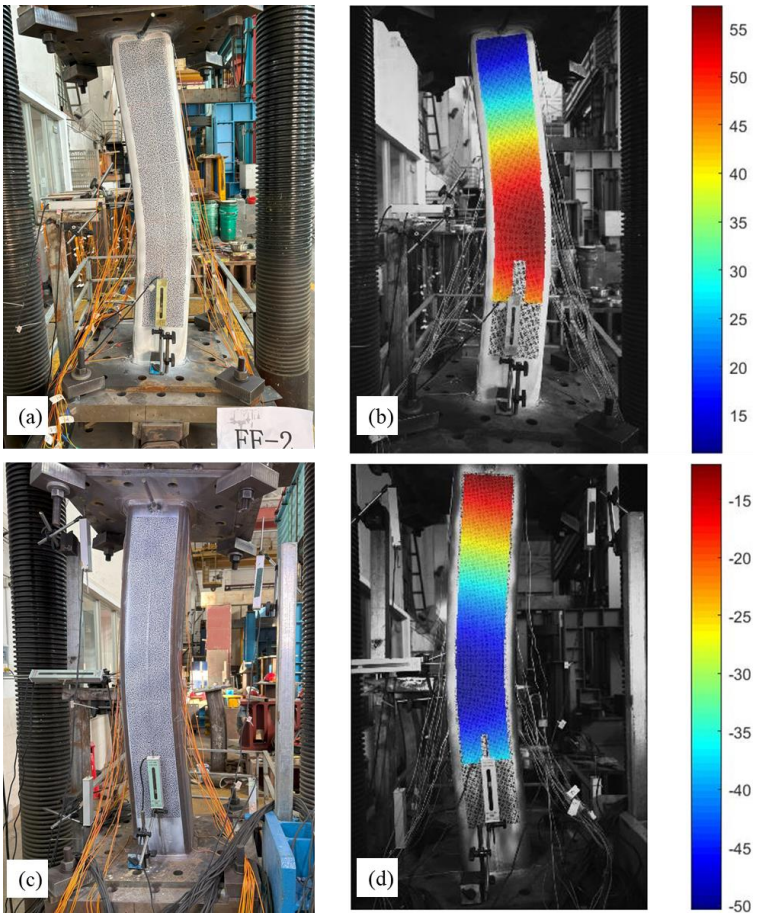

Fig. 6 Typical failure mode of SS/SC specimens and DIC results:(a) Failure mode of type SS; (b) DIC result of type SS; (c) Failure mode of type SC; (d) DIC result of type SC

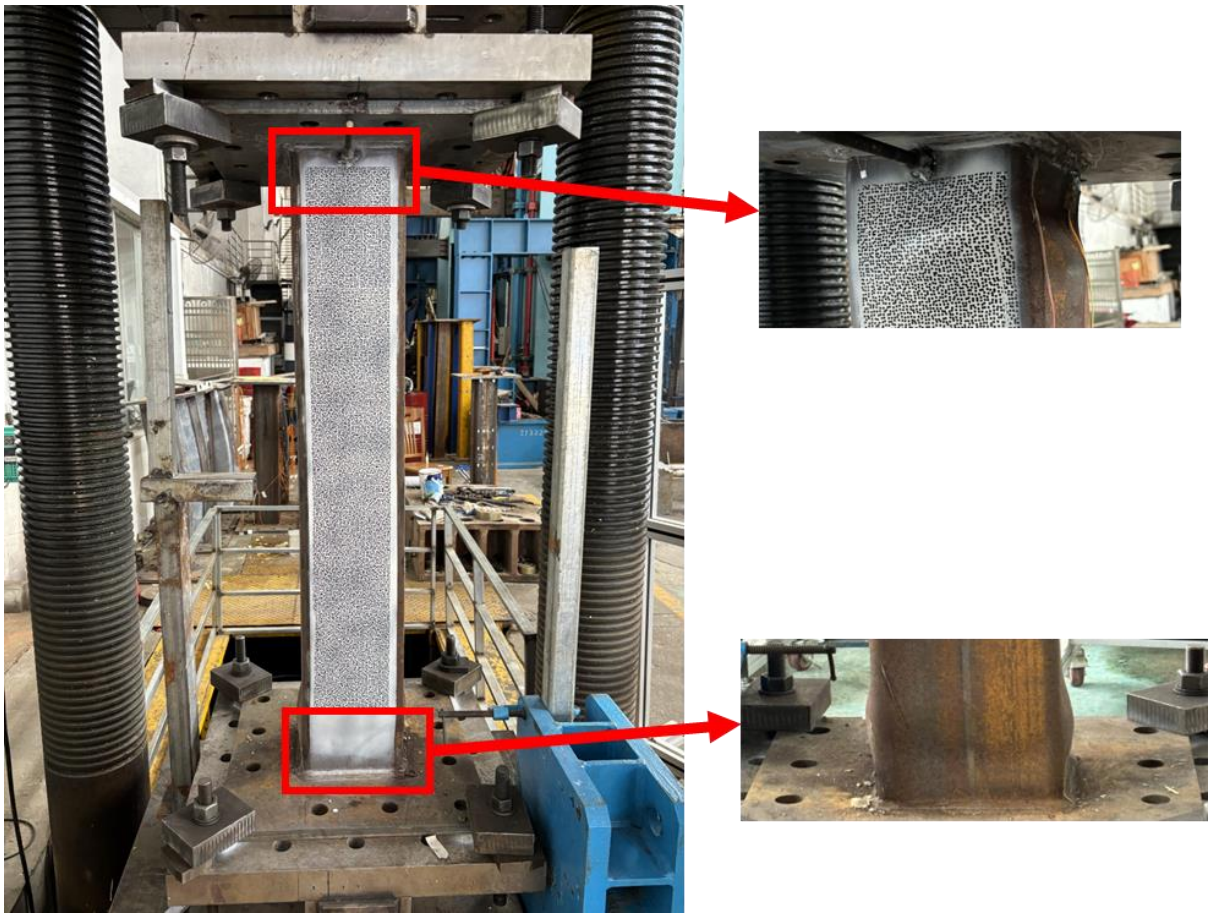

Fig. 7 Typical failure mode of type-S specimens

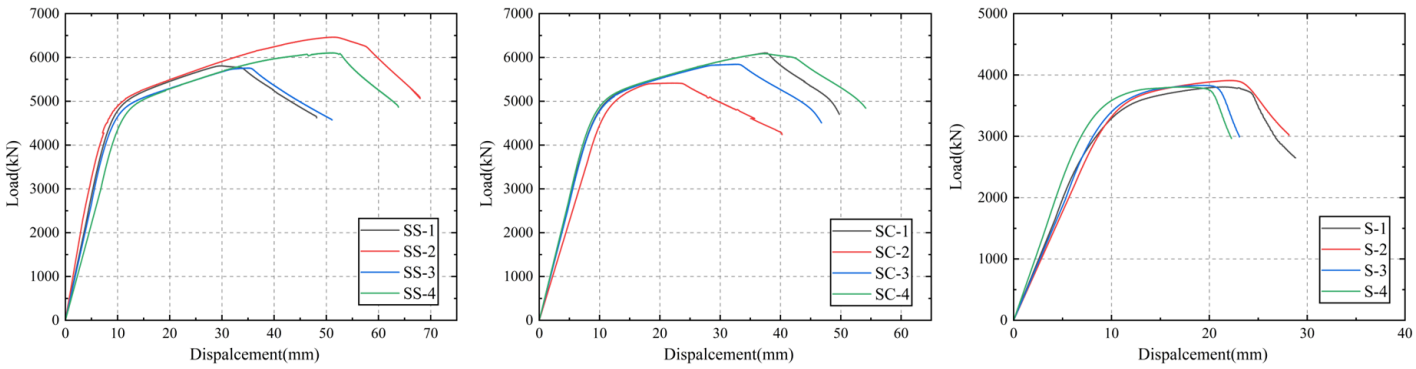

(a) Type-SS (b) Type-SC (c) Type-S

Fig. 8 Load-axial displacement curves from experimental tests

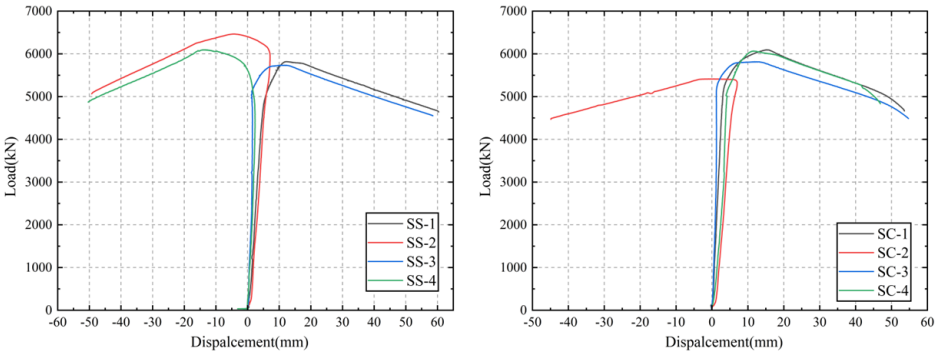

(a) Type-SS (b) Type-SC

Fig. 9 Load-lateral displacement curves from experimental tests

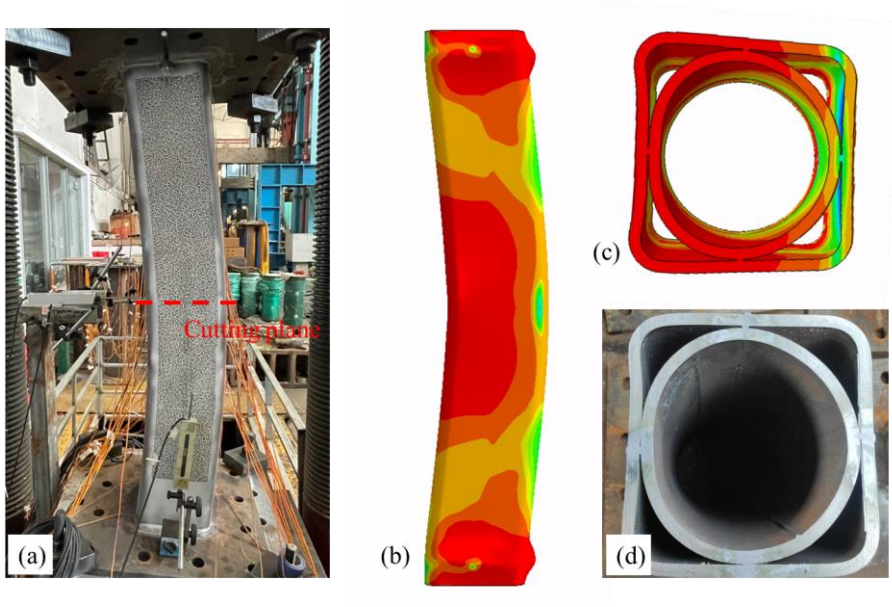

Fig. 10 Comparison of failure modes of type-SS column: experiment vs. FE simulation: (a) Experimental failure mode; (b) FE simulation – side view of displacement contour; (c) FE simulation – section view of displacement contour; (d) Cross-sectional deformation after test.

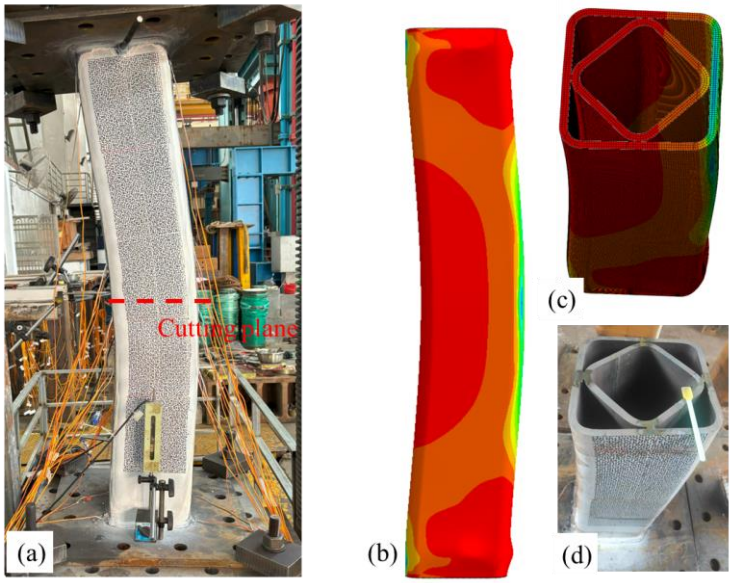

Fig. 11 Comparison of failure modes of type-SC column: experiment vs. FE simulation: (a) Experimental failure mode; (b) FE simulation – side view of displacement contour; (c) FE simulation – section view of displacement contour; (d) Cross-sectional deformation after test.

2.2.2. Results of axially compressive tests

The typical failure modes and in-plane deformation contours obtained via 2D-DIC are shown in **Fig. 6**, while the load–displacement curves for the type-SS and SC specimens are presented in **Fig. 8**. Specimens consistently exhibited three-phase responses: elastic stage, strain hardening, progressive softening, confirming material strength-dominated failure behavior.

At the initial stage of loading, all specimens exhibited an elastic load–displacement response, characterized by predominant axial compression and negligible cross-sectional deformation. As the load increased, lateral bending gradually developed in the type-SS/SC columns, accompanied by rotation at the rotational hinges. In contrast, local buckling at both loaded ends was observed in the type-S columns, as shown in **Fig. 7**. Moreover, the unloading slope K_{un} of the type-S columns was noticeably steeper than that of the type-SS/SC columns as shown in **Table 4**, indicating a more abrupt loss of strength. The failure modes are summarized in **Table 4**. It can be observed that all composite-section specimens exhibited global buckling as the primary failure mode, whereas the specimen without an inner tube experienced local buckling failure.

These observations suggest that the composite SS/SC columns effectively prevent premature local buckling and exhibit a slower strength degradation after peak load, maintaining a certain load-bearing capacity even under large deformations.

Fig. 9 presents the load–lateral displacement curves for the type-SS and type-SC columns. The lateral displacement initially exhibited a linear increase of approximately 5 mm before reaching the peak load. As global deformation developed, the lateral displacement abruptly increased in different directions, due to initial imperfections and variations in column placement orientation. At the point of unloading, the average lateral displacement reached 57.7 mm for the type-SS columns and 47.6 mm for the type-SC columns, indicating that both types of composite columns experienced significant global bending deformation during the failure process.

In addition, the post-failure cross-sectional deformation characteristics observed through wire-cutting are also presented. **Fig. 10** and **Fig. 11** compare the cross-sectional deformation patterns of type-SS and type-SC columns. It can be seen that the inner circular tube in the SC configuration experiences more significant deformation than that in the SS configuration. This observation is consistent with the load–displacement curves shown in **Fig. 8**, where the type-SS columns exhibit a longer ascending branch and an average ultimate load approximately 3% higher than that of the type-SC columns (6027.50 kN vs. 5847.86 kN). These results indicate that the square inner tube in the SS configuration provides more effective confinement and strengthening compared to the circular inner tube in the SC configuration.

Since the 2D-DIC system is limited to capture in-plane deformations, only

the DIC results for the type-SS and type-SC columns are reported, as shown in **Fig. 6**(b) and **Fig. 6**(d). These figures display the lateral displacement contour plots of two representative specimens, SS-2 and SC-1. It can be observed that the deformation patterns are generally consistent with the load–lateral displacement curves presented in **Fig. 9**.

Table 4
Comparison of load-bearing capacities among experiment, FE Analysis and code-based calculations

Specimens	$N_{y,EXP}$/kN	$N_{u,EXP}$/kN	N_{EU}	N_{GB}	$N_{u,t,a}$/kN	$N_{u,FEA}$/kN	$N_{u,t,a}$ / $N_{u,fea}$	$N_{u,EXP}$ / N_{EU}	$N_{u,EXP}$ / N_{GB}	K_{un}	Failure mode
SS-1	4930.0	5817.37	4326.79	4210.6	6027.50	5780.75	1.01	1.34	1.38	25.19	G
SS-2	4954.1	6463.92					1.12	1.49	1.54	20.88	G
SS-3	4760.0	5734.40					0.99	1.33	1.36	23.59	G
SS-4	4870.8	6094.31					1.05	1.41	1.45	19.56	G
SC-1	4995.0	6095.84	4439.20	4329.8	5847.86	5891.14	1.03	1.37	1.41	28.43	G
SC-2	4866.9	5411.79					0.92	1.22	1.25	29.64	G
SC-3	4967.4	5816.91					0.99	1.31	1.34	29.02	G
SC-4	5061.0	6066.92					1.03	1.37	1.40	23.40	G
S-1	3311.0	3796.3	2725.40	2682.88	3823.98	/	/	1.39	1.42	38.29	L
S-2	3501.0	3894.59						1.43	1.45	31.36	L
S-3	3435.8	3814.65						1.40	1.42	36.46	L
S-4	3418.0	3790.39						1.39	1.41	37.09	L
Average							1.02	1.37	1.40		
Variance							0.003	0.004	0.004		

Note: "G" denotes global buckling and "L" denotes local buckling

2.2.3. Comparison of load-bearing capacity against design codes

A comparison between the experimental results and the resistances calculated according to EN 1993-1-1:2022 and GB 50017-2017 is presented in **Table 4**.

The axial load capacities in both design codes can be expressed using a reduction factor, with the calculation methods detailed as follows: First, the normalized slenderness ratio was calculated using Eq. (3) and (4), where L_{cr} is the effective length, i is the radius of gyration about the relevant axis, determined based on the properties of the gross cross-section; E is the elastic modulus, and f_y is the yield strength of the steel.

For EN 1993-1-1:2022, the reduction factor χ was computed using Eq. (5) and (6), where the imperfection factor α depends on the cross-section class.

$$\lambda_n = \frac{L_{\mathrm{cr}}}{i}\frac{1}{\lambda_1} \tag{3}$$

$$\lambda_1 = \pi\sqrt{\frac{E}{f_y}} \tag{4}$$

$$\chi = \frac{1}{\Phi+\sqrt{\Phi^2-\lambda_n^2}} \qquad \mathrm{but}\chi \le 1.0 \tag{5}$$

$$\Phi = 0{,}5[1+\alpha(\lambda_n - 0{,}2)+\lambda_n^2] \tag{6}$$

For GB 50017-2017, when the normalized slenderness $\lambda_n \le 0.215$, the reduction factor χ is calculated using Equation (7); when $\lambda_n > 0.215$, χ is determined by Eq. (8). The coefficients α_1, α_2, and α_3 depend on the cross-section type.

$$\chi = 1 - \alpha_1\lambda_n^2 \tag{7}$$

$$\chi = \frac{1}{2\lambda_{\mathrm{n}}^2}\left[(\alpha_2+\alpha_3\lambda_{\mathrm{n}}+\lambda_{\mathrm{n}}^2) - \sqrt{(\alpha_2+\alpha_3\lambda_{\mathrm{n}}+\lambda_{\mathrm{n}}^2)^2 - 4\lambda_{\mathrm{n}}^2}\right] \tag{8}$$

According to the EN 1993-1-1 classification, type-SS and type-SC columns were compared with cross-section class a_0, while type-S columns were classified as class a. Accordingly, in Eq. (6), the imperfection factor α was taken as 0.13 for curve a_0 and 0.21 for curve a. In contrast, under the GB 50017-2017 specification, all column types were compared with cross-section class a. Based on the Chinese code, the coefficients α_1, α_2, and α_3 used in Eq. (7) and (8) were taken as 0.41, 0.986, and 0.152, respectively.

It can be observed that the design resistances specified by both the Eurocode and the Chinese code are significantly lower than the experimental results.

This discrepancy can be primarily attributed to the higher manufacturing precision achieved through laser welding. As shown in **Table 3**, the maximum measured initial geometric imperfection is 0.41‰, whereas GB 50017-2017 recommends a geometric imperfection of 1/1000, and EN 1993-1-1:2022 suggests an equivalent imperfection in the range of 1/150 to 1/100. The lower initial geometric imperfection allows the member to reach the yield stress before significant instability occurs, enabling the material to enter the strain hardening stage. As a result, the stress continues to increase beyond yielding, leading to an ultimate strength higher than the nominal yield capacity.

3. Numerical study

To further investigate the axial compression behavior of the laser-welded composite columns (type-SS and type-SC), numerical simulations and parametric analysis were conducted. A finite element (FE) model was developed using the commercial software ABAQUS. The model was calibrated and validated against the experimental results described earlier.

The FE model incorporates the measured initial geometric imperfections reported in Section 2.1.3, and adopts the same boundary conditions and loading scheme as used in the experiment study.

After validating the FE model, a series of parametric analyses were performed to study the influence of slenderness on axial load capacity by varying the effective length of the columns. For each case, both a first-order linear elastic buckling analysis and a nonlinear static analysis with initial imperfections were carried out.

Initial geometric imperfections were introduced into the model by modifying the ABAQUS input keywords.

3.1. Material properties, element type and boundary conditions

In the finite element model, the steel was modeled using the classical metal plasticity model with isotropic hardening, and the material parameters were derived from the aforementioned tensile test results. Eight-node linear brick elements with reduced integration (C3D8R) were employed for the mesh discretization. To accurately capture the local buckling and bending behavior of the plate elements under axial compression, the global mesh size was refined to 3 mm, corresponding to three elements through the plate thickness.

Since the column ends were welded to end plates in the experiments, and the end plates were fitted to the knife-edge supports, the same boundary condition was replicated in the FE model. All nodes on the end cross-sections were coupled to reference points located 0.32 m away from the end face

centroids, representing the distance between the knife hinge rotation center and the support plane. All degrees of freedom at the reference points were constrained except for the rotation about a single axis and the axial translation (Z-direction) at one of the reference points. The finite element models of both type-SS and type-SC columns are shown in **Fig. 12**.

The axial load was applied via displacement-controlled loading, enabling precise determination of both the peak load and post-peak behavior. The load–displacement curves were obtained by extracting the reaction force and displacement at the reference points.

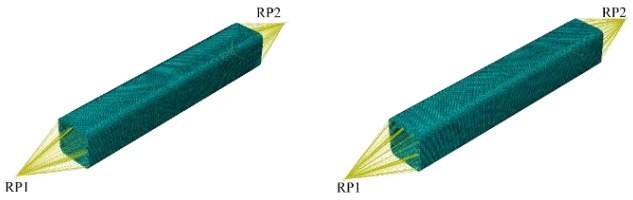

(a) Type SS (b) Type SC

Fig. 12 Finite element model of columns

3.2. Initial geometric imperfections

During the application of initial geometric imperfections in the validation of the finite element model, the imperfection amplitude was set equal to the maximum measured value for each specimen group, as reported in Section 2.1.3. The imperfection shape was taken as the lowest-order global buckling mode obtained from linear elastic buckling analysis. Specifically, the buckling mode shape was imported into the nonlinear axial compression model via the ABAQUS input file, and the imperfection amplitude was scaled according to the effective length of each column. For the type-SS columns, the applied imperfection amplitude was 0.30‰, while for the type-SC columns, it was 0.41‰.

In the subsequent parametric analysis, in order to evaluate and compare the performance of laser-welded composite columns with existing design codes, the imperfection amplitude was uniformly set to L/1000, where L is the effective length of the column., as recommended by GB 50017-2017. The imperfection shape followed the first global buckling mode derived from linear buckling analysis.

3.3. Validation of finite element model

Table 4 presents the results of the finite element (FE) analysis in terms of axial resistance, showing a maximum error of 12% for the type-SS columns and 8% for the type-SC columns. The average error across all specimens is approximately 2%, indicating good agreement in predicting the bearing capacity.

Fig. 10 and **Fig. 11** compare the deformation patterns of typical type-SS and type-SC columns observed in the experiments and those predicted by the finite element (FE) model.

The results demonstrate that the FE model successfully reproduces the global deformation behavior of the columns, as well as the local buckling of the outer wall plates (**Fig. 10**a, b), and the deformation of the inner steel tube (**Fig. 10**c, d). These findings confirm that the FE model is capable of accurately capturing the key deformation and failure mechanisms under axial loading of laser-welded composite columns.

3.4. Parametric study

To assist engineers in selecting appropriate design curves for the effective use of laser-welded composite columns, a series of axial compression simulations were conducted using the validated finite element (FE) model to investigate the performance of composite columns with varying slenderness ratios.

The actual column lengths ranged from 1200 mm to 6600 mm, at intervals of 600 mm. For each length, a finite element (FE) analysis was conducted to determine the ultimate axial load capacity, with the initial imperfection amplitude set to L/1000. Based on the results, the reduction factor (defined as the ratio of the ultimate load to the yield load) was calculated. The corresponding normalized slenderness ratios were determined using the section moment of inertia, radius of gyration, and effective length.

The results were compared with the design curves specified in EN 1993-1-1:2022 and GB 50017-2017, as shown in **Fig. 13** and **Fig. 14**. It is observed that, under EN 1993-1-1:2022, the ultimate axial capacities of type-SS columns closely align with the resistance curve for cross-section class a₀, while those of type-SC columns slightly exceed this curve. In contrast, under GB 50017-2017, the ultimate strengths of both type-SS and type-SC columns are consistently higher than the class a design curve.

Table 5 summarizes the selected column lengths, the calculated normalized slenderness ratios, and the corresponding reduction factors. It also presents the detailed results of the parametric analysis, including a comparison between the reduction factors obtained from finite element simulations and those predicted by the design codes. It is evident that both design codes provide conservative estimates compared to the FE results, with EN 1993-1-1:2022 showing closer agreement than GB 50017-2017.

Table 5
Parametric analysis results for type SS and SC with different slenderness

Section type	L/mm	$\bar{\lambda}$	$N_{u,FEA}$/kN	γ_{FEA}	$\gamma_{EU,a0}$	$\gamma_{GB,a}$	$\gamma_{FEA}/\gamma_{EU,a0}$	$\gamma_{FEA}/\gamma_{GB,a}$
SS	1200	0.39	4326.79	0.976	0.972	0.950	1.00	1.03
	1800	0.51	4211.96	0.951	0.948	0.922	1.00	1.03
	2400	0.64	4109.63	0.927	0.916	0.884	1.01	1.05
	3000	0.77	3901.69	0.880	0.869	0.833	1.01	1.06
	3600	0.89	3530.78	0.797	0.801	0.763	1.00	1.04
	4200	1.02	3062.11	0.691	0.711	0.678	0.97	1.02
	4800	1.15	2495.64	0.563	0.613	0.588	0.92	0.96
	5400	1.27	2259.88	0.510	0.523	0.505	0.97	1.01
	6000	1.40	1997.22	0.451	0.447	0.433	1.01	1.04
	6600	1.52	1726.60	0.390	0.384	0.374	1.02	1.04
SC	1200	0.38	4495.90	0.989	0.974	0.952	1.02	1.04
	1800	0.50	4357.25	0.958	0.951	0.925	1.01	1.04
	2400	0.62	4243.88	0.933	0.921	0.891	1.01	1.05
	3000	0.75	4050.00	0.891	0.879	0.843	1.01	1.06
	3600	0.87	3898.51	0.857	0.816	0.778	1.05	1.10
	4200	0.99	3426.81	0.754	0.732	0.697	1.03	1.08
	4800	1.11	3037.17	0.668	0.637	0.610	1.05	1.10
	5400	1.24	2486.05	0.547	0.547	0.527	1.00	1.04
	6000	1.36	2207.07	0.485	0.469	0.455	1.03	1.07
	6600	1.48	1881.46	0.414	0.404	0.393	1.02	1.05
Average							1.01	1.04

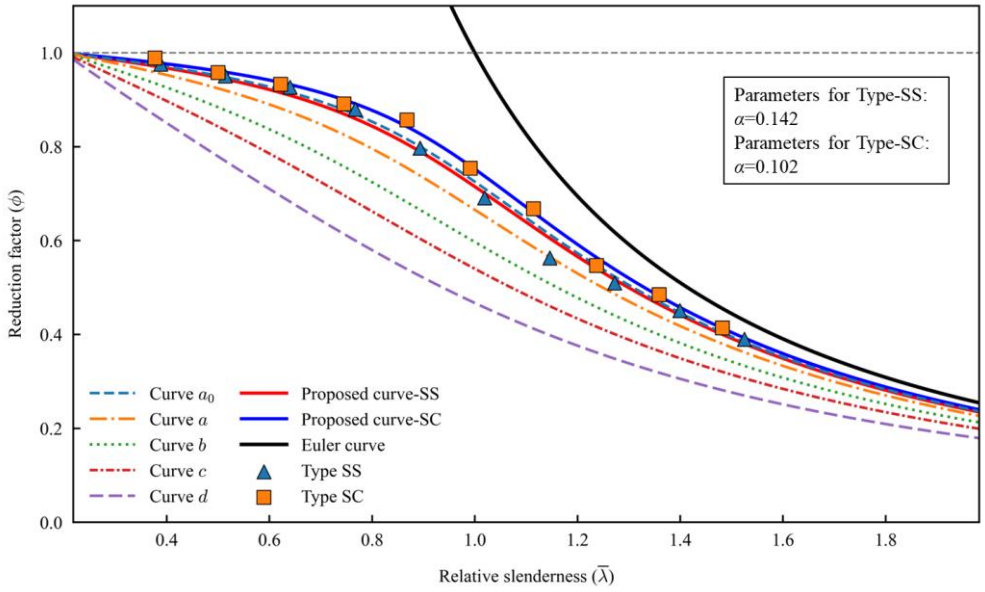

Fig. 13 Comparison of reduction factor between FE results and EN 1993-1-1:2022

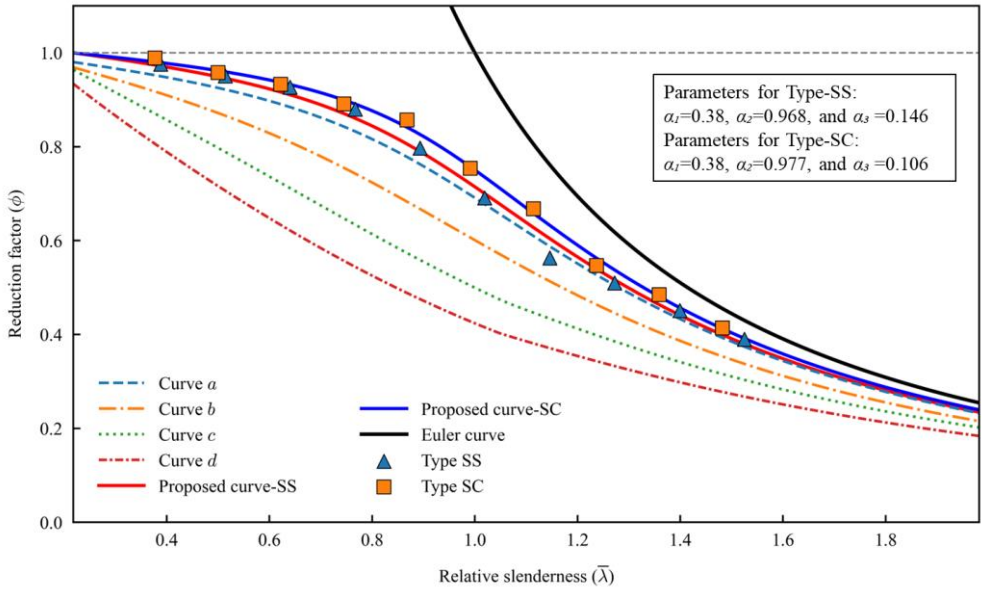

Fig. 14 Comparison of reduction factor between FE results and GB 50017-2017

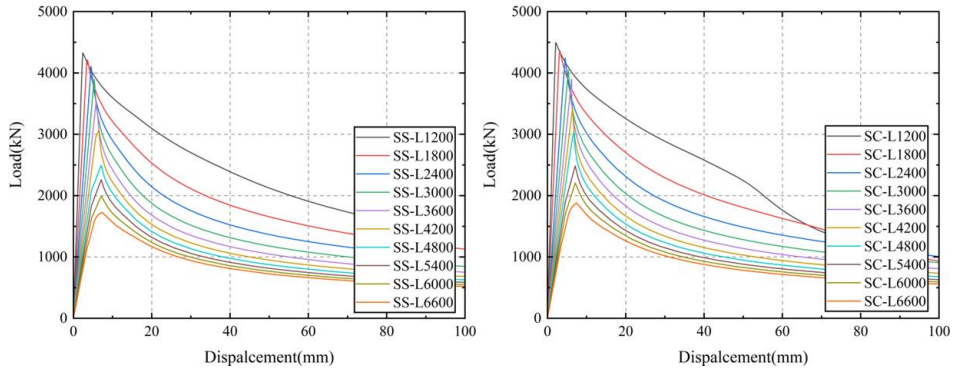

(a) Type-SS (b) Type-SC

Fig. 15 Load–displacement curves with different lengths

As both design codes exhibit varying degrees of conservatism in predicting the bearing capacities of the two composite cross-sections, a regression analysis was conducted to minimize the error (in terms of R-squared) with respect to the parametric FE results. Based on this analysis, the following optimized parameters were obtained:

For the calculation method proposed in EN 1993-1-1:2022 (Eq. 5-6), the

recommended imperfection factor α is 0.142 for type-SS columns and 0.102 for type-SC columns. For the calculation method specified in GB 50017-2017 (Eq. 7-8), the recommended values of α_1, α_2, and α_3 for type-SS columns are 0.38, 0.968, and 0.146, respectively; for type-SC columns, the corresponding values are 0.38, 0.977, and 0.106. The curves of regression fitting results are also illustrated in **Fig. 13** and **Fig. 14**.

Fig. 15 presents the load–displacement curves obtained from FE analysis for type-SS and type-SC columns with various lengths. As the column length increases, the ultimate load capacity gradually decreases, while the displacement corresponding to the peak load increases.

Notably, under the assumption of an initial imperfection amplitude of L_{cr}/1000, the type-SC columns exhibit higher ultimate strengths than the type-SS columns at the same length. This trend is in contrast to the results obtained from simulations using the measured imperfections, as well as from the experimental tests. This discrepancy may indicate that the square-in-square (type-SS) composite configuration is more sensitive to global imperfections. Further investigation into this behavior is therefore recommended.

4. Conclusions

This study conducted experimental investigations and numerical simulations to evaluate the compressive behavior of LAHW tube-in-tube composite steel columns made from S355J0 steel. Key conclusions from this research are summarized as follows:

(1) Both composite column types (square-in-square and circular-in-square) demonstrated superior post-peak behavior compared to the traditional single square hollow section columns, effectively preventing premature local buckling and exhibiting gradual strength degradation after peak load.

(2) Composite columns fabricated by LAHW exhibited minimal initial imperfections, significantly lower than the values recommended by current design standards, thereby achieving higher precision and improved axial load performance.

(3) Finite element models validated by the experiments accurately predicted the ultimate loads and failure modes, including global and local deformation behavior, confirming their suitability for structural analysis and design applications.

(4) The parametric analysis showed that the normalized slenderness significantly affects the ultimate strength of composite columns. Both the EN 1993-1-1:2022 and GB 50017-2017 standards provided conservative predictions compared to experimental and numerical results, with EN 1993-1-1:2022 offering slightly better agreement.

(5) Under a uniform initial imperfection amplitude assumption (L/1000), numerical simulations indicated that circular-in-square (SC) columns exhibited marginally higher ultimate strengths than square-in-square (SS) columns for identical lengths. This finding contrasts with the experimental outcomes and highlights the potential sensitivity of SS configurations to global imperfections, warranting further investigation.

In summary, this study suggests that the class a_0 curve from EN 1993-1-1:2022 or the class a curve from GB 50017-2017 can serve as suitable design curves, balancing safety and structural economy for LAHW composite steel columns.

Acknowledgements

This work was supported by grants from the Basic and Applied Basic Research Foundation of Guangdong Province (Grant No. 2025A1515010443). The authors also gratefully acknowledge Peak Kong Special Steel Company Limited for providing the experimental materials and conducting the welding procedures.

References

[1] Ferdous, W., Y. Bai, T. D. Ngo, A. Manalo, and P. Mendis, "New advancements, challenges and opportunities of multi-storey modular buildings – a state-of-the-art review", *Engineering Structures*, 183, 883–893, 2019.

[2] Boyd, N., M. M. A. Khalfan, and T. Maqsood, "Off-site construction of apartment buildings", *Journal of Architectural Engineering*, 19, 51–57, 2013.

[3] Wang, J., S. Afshan, N. Schillo, M. Theofanous, M. Feldmann, and L. Gardner, "Material properties and compressive local buckling response of high strength steel square and rectangular hollow sections", *Engineering Structures*, 130, 297–315, 2017.

[4] Ma, J.-L., T.-M. Chan, and B. Young, "Tests on high-strength steel hollow sections: A review", *Proceedings of the Institution of Civil Engineers - Structures and Buildings*, 170, 621–630, 2017.

[5] Yang, L., F. Yin, J. Wang, A. Bilal, A. H. Ahmed, and M. Lin, "Local buckling resistances of cold-formed high-strength steel SHS and RHS with varying corner radius", *Thin-Walled Structures*, 172, 2022.

[6] Li, B., Y. Wang, X. Zhi, Y. Zhang, and C. C. Baniotopoulos, "Testing, modelling and design of 7A04-T6 high-strength aluminium alloy RHS columns under axial compression", *Journal of Building Engineering*, 57, 104910, 2022.

[7] Zhu, Y., Z. Yang, S. Su, Y. Chen, M. Zhang, and G.-Q. Li, "Cross-sectional behaviour and design of hot-rolled carbon steel circular hollow section beams under moment gradients", *Thin-Walled Structures*, 215, 113454, 2025.

[8] Lin, Y.-J., K.-Q. Liu, T.-J. Li, and Y. Zhou, "Numerical study and design method of high strength steel welded box columns", *Advanced Steel Construction*, 17, 127–135, 2021.

[9] Yan, J.-B., B. Zhang, J.-Y. Feng, Y.-S. Du, Y.-B. Luo, and Y.-D. Shi, "Low-temperature compression behaviour of circular stub stainless-steel tubular columns", *Advanced Steel Construction*, 18, 670–678, 2022.

[10] Meng, X., S. Whitfield, S. Boudjabeur, and L. Gardner, "Stability of hot-finished and cold-formed steel hollow section columns: A comparative study", *Structures*, 68, 107192, 2024.

[11] Wang, Y., A. Su, H. Yang, J. Zhao, and Y. Wang, "S890 hot-rolled ultra-high strength steel (UHSS) seamless circular hollow section beam–columns: Testing, modelling and design", *Thin-Walled Structures*, 197, 111583, 2024.

[12] Wang, Y., H. Yang, Y. Wang, and A. Su, "Testing, numerical modelling and design of S890 and S960 ultra-high strength steel circular hollow sections under combined loading", *Thin-Walled Structures*, 192, 111102, 2023.

[13] Yin, F., J. Wang, L. Yang, N. Kang, and F. Elliott, "Testing and design of cold-formed high strength steel square hollow section columns", *Journal of Constructional Steel Research*, 213, 108394, 2024.

[14] Li, Y.-C., Y. Lu, A.-H. Han, W.-H. Li, X.-W. Wang, and Z.-L. Wu, "Local buckling mechanism of cold-formed steel built-up columns: Experimental and numerical investigation", *Advanced Steel Construction*, 21, 218–230, 2025.

[15] Zhao, J., Y. Peng, H.-X. Li, X.-X. Zhang, and J. Dong, "Structural properties of cold-formed thin-walled rectangular high-strength stainless-steel spliced tubular columns under axial compression and compression-bending", *Advanced Steel Construction*, 21, 182–193, 2025.

[16] Yin, F., X. Li, C. Chen, L. Zhao, Y. Peng, and Z. Tian, "Microstructure and mechanical properties of weld metal in laser and gas metal arc hybrid welding of 440-MPa-grade high-strength steel", *Journal of Iron and Steel Research International*, 28, 853–861, 2021.

[17] Zhang, M., Z. Zhang, K. Tang, C. Mao, Y. Hu, and G. Chen, "Analysis of mechanisms of underfill in full penetration laser welding of thick stainless steel with a 10 kW fiber laser", *Optics & Laser Technology*, 98, 97–105, 2018.

[18] Yan, R.-Z., C.-L. Zhang, S. Wang, J.-Q. Liu, and T. Sun, "Distribution of residual stress in the sphere-pipe connection welds of welded hollow spherical joints", *Advanced Steel Construction*, 19, 262–272, 2023.

[19] Wang, J.-X., X.-G. Shi, Z.-L. Liu, T. Ding, Q.-Z. Xiang, and Z.-H. Huang, "STUDY ON FRACTURE BEHAVIOR OF CHS-X JOINTS WITH WELD DEFECTS", *Advanced Steel Construction*, 21, 253–264, 2025.

[20] Liu, X.-Y., Y.-Q. Wang, Y.-D. Bu, and Y. Guan, "Study on micromechanical fracture models of structural steel and its welds", *Advanced Steel Construction*, 17, 104–126, 2021.

[21] Jie, Z.-Y., W.-J. Wang, P. Zhuge, Y.-D. Li, and X. Wei, "Fatigue properties of inclined cruciform welded joints with artificial pits", *Advanced Steel Construction*, 17, 20–27, 2021.

[22] Sokolov, M., A. Salminen, V. Somonov, and A. F. H. Kaplan, "Laser welding of structural steels: Influence of the edge roughness level", *Optics & Laser Technology*, 44, 2064–2071, 2012.

[23] Sokolov, M., A. Salminen, M. Kuznetsov, and I. Tsibulskiy, "Laser welding and weld hardness analysis of thick section S355 structural steel", *Materials & Design*, 32, 5127–5131, 2011.

[24] Zhong, Y., Y. Liang, and O. Zhao, "Membrane residual stresses and compressive behaviour of laser-welded stainless steel T-sections", *Thin-Walled Structures*, 189, 110741, 2023.

[25] Yang, S., D. Wang, L. Yang, F. Zhang, C. Zhang, B. Zhou, C. Liu, and G. Huang, "Effects of laser-arc hybrid welding on microstructure and mechanical properties of dissimilar steel joint", *Optik*, 268, 169795, 2022.

[26] Zhang, C., M. Gao, and X. Zeng, "Influences of synergy effect between laser and arc on laser-arc hybrid welding of aluminum alloys", *Optics & Laser Technology*, 120, 105766, 2019.

[27] Hu, B. and G. Den Ouden, "Synergetic effects of hybrid laser/arc welding", *Science and Technology of Welding and Joining*, 10, 427–431, 2005.

[28] Hu, B. and G. Den Ouden, "Laser induced stabilisation of the welding arc", *Science and Technology of Welding and Joining*, 10, 76–81, 2005.

[29] Sokolov, M. and A. Salminen, "Experimental investigation of the influence of edge morphology in high power fiber laser welding", *Physics Procedia*, 39, 33–42, 2012.

[30] Design standard for steel structures: GB50017-2017, Beijing: China Construction Industry Press, Beijing, 2017.

[31] Eurocode 3. Design of steel structures. Part 1-1, general rules and rules for buildings, British Standards Institution, London, 2023.

[32] Metallic materials — Tensile testing — Part 1: Method of test at room temperature, the International Organization for Standardization, Geneva, Switzerland, 2019.

[33] Specification and qualification of welding procedures for metallic materials — Welding procedure specification — Part 1: Arc welding, International Organization for Standardization, Geneva, Switzerland, 2019.

Advanced Steel Construction – Vol. 21 No. 4 (2025) 357–366
DOI:10.18057/IJASC.2025.21.4.8

FROM CLASSICAL MODELS TO NEURAL OPERATORS: A STUDY ON MOORING TENSION PREDICTION FOR FLOATING OFFSHORE WIND TURBINE

Lang-Wei Zhong [1, 2], Yu-Ping Lan [1, 2], Xi-Wei Tang [1], Wei Huang [1, 2, *], Jian-Wen He [3] and Si-Wei Liu [4]

[1] *School of Civil Engineering, Sun Yat-Sen University, Guangzhou, China*
[2] *State Key Laboratory of Coastal and Offshore Engineering, Dalian University of Technology, Dalian, China*
[3] *Research Center of Submarine Pipeline and Cable, Research Institute of Tsinghua University in Shenzhen, Shenzhen, China*
[4] *Department of Civil and Environmental Engineering, The Hong Kong Polytechnic University, Hung Hom, Kowloon, Hong Kong, China*
** (Corresponding author: E-mail: huangw288@mail.sysu.edu.cn)*

ABSTRACT

Offshore wind technology has emerged as a promising solution for harnessing wind resources in both shallow and deep waters. For floating offshore wind turbines, mooring systems play a critical role in maintaining station-keeping functions. Effective monitoring of mooring loads is essential to ensure safe and cost-efficient operation and maintenance. However, direct measurement of dynamic mooring line tensions is often costly and impractical. To address this challenge, this paper focuses on predicting mooring tensions using accessible motion data from the floating platform. We propose the use of deep learning algorithms, including deep neural networks and deep operator networks, to predict the mooring tension of floating offshore wind turbines based on six-degree-of-freedom (6-DOF) platform motions from OpenFAST or OrcaFlex under extreme sea conditions as input. We compare the prediction accuracy and generalization performance of various models, with the Transformer model under a local attention mechanism (LA-Transformer) and the multi-input deep operator network with an attention mechanism (MIONet-ATT) standing out as the top performers. Specifically, LA-Transformer inherits the precise and efficient foundational architecture of Transformer while pruning timing-independent components, achieving an optimal balance between computational complexity and accuracy. It is a novel model with outstanding precision and a moderate parameter size. MIONet-ATT, designed based on the concept of operator networks, offers better interpretability and generalization. Additionally, it demonstrates promising potential in non-extreme sea state applications.

ARTICLE HISTORY

Received: 16 February 2025
Revised: 7 August 2025
Accepted: 7 August 2025

KEYWORDS

Neural networks;
Deep operator networks;
Semi-submersible floating offshore wind turbine;
Moooring tension;
Transformer

1. Introduction

As the effects of global climate change and environmental degradation intensify, the development of renewable energy has emerged as a key priority for governments and research institutions worldwide. Wind energy, as a clean and inexhaustible resource, is particularly significant in supporting global sustainability initiatives [1, 2]. Offshore wind power presents unique benefits compared to onshore wind farms, including richer wind reserves, reduced noise disturbances, and no competition for land resources.

Offshore wind turbines are typically categorized into three groups depending on water depth: shallow (0–30m), intermediate (30–60m), and deep-water installations (beyond 60m). In deeper marine areas, floating offshore wind turbines (FOWTs) are deployed to maximize energy extraction. However, predicting the dynamic behavior of FOWTs remains a complex challenge due to their intricate coupling with oceanic conditions. Reliable response predictions are crucial for operational supervision, maintenance planning, and adaptive control strategies, all of which are vital for ensuring safe and efficient performance [3].

For example, anticipating mooring line tension with high accuracy allows for preemptive actions to mitigate risks such as structural damage or system failure, while also improving cost-effectiveness. Precise tension forecasting not only enhances the operational reliability of FOWTs but also extends their service life and optimizes energy production [4].

To assess the structural integrity of mooring systems and reduce the likelihood of degradation—including corrosion, wear, and fatigue—routine inspections are essential. At present, in-service physical examinations remain the most trusted method [5, 6]. However, this inspection-based approach for evaluating mooring system health is both expensive and time-consuming, similar as other topics like local scour of the monopile based on CFD-DEM [7, 8], dynamic analysis and fatigue analysis for TLP in time domain [9, 10]. As a result, researchers and industry professionals are increasingly shifting their attention toward digital real-time monitoring solutions.

Previous approaches to calculating the dynamic response of mooring lines have largely relied on numerical simulation techniques, exemplified by the contributions of Hall et al. [1], Chen et al. [2], and Zhang et al. [3], which encompass methods such as finite elements [11-14], finite difference, and lumped mass models. However, a significant challenge for these numerical methods remains achieving a balance between computational accuracy and efficiency, rendering them inadequate for the task of providing high-precision, real-time predictions of mooring tension. In their work, Sidarta et al. [4] leveraged an Artificial Neural Network (ANN) to forecast mooring line tension, utilizing vessel motion data as input parameters. Upon training, this ANN model demonstrated the capability to predict mooring line tensions across diverse sea conditions. Qiao et al. [5] observed that identical vessel motions could result in differing mooring line tensions, attributed to the vessel's reciprocating movements. This realization underscored the importance of capturing the temporal sequence dynamics between vessel motion and mooring line tension. To address this, they employed a Long Short-Term Memory (LSTM) network, a potent deep learning architecture, to develop a real-time predictor for mooring line responses. Recognizing that mooring line tension often exhibits both low-frequency and wave-frequency components, Wang et al. [6] adopted a preprocessing step involving a low-pass filter to segregate the cable tension and platform motion into their respective wave-frequency and low-frequency constituents within the training dataset. Subsequently, they utilized two separate LSTM models to train and predict the low-frequency and wave-frequency components of the cable tension, ultimately combining these predictions. Huang, Huang and Tang [15] have applied the LSTM method to predict the mooring tensions of the spread catenary and taut mooring system considering the dynamic stiffness of the polyester ropes, Tang et al. predicted the mooring tension of the FOWT combined the CNN-LSTM-ATT method and Chebyshev polynomials [16].

In a comparative analysis, Payenda et al. [17] evaluated three recurrent neural network models for predicting mooring cable tension in semi-submersible floating wind turbines, concluding that the Bidirectional LSTM model exhibited superior performance. In mostly previous studies, the input data for ANNs in the field of mooring line tension prediction were the six-degree-of-freedom (6-DOF) responses of the floater. The responses of floating platform motions can be readily obtained in practice through a global positioning system (GPS), which offers high accuracy and stability, or by utilizing sensors such as gyroscopes, accelerometers, magnetometers, or other direct and convenient measurement devices [18].

We believe that the task of predicting mooring line tension based on platform motion falls into the category of short-term dependent time series prediction. Although the platform's reciprocating motion may lead to different mooring line tensions at the same position, the current mooring line tension is predominantly influenced by recent motions rather than those from the distant past. As a result, LSTM is undoubtedly the benchmark model for this prediction task and remains the mainstream approach in existing literature. In addition to LSTM, other models such as one-dimensional convolutional neural networks (CNNs), GRU, BiLSTM and modified Transformers are also suitable for short-term dependencies. It is worth noting that while native Transformers are primarily designed for handling long-term dependencies[9], they can be adapted to short-term tasks by limiting attention windows or adjusting network architectures. Furthermore, hybrid models combining these techniques may

offer additional benefits [19]. Besides these deep neural network models, we also explore the use of neural operators like DeepONet for this prediction task. Neural operators are designed to learn mappings between functional spaces and offer strong generalization capabilities. Compared to the criticized "black box property" of traditional deep neural network models, deep operator networks are considered to have better interpretability [20]. In recent years, this method has gained increasing application in the field of ocean engineering. Cao et al. [21] conducted a comprehensive evaluation of three neural operators - the Deep Operator Network (DeepONet), Fourier Neural Operator (FNO), and Wavelet Neural Operator (WNO) - for predicting floating structures' dynamic responses. Their findings demonstrated that these neural operators outperform GRU models in terms of prediction accuracy.

Subsequent research has further advanced this field. Zhao et al. [22] developed a fully adaptive time-frequency coupling forecasting model (FTD) by integrating deep operator networks with a self-attention mechanism. This innovative approach exhibited superior prediction accuracy and generalization capability compared to the original DeepONet model. In another study, Zhang et al. [23] proposed a Multiple-Input Operator Network (MIONet), which demonstrated enhanced accuracy and broader applicability when benchmarked against both LSTM and DeepONet models. Similarly, Zhao et al. [22] confirmed that the Multi-Branch DeepONet Model achieves higher precision in ship motion prediction, reinforcing the effectiveness of neural operator-based approaches in marine engineering applications.

In recent years, the prediction of mooring line tension has been extensively studied in ocean engineering, with various deep learning models being employed for this purpose. Long Short-Term Memory (LSTM) networks have emerged as the most prevalent approach, alongside Gated Recurrent Units (GRU) and Transformer architectures. Earlier research also utilized Backpropagation (BP) neural networks for this task. While newer approaches like Deep Operator Networks (DeepONet) have begun gaining attention in ocean engineering applications, their specific application to mooring line tension prediction remains unexplored in the literature.

This study begins by examining the fundamental paradigms of deep neural networks before delving into the methodology of deep operator networks. Building on this foundation, the paper proposes a novel operator network architecture that incorporates dual branches for displacement and velocity inputs. The research systematically compares the predictive accuracy and generalization capabilities of traditional deep learning models with those of neural operator approaches, providing valuable insights into their respective strengths and limitations.

The novelty of this paper lies in three key aspects. First, this study addresses the mooring line tension prediction problem for floating wind turbines from a dual perspective of ocean engineering and artificial intelligence. It conducts a comprehensive comparative analysis of time-series prediction neural network models designed for short-term dependencies. Second, it formulates the mooring line tension as a functional relationship dependent on the position and velocity of the fairlead. This relationship is derived by applying position and velocity operators to time-series data of mooring tension and 6-DOF platform motions, with DeepONet utilized to execute these operator-based computations. Third, the paper contrasts mature, well-established, and validated neural network models with neural operators, which are particularly suitable for modeling physical fields. These three aspects have not been thoroughly explored in existing literature, making this study an innovative contribution to the field.

2. Methodology

2.1. Numerical modeling of floating offshore wind turbine

A numerical model of the OC4-DeepCWind semi-submersible platform supporting the NREL 5-MW wind turbine was simulated using OrcaFlex and OpenFAST. OrcaFlex is designed for analyzing the dynamic behavior of offshore structures in marine and subsea applications. It models the response of floating and fixed structures to environmental forces, including waves, wind, and currents [24]. The software calculates hydrodynamic loads using the Morison equation for slender structures and potential flow theory for surrounding fluids. Aerodynamic loads on the wind turbine are computed using the blade element momentum (BEM) theory. For mooring systems, OrcaFlex employs the lumped mass method, solving mooring chain tensions through numerical techniques like the Runge-Kutta method and General alpha method. By providing time-domain simulations, OrcaFlex enables the evaluation of motion responses of floating offshore wind turbines (FOWTs), including mooring tensions, displacements, and dynamic stability under varying environmental conditions. In contrast, OpenFAST is an open-source, integrated simulation tool developed by the National Renewable Energy Laboratory (NREL) for modeling the dynamic behavior of wind turbines. It simulates wind turbine responses under various loading conditions, incorporating aeroelasticity, hydrodynamics, and control systems. This research focuses on the OC4-DeepCWind semi-submersible platform, which features three side columns arranged around a central column supporting the wind turbine. The angle between any two adjacent side columns is 120 degrees, as illustrated in Fig. 1. The mooring system of the floating wind turbine consists of three catenary lines, with a platform draft of 20m and a mooring anchor depth of 200m. The mooring tension predicted in this article refers to the fairlead tension of the mooring line aligned with the wind direction, such as Line 1 in Fig. 1, which has the maximum tension and deformation.

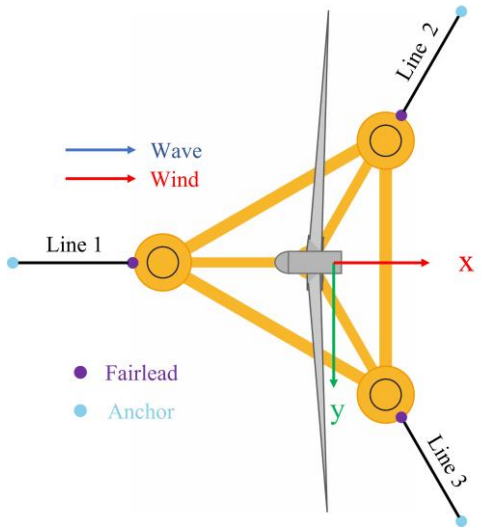

Fig. 1 The wind turbine semi-submersible platform diagram

2.2. Recurrent neural networks

Recurrent Neural Networks (RNNs) are a class of artificial neural networks designed for sequential data, where the temporal dependency among data points is crucial. By leveraging internal memory, RNNs can retain information about previous inputs, enabling them to process sequences of arbitrary length. However, standard RNNs face challenges when dealing with long-term dependencies due to the vanishing or exploding gradient problem during backpropagation through time (BPTT) [25].

LSTM networks were introduced as an extension to RNNs to address the issue of long-term dependency. LSTMs use a unique architecture incorporating three gates—input, forget, and output gates—along with a cell state to regulate the flow of information, as shown in Fig. 2. The forget gate allows LSTMs to selectively retain or discard information, while the input and output gates control the addition of new information and its propagation to the next time step. This gating mechanism makes LSTMs highly effective for capturing both short-term and long-term temporal patterns, particularly in tasks such as time-series prediction, language modeling, and speech recognition. It is worth mentioning that while LSTM is designed as an improved version of RNN specifically to address long-term dependencies, it also excels in handling short-term dependencies. This capability is attributed to the gate mechanisms of LSTM, which provide the flexibility to dynamically balance and process both short-term and long-term dependencies simultaneously [26].

The output of LSTM is denoted as y_t, and the output of LSTM cell h_t at the time t can be calculated as follows:

$$i_t = \sigma(W_i x_t + U_i h_{t-1} + b_i) \tag{1}$$

$$f_t = \sigma\left(W_f x_t + U_f h_{t-1} + b_f\right) \tag{2}$$

$$o_t = \sigma(W_o x_t + U_o h_{t-1} + b_o) \tag{3}$$

$$\widetilde{C_t} = \tanh(W_c x_t + U_c h_{t-1} + b_c) \tag{4}$$

$$C_t = f_t \odot C_{t-1} + i_t \odot \widetilde{C_t} \tag{5}$$

$$h_t = o_t \odot \tanh(C_t) \quad (6)$$

$$y_t = \sigma(W_y h_t + b_y) \quad (7)$$

where σ and $tanh$ are the sigmoid activation function and hyperbolic tangent activation function, respectively; i_t denotes input gate, f_t denotes forget gate, o_t denotes output gate, $\odot$ denotes the product of vector elements; W_*, U_* and b_* are the corresponding weight matrices to be learned, $*\in \{i, f, o, c, y\}$, and $\tilde{C}_t$ is the temporary state of the input at time t.

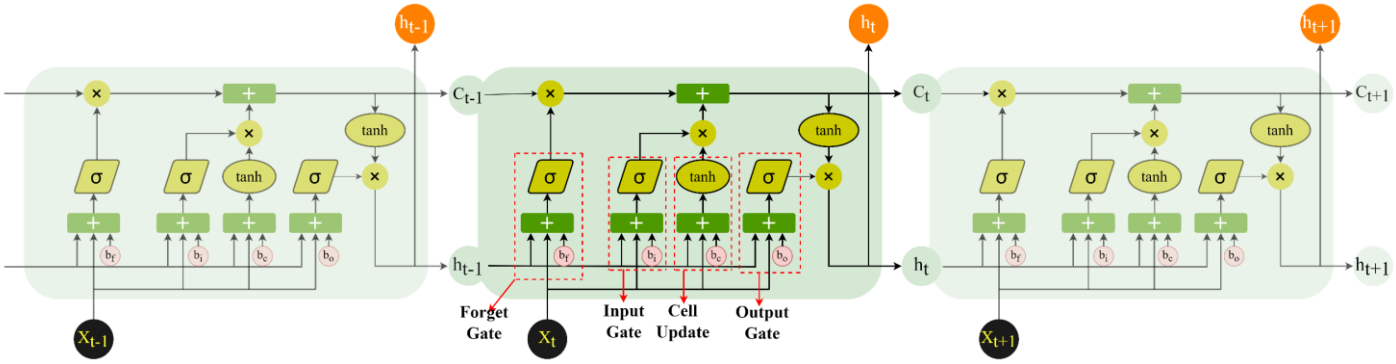

Fig. 2 The neural network structure based on the LSTM model

Bidirectional LSTM (BiLSTM) networks extend LSTMs by processing input sequences in both forward and backward directions, as shown in Fig. 3. This dual processing allows BiLSTMs to capture contextual information from both past and future time steps, making them particularly suitable for tasks where understanding the entire sequence is important, such as natural language processing (NLP) and video analysis. While BiLSTMs increase computational complexity and memory requirements, their ability to leverage bidirectional context often results in improved performance compared to unidirectional LSTMs. The output of the BiLSTM cell h_t at the time t can be calculated as follows:

$$\overrightarrow{h_t} = LSTM_{forward}(x_t, h_{t+1}) \quad (8)$$

$$\overleftarrow{h_t} = LSTM_{backward}(x_t, h_{t+1}) \quad (9)$$

$$h_t = [\overrightarrow{h_t}; \overleftarrow{h_t}] \quad (10)$$

$$y_t = \sigma(W_y h_t + b_y) \quad (11)$$

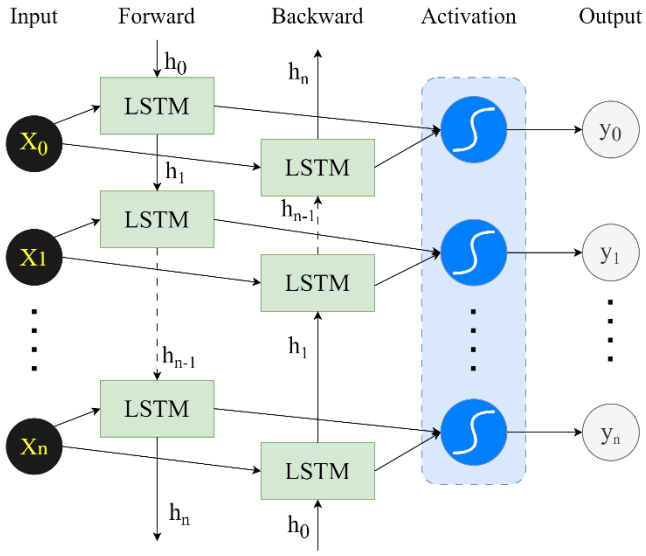

Fig. 3 BiLSTM architecture

The Gated Recurrent Unit (GRU) is another variant of RNNs, designed as a simpler alternative to LSTMs. GRUs merge the forget and input gates into a single update gate, and the cell state is directly combined with the hidden state, reducing the number of parameters, as shown in Fig. 4. Despite its simpler structure, GRUs often achieve comparable performance to LSTMs while being computationally more efficient. GRUs are particularly advantageous in scenarios with limited computational resources or datasets, where model simplicity is critical.

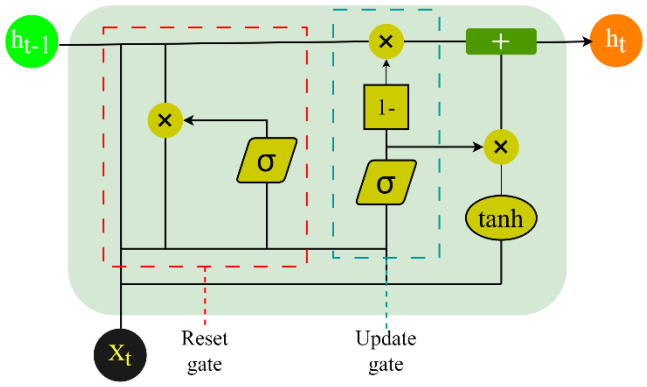

Fig. 4 GRU architecture

2.3. Convolutional neural networks

The primary goal of a Convolutional Neural Network (CNN) is to extract salient features from input data. A typical CNN architecture includes convolutional, pooling, dropout, and fully connected layers. Convolutional and pooling layers act as preprocessing layers, filtering input data and extracting valuable information for subsequent fully connected layers. Convolutional layers perform convolution operations between input data and kernels to generate feature values. These layers require structured matrix inputs, as they were initially designed for image datasets [27]. The convolution kernel, a small matrix of coefficients, slides across the input matrix, computing feature values for each subregion. Multiple kernels produce various feature maps, capturing more meaningful information than raw inputs, enhancing the model's learning and generalization capabilities. Convolutional layers are followed by nonlinear activation functions (e.g., ReLU) and pooling layers. Pooling reduces feature map dimensions, lowering computational complexity and preventing overfitting. Common methods include max pooling (selecting the maximum value) and average pooling (calculating the average value). Pooling preserves key features by summarizing local information, ensuring translation invariance. Although pooling layers lack learnable parameters, they simplify data representation and enable deeper networks. For mooring tension prediction, CNNs extract features from one-dimensional data using PyTorch's "Conv1d" and "MaxPool1d" functions. This process effectively captures patterns in time series data, supporting accurate tension prediction.

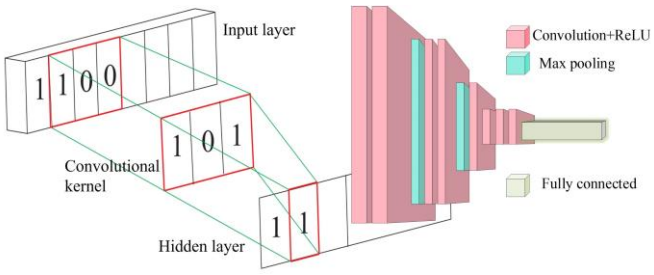

Fig. 5 Convolution layers and CNN architecture

2.4. Transformer and attention mechanism

The Attention Mechanism is a general computational framework that dynamically assigns weights to different parts of an input sequence based on their relevance to a given query. By computing a weighted sum of values, where the weights are determined by the compatibility between the query and a set of keys, it enables models to focus on the most relevant information. Self-Attention, a specialized form of the Attention Mechanism, derives queries, keys, and values from the same input sequence, allowing it to capture dependencies within the sequence by computing relationships between all positions. Building on this, the Transformer, a neural network architecture introduced by Vaswani et al. [28], replaces traditional recurrent or convolutional layers entirely with self-attention mechanisms. This design enables the Transformer to process sequences in parallel, efficiently capturing both local and global dependencies, and has revolutionized tasks in natural language processing and beyond. It is worth noting that the computational complexity of the self-attention mechanism in the original Transformer model is $O(T^2)$, where T represents the sequence length. However, for predicting mooring line tension, focusing on motion data from the distant past is often irrelevant to the current tension. To address this, we optimized the model by introducing a local attention mechanism, reducing the computational complexity to $O(nT)$, where n denotes the local range size of the attention mechanism. It is worth noting that this simplification does not come at the cost of accuracy. In other words, by applying local attention mechanisms to focus on platform motion near the current time step, the model can effectively predict tension while achieving significantly better computational efficiency—a critical advantage for edge-side deployment.

Specifically, the Transformer model with local attention used in this study has a parameter count comparable to traditional LSTMs or GRUs. Depending on operational conditions, the model size ranges between 100,000 and 1,000,000 parameters, with the original PyTorch model file typically occupying around 0.4 MB to 4 MB.

Furthermore, by applying model compression techniques such as quantization, pruning, and knowledge distillation, the model can be further reduced in size. Even low-end edge AI chips with as little as 0.5 TOPS (Tera Operations Per Second) can easily handle the deployment of such optimized models.

This design ensures high performance in real-world edge applications without sacrificing computational feasibility.

2.5. Deep operator network

DeepONet (Deep Operator Network) is a deep neural network architecture designed for learning nonlinear operators, as introduced in [29]. The DeepONet model facilitates mappings between two infinite-dimensional spaces by training on finite input-output pairs. At its core, DeepONet approximates nonlinear operators using neural networks, enabling efficient handling of high-dimensional input and output spaces. The architecture comprises two primary subnetworks: the Branch Net and the Trunk Net. The Branch Net processes information from input functions, which are typically represented in discrete form (e.g., function values at specific points), and encodes this information into a feature vector. The Trunk Net, on the other hand, processes the location information of output points, mapping their coordinates into another feature vector. Together, these subnetworks enable DeepONet to effectively model complex nonlinear relationships in high-dimensional spaces, as shown in Fig. 6. Ultimately, the output of DeepONet is the dot product of the outputs of branch networks and trunk networks:

$$\mathrm{G}(u)(y) = \sum_{i=1}^{p} b_i(u) \cdot t_i(y) \tag{12}$$

$G(u)$ is the output function corresponding to the input function u, where y represents the position of the output point, $b_i(u)$ is the output of the branch network, $t_i(y)$ is the output of the trunk network, and p is the dimension of the feature vector.

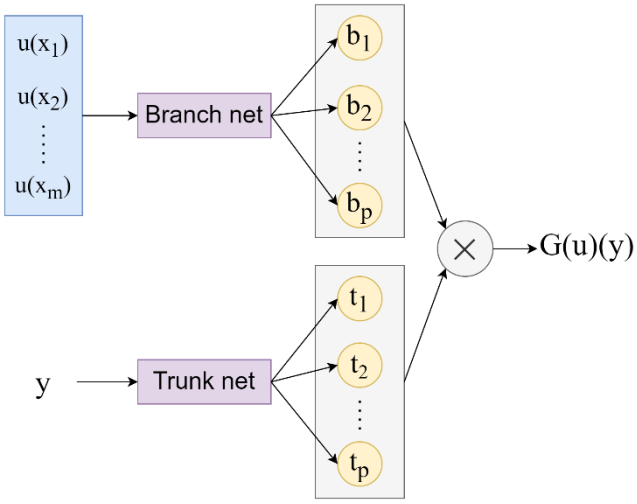

Fig. 6 Architecture of Deep operator network

The functional of mooring line tension can be expressed as a nonlinear operator mapping of fairlead position and velocity:

$$T_{moor}(t) = G_T\big(t; \dot{x}(t), x(t)\big) \tag{13}$$

3. Implemetation process

3.1. Neural network method technical route

Firstly, simulation data was obtained from OpenFAST and OrcaFlex. Secondly, the data underwent pre-processing steps, including normalization, data splitting, and sliding window processing, to prepare it for neural network training. Thirdly, the hyperparameters of the neural network were optimized to enhance model performance. Subsequently, the neural network model was trained and saved. Finally, the trained model was utilized to predict the mooring tension of the FOWT, as shown in Fig. 7.

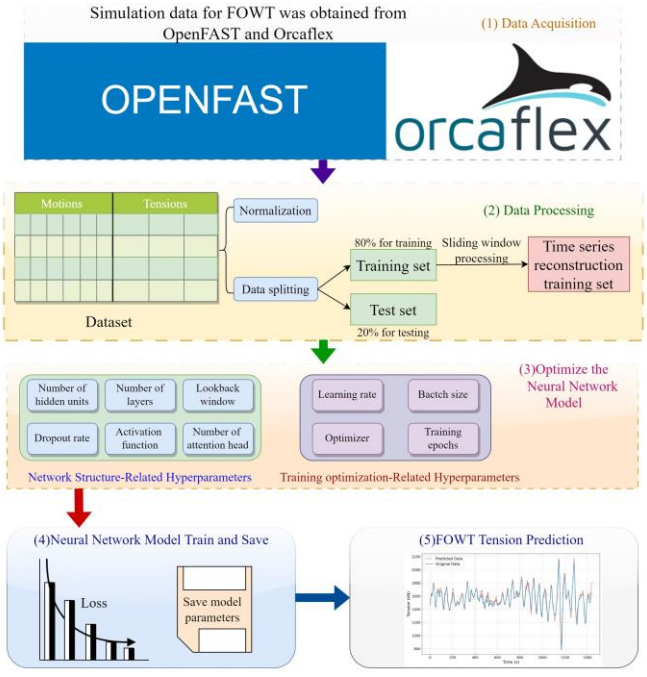

Fig. 7 Neural network method technical route

3.2. Deep operator network method technical route

For the DeepONet model, the first step involves transforming the six degrees of freedom (6-DOF) motion of the platform into the position of the cable hole using the Euler rotation matrix. The Euler rotation matrix R is defined as follows:

$$R = R_z(\psi) \cdot R_y(\theta) \cdot R_x(\phi) \tag{14}$$

where ψ, θ, and ϕ represent the yaw, pitch, and roll angles, respectively. Subsequently, the corresponding velocity is calculated through differential computation using the finite difference method:

$$v(t) = \frac{p(t + \Delta t) - p(t)}{\Delta t} \tag{15}$$

where $p(t)$ denotes the position at time t, and Δt is the time step.

In addition, the DeepONet model can be enhanced by integrating an attention mechanism. In this approach, the position and velocity data are processed by two separate branch networks, respectively. The position branch network $\mathcal{N}_p$ and the velocity branch network $\mathcal{N}_v$ are designed as fully connected neural networks. The outputs of these two branches are then combined using a self-attention mechanism $\mathcal{A}$, which computes the weighted sum of the features based on their importance. We refer to this method as $MIONet - ATT$, a multi-input DeepONet framework that incorporates an attention mechanism. The overall architecture can be expressed as:

$$y = \mathcal{A}\left(\mathcal{N}_p(p), \mathcal{N}_v(v)\right) \tag{16}$$

where p and v denote the position and velocity inputs, respectively. The key distinction between MIONet-ATT and DeepONet lies in their feature weighting strategies. MIONet-ATT employs an attention mechanism to dynamically and intelligently weight velocity and displacement vectors, enabling more precise characterization of their varying influences on tension prediction across different temporal stages. This adaptive weighting approach captures the temporal dependencies leading to superior output accuracy in modeling physical systems.

Attention mechanisms have demonstrated transformative potential across multiple AI domains through their ability to learn context-aware feature relevance. In computer vision, the evolution from YOLOv11 [30] to YOLOv12 [31] exemplifies this paradigm shift, where the traditional CNN backbone was replaced by a Transformer architecture enhanced with region attention modules, yielding significant improvements in object detection performance. The natural language processing domain has witnessed similar advancements, with models like Kimi-K2 achieving state-of-the-art results through optimized attention head configurations and innovative sparsity patterns.

The widespread adoption of attention mechanisms stems from their unique advantages, including dynamic feature relevance scoring, interpretable weight distributions, and flexible integration with various neural architectures. These characteristics make attention mechanisms particularly valuable for scientific machine learning tasks that require modeling complex physical relationships. In this work, we extend their utility by integrating attention mechanisms with DeepONet's operator learning framework, creating a hybrid approach that combines the strengths of both methodologies for enhanced physical system modeling. The resulting architecture not only improves prediction accuracy but also provides insights into the relative importance of different physical variables across temporal and spatial domains.

3.3. Model evaluation criteria

Models' performance was evaluated using three common metrics: mean absolute error (MAE), root mean square error (RMSE), and mean absolute percentage error (MAPE). These metrics quantify the difference between predicted and actual values, with lower values indicating better forecasting accuracy. Additionally, the coefficient of determination (R^2) was considered, with values closer to 1 indicating higher prediction quality. The detailed mathematical expressions for the above evaluation indicators are shown below [24].

$$R^2 = 1 - \frac{\sum_{i=1}^{n}(y_i - \hat{y}_i)^2}{\sum_{i-1}^{n}(y_i - \bar{y}_i)^2} \tag{17}$$

$$MAE = \frac{1}{n}\sum_{i=1}^{n}|y_i - \hat{y}_i| \tag{18}$$

$$RMSE = \sqrt{\frac{\sum_{i=1}^{n}(y_i - \hat{y}_i)^2}{n}} \tag{19}$$

$$MAPE = \frac{1}{n}\sum_{i=1}^{n}\left|\frac{y_i - \hat{y}_i}{y_i}\right| \times 100\% \tag{20}$$

where the y_i and $\hat{y}_i$ symbolize the measured and predicted values, respectively, and $\bar{y}$ represents the mean of all the true values.

Table 1
Environmental conditions and load cases

No.	V_w (m/s)	H_s (m)	T_p (s)	V_c (m/s)	θ_{wave} (°)
Case 1	11.4	7.5	14.8	0	0
Case 2	25.0	13.1	14.9	1.20	30
Case 3	25.0	12.6	13.7	1.27	0

In our experimental setup, we employed a systematic grid search approach to optimize the hyperparameters across all models. Given the diverse range of architectures involved in this study and potential variations in computational environments, we provide both a concise description of our hyperparameter optimization strategy and a comprehensive reference table detailing the parameter ranges (Table 2).

The model architectures in this work typically contain between 100,000 to 500,000 trainable parameters. To illustrate, our baseline LSTM implementation consists of three stacked LSTM layers with 192 units each, combined with fully-connected input and output layers, resulting in approximately 450,000 parameters. This parameter scale has proven sufficient for capturing the complex temporal dependencies in our regression tasks while maintaining computational efficiency.

For training configuration, we established 100 epochs as the upper limit while implementing an early stopping criterion that terminates training when the validation loss fails to improve for 10 consecutive epochs. In practice, most models converged within 40-60 epochs, demonstrating stable learning dynamics. This balanced approach ensures thorough optimization without unnecessary computational overhead.

The complete hyperparameter search space, including learning rates, batch sizes, and regularization coefficients, is systematically documented in the supplementary materials to facilitate reproducibility and future benchmarking efforts.

Table 2
Hyperparameters and model configurations

Hyperparameters	Reference range
Number of layers	2-4 layers
Number of units (hidden_size)	96-256 units
Initial learning rate	4×10^{-3}
Batch size	32
Activation function	ReLU
Optimizer	Adam (β_1=0.9, β_2=0.999)

4. Case study

This paper refers to the extreme sea conditions in the South China Sea and sets four cases to explore the predictive performance of different models. The wind conditions are characterized by turbulence, adhering to a Kaimal wind spectrum and blowing in a positive x-axis direction. The waves follow a Jonswap spectrum, while the flow is maintained as constant. Specific parameters are listed in Table. 1, where the abbreviation "*w*" stands for "wind", and "*c*" stands for "current".

4.1. Performance evaluation of neural/operator network models

We will divide the models into three groups: Group A (GRU, LTSM,

BiLSTM), Group B (LSTM, CNN-LSTM-ATT, LA-Transformer (Local Attention Transformer)), and Group C (LSTM, DeepONet, MIONet-ATT), using the LSTM model as the benchmark model to evaluate these models' performance.

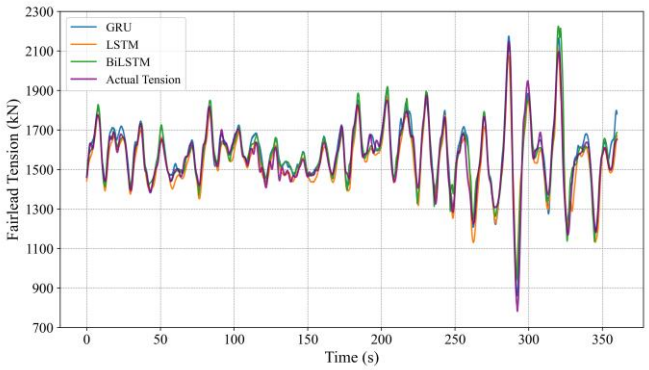

Fig. 8 Comparison of the performance metrics of different models (Case 1, Group 1)

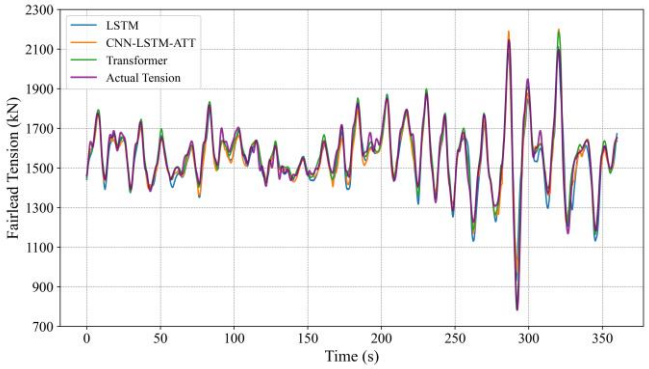

Fig. 9 Comparison of the performance metrics of different models (Case 1, Group 2)

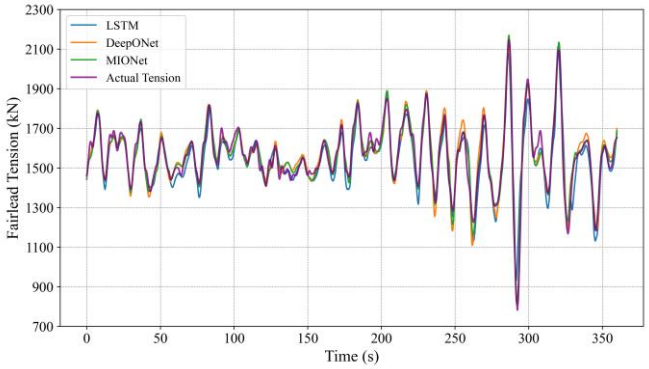

Fig. 10 Comparison of the performance metrics of different models (Case 1, Group 3)

Table 3
Comparison of Performance Metrics for Different Models: Case 1

Model	RMSE (kN)	MAE (kN)	MAPE	R^2
GRU	41.80	30.62	2.02%	0.953
LSTM	52.60	37.90	2.51%	0.913
BiLSTM	52.14	34.52	2.38%	0.919
CNN-LSTM-ATT	42.25	31.24	2.07%	0.951
LA-Transformer	28.52	21.71	1.42%	0.969
DeepONet	37.75	29.27	1.93%	0.945
MIONet-ATT	31.65	23.39	1.53%	0.961

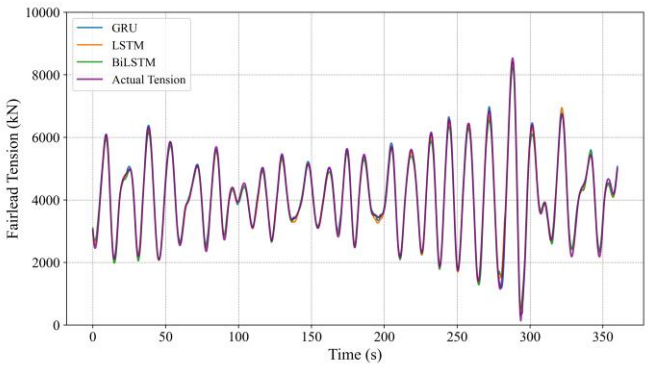

Fig. 11 Comparison of the performance metrics of different models (Case 2, Group 1)

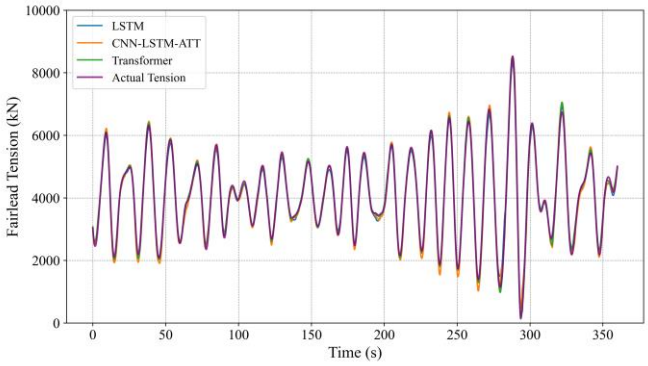

Fig. 12 Comparison of the performance metrics of different models (Case 2, Group 2)

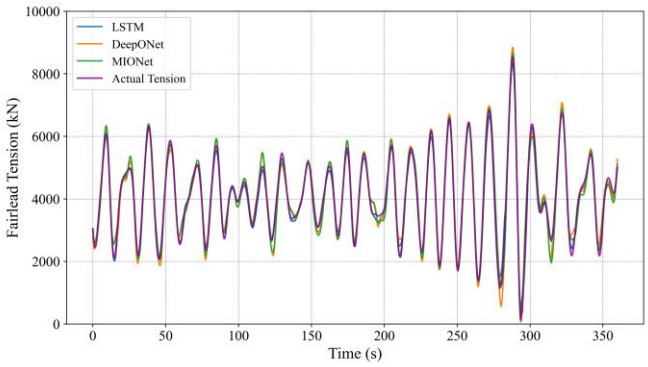

Fig. 13 Comparison of the performance metrics of different models (Case 2, Group 3)

Table 4
Comparison of Performance Metrics for Different Models: Case 2

Model	RMSE (kN)	MAE (kN)	MAPE	R^2
GRU	95.39	70.22	2.30%	0.995
LSTM	114.87	91.32	3.18%	0.992
BiLSTM	117.70	88.36	3.08%	0.992
CNN-LSTM-ATT	128.87	97.62	3.40%	0.990
LA-Transformer	80.29	59.56	1.83%	0.996
DeepONet	231.23	177.96	5.67%	0.968
MIONet-ATT	213.34	163.90	5.02%	0.972

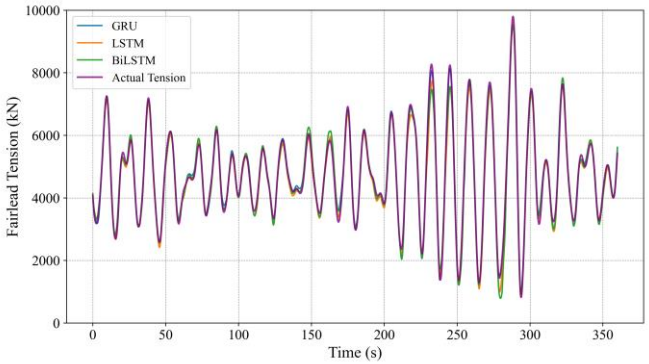

Fig. 14 Comparison of the performance metrics of different models (Case 3, Group 1)

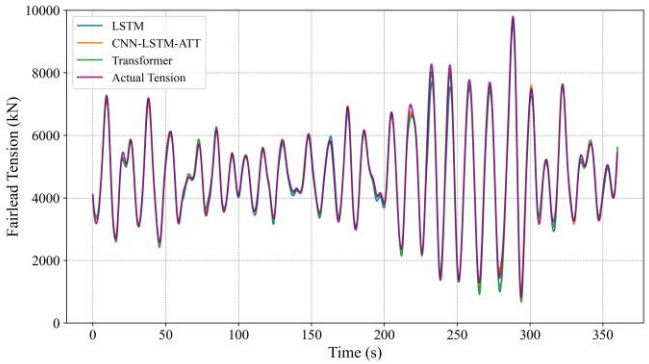

Fig. 15 Comparison of the performance metrics of different models(Case 3, Group 2)

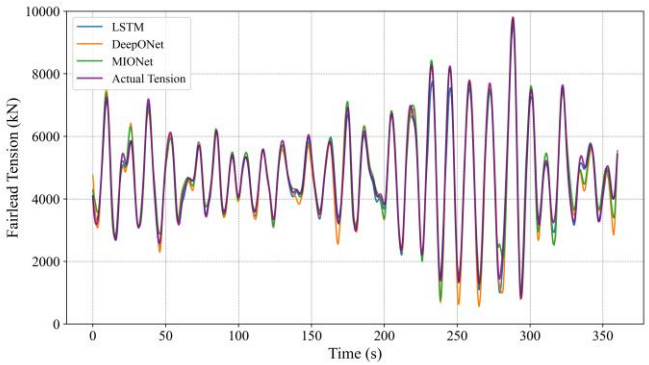

Fig. 16 Comparison of the performance metrics of different models(Case 3, Group 3)

Table 5
Comparison of Performance Metrics for Different Models: Case 3

Model	RMSE (kN)	MAE (kN)	MAPE	R^2
GRU	123.76	96.09	2.39%	0.993
LSTM	180.31	126.75	2.92%	0.985
BiLSTM	189.94	132.39	3.05%	0.983
CNN-LSTM-ATT	92.67	70.47	1.75%	0.996
LA-Transformer	128.94	88.89	2.33%	0.992
DeepONet	312.01	229.54	6.18%	0.955
MIONet-ATT	264.67	198.74	5.21%	0.968

In order to ensure a fair comparison between different neural network architectures, we adjust the number of layers and the number of neurons in each layer of the models. This adjustment aims to keep the parameter counts of the models on the same order of magnitude. For example, the number of layers in the LSTM model is set to be twice that of the BiLSTM model. Neural networks demonstrate strong predictive performance, with the Transformer model achieving the highest accuracy. This validates our approach to predicting mooring line tension based on short-term dependency time series data. However, the neural operator exhibits slightly reduced accuracy under once-in-a-century sea conditions, particularly at peak and trough regions, as shown in Fig. 17. These regions coincide with significant velocity changes, where errors in velocity—derived from position differences—are more pronounced. Additionally, the input velocity data itself contains inherent uncertainties, which may contribute to these inaccuracies.

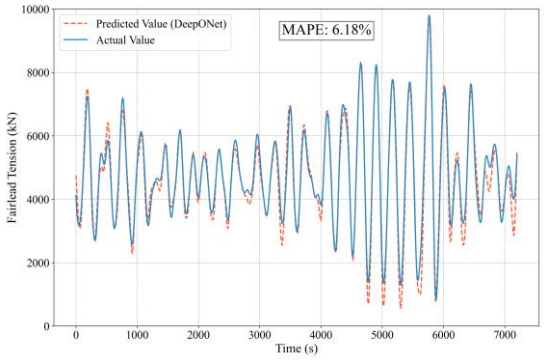

(a) DeepONet, Case 2

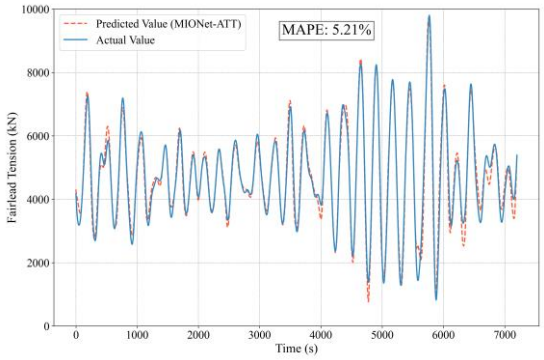

(b) MIONet-ATT, Case 2

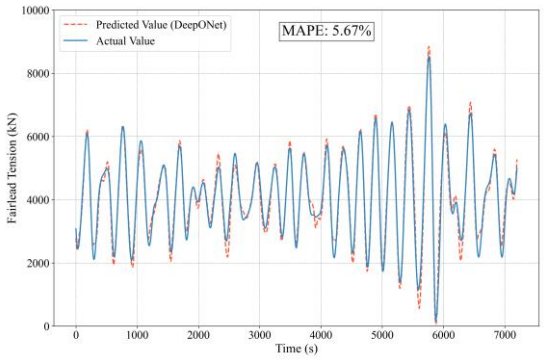

(c) DeepONet, Case 3

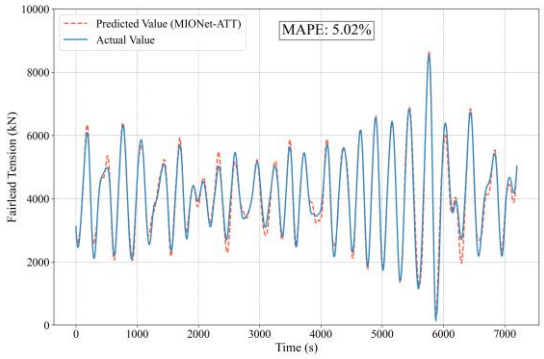

(d) MIONet-ATT, Case 3

Fig. 17 Performance evaluation of DeepONet and MIONet-ATT in Case 2 and Case 3

4.2. Generalization performance comparison of operator networks and neural networks

The concept of generalization refers to a model's ability to perform well on unseen data, a critical metric for real-world applicability. In this study, we compare the generalization performance of operator networks (e.g., DeepONet, MIONet) with traditional neural networks (e.g., LSTM, Transformer). Operator networks learn mappings between function spaces, making them effective for modeling physical fields [32, 33], while traditional networks excel at capturing discrete temporal dependencies.

To empirically evaluate generalization, we design Case 4—a loading condition intermediate between Cases 2 and 3 (Table 6.). Models are trained on 50% of time-series segments from Cases 2-3 and 20% from Case 4, then tested on unseen segments of Case 4. This validates their ability to extrapolate under novel sea conditions.

The fundamental distinction between generalization testing and accuracy testing lies in the relationship between the training and testing datasets. In accuracy testing, where both training and testing data are drawn from different temporal segments of the same sea state, we evaluate a model's ability to make predictions within a specific, known environmental condition. In contrast, generalization testing employs training and testing sets from different sea states altogether, assessing whether a model trained on one set of conditions can be effectively applied to similar or even substantially different environmental scenarios. This capability for cross-condition prediction is particularly valuable for practical deployment, as it enables the use of fewer models across varying operational conditions, thereby conserving computational resources and simplifying implementation.

Notably, inputs differ between architectures: platform 6-DOF motions for neural networks versus fairlead position/velocity for neural operators.

Table 6
Environmental condition and load case for generalization validation

No.	V_w (m/s)	H_s (m)	T_p (s)	V_c (m/s)	θ_{wave} (deg)
Case 4	25.0	12.8	14.3	1.24	0

The generalization test results are as follows:

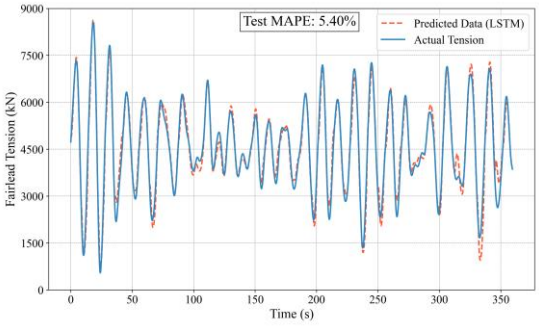

(a) LSTM

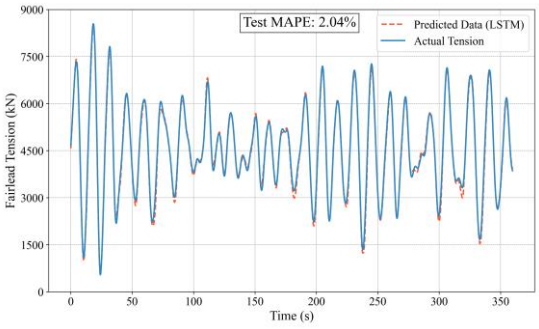

(b) LA-Transformer

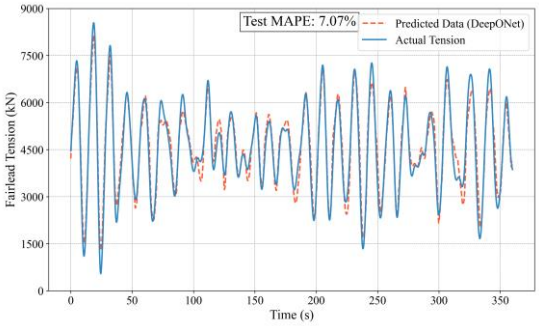

(c) DeepONet

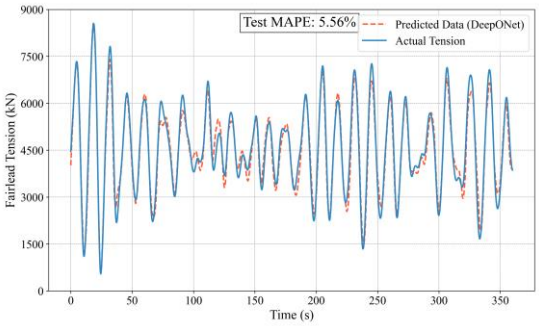

(d) MIONet-ATT

Fig. 18 Generalization validation of neural network models and neural operator models

Table 7
Comparison of generalization performance for different models: Case 4

Model	RMSE (kN)	MAE (kN)	MAPE	R^2
LSTM	265.88	193.64	5.40%	0.965
LA-Transformer	104.67	76.26	2.04%	0.995
DeepONet	328.45	257.55	7.07%	0.946
MIONet-ATT	279.98	199.38	5.56%	0.962

From the generalization test results, the LA-Transformer demonstrates superior performance, while the LSTM closely follows the MIONet-ATT, and the DeepONet lags slightly behind. Although the accuracy of neural operators is not outstanding, they still hold promising application prospects. As previously mentioned, in neural operators, the velocity vector is derived by differentiating the position vectors. During the reciprocating motion of floating platforms, the velocity undergoes significant fluctuations, which can adversely affect the accuracy of neural operators. Under other sea conditions, however, the accuracy is expected to improve. Additionally, the data sampling interval in this study is 0.05 seconds, simulating a 20Hz GPS or sensor signal. If the sampling frequency is increased, the differential velocity obtained would be more accurate. Finally, the MIONet-ATT model exhibits a notable improvement in accuracy compared to the DeepONet model, and there remains ample room for further exploration of optimization methods for neural operators. At the end of this section, we provide a proof that extreme sea conditions amplify the approximation error of first-order differences. The truncation error of first-order difference is approximately $O(\Delta t \cdot a)$, where a is the acceleration and Δt is the time step. The truncation error of $O(\Delta t \cdot a)$ in first-order difference schemes originates from Taylor series expansion analysis. The formal derivation proceeds as follows:

a. Taylor Expansion of Displacement

Consider the displacement function $s(t)$. Its Taylor expansion around time t is:

$$s(t + \Delta t) = s(t) + v(t)\Delta t + \frac{1}{2}(\Delta t)^2 + O((\Delta t)^3) \tag{21}$$

where, $v(t)$ is the instantaneous velocity, $a(t)$ is the instantaneous acceleration, $O((\Delta t)^3)$ is the higher-order infinitesimals.

b. First-Order Difference Definition

The first-order difference approximation of velocity is:

$$v_{diff}(t) \approx \frac{s(t+\Delta t) - s(t)}{\Delta t} \tag{22}$$

c. Substitution of Taylor Expansion

$$v_{diff}(t) = v(t) + \frac{a(t)}{2}\Delta t + O((\Delta t)^2) \tag{23}$$

d. Truncation Error Expression

The error between true velocity $v(t)$ and approximated velocity $v_{diff}(t)$ is

$$Error = v_{diff}(t) - v(t) = \frac{a(t)}{2}\Delta t + O((\Delta t)^2) \tag{24}$$

Neglecting higher-order terms $O((\Delta t)^2)$, the dominant error term is:

$$Error \approx \frac{a(t)}{2}\Delta t \tag{25}$$

The truncation error $O(\Delta t \cdot a)$ of the first-order difference is essentially a linear approximation defect of Taylor expansion, which is significantly enlarged when the acceleration is large or the time step is coarse. The acceleration surge under extreme sea conditions is the fundamental reason for the aggravation of the error.

We have added three non extreme sea conditions, in which the operator network has higher accuracy. The sea conditions are as follows:

Table 8
Environmental conditions in moderate sea states

No.	V_w (m/s)	H_s (m)	T_p (s)	V_c (m/s)	θ_{wave} (°)
Case 5	11.4	2	3.5	0.3	0
Case 6	11.4	5	4.5	0	0
Case 7	11.4	6	4.7	0.1	0

The operator networks demonstrates superior prediction accuracy in moderate sea states, as shown in Fig. 19.

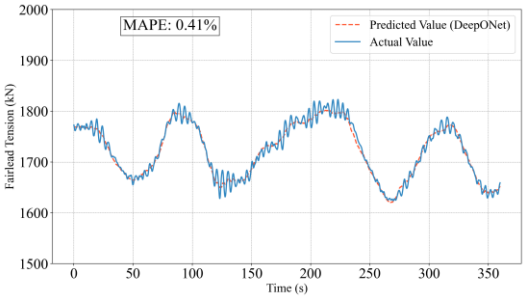

(a) DeepONet, Case 5

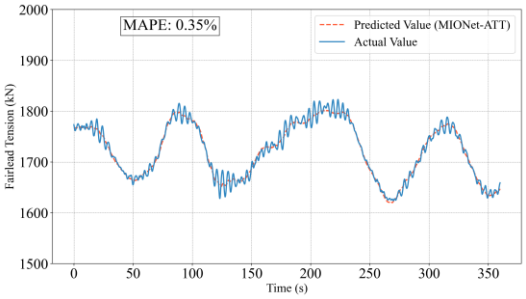

(b) MIONet-ATT, Case 5

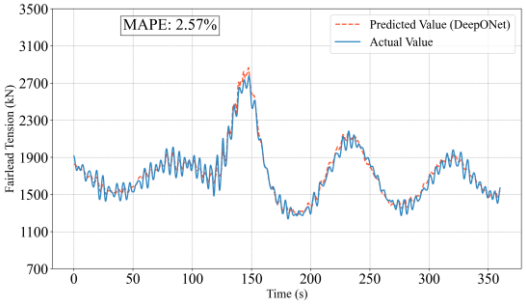

(c) DeepONet, Case 6

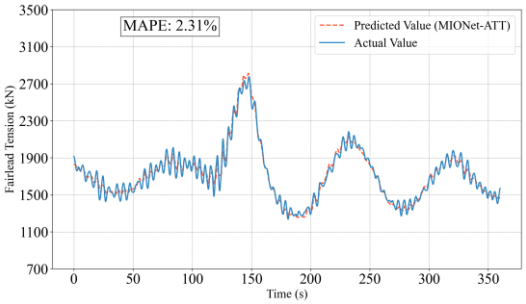

(d) MIONet-ATT, Case 6

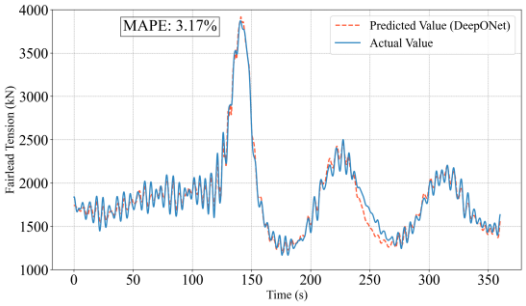

(e) DeepONet, Case 7

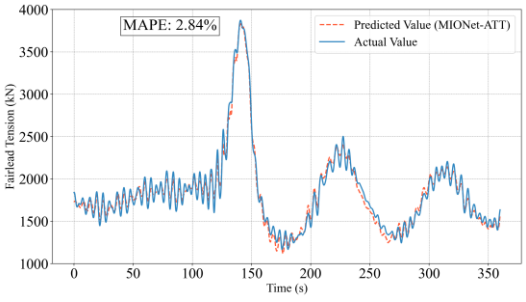

(f) MIONet-ATT, Case 7

Fig. 19 Prediction accuracy/performance of operator networks in moderate sea states

5. Conclusions

In this study, we developed several neural networks and operator networks to predict the dynamic mooring tension behavior of a semi-submersible floating wind turbine. The training and testing datasets are obtained from coupled numerical simulations in Orcaflex and OpenFAST. The neural network method utilizes the six-degree-of-freedom (6-DoF) time series of the platform as input and selects a neural network model suitable for short-term dependency time series prediction to forecast the mooring line tension of floating wind turbines. On the other hand, the operator network method first transforms the 6-DoF motion of the platform into the position of the fairlead through Euler rotation. The velocity is then obtained by differentiating the position, and the mooring tension is assumed to depend solely on the position and velocity of the fairlead, without considering changes in hydrodynamic forces. Consequently, time, position, and velocity operators are employed to represent variations in mooring

cable tension. The main conclusions of this study are as follows:

- In neural network models, the selected architectures demonstrate strong performance in predicting mooring line tension, with the Transformer model under a local attention mechanism (LA-Transformer) achieving the highest accuracy.
- In operator networks, the DeepONet combined with an attention mechanism (MIONet-ATT) shows significant improvement in prediction accuracy compared to the traditional DeepONet, along with better generalization capabilities.
- The accuracy of the operator network is closely related to the precision of the velocity in the input data. The drastic velocity changes during extreme sea conditions pose a challenge to the accuracy of operator networks. Nevertheless, the MIONet-ATT model still achieves reasonably high accuracy, indicating that operator networks hold great potential in the field of mooring line tension prediction.
- In summary, while relatively mature neural network models undoubtedly excel in purely data-driven applications, emerging operator networks are beginning to show promise, particularly due to their potential for integrating physical principles, which is highly encouraging.

Acknowledgement

The present work is Supported by the Open Fund of State Key Laboratory of Coastal and Offshore Engineering with grant No. LP2521, Guangdong Basic and Applied Basic Research Foundation (No. 2022B1515250002), and the Hong Kong SAR Government on the project Second-order direct analysis for the design of steel members with irregular cross-sections (PolyU 15203121/22E).

References

[1] Hall M, Goupee A. Validation of a lumped-mass mooring line model with DeepCwind semisubmersible model test data. Ocean Engineering. 2015;104:590-603.
[2] Chen L, Basu B, Nielsen SR. A coupled finite difference mooring dynamics model for floating offshore wind turbine analysis. Ocean Engineering. 2018;162:304-15.
[3] Zhang Y, Shi W, Li D, Li X, Duan Y. Development of a numerical mooring line model for a floating wind turbine based on the vector form intrinsic finite element method. Ocean Engineering. 2022;253:111354.
[4] Sidarta DE, Kyoung J, O'Sullivan J, Lambrakos KF. Prediction of offshore platform mooring line tensions using artificial neural network. International Conference on Offshore Mechanics and Arctic Engineering: American Society of Mechanical Engineers; 2017. p. V001T01A79.
[5] Qiao D, Li P, Ma G, Qi X, Yan J, Ning D, et al. Realtime prediction of dynamic mooring lines responses with LSTM neural network model. Ocean Engineering. 2021;219:108368.
[6] Wang Z, Qiao D, Yan J, Tang G, Li B, Ning D. A new approach to predict dynamic mooring tension using LSTM neural network based on responses of floating structure. Ocean engineering. 2022;249:110905.
[7] Zheng Z, Hu Z, Xie X, Huang W. Local scour around the monopile: A microscopic perspective using CFD-DEM. Ocean Engineering. 2024;299:117318.
[8] Ma H, Zhang S, Li B, Huang W. Local scour around the monopile based on the CFD-DEM method: Experimental and numerical study. Computers and Geotechnics. 2024;168:106117.
[9] Li B, Huang W, Chen X. Tendon fatigue analysis of tension leg platform using a new time-domain quasi-dynamic method. Marine Structures. 2025;99:103701.
[10] Huang W, Li B, Chen X. A new quasi-dynamic method for the prediction of tendon tension of TLP platform. Ocean Engineering. 2023;270:113590.
[11] Ning J-H, Liu S-W, Wan J-H, Huang W. Line-element formulation for upheaval buckling analysis of buried subsea pipelines due to thermal expansion. Adv Steel Constr. 2021;17:210-20.
[12] Ning J, Lin T, Liu S, Bai R, Huang W. Three-dimensional pipeline element formulation for global buckling analysis of submarine pipelines with sleeper. Marine Structures. 2023;90:103428.
[13] Wang C, Liu J, Li B, Huang W. The absolute nodal coordinate formulation in the analysis of offshore floating operations, Part II: Code validation and case study. Ocean Engineering. 2023;281:114650.
[14] Li B, Wang C. The absolute nodal coordinate formulation in the analysis of offshore floating operations Part I: Theory and modeling. Ocean Engineering. 2023;281:114645.
[15] Huang W, Tang X. Prediction of the dynamic response on the spread catenary mooring system for FPSO by long short-term memory method. Ocean Engineering. 2025;340:122113.
[16] Tang X, Huang W, Li X, Ma G. Prediction of mooring tension of floating offshore wind turbines by CNN-LSTM-ATT and Chebyshev polynomials. Ocean Engineering. 2025;331:121327.
[17] Payenda MA, Wang S, Jiang Z, Prinz A. Prediction of mooring dynamics for a semi-submersible floating wind turbine with recurrent neural network models. Ocean Engineering. 2024;313:119490.
[18] Das S, Saha P. A review of some advanced sensors used for health diagnosis of civil engineering structures. Measurement. 2018;129:68-90.
[19] Wan A, Chang Q, Khalil A-B, He J. Short-term power load forecasting for combined heat and power using CNN-LSTM enhanced by attention mechanism. Energy. 2023;282:128274.
[20] Li Y, Xiao L, Wei H, Kou Y, Yang L, Li D. A time–frequency physics-informed model for real-time motion prediction of semi-submersibles. Ocean Engineering. 2024;299:117379.
[21] Cao Q, Goswami S, Tripura T, Chakraborty S, Karniadakis GE. Deep neural operators can predict the real-time response of floating offshore structures under irregular waves. Computers & Structures. 2024;291:107228.
[22] Zhao J, Zhao Y, Zou L. A fully adaptive time–frequency coupling model using self-attention mechanism based on deep operator network for very short-term forecasting of ship motion. Physics of Fluids. 2024;36.
[23] Zhang Q, Zhang H, Zhao X, Ding J, Xu D. Multiple-input operator network prediction method for nonlinear wave energy converter. Ocean Engineering. 2025;317:120106.
[24] Thomsen JB, Bergua R, Jonkman J, Robertson A, Mendoza N, Brown C, et al. Modeling the TetraSpar floating offshore wind turbine foundation as a flexible structure in OrcaFlex and OpenFAST. Energies. 2021;14:7866.
[25] Salehinejad H, Sankar S, Barfett J, Colak E, Valaee S. Recent advances in recurrent neural networks. arXiv preprint arXiv:180101078. 2017.
[26] Graves A. Long short-term memory. Supervised sequence labelling with recurrent neural networks. 2012:37-45.
[27] Krizhevsky A, Sutskever I, Hinton GE. Imagenet classification with deep convolutional neural networks. Advances in neural information processing systems. 2012;25.
[28] Vaswani A, Shazeer N, Parmar N, Uszkoreit J, Jones L, Gomez AN, et al. Attention is all you need. Advances in neural information processing systems. 2017;30.
[29] Lu L, Jin P, Karniadakis GE. Deeponet: Learning nonlinear operators for identifying differential equations based on the universal approximation theorem of operators. arXiv preprint arXiv:191003193. 2019.
[30] Khanam R, YOLOv11 MH. an overview of the key architectural enhancements. Published online October 23, 2024. 2024. doi: 10.48550. arXiv preprint arXiv241017725.
[31] Tian Y, Ye Q, Doermann D. Yolov12: Attention-centric real-time object detectors. arXiv preprint arXiv:250212524. 2025.
[32] Chen Y, Yuan L, Qin L, Zhang N, Li L, Wu K, et al. A forecasting model with hybrid bidirectional long short-term memory for mooring line responses of semi-submersible offshore platforms. Applied Ocean Research. 2024;150:104145.
[33] Lee S, Shin Y. On the training and generalization of deep operator networks. SIAM Journal on Scientific Computing. 2024;46:C273-C96.